A Multi-Wavelength Study of Super Soft X-ray Sources in the Magellanic Clouds

Alida Odendaal

Submitted in fulfilment of the requirements for the degree
Magister Scientiae
in the Faculty of Natural and Agricultural Sciences,
Department of Physics,
University of the Free State,
South Africa

Date of submission: 10 February 2012

Supervised by: Prof P.J. Meintjes, Department of Physics

The financial assistance of the South African Square Kilometre Array Project towards this research is hereby acknowledged. Opinions expressed and conclusions arrived at, are those of the author and are not necessarily to be attributed to the NRF.

Abstract

Supersoft X-ray Sources (SSS) form a highly luminous class of objects that emit more than $\sim 90\%$ of their energy in the supersoft X-ray band, i.e. below 0.5 keV. They are generally believed to consist of a white dwarf with a more massive binary companion, resulting in thermal time-scale mass transfer to the white dwarf and associated accretion. The high accretion rate of material onto the white dwarf is sufficient to drive nuclear burning and accompanying soft X-ray emission on the white dwarf surface, and may imply the presence of an accretion disc and significant mass outflow from some of these sources. However, SSS do not form a homogeneous class and also include objects like planetary nebulae, symbiotic novae and cataclysmic variables exhibiting nova outbursts. To investigate the phenomenon of accretion and the nature of possible mass outflow in SSS, a sample of 3 candidate sources in the Magellanic Clouds were identified for optical spectroscopic and X-ray studies: CAL 83, N67 and SMC 13. The galactic symbiotic nova RR Tel was also included in the study due to the evidence for an accretion disc implied by the double-peaked Raman-scattered O VI emission. Signatures of disc accretion and mass ejection in close binary supersoft sources (CBSS) like CAL 83, may provide evidence that such systems can evolve towards another class of binary system, namely the cataclysmic variables. Optical spectroscopic studies of CAL 83, N67 and RR Tel were performed with the Southern African Large Telescope (SALT) and the SAAO 1.9-m Telescope, and archived *Chandra* and XMM-Newton observations of the sources SMC 13 and CAL 83 were also analysed. The optical spectra of CAL 83 exhibit evidence of line broadening due to radial motion in an accretion disc, and a signature of possible disc outflows is also present. A search for periodicity in the X-ray data of CAL 83 revealed indication of consistent periodic modulations at $P \sim 67$ s, which could possibly be associated with the rotation period of a spun-up white dwarf. The presence of a fast rotating WD could provide a mechanism to explain the outflow inferred from the optical spectrum. The widths of nebular emission lines of the planetary nebula N67, as well as that of typical nebular lines in RR Tel are consistent with the known expansion velocities of nebulae surrounding the central objects in these systems.

Keywords: supersoft X-ray source – binary system – white dwarf – rotation period – accretion – accretion disc – spectroscopy – emission line – orbital modulation – stellar evolution

Opsomming

Sagte X-straal bronne (SSS) vorm 'n klas van voorwerpe met 'n baie hoë helderheid, sodanig dat meer as $\sim 90\%$ van die energie in die sagte X-straal band (≤ 0.5 keV) uitgestraal word. Daar word in die algemeen geglo dat hierdie bronne bestaan uit 'n wit dwerg en 'n swaarder binêre geselster, wat aanleiding gee tot massa-oordrag na die wit dwerg op 'n termiese tydskaal, sowel as gepaardgaande akkresie. Die hoë akkresietempo van materiaal op die oppervlak van die wit dwerg is voldoende om kernbranding en gepaardgaande sagte X-straal emissie op die wit dwerg se oppervlak aan te dryf, en mag die teenwoordigheid van 'n akkresie-skyf en beduidende massa-uitvloei vanaf sommige van hierdie bronne impliseer. SSS vorm egter nie 'n homogene klas nie en sluit ook voorwerpe in soos planetêre newels, simbiotiese novas en kataklismiese veranderlikes wat nova-uitbarstings ondergaan. Om die verskynsel van akkresie en die aard van moontlike massa-uitvloei in SSS te ondersoek, is 'n seleksie van 3 kandidaatbronne in die Magellaanse Wolke geidentifiseer vir optiese spektroskopiese en X-straal studies: CAL 83, N67 en SMC 13. Die galaktiese simbiotiese nova RR Tel is ook in die studie ingesluit as gevolg van die bewyse vir 'n akkresie-skyf wat deur die dubbelpieke van die Raman-verstrooide O VI straling geïmpliseer word. Kenmerke van skyfakkresie en massa-uitwerping in binêre sagte X-straal bronne waarin die twee sterre naby aan mekaar is, soos CAL 83, kan bewyse verskaf dat sulke sisteme kan ontwikkel na 'n ander klas van binêre sisteme, naamlike die kataklismiese veranderlikes. Optiese spektroskopiese studies van CAL 83, N67 en RR Tel is uitgevoer met die Suider-Afrikaanse Groot Teleskoop (SALT) en die SAAO 1.9-m Teleskoop, en waarnemings uit die argiewe van *Chandra* en XMM-Newton is ook geanaliseer. Die optiese spektra van CAL 83 toon bewyse van lynverbreding as gevolg van radiale beweging in 'n akkresieskyf, en 'n kenmerk van 'n moontlike skyfuitvloei is ook teenwoordig. 'n Soektog na periodisiteit in die X-straal data van CAL 83 het 'n aanduiding van konsekwente periodiese modulasies by $P \sim 67$ s opgelewer, wat moontlik geassosieer kan word met die rotasieperiode van 'n opgespinde wit dwerg. Die teenwoordigheid van 'n vinnig-roterende wit dwerg kan 'n meganisme verskaf wat die uitvloei wat deur die optiese spektrum geïmpliseer word, kan verduidelik. Die wydtes van die emissie-lyne van die planetêre newel N67, sowel as die tipiese newel-lyne in RR Tel is in ooreenstemming met die bekende uitsettingsnelhede van die newels wat die sentrale voorwerpe in hierdie bronne omring.

Contents

Chapter 1

Introduction

The discovery of Supersoft X-ray Sources (SSS) in the 1980s with the Einstein satellite, and the subsequent discovery of more SSS with ROSAT, initiated wide interest in these systems. They were initially associated with accreting black holes or neutron stars, but later studies revealed that these systems are most probably associated with white dwarfs in binary systems accreting mass at a rate close to the Eddington limit. However, the SSS class also includes objects like symbiotic novae and planetary nebulae.

The association of close binary SSS with accreting white dwarfs in binary systems poses an interesting question related to their possible evolution to cataclysmic variable stars. This question becomes more relevant when the properties of cataclysmic variables like AE Aquarii, e.g. a short rotation period, can only be explained in terms of a high mass accretion history which required the magnetic white dwarf to have accreted mass at a rate comparable to the Eddington rate (e.g. Meintjes 2002; Schenker et al. 2002).

Associated with the high mass accretion rate is the transfer of angular momentum to the accreting white dwarf. This may result in the compact white dwarf being spun-up over time-scales comparable to that of the thermal time-scale over which mass transfer takes place. The accretion of material at a rate close to the Eddington limit may also sustain nuclear burning on the surface, resulting in supersoft X-ray emission.

The accretion of matter onto the surface of the white dwarf at a rate that can sustain nuclear burning implies the presence of a well-developed accretion disc in the system. The availability of the Southern African Large Telescope (SALT) with the Robert Stobie Spectrograph (RSS), as well as the capabilities of the Grating Spectrograph on the SAAO 1.9-m Telescope, opens up interesting possibilities for spectroscopic studies of these systems to identify features associated with extended

accretion discs and magnetosphere-disc interactions that may drive significant mass outflow from the system. Mass outflow may provide a significant drain of orbital angular momentum that could sculpt the evolution of these systems. In this regard, it is interesting to note that the recent discovery of circumbinary dust discs around several cataclysmic variables by the Spitzer Space Telescope (e.g. Brinkworth et al. 2007) provides new evidence for mass outflow from white dwarf systems.

Of special interest would be the possible identification of a modulation in the X-ray data that may be associated with the rotation period of an accreting white dwarf. The discovery of a spin modulation $P \lesssim 100$ s will provide a valuable framework within which the peculiar properties of a system like AE Aqr can be evaluated. Therefore, a sample of SSS has been identified for optical spectroscopic and X-ray studies. The Magellanic Cloud targets chosen are the close binary supersoft source CAL 83 in the Large Magellanic Cloud (LMC), the planetary nebula N67 (1E 0056.8-7154) in the Small Magellanic Cloud (SMC) and the peculiar short-period SSS in the SMC, 1E 0035.4-7230 (hereafter referred to as SMC 13). In addition to these main Magellanic Cloud sources, the symbiotic nova RR Telescopii in the Milky Way has also been included due to an intriguing mechanism signalling the presence of an accretion disc around the white dwarf, i.e. Raman scattering of O VI disc emission from a region near the secondary star.

The first component of the observational investigation involves the application of the technique of optical spectroscopy to the optical spectra of the binary systems CAL 83 and RR Tel, aiming to identify accretion disc and mass outflow signatures and the location of the associated emission regions. The optical spectral lines that were detected in N67 are also discussed, and their structure explained by considering the possible temperatures in the system and the expected expansion velocity of material moving away from the nucleus.

The second observational component comprises a discussion of X-ray data analysis for the sources SMC 13 and CAL 83. Results of spectral and timing analysis of *Chandra* data of SMC 13 is presented, which is utilized to constrain the white dwarf mass and orbital modulation in the binary system. A search for periodic X-ray modulation, possibly associated with rapidly rotating white dwarfs, has been carried out. Indications of such a modulation has been found in XMM-Newton data of CAL 83.

The thesis is structured as follows: In Chapter 2 some of the basic properties of binary emission are discussed. In Chapter 3, a discussion of spectroscopy as a diagnostic tool in astrophysical environments is presented. Chapter 4 presents a broad overview of the general properties of supersoft X-ray sources. In Chapter 5, a literature review of the targets selected for this study is presented, providing a multi-

wavelength perspective on relevant accretion-related phenomena in each source. The results of the optical spectroscopic and X-ray studies are presented in Chapter 6 and Chapter 7 respectively. Chapter 8 summarizes the main results and provides a perspective of future work that is perceived for the targets under discussion.

Chapter 2

Accretion in Binary Stars

2.1 Binary stars

Probably more than half the stars in the universe are actually multiple systems, consisting of two (or even more) stars orbiting their centre of mass. A binary system consists of two stars which are in continuous orbital motion about their centre of mass. The angle between the normal to the orbital plane and the line of sight to an earthly observer is called the *inclination* of the binary system (see e.g. Carroll and Ostlie 1996, Chapter 7). The orbital motion of the two stars is governed by Kepler's third law:

$$G(M_1 + M_2)P_{\rm orb}^2 = 4\pi^2 a^3 \ , \tag{2.1}$$

where G is the gravitational constant[1], M_1 and M_2 the masses of the two stars, $P_{\rm orb}$ the orbital period, and $a = a_1 + a_2$ the semi-major axis of the orbit (also called the binary separation). The distances a_1 and a_2 are the semi-major axes of the orbits of the two stars about the centre of mass of the system respectively.

If the two stars can be visually resolved, the system is called a *visual binary*. In most cases, the stars are too close together and/or too far away to be visually resolved, and the spectra of the two stars will then blend into one spectrum. However, if the inclination of such a system is larger than 0°, periodic Doppler shifts in the observed spectral lines can still reveal the binary nature of such a system. These are called *spectroscopic binaries*. More details related to spectral lines and the Doppler effect are presented in Chapter 3.

If only one of the stars has an observable spectrum, with the other one being too faint, the system is classified as a *single-lined spectroscopic* system. The changing radial component of the orbital velocity of the bright star will cause the central wavelength of each of its spectral lines to continuously oscillate about its rest wavelength at a period equal to the binary period $P_{\rm orb}$. If the spectrum of the other star

[1] A list of all the physical constants used in this work is provided in Appendix A.

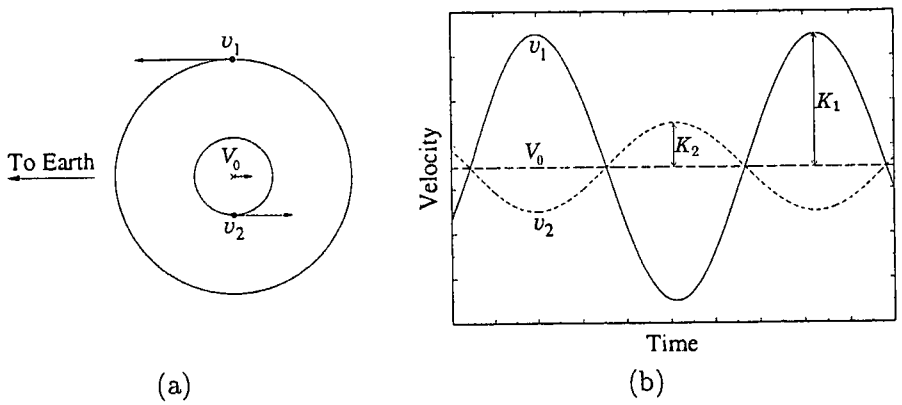

Fig. 2.1: (a) Circular orbits ($\varepsilon = 0$) of the components of a binary star about their centre of mass. (b) The corresponding sinusoidal radial velocity curves, with the semi-amplitudes K_1 and K_2 indicated. The radial velocity of the centre of mass is V_0 — this is also known as the systemic velocity of the system. It is assumed that $i = 90°$. (Adapted from Carroll and Ostlie 1996, p. 209, Fig. 7.5.)

is visible as well, the same periodic changes in the spectral line positions will be observed — however, when one star is moving towards us, the other will be moving away from us and vice versa, therefore the lines from the two stars will alternately oscillate in different directions about the rest wavelength. This is called a *double-lined spectroscopic* system.

A radial velocity curve can be constructed by measuring the wavelength changes of the spectral lines over time, and from this the binary period and also the semi-amplitude of the radial velocity curve, K, can be determined. An example of a double-lined spectroscopic system with an inclination of 90°, together with its radial velocity curves, is shown in Fig. 2.1. When the orbital eccentricity, ε, is non-zero, the radial velocity curves have a different shape and become skewed.

However, the orbits of many binaries are nearly circular, and therefore the eccentricity is very small ($\varepsilon \ll 1$). Then the speeds of the two stars are more or less constant, with v_1 and v_2 the speeds of the stars with masses M_1 and M_2 respectively. Then the speeds are given by

$$v_1 = \frac{2\pi a_1}{P_{\rm orb}} \qquad \text{and} \qquad v_2 = \frac{2\pi a_2}{P_{\rm orb}} \,. \tag{2.2}$$

Also, from the definition of the centre of mass,

$$\frac{M_1}{M_2} = \frac{a_2}{a_1} \,, \tag{2.3}$$

which, when substituting a_1 and a_2 from Eq. (2.2), yields

$$\frac{M_1}{M_2} = \frac{v_2}{v_1} \ . \tag{2.4}$$

The radial velocity semi-amplitudes for the two stars are given by

$$K_1 = v_1 \sin i \qquad \text{and} \qquad K_2 = v_2 \sin i \ , \tag{2.5}$$

Using Eq. (2.5), Eq. (2.4) can now be rewritten in terms of the semi-amplitudes:

$$\frac{M_1}{M_2} = \frac{K_2}{K_1} \ . \tag{2.6}$$

By using Eq. (2.2) and Eq. (2.5), the binary separation can be expressed as

$$a = a_1 + a_2 = \frac{P_{\rm orb}}{2\pi}(v_1 + v_2) = \frac{P_{\rm orb}}{2\pi}\left(\frac{K_1 + K_2}{\sin i}\right) \ . \tag{2.7}$$

Substituting the above into Kepler's third law, Eq. (2.1), yields the following expression for the total mass of the system:

$$M_1 + M_2 = \frac{P_{\rm orb}}{2\pi G}\frac{(K_1 + K_2)^3}{\sin^3 i} \ . \tag{2.8}$$

The period $P_{\rm orb}$ is represented by one full wavelength on the radial velocity curve of any one of the stars. If the inclination i is also known, it is evident that the sum of the masses can only be obtained if the radial velocities of *both* stars can be measured. After substitution of $K_2 = K_1 M_1/M_2$ from Eq. (2.6), Eq. (2.8) becomes

$$M_1 + M_2 = \frac{P_{\rm orb}}{2\pi G}\frac{K_1^3}{\sin^3 i}\left(1 + \frac{M_1}{M_2}\right) \tag{2.9}$$

or, after some rearrangement,

$$\frac{M_2^3}{(M_1 + M_2)^2}\sin^3 i = \frac{P_{\rm orb}}{2\pi G}K_1^3 \ . \tag{2.10}$$

The right-hand side of the equation above is known as the *mass function*, and depends only on the binary period and the radial velocity semi-amplitude of one of the stars. In the case of a single-lined spectroscopic binary, Eq. (2.6) does not provide information on the mass ratio, as K_2 is unknown, and the mass function can now only provide information on the masses of the stars if one of them can be estimated by e.g. its spectral class. In the case of a double-lined spectroscopic binary, exact values of M_1 and M_2 can be obtained if the inclination i is known or can be estimated.

In some binary systems, mass is transferred from one star (called the secondary)

to the other (called the primary). The transferred mass is "captured" or *accreted* by the primary star, with the subsequent release of energy. Of particular interest to our discussion is the class of *compact binaries*, where the primary star is either a white dwarf, a neutron star or a black hole. The next couple of sections provide an overview of the fascinating physical processes associated with mass transfer and accretion, and also of the properties of accretion discs, which often form around the primary star in accreting binaries. The discussion is mainly based on the approach of Frank, King and Raine (2002, Chapters 1, 4, 5 and 6), with contributions from similar discussions by Longair (1994, Chapter 16) and Vietri (2008, Chapters 6 and 7).

2.2 Accretion luminosity

Consider a star with mass M and radius R_*. The gravitational potential energy that will be released by a mass m accreting onto the surface of the star is given by

$$\Delta E_{\rm acc} = \frac{GMm}{R_*} \ . \tag{2.11}$$

If we assume that all the gravitational potential energy of the infalling matter is converted to radiation at the surface of the star, we are led to the following expression for the accretion luminosity:

$$L_{\rm acc} = \frac{GM\dot{m}}{R_*} \ . \tag{2.12}$$

It is evident that the accretion luminosity of a star with a certain compactness M/R_*, is dependent on the accretion rate $\dot{m}$. However, at high luminosity, the outward momentum which is transferred from the radiation to the accreting matter will have a significant effect on the accretion process. This means that there exists a maximum luminosity for a star with a given mass. This is known as the Eddington limit.

2.3 The Eddington limit

We can estimate the Eddington limit by making the following assumptions: the accretion is steady and spherically symmetric and the accreting material mainly consists of ionized hydrogen. The radiation exerts an outward force on the accreting material through Thomson scattering, which can be described as the interaction of photons with charged particles. The Thomson scattering cross-section for electrons is given by (Longair, 1992, p. 94)

$$\sigma_{\rm T} = \frac{8\pi}{3}\left(\frac{e^4}{m_{\rm e}^2 c^4}\right) = 6.65 \times 10^{-25} \ {\rm cm}^2 \ , \tag{2.13}$$

where e is the charge of an electron, m_e the mass of an electron and c the speed of light in vacuum. The scattering cross-section for protons is smaller than that for electrons by a factor of $m_e^2/m_p^2 \approx 3 \times 10^{-7}$, with m_p the mass of a proton. The effect of Thomson scattering will therefore be much larger for the free electrons than for the protons, but the attractive electrostatic force between the protons and electrons will drag the protons along.

It can be shown that the outward radial force of radiation with luminosity L acting on each proton-electron pair is equal to the rate at which the electron absorbs momentum from the radiation, i.e.

$$F_r = \frac{\sigma_T L}{4\pi r^2 c} , \tag{2.14}$$

where r is the radial distance from the source. The inward gravitational force acting on each proton-electron pair is given by

$$F_g = \frac{GM\,(m_p + m_e)}{r^2} \approx \frac{GMm_p}{r^2} . \tag{2.15}$$

The Eddington limit represents the situation where the inward and outward forces are equal ($F_g = F_r$) and the associated luminosity is called the Eddington luminosity L_E. Therefore, from Eq. (2.14) and Eq. (2.15),

$$L_E = \frac{4\pi cGMm_p}{\sigma_T} \approx 1.25 \times 10^{38} \frac{M}{M_\odot} \text{ erg s}^{-1} , \tag{2.16}$$

where $M_\odot$ is the solar mass[2]. (If the accretion only takes place over a fraction f of the star surface, the limiting luminosity will be fL_E.)

For accretion power exceeding L_E, the larger radiation pressure will inhibit accretion onto the compact object. If all the source luminosity was accretion driven, the source would hereby be switched off. However, if there were other contributions to the luminosity, e.g. nuclear fusion, the outer layers of source material would be blown off by the radiation pressure.

There exists a sub-class of low-mass X-ray binaries (LMXBs) called "X-ray bursters", which are characterized by rapid and dramatic X-ray bursts caused by explosive thermonuclear explosions on the surface of an accreting neutron star. The maximum burst luminosity of these sources was found to be $\approx 1.8 \times 10^{38}$ erg s^{-1}, which corresponds to the Eddington limit for a $1.4M_\odot$ neutron star according to Eq. (2.16) (Seward and Charles, 2010, p. 209-211). Because neutron stars in different binary systems have more or less the same mass, this maximum burst flux from an X-ray

[2]See Appendix A.

burster can therefore be used as a "standard candle" to estimate the distance to such a source.

2.4 Mass transfer in binary systems

The two main processes through which mass transfer in binary systems occurs, are Roche lobe overflow and stellar winds. Roche lobe overflow and accretion disc formation will be the focus of discussion in this section. In some cases where the Roche lobe of the secondary is not filled, mass transfer may still take place when the primary accretes matter from a stellar wind blowing from the secondary star. See e.g. Bondi and Hoyle (1944) for more details.

2.4.1 Roche lobe overflow

In the Roche approach, we consider the behaviour of a test particle influenced by the resultant gravitational field of two massive bodies orbiting each other — in this case, the two stars in the binary system. We assume the following: the stars are so massive that the test particle does not have an influence on their orbits, and they can be regarded as condensed point masses for the purposes of the analysis. This implies that the stars trace out Keplerian orbits about each other in a plane, according to Eq. (2.1). The gas flow between the stars must obey the Euler equation, which describes the conservation of momentum for each gas element. The general Euler equation is

$$\rho\frac{\partial \mathbf{v}}{\partial t} + \rho(\mathbf{v}\cdot\nabla)\mathbf{v} = -\nabla P + \mathbf{f} \ , \tag{2.17}$$

where $\mathbf{v}$ is the velocity field, ρ the density and P the pressure of the gas and $\mathbf{f}$ the density of external forces acting on the gas. Written in terms of a reference frame that rotates with the binary system, the Euler equation has the form

$$\frac{\partial \mathbf{v}}{\partial t} + (\mathbf{v}\cdot\nabla)\mathbf{v} = -\nabla\Phi_{\mathrm{R}} - 2\omega\times\mathbf{v} - \frac{1}{\rho}\nabla P \ , \tag{2.18}$$

where ω is the angular velocity of the binary system relative to an inertial frame, which can be expressed as

$$\omega = \left[\frac{GM}{a^3}\right]^{\frac{1}{2}}\mathbf{e} \tag{2.19}$$

if $\mathbf{e}$ is a unit vector perpendicular to the orbital plane. The first term on the left-hand side of Eq. (2.18) represents local acceleration, and the second the convection of momentum by velocity gradients. The term $-2\omega\times\mathbf{v}$ represents the Coriolis force per unit mass, while $-\frac{1}{\rho}\nabla P$ represents the effect of pressure gradients. The term $-\nabla\Phi_{\mathrm{R}}$ incorporates gravitational and centrifugal forces, where Φ_{R} is the Roche

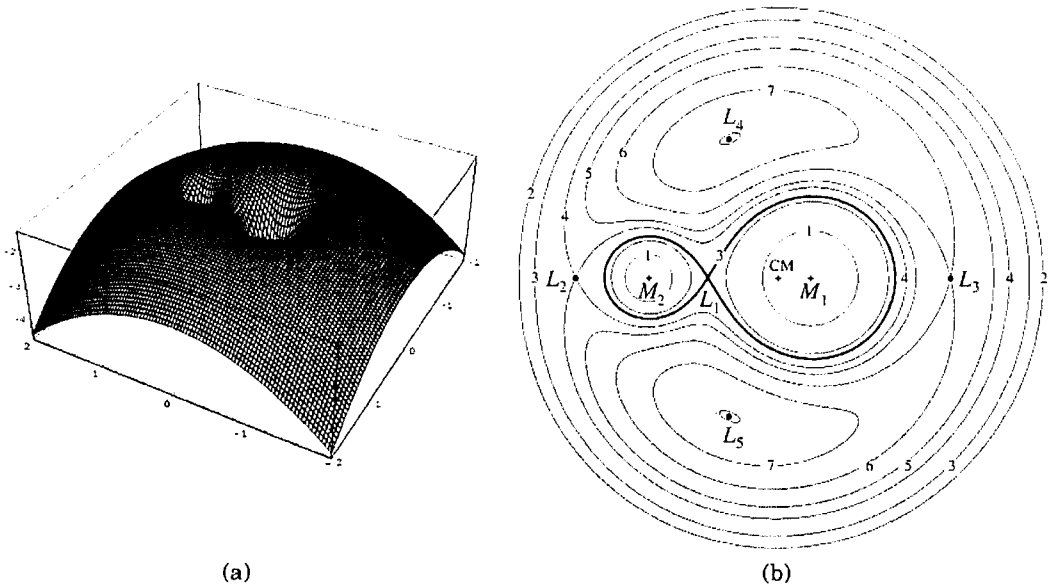

Fig. 2.2: (a) The Roche potential surface for a binary system with a mass ratio of $q = 0.25$ and (b) its sections in the orbital plane for Φ_R constant. The labels 1 to 7 indicates surfaces of increasing Φ_R. Also shown are the centre of mass (CM) and the Lagrange points $L_1 - L_5$. (Adopted from Frank et al. 2002, p. 51-52, Fig. 4.2. and Fig. 4.3.)

potential, given by

$$\Phi_R(\mathbf{r}) = -\frac{GM_1}{|\mathbf{r}-\mathbf{r}_1|} - \frac{GM_2}{|\mathbf{r}-\mathbf{r}_2|} - \frac{1}{2}(\omega \times \mathbf{r})^2 \ . \tag{2.20}$$

The vector $\mathbf{r}$ extends from the centre of mass of the system to any particular point at which $\Phi_R(\mathbf{r})$ is evaluated. The vectors $\mathbf{r}_1$ and $\mathbf{r}_2$ represent the positions of the centres of the primary and the secondary star respectively, also measured from the centre of mass. In Fig. 2.2, the three-dimensional Roche potential and its projection are plotted for a binary with a mass ratio of $q = M_2/M_1 = 0.25$; however, the qualitative features are applicable to any mass ratio. The figure-of-eight curve is especially significant. When it is plotted in 3 dimensions, it has a dumbbell shape which forms a teardrop shaped lobe around each star which is known as the Roche lobe of the star. The connecting point between the Roche lobes is L_1, the inner Lagrange point. L_1 is a saddle point in the function Φ_R, therefore material close to L_1 in one of the lobes will rather pass through L_1 to the other lobe than escaping the critical surface entirely.

If both of the stars are considerably smaller than their respective Roche lobes, and if the axial rotation of each is synchronous with the orbital motion, the surface of each will correspond to one of the circular equipotential surfaces within the Roche lobe that are illustrated in Fig. 2.2. No mass is transferred through the L_1 point and the binary is said to be *detached*. If one of the stars fills its Roche lobe, thermal motions

can push gas across the L_1 point into the Roche lobe of the primary star, where it will eventually accrete onto the primary. The lobe-filling condition can be maintained either by further evolutionary expansion of the secondary, or by shrinkage of its Roche lobe as a result of the loss of angular momentum from the binary system. Such a system is called a *semi-detached* binary. If both stars fill their Roche lobes at the same time, the system is classified as a *contact binary*.

2.4.2 Roche lobe geometry

The dimensions of each Roche lobe can be described in terms of a sphere with the same volume as the teardrop shaped lobe. The approximate formula of Eggleton (1983),

$$\frac{R_{\mathrm{L},2}}{a} = \frac{0.49q^{2/3}}{0.6q^{2/3} + \ln\left(1 + q^{1/3}\right)} , \tag{2.21}$$

is quite accurate for all values of the mass ratio q, where $R_{\mathrm{L},2}$ is the Roche lobe radius of the secondary. The Roche lobe radius of the primary ($R_{\mathrm{L},1}$) is obtained by replacing q with q^{-1}. According to Paczyński (1967), the following simplified formula can be used for $0.1 \lesssim q \lesssim 0.8$:

$$\frac{R_{\mathrm{L},2}}{a} = \frac{2}{3^{4/3}} \left(\frac{M_2}{M_1 + M_2}\right) . \tag{2.22}$$

The distance b_1 from the centre of the primary star to the L_1 point is given by a fitted formula of Plavec and Kratochvil (1964):

$$\frac{b_1}{a} = 0.500 - 0.227 \log q . \tag{2.23}$$

2.4.3 Binary evolution

Mass transfer from the secondary to the primary will obviously change the mass ratio q. The redistribution of angular momentum through the mass transfer can also cause a change in the period P_{orb} and binary separation a, which are directly linked to the sizes of the Roche lobes. It can easily be shown that the orbital angular momentum J of the binary system can be expressed as

$$J = M_1 M_2 \left(\frac{Ga}{M}\right)^{1/2} . \tag{2.24}$$

Logarithmic differentiation of Eq. (2.24) with respect to time yields

$$\frac{\dot{a}}{a} = 2\frac{\dot{J}}{J} + \frac{\dot{M}}{M} - 2\frac{\dot{M}_1}{M_1} - 2\frac{\dot{M}_2}{M_2} . \tag{2.25}$$

Since the secondary star is losing mass, $\dot{M}_2 < 0$. It can usually be assumed that all the material lost by the secondary is accreted onto the primary, therefore $\dot{M} = \dot{M}_1 + \dot{M}_2 = 0$. Then Eq. (2.25) becomes

$$\frac{\dot{a}}{a} = \frac{2\dot{J}}{J} + \frac{2(-\dot{M}_2)}{M_2}(1-q) \ . \tag{2.26}$$

In the case of *conservative mass transfer*, not only the total binary mass, but also the angular momentum is conserved. When substituting $\dot{J} = 0$ in Eq. (2.26), it becomes clear that the binary separation will increase ($\dot{a} > 0$) if conservative mass transfer takes place from the less massive to the more massive star ($q < 1$), and that transfer from the more massive to the less massive star ($q > 1$) will decrease the binary separation.

Logarithmic differentiation of Eq. (2.22) and the combination of the result with Eq. (2.26) yields

$$\frac{\dot{R}_{\mathrm{L},2}}{R_{\mathrm{L},2}} = \frac{2\dot{J}}{J} + \frac{2(-\dot{M}_2)}{M_2}\left(\frac{5}{6} - q\right) \ . \tag{2.27}$$

If $q > 5/6$, conservative mass transfer will shrink the Roche lobe down on the secondary star and any angular momentum loss from the system will enhance this effect. The Roche lobe overflow in such a case can become very unstable and occurs on a dynamical time-scale if the star has a convective envelope, and on a thermal time-scale if the star has a radiative envelope. If $q < 5/6$, conservative transfer will cause an expansion of the Roche lobe of the secondary, in which case overflow may only continue if the secondary expands or if the binary system loses angular momentum.

2.4.4 Time-scales

The different time-scales that are important in binary evolution are the following (e.g. Verbunt 1993), related to the secondary star:

- The *nuclear time-scale* is given by

$$\tau_{\mathrm{nuc}} \approx 10^{10}\left(\frac{M_2}{M_\odot}\right)\left(\frac{L_\odot}{L_2}\right) \ \mathrm{yr} \ , \tag{2.28}$$

  where $L_\odot$ is the solar luminosity. This is the time-scale on which the star expands due to hydrogen burning in its core.

- The *thermal time-scale*,

$$\tau_{\mathrm{th}} \approx 3.1 \times 10^7\left(\frac{M_2}{M_\odot}\right)^2\left(\frac{R_\odot}{R_2}\right)\left(\frac{L_\odot}{L_2}\right) \ \mathrm{yr} \ , \tag{2.29}$$

represents the time-scale on which the star tries to restore perturbed thermal equilibrium.

- The time-scale on which a star restores its perturbed hydrostatic equilibrium is the *dynamical time-scale*, i.e.

$$\tau_{\rm dyn} \approx 0.04 \left(\frac{M_\odot}{M_2}\right)^{1/2} \left(\frac{R_2}{R_\odot}\right) \text{ days} . \tag{2.30}$$

2.4.5 Accretion disc formation

The material transferred from the secondary star through the L_1 point usually has a very high specific angular momentum, preventing it from accreting directly onto the primary star. Unless the orbital period of the binary system is very long, the material transferred through L_1 (when viewed from the primary) will appear to move almost orthogonally to the line joining the two stars. This can be illustrated as follows: From Eq. (2.1), the binary separation can be conveniently expressed as $a = 2.9 \times 10^{11} (m_1)^{1/3} (1+q)^{1/3} P_{\rm day}^{2/3}$ cm, where $m_1 = M_1/M_\odot$. The component of the stream velocity orthogonal to the line of centres in a non-rotating frame is given by

$$v_\perp \sim b_1 \omega \sim (0.5a) \left(\frac{2\pi}{P_{\rm orb}}\right) \sim 10^7 (m_1)^{1/3} (1+q)^{1/3} P_{\rm day}^{-1/3} \text{ cm s}^{-1} . \tag{2.31}$$

However, if the secondary surface temperature near the L_1 point is $\sim 10^5$ K, then the local sound speed is $c_{\rm s} \sim 10^6$ cm s^{-1}, in which case $v_\perp$ will typically be highly supersonic.

After entering the Roche lobe of the primary, the material falls ballistically into the gravitational field of the primary star. During such a ballistic trajectory, gravitational potential energy is converted to kinetic energy, but there is no energy losses due to friction, shocks or radiation. The ballistic stream will intercept itself several times while falling through the Roche lobe of the primary, with energy loss occurring through shocks and the associated emission of radiation.

However, the material still possesses all the angular momentum it had when passing through L_1, and it will eventually tend to orbit the primary in the binary plane in an orbit corresponding to the lowest energy for the angular momentum it possesses, i.e. a circular Keplerian orbit. This Keplerian orbit must have the same associated specific angular momentum as the transferred gas had when emerging from L_1, and the Keplerian radius at which this condition is met, is called the circularization radius, $R_{\rm circ}$. It can be shown that the circularization radius for Roche lobe overflow

is given by

$$\frac{R_{\rm circ}}{a} = \left(\frac{4\pi^2 a^3}{GM_1 P_{\rm orb}}\right)\left(\frac{b_1}{a}\right)^4 ,$$

which becomes

$$\frac{R_{\rm circ}}{a} = (1+q)\left(\frac{b_1}{a}\right)^4$$

by means of Eq. (2.1). Applying the formula of Plavec and Kratochvil (1964) in Eq. (2.23) then yields

$$\frac{R_{\rm circ}}{a} = (1+q)(0.500 - 0.227\log q)^4 . \tag{2.32}$$

The radius $R_{\rm circ}$ is always smaller than $R_{\rm L,1}$ the Roche lobe radius of the primary. If the primary star is a compact object, $R_{\rm circ}$ will be larger than the radius of the primary. For some systems with an extended primary (e.g. the Algol variables), $R_{\rm circ}$ may be smaller than the radius of the primary star, resulting in the accreting material crashing onto the primary surface without the formation of an accretion disc.

The original ring of matter at $R = R_{\rm circ}$ will spread out to smaller and larger radii due to the effect of viscosity. The inner parts of the ring will transfer angular momentum to the outer parts and will spiral closer to the primary due to the angular momentum loss. The outer parts, having gained angular momentum, move to orbits farther away from the primary. This extended disc of material that is slowly spiralling in towards the primary star is called an accretion disc. The outer edge of the disc will be at a radius $R_{\rm out}$ obeying $R_{\rm circ} < R_{\rm out} < R_{\rm L,1}$. The angular momentum transferred to the outer edge of the disc is possibly recanalized into the binary orbit by tidal forces exerted by the secondary star on the outer region of the disc.

2.5 Accretion discs

2.5.1 Thin disc properties

In the *thin disc approximation*, it is assumed that the disc material lies very close to the plane $z = 0$ in cylindrical polar coordinates (R, ϕ, z) and the disc is essentially regarded as a two-dimensional gas flow.

The density and total mass of the disc material is much lower than that of the primary, therefore the self-gravity of the disc is negligible and the orbits of the spiralling material will be Keplerian, with the angular velocity given by

$$\Omega_{\rm K}(R) = \left(\frac{GM}{R^3}\right)^{1/2} \tag{2.33}$$

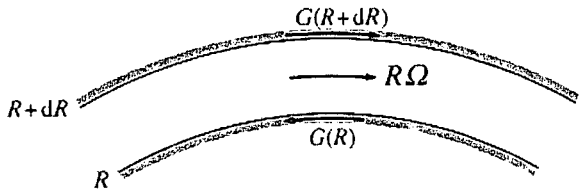

Fig. 2.3: Differential viscous torque acting on an accretion disc annulus. (Adopted from Frank et al. 2002, p. 68, Fig. 4.9.)

and the circular velocity by

$$v_{\rm K} = R\Omega_{\rm K}(R) = \left(\frac{GM}{R}\right)^{1/2} , \tag{2.34}$$

where, for the sake of brevity, M is now used instead of M_1 for the mass of the primary star. The spiralling motion can be described by a radial "drift" velocity v_R, which is a function of R and t. Near to the primary, v_R is negative, signifying movement towards the primary star.

It is quite obvious from Eq. (2.33) that gas elements at different radii will move at different angular velocities. This enables the transfer of angular momentum in directions orthogonal to the gas motion by the process of *shear viscosity*. It can be shown that the viscous torque exerted by the *outer* ring on the *inner* ring at a radius R in an accretion disc is given by

$$G(R) = 2\pi R\nu\Sigma R^2\Omega' , \tag{2.35}$$

where ν is the coefficient of kinematic viscosity, and $\Omega' = \frac{d\Omega}{dR}$. The mass per unit surface area is described by the surface density, Σ, which is a function of R and t. The viscous torque exerted by the *inner* ring on the *outer* ring has the same magnitude as the expression in Eq. (2.35), but with an opposite sign. Since $\Omega' < 0$, this means that the outer ring exerts a negative torque on the inner ring, confirming the braking of the inner layers as a result of the friction exerted by the outer layers.

An annulus of disc material between R and $R + dR$ is subject to the competing torques $G(R)$ and $G(R + dR)$, as shown in Fig. 2.3. $G(R + dR)$ will tend to remove angular momentum from the material, while increasing the orbital speed $v_{\rm K}$, corresponding to an orbit closer to the primary. $G(R)$ will tend to transfer angular momentum to the material, while decreasing the orbital speed $v_{\rm K}$, corresponding to a wider orbit. The difference between the two torques can be expressed as $\frac{\partial G(R)}{\partial R}dR$, which is the net torque trying to speed up the material. The rate of work by viscous

torques is therefore given by

$$\Omega \frac{\partial}{\partial R} G(R) dR = \frac{\partial}{\partial R}[G(R)\Omega] dR - G(R)\Omega' dR \ . \tag{2.36}$$

The first term on the right-hand side describes the transfer of angular momentum through the disc, while the second term represents the rate of viscous dissipation, i.e. the rate at which energy is "lost" to radiation. This energy is radiated from the upper and lower surfaces of the accretion disc. Each ring has an upper and a lower plane surface each with area $2\pi R dR$, therefore the rate of emission per unit plane surface area can be expressed as

$$D(R) = \frac{G(R)\Omega' dR}{2(2\pi R dR)} = \frac{G(R)\Omega'}{4\pi R} = \frac{1}{2}\nu\Sigma(R\Omega')^2 \ , \tag{2.37}$$

or, for a Keplerian disc, from Eq. (2.33),

$$D(R) = \frac{9}{8}\nu\Sigma\frac{GM}{R^3} \ . \tag{2.38}$$

The total mass of an annulus between R and $R + dR$ is $2\pi R\Sigma dR$, and its total angular momentum is $2\pi R\Sigma R^2\Omega dR$. By differentiating the mass expression with respect to time, it can be shown that the mass conservation equation is

$$R\frac{\partial\Sigma}{\partial t} + \frac{\partial}{\partial R}\left(R\Sigma v_R\right) = 0 \ . \tag{2.39}$$

The equation for the conservation of angular momentum is obtained in a similar way, and is given by

$$R\Sigma v_R \frac{\partial}{\partial R}(R^2\Omega) = \frac{1}{2\pi}\frac{\partial}{\partial R}G(R) \ , \tag{2.40}$$

after including the contribution of angular momentum transport by viscous torques, and after simplifying by means of Eq. (2.39) (assuming that $\partial\Omega/\partial t = 0$).

Eliminating v_R by combining Eq. (2.39) and Eq. (2.40), and by using the expressions for Ω and $G(R)$ in Eq. (2.33) and Eq. (2.35), the equation describing the time evolution of the surface density in a Keplerian disc is obtained:

$$\frac{\partial\Sigma}{\partial t} = \frac{3}{R}\frac{\partial}{\partial R}\left[R^{1/2}\frac{\partial}{\partial R}\left(\nu\Sigma R^{1/2}\right)\right] \ . \tag{2.41}$$

It also follows from Eq. (2.35) and Eq. (2.40) that the drift velocity is given by

$$v_R = \frac{-3}{\Sigma R^{1/2}}\frac{\partial}{\partial R}\left(\nu\Sigma R^{1/2}\right) \ . \tag{2.42}$$

It is evident that the kinematic viscosity ν plays a key role in the quantification

of the properties of the accretion disc. However, it is no trivial exercise to obtain an appropriate value for ν. In this regard, the famous α-prescription of Shakura and Sunyaev (1973) plays a very important role in the description of viscosity, and therefore of many structural properties, of accretion discs.

For any gas flow, the Reynolds number is defined as

$$\Re \approx \frac{L^2}{\nu T} = \frac{VL}{\nu} , \tag{2.43}$$

with L, V and T the typical dimensions of length, velocity and time for the flow. For small $\Re$, molecular viscosity plays a dominant role, while for large values, i.e. $\Re \geq 10^3$, the flow becomes turbulent. An estimate of the Reynolds number by considering typical parameters for accretion discs around compact objects yields $\Re \gtrsim 10^{12}$, and this may lead to the conclusion that the gas flow in an accretion disc is turbulent.

The problem with this possibility is that, since $\Omega' < 0$ in Keplerian discs, they are actually stable against hydrodynamic turbulence, i.e. the Rayleigh criterion

$$\frac{d}{dR}(R^2\Omega)^2 > 0 \tag{2.44}$$

is satisfied in the disc. Therefore, stabilizing Coriolis forces will tend to smooth out any hydrodynamic instabilities in the disc (see Balbus and Hawley (1998) and references therein). The stabilization will take place on a dynamical time-scale, which is of the order of the Keplerian period at that particular point in the disc. At the outer edge of the disc, this is of the order of ~ 1 hour.

In a turbulent flow, it is observed that the large-scale eddies divide into smaller and smaller whirls and eddies down to a microscopic scale. This process through which the kinetic energy of large-scale turbulent motion is successively subdivided until it contributes to the thermal motion of particles on atomic level, is known as a Kolmogorov cascade. For turbulent motion in an accretion disc near to the outer edge of the disc, the time required for the energy of turbulent motion to be subdivided to the scale of thermal motion, is of the same order as the dynamical time-scale (or Keplerian period as mentioned above). This means that the turbulent kinetic energy can be converted to thermal energy before the turbulence is smoothed out, and the higher local gas temperature can then increase the disc viscosity.

Even though hydrodynamic turbulence can not be sustained in a Keplerian disc, magneto-hydrodynamic (MHD) processes in a magnetized disc can succeed in creating sustainable turbulence. Coupling of fluid elements at different radii by magnetic

field lines may also be an effective way of transferring angular momentum in the disc. The origin of the magnetic fields may be related to dynamo effects. However, the exact nature and origin of MHD processes is still not quite clear.

If we can indeed consider the viscosity as turbulent, then the viscosity parameter can be expressed by $\nu \sim \lambda_{\rm turb} v_{\rm turb}$, where $\lambda_{\rm turb}$ is the scale of the turbulent eddies and $v_{\rm turb}$ is their turnover velocity. It can safely be assumed that $v_{\rm turb}$ is subsonic, otherwise shocks would most likely thermalize the turbulent motion. Also, $\lambda_{\rm turb} \lesssim H$. Thus, under the assumption of turbulence (which is not at all certain), the viscosity can be written as

$$\nu = \alpha c_{\rm s} H \ , \tag{2.45}$$

where we expect $\alpha \lesssim 1$. This is only a parametrization rather than a solution, as our uncertainty related to the viscosity is now just confined to α. However, the thin disc structure can be solved in terms of α, and observed properties of accreting systems can then be used to obtain empirical values of α. According to King, Pringle and Livio (2007), observational evidence suggests that, for thin, fully ionized discs, the typical range for α is $\sim 0.1 - 0.4$, while many theoretical models predict α-values that are at least an order of magnitude smaller than this. According to Balbus and Hawley (1998), typical values of α from three-dimensional MHD simulations range from $\sim 0.01 - 0.6$. However, the determination of appropriate values of α for different accretion disc scenarios is still a subject of considerable controversy.

2.5.2 Steady thin discs

When external conditions does not change on short time-scales, the disc structure is approximately in a steady state, i.e. $\partial/\partial t = 0$. Then the integration of the mass conservation equation, Eq. (2.39), yields $R\Sigma v_R =$ constant. This quantity represents the inward flow of mass through every point on the disc, and because $v_R < 0$, the mass accretion rate (in g s^{-1}) can be written as

$$\dot{m} = 2\pi R \Sigma (-v_R) \ . \tag{2.46}$$

Integration of the momentum conservation equation, Eq. (2.40) yields the following, where $G(R)$ is obtained from Eq. (2.35):

$$-\nu\Sigma\Omega' = \Sigma(-v_R)\Omega + \frac{C}{2\pi R^3} \ . \tag{2.47}$$

The integration constant C in the equation above is related to the rate of angular momentum transfer from the inner part of the disc to the primary star.

If the disc extends all the way to the surface of the primary star, mass accretion

occurs at the *boundary layer*. The angular velocity of the stellar material on the primary surface must be smaller than the Keplerian velocity to prevent break-up, i.e. $\Omega_* < \Omega_K(R_*)$. Therefore, the angular velocity in the disc increases with decreasing R according to Kepler's law, until it starts to decrease to the final value Ω_* (at $R = R_*$). The initial increase, followed by a decrease, implies that there is a radius $R = R_* + b$ where $\Omega' = 0$. The radius $R_* + b$ is defined to be the outer limit of the boundary layer with radial thickness b.

In practice, usually $b \ll R_*$. and Ω can then be approximated with its Keplerian value from Eq. (2.33) at the point where $\Omega' = 0$. When using this assumption, and $R = R_* + b \approx R_*$ in Eq. (2.47), the integration constant becomes

$$C = -\dot{m}(GMR_*)^{1/2} , \tag{2.48}$$

with the accretion rate given by Eq. (2.46). With this value of C, Eq. (2.47) yields

$$\nu\Sigma = \frac{\dot{m}}{3\pi}\left[1 - \left(\frac{R_*}{R}\right)^{1/2}\right] . \tag{2.49}$$

Eq. (2.49) can now be substituted into Eq. (2.38) to yield an expression for the viscous dissipation rate per unit surface area that is independent of viscosity:

$$D(R) = \frac{3GM\dot{m}}{8\pi R^3}\left[1 - \left(\frac{R_*}{R}\right)^{1/2}\right] . \tag{2.50}$$

As there is basically no vertical (i.e. in the z-direction) flow of matter through disc, hydrostatic equilibrium must hold in the z-direction. The external force on the disc elements is the gravitation of the primary, and for a thin disc, we assume that $z \ll R$. Then the equilibrium is described as follows by the z-component of the Euler equation, Eq. (2.17), with all the velocity terms equal to zero:

$$\frac{1}{\rho}\frac{\partial P}{\partial z} = \frac{-GMz}{R^3} . \tag{2.51}$$

The local sound speed is given by

$$c_s^2 = \frac{P}{\rho} , \tag{2.52}$$

and with H the vertical scaleheight of the accretion disc, we have $\partial P/\partial z \sim P/H$ and $z \sim H$. From Eq. (2.51), the scaleheight can then be expressed as

$$H \approx Rc_s\left(\frac{R}{GM}\right)^{1/2} = R\frac{c_s}{v_K} , \tag{2.53}$$

where $v_{\rm K}$ is given by Eq. (2.34). Because $z \sim H$, we have $H \ll R$, therefore it is required that

$$c_{\rm s} \ll v_{\rm K} = \left(\frac{GM}{R}\right)^{1/2} . \tag{2.54}$$

In other words, under the thin disc approximation, the local Keplerian velocity must be highly supersonic.

From Eq. (2.46) and Eq. (2.49), it is evident that the drift velocity can be expressed as

$$v_R = -\frac{3\nu}{2R}\left[1 - \left(\frac{R_*}{R}\right)^{1/2}\right]^{-1} , \tag{2.55}$$

therefore v_R is of the order ν/R. From the α-parametrization in Eq. (2.45), we obtain

$$v_R \sim \frac{\nu}{R} \sim \alpha c_{\rm s}\frac{H}{R} \ll c_{\rm s} , \tag{2.56}$$

proving that v_R is highly subsonic.

In situations where the thin disc approximation is valid, the temperature and pressure gradients are along the z-direction, and the vertical disc structure at a certain radius can be treated as a one-dimensional case of normal stellar structure. If the disc material is isothermal in the z-direction, solution of Eq. (2.51) yields

$$\rho(R,z) = \rho_c(R)e^{-z^2/2H^2} , \tag{2.57}$$

with $\rho_c(R)$ the central disc density (at $z = 0$). An approximate central density can be obtained with $\rho = \Sigma/H$.

The disc pressure can be expressed as the sum of the gas pressure and radiation pressure:

$$P = \frac{\rho k T_{\rm c}}{\mu m_{\rm p}} + \frac{4\sigma}{3c}T_{\rm c}^4 , \tag{2.58}$$

where μ is the mean molecular weight and σ the Stefan-Boltzmann constant, and it is assumed that $T(R,z) \approx T_{\rm c}(R) = T(R,0)$. If the disc is optically thick, i.e. $\tau = \rho H \kappa_{\rm R} = \Sigma\kappa_{\rm R} \gg 1$ (see Section 2.7 for a discussion of optical depth), the flux of radiant energy through a surface for which $z =$ constant is

$$F(z) = \frac{-16\sigma T^3}{3\kappa_{\rm R}\rho}\frac{\partial T}{\partial z} \sim \frac{4\sigma}{3\tau}T^4(z) , \tag{2.59}$$

where $\kappa_{\rm R}$ is the Rosseland mean opacity. If $T_{\rm c}^4 \gg T^4(H)$, it can be shown that the

dissipation rate per unit surface area in Eq. (2.50) can also be approximated as

$$D(R) = F(H) - F(0) = \frac{4\sigma}{3\tau} T_{\rm c}^4 \ . \tag{2.60}$$

The equations describing the structure of a steady, thin disc are summarized below. The eight unknowns, ρ, Σ, H, $c_{\rm s}$, P, $T_{\rm c}$, τ and ν, can be solved as functions of $\dot{m}$, M, R and α, or any other parameters determining ν.

$$\begin{aligned}
\rho &= \frac{\Sigma}{H} \\
H &= R c_{\rm s} \left(\frac{R}{GM} \right)^{1/2} \\
c_{\rm s}^2 &= \frac{P}{\rho} \\
P &= \frac{\rho k T_{\rm c}}{\mu m_{\rm p}} + \frac{4\sigma}{3c} T_{\rm c}^4 \\
D(R) &= \frac{4\sigma}{3\tau} T_{\rm c}^4 = \frac{3GM\dot{m}}{8\pi R^3} \left[1 - \left(\frac{R_*}{R} \right)^{1/2} \right] \\
\tau &= \Sigma \kappa_{\rm R}(\rho, T_{\rm c}) = \tau(\Sigma, \rho, T_{\rm c}) \\
\nu\Sigma &= \frac{\dot{m}}{3\pi} \left[1 - \left(\frac{R_*}{R} \right)^{1/2} \right] \\
\nu &= \nu(\rho, T_{\rm c}, \Sigma, \alpha, ...)
\end{aligned} \tag{2.61}$$

2.5.3 Solution for the standard α-model

The steady disc equations in the previous section can now be solved for the simple case where the viscosity is described by the α-parametrization in Eq. (2.45), and where ρ and $T_{\rm c}$ have such values that Kramer's law can be used to approximate the Rosseland mean opacity:

$$\kappa_{\rm R} = 5 \times 10^{24} \rho T_{\rm c}^{-7/2} \ {\rm cm}^2 \ {\rm g}^{-1} \ . \tag{2.62}$$

Also, the radiation pressure term, $(4\sigma/3c)T_{\rm c}^4$, is omitted from the fourth equation in the system (2.61). A value of 0.615 is used for μ, representing a fully ionized "cosmic" gas mixture. The equations in (2.61) is now solved algebraically, and the α-disc solution of Shakura and Sunyaev (1973) becomes the following, with

$f^4 = 1 - (R_*/R)^{1/2}$, $R_{10} = R/(10^{10}\ \mathrm{cm})$, $m_1 = M/M_\odot$ and $\dot{m}_{16} = \dot{m}/(10^{16}\ \mathrm{g\ s^{-1}})$:

$$\begin{aligned}
\Sigma &= 5.2\alpha^{-4/5}\dot{m}_{16}^{7/10}m_1^{1/4}R_{10}^{-3/4}f^{14/5}\ \mathrm{g\ cm^{-2}} \\
H &= 1.7\times10^{8}\alpha^{-1/10}\dot{m}_{16}^{3/20}m_1^{-3/8}R_{10}^{9/8}f^{3/5}\ \mathrm{cm} \\
\rho &= 3.1\times10^{-8}\alpha^{-7/10}\dot{m}_{16}^{11/20}m_1^{5/8}R_{10}^{-15/8}f^{11/5}\ \mathrm{g\ cm^{-3}} \\
T_\mathrm{c} &= 1.4\times10^{4}\alpha^{-1/5}\dot{m}_{16}^{3/10}m_1^{1/4}R_{10}^{-3/4}f^{6/5}\ \mathrm{K} \\
\tau &= 190\alpha^{-4/5}\dot{m}_{16}^{1/5}f^{4/5} \\
\nu &= 1.8\times10^{14}\alpha^{4/5}\dot{m}_{16}^{3/10}m_1^{-1/4}R_{10}^{3/4}f^{6/5}\ \mathrm{cm^2\ s^{-1}} \\
v_R &= 2.7\times10^{4}\alpha^{4/5}\dot{m}_{16}^{3/10}m_1^{-1/4}R_{10}^{-1/4}f^{-14/5}\ \mathrm{cm\ s^{-1}}
\end{aligned} \tag{2.63}$$

2.5.4 Disc spectrum

If the accretion disc is optically thick in the z-direction, every disc element radiates more or less as a blackbody with temperature $T(R)$, and the dissipation rate per unit surface area is given by

$$D(R) = \sigma T^4(R) \tag{2.64}$$

with the right-hand side representing the blackbody flux. From Eq. (2.50), we obtain

$$T(R) = \left\{\frac{3GM\dot{m}}{8\pi R^3\sigma}\left[1-\left(\frac{R_*}{R}\right)^{1/2}\right]\right\}^{1/4} \tag{2.65}$$

or, for $R \gg R_*$,

$$T(R) = T_*\left(\frac{R}{R_*}\right)^{-3/4} \qquad \text{where} \qquad T_* = \left(\frac{3GM\dot{m}}{8\pi R_*^3\sigma}\right)^{1/4}. \tag{2.66}$$

The spectrum emitted from each disc element is now approximated by the Planck function, i.e.

$$I_\nu = B_\nu = \frac{2h\nu^3/c^2}{e^{h\nu/kT(R)}-1}, \tag{2.67}$$

where the effect of the optically thin atmosphere of the disc has been neglected. (The radiation frequency ν used in the rest of this chapter is not to be confused with the viscosity parameter ν used earlier.) An observer situated at a distance D from the disc will observe a flux

$$F_\nu = \frac{4\pi h\cos i\nu^3}{c^2D^2}\int_{R_\mathrm{in}}^{R_\mathrm{out}}\frac{RdR}{e^{h\nu/kT(R)}-1}, \tag{2.68}$$

which is obtained by integrating I_ν over the whole disc, and using the fact that the solid angle subtended by each disc ring between R and $R+dR$ is $2\pi RdR\cos i/D^2$, where i is the binary inclination. For non-magnetic white dwarfs and neutron stars, the inner disc radius is equal to the stellar radius, i.e. $R_\mathrm{in} = R_*$; for magnetized

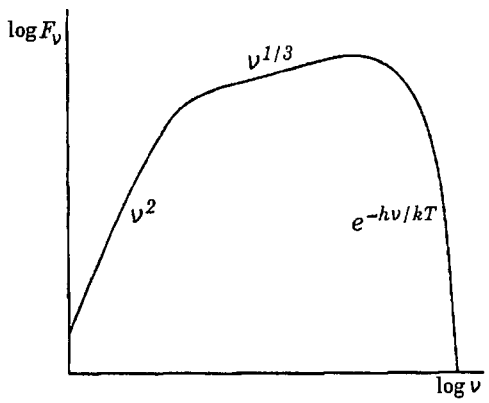

Fig. 2.4: A schematic diagram of the emission spectrum of an optically thick accretion disc, illustrating the 3 regions with different ν-dependencies. (Adopted from Longair 1994, p. 152, Fig. 16.7.)

objects, $R_{\rm in} = R_M$ (see Section 2.6.2).

The shape of the spectrum given by Eq. (2.68) is shown in Fig. 2.4. For $\nu \ll kT(R_{\rm out})/h$, the Planck function has the Rayleigh-Jeans form, i.e. $2kT\nu^2/c^2$, yielding $F_\nu \propto \nu^2$, while for $\nu \gg kT_*/h$, the Planck function has the Wien form, i.e. $2h\nu^3 c^{-2} e^{-h\nu/kT}$ and the spectrum has an exponential form. For frequencies in between, it can be shown that $F_\nu \propto \nu^{1/3}$.

The "flattened" region of the spectrum in Fig. 2.4 where $F_\nu \propto \nu^{1/3}$ is considered to be characteristic of a disc spectrum. However, this part of the curve is only substantial if the outer disc temperature is much lower than that of the inner disc, or, in other words, if $R_{\rm out} \gg R_{\rm in}$. For white dwarfs, $R_{\rm out} \sim 10^2 R_{\rm in}$, and the expected disc spectrum is very close to an ordinary blackbody curve.

In addition to the continuum emission discussed above, the observation of emission lines can be expected from the optically thin gas in the accretion disc atmosphere. Due to the rotational movement of the disc, such lines often have double-peaked profiles, which are explained in Section 3.4.3.

2.5.5 Disc luminosity

The luminosity of a disc annulus between R_1 and R_2 is obtained by integrating the energy flux in Eq. (2.50) over the surface area (upper and lower) of the annulus, and is given by

$$L(R_1, R_2) = \frac{3GM\dot{m}}{2} \left\{ \frac{1}{R_1} \left[1 - \frac{2}{3} \left(\frac{R_*}{R_1} \right)^{1/2} \right] - \frac{1}{R_2} \left[1 - \frac{2}{3} \left(\frac{R_*}{R_2} \right)^{1/2} \right] \right\} . \quad (2.69)$$

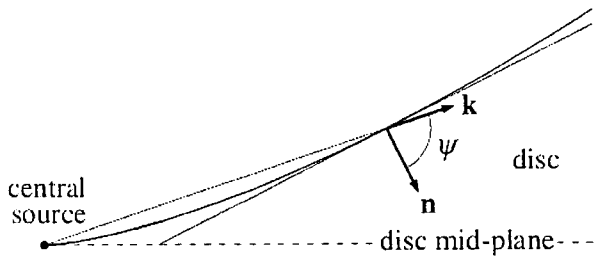

Fig. 2.5: The geometry of an irradiated accretion disc. The unit vector **k** indicates the direction of the incident radiation, and the unit vector **n** is normal to the disc surface. (Adopted from Frank et al. 2002, p. 130, Fig. 5.16.)

The intrinsic luminosity of the whole disc is obtained by setting $R_1 = R_*$ and $R_2 \to \infty$, yielding

$$L_{\rm disc} = \frac{GM\dot{m}}{2R_*} \ , \tag{2.70}$$

and comparison with Eq. (2.12) then shows that the disc luminosity is equal to one half of the accretion luminosity. The remaining half is released by other mechanisms close to the primary star.

2.5.6 Irradiated accretion discs

Accretion discs are often irradiated by the central object, and in some circumstances the disc luminosity arising from irradiation by the central star can even exceed the accretion luminosity of the disc itself. In this section, the effective temperatures for irradiated and unirradiated discs will be compared in order to quantify the importance of this effect. The geometry of an irradiated accretion disc is shown in Fig. 2.5. The details of changes in the physical structure of the disc by irradiation (disc "warping") will not be discussed here. More information can be found in Frank et al. (2002, Section 5.10).

We will consider the central star as a point source with luminosity $L_{\rm pt}$. This luminosity is defined by $L_{\rm pt} = 4\pi R_*^2 \sigma T_{\rm eff}^4$, where $T_{\rm eff}$ is the effective source temperature and R_* the average source radius (which is non-zero, even though we consider it as a point source in the analysis below!). The flux from the central star at disc radius R is $L_{\rm pt}/4\pi R^2$, and the flux entering the disc surface at R is

$$F = \frac{L_{\rm pt}}{4\pi R^2}(1-\beta)\cos\psi \ , \tag{2.71}$$

where β is the fraction of incident radiation that is scattered from the disc surface without being absorbed (also called the albedo). Here ψ is the angle between the disc normal and the incident radiation (the vectors **n** and **k** in Fig. 2.5). It can be shown that $\cos\psi \approx dH/dR - H/R$. If we define an effective blackbody temperature $T_{\rm pt}$ that results from the irradiation of the disc at R by the central point source, it

follows from Eq. (2.71) that

$$T_{\rm pt}^4 = \frac{L_{\rm pt}}{4\pi R^2 \sigma}\left(\frac{H}{R}\right) g(1-\beta) \tag{2.72}$$

or

$$\left(\frac{T_{\rm pt}}{T_{\rm eff}}\right)^4 = \frac{H}{R}\left(\frac{R_*}{R}\right)^2 g(1-\beta)\ , \tag{2.73}$$

where $g = \left[\frac{d\ln H}{d\ln R} - 1\right]$. From the second equation in the system (2.63), it is evident that $H \propto R^{9/8}$ for an unirradiated disc. It can be shown that $H \propto R^{9/7}$ for a disc which acquires all its luminosity from irradiation by the central star. Therefore the factor g will lie between 1/8 and 2/7. Because the ratio H/R has more or less a constant value everywhere in the disc, $T_{\rm pt} \propto R^{-1/2}$. Therefore, for large values of R (i.e. a large disc) the temperature $T_{\rm pt}$ resulting from irradiation can dominate the effective temperature of the disc itself, which, from Eq. (2.66), falls off as $R^{-3/4}$. Combining Eq. (2.66) with Eq. (2.72) yields the relationship between these two temperatures:

$$\left(\frac{T_{\rm pt}}{T(R)}\right)^4 = \frac{2}{3}\frac{RL_{\rm pt}}{GM\dot{m}}\frac{H}{R}g(1-\beta)\ . \tag{2.74}$$

It can be shown that the spectrum of an irradiated disc is similar to that of an unirradiated disc, exhibiting a Rayleigh-Jeans law for small frequencies and the Wien law for large frequencies. However, in the intermediate region, there is a considerable difference, and it is found that $F_\nu \propto \nu^{-1}$.

The discussion above is based on the assumption that the central source can be regarded as a point source. However, in some cases, and often in discs in white dwarf systems, this is not quite a valid assumption, and it is necessary to perform a more complicated analysis for an extended central source. Such a consideration yields

$$\begin{aligned} \left(\tfrac{T_{\rm ex}}{T_{\rm eff}}\right)^4 &\to \tfrac{(1-\beta)}{2} && \text{for } R \to R_* \\ \left(\tfrac{T_{\rm ex}}{T_{\rm eff}}\right)^4 &\approx \tfrac{2}{3\pi}\left(\tfrac{R_*}{R}\right)^3(1-\beta) && \text{for } R \gg R_* \end{aligned}\ , \tag{2.75}$$

where $T_{\rm ex}$ is the effective temperature caused by the irradiation of the disc by the extended central source. Therefore it turns out that $T_{\rm ex}$ has the same dependence on the radius as the effective temperature of the disc itself ($\propto R^{-3/4}$) for large values of R. Comparison with Eq. (2.66) yields

$$\left(\frac{T_{\rm ex}}{T(R)}\right)^4 = \frac{4}{9\pi}\frac{L_*}{L_{\rm acc}}(1-\beta)\ , \tag{2.76}$$

where $L_* = 4\pi R_*^2 \sigma T_*^4$, and $L_{\rm acc}$ is given by Eq. (2.12).

The heating of the accretion disc by X-rays from the central compact object can also

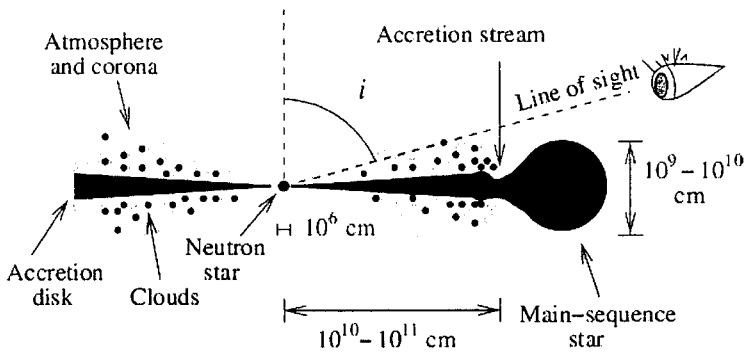

Fig. 2.6: Schematic representation of an accretion disc corona in a LMXB with a neutron star primary. At high inclinations, an observer may still see scattered X-rays from the corona, even though the neutron star itself is obscured. (Adopted from Jimenez-Garate, Raymond and Liedahl 2002, Fig. 1.)

cause the formation of a hot, extended disc atmosphere or *corona*, as illustrated in Fig. 2.6 for a neutron star in a LMXB (see Seward and Charles 2010, p. 207-209). A similar corona can form in white dwarf systems, but a lower effective primary temperature will decrease the temperature and extent of the corona.

2.6 Accretion onto a compact object

The nature of the mechanism by which the other half of the accretion luminosity is released at the primary star depends strongly on the nature of the primary, and specifically, on the magnitude of the primary's magnetic field. In compact binaries, two basic mechanisms can be distinguished: boundary layer accretion and column accretion onto the polar caps of a magnetized compact object.

2.6.1 Boundary layer accretion

When a magnetic field is absent or negligible, the accretion disc will terminate at the surface of the star. Accretion will take place in a thin layer with thickness b onto the primary surface. The angular velocity relationships in the vicinity of the boundary layer were already explained in Section (2.5.2).

The radial component of the Euler equation, Eq. (2.17), can be written as

$$\frac{1}{2}\frac{\partial v_R^2}{\partial R} + \frac{1}{\rho}\frac{\partial P}{\partial R} - \frac{v_\phi^2}{R} + \frac{GM}{R^2} = 0 \,, \tag{2.77}$$

where the external force has a centrifugal (v_ϕ^2/R) and a gravitational (GM/R^2) component. Since the angular velocity of material in the boundary layer is smaller than the angular Keplerian velocity, i.e. $\Omega < \Omega_{\rm K}(R_*)$, we also have $v_\phi < v_{\rm K} = \sqrt{GM/R}$. The gravity term in the equation above must therefore be balanced by

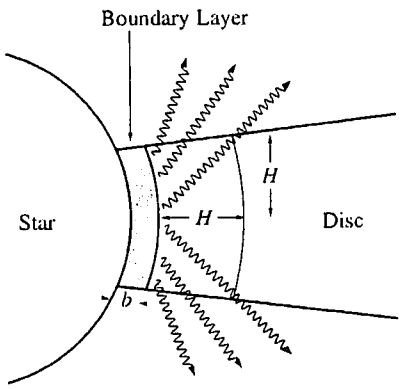

Fig. 2.7: An optically thick boundary layer (not drawn to scale). (Adopted from Frank et al. 2002, p. 156, Fig. 6.2.)

either the first or the second term on the left-hand side. From Eq. (2.56), we know that $v_R \ll c_\mathrm{s}$, therefore the pressure gradient is expected to be dominant relative to the term containing v_R. From the expression for the local sound speed given by Eq. (2.52), and by using $\partial/\partial R \sim b^{-1}$, Eq. (2.77) becomes

$$\frac{c_\mathrm{s}^2}{b} \approx \frac{GM}{R_*^2} \,, \tag{2.78}$$

with which b can be determined. Evaluating H at R_* by means of Eq. (2.53) yields $H = R_* c_\mathrm{s} [R_*/(GM)]^{1/2}$, and we also find that $b = H^2/R_* \ll H \ll R_*$. Deceleration of the accreting material occurs because of the significant pressure gradient, and this is accompanied by an increase in the local temperature compared to adjacent regions where the centrifugal force instead of the pressure gradient provides support against gravitation. The temperature excess causes a radiation excess, and if the boundary layer is assumed to be optically thick, it can be approximated as a blackbody emitter.

The boundary layer geometry is illustrated in Fig. 2.7. The radiation from the boundary layer passes through a region with radial extent $\sim H$ on the upper and lower disc faces. The area associated with the blackbody emission is $\sim 2 \times 2\pi R_* H$, and because the associated luminosity is known to be $\frac{1}{2} L_\mathrm{acc} = GM\dot{m}/2R_*$, the effective blackbody temperature of the boundary layer is given by

$$4\pi R_* H \sigma T_\mathrm{BL}^4 \sim \frac{GM\dot{m}}{2R_*} \,. \tag{2.79}$$

Comparison with Eq. (2.66) shows that

$$T_\mathrm{BL} \sim \left(\frac{R_*}{3H}\right)^{1/4} T_* \,, \tag{2.80}$$

or, with $c_{\rm s}^2 = P/\rho \sim kT_*/\mu m_{\rm p}$,

$$T_{\rm BL} \sim T_* \left(\frac{T_{\rm S}}{T_*}\right)^{1/8} , \tag{2.81}$$

with

$$T_{\rm S} = \frac{3GM\mu m_{\rm p}}{8kR_*} \tag{2.82}$$

the shock temperature that would have been associated with radial accretion onto the star.

2.6.2 Accretion onto magnetized objects

Alfvén radius

White dwarfs and especially neutron stars often have magnetic fields that range between $10^6 - 10^{12}$ G, which is strong enough to disrupt the flow of material in an accretion disc. As a simple approximation, the disruption of an accretion flow that is essentially spherical far from the star will be considered. If the magnetic field has a dipole nature, the magnetic field strength varies as $B \sim \mu_{\rm m}/r^3$ at a radial distance r from the star, where $\mu_{\rm m} = B_* R_*^3$ is the magnetic moment. The associated magnetic pressure is given by

$$P_{\rm mag} = \frac{B^2}{8\pi} = \frac{\mu_{\rm m}^2}{8\pi r^6} , \tag{2.83}$$

which increases sharply as r decreases. At a certain radius r_M, which is the spherical Alfvén radius, the magnetic pressure will start to exceed the ram pressure and gas pressure of the accreting flow, which will then be controlled by the magnetic field for $r < r_M$. It can be shown that in spherically symmetric accretion, the flow velocity close to the star is highly supersonic and close to the free-fall value of $(2GM/r)^{1/2}$, therefore the influence of the ram pressure (ρv^2) is much more important than that of the gas pressure ($\rho c_{\rm s}^2$). Also, because $\rho(-v)$ represents the inward flux of material, we have $|\rho v| = \dot{m}/4\pi r^2$. Therefore, by setting $P_{\rm mag}(r_M) = \rho v^2|_{r_M}$, we obtain

$$r_M = 2^{-3/7} G^{1/7} \dot{m}^{-2/7} M^{1/7} \mu_{\rm m}^{4/7} = 5.1 \times 10^8 \dot{m}_{16}^{-2/7} m_1^{-1/7} \mu_{30}^{4/7} \text{ cm} , \tag{2.84}$$

where $\mu_{30} = \mu_{\rm m}/(10^{30}$ G cm$^3)$. As $\mu_{30} \approx 1$ for typical values of B_* and R_* for magnetized white dwarfs and neutron stars, the order of r_M above suggests that the disruption of the disc structure may occur far enough from the primary surface to be an observable effect.

Returning from spherically symmetric accretion to disc accretion; we need to find the cylindrical radius R_M at which the magnetic torque on the disc is equal to the viscous torque $G(R_M)$. Finding an expression for the magnetic torque is quite involved, and many estimates of the resulting cylindrical Alfvén radius R_M shows it

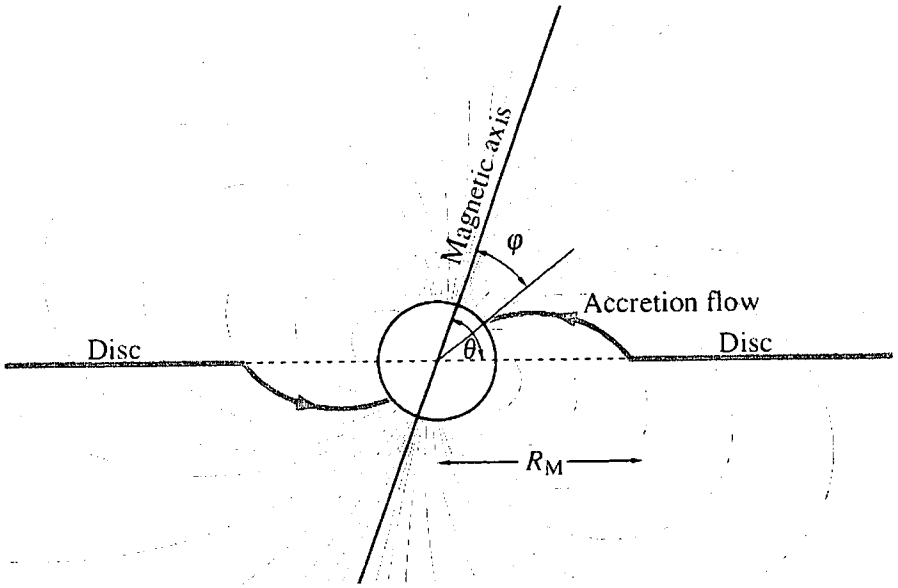

Fig. 2.8: Cross-section view of the accretion of material from a disc onto the polecaps of the magnetized white dwarf or neutron star. (Adopted from Frank et al. 2002, p. 161, Fig. 6.4.)

to be of the order of r_M; typically

$$R_M \sim 0.5 r_M = 2.6 \times 10^8 \dot{m}_{16}^{-2/7} m_1^{-1/7} \mu_{30}^{4/7} \text{ cm} , \tag{2.85}$$

although other estimates yield values that are up to 4 times larger. The exact results will also depend on the angle θ between the disc plane and the inclination of the dipole axis. Rewriting Eq. (2.85) in terms of the accretion luminosity, with parametrizations applicable to white dwarfs and neutron stars yields

$$R_M \sim \begin{cases} 2.8 \times 10^8 m_1^{1/7} R_9^{-2/7} L_{33}^{-2/7} \mu_{30}^{4/7} \text{ cm} \\ 1.5 \times 10^8 m_1^{1/7} R_6^{-2/7} L_{37}^{-2/7} \mu_{30}^{4/7} \text{ cm} \end{cases} \tag{2.86}$$

where $R_9 = R/(10^9 \text{ cm})$, $L_{33} = L_{\rm acc}/(10^{33} \text{ erg s}^{-1})$, etc. Inside $R = R_M$, the accreting material leaves the disc structure and falls in towards the polecaps along the magnetic field lines, as illustrated in Fig. 2.8.

The primary star and its magnetic field pattern rotates with angular velocity Ω_*, generally in the same direction as the disc rotation. The "fastness parameter" is defined as

$$\omega_* = \frac{\Omega_*}{\Omega_{\rm K}(R_M)} . \tag{2.87}$$

For steady accretion of material along the fieldlines, it is required that $\omega_* < 1$, otherwise particles at R_M will be ejected centrifugally.

For some white dwarf systems with $P_{\rm orb} \lesssim 4$ h, the magnetic moment is large enough to yield $R_M > a$. In these systems, called polars, no accretion disc is formed and the accretion stream couples directly with the magnetic field, whereafter it flows to the polecap regions. For weaker magnetic fields or longer periods, an accretion disc can form, even though it can be disrupted at R_M as shown in Fig. 2.8. The most basic condition for disc formation is that the minimum distance of approach ($\sim 0.5 R_{\rm circ}$) of the accreting stream to the white dwarf should be larger than the "obstacle" that the magnetosphere presents to the flow, which may be estimated to have a size of $\sim 0.37 r_M$.

Accreting polecap area

If plasma instabilities are neglected, it is evident that material can not accrete outside of a polecap with half-angle φ, since the field lines crossing the star surface at half-angles larger than φ cross the disc plane inside R_M, an area which is not accessible to accreting material (see Fig. 2.8). It can easily be shown that the area of an accreting polecap as a fraction of the total stellar surface is

$$f \sim \frac{\pi (R_* \sin \varphi)^2}{4\pi R_*^2} = \frac{R_* \sin^2 \theta}{4 R_M} \ . \tag{2.88}$$

If accretion takes place on both polecaps, the fraction is simply doubled, and can be approximated by

$$f \sim \frac{R_*}{2 R_M} \tag{2.89}$$

if θ is close to 90°. Typical values for f are between 10^{-1} and 10^{-4}.

Column accretion onto white dwarfs

We will now take a closer look at what happens to the accretion stream after being channelled toward the polecaps. The structural configuration that forms is known as an *accretion column*. Because the white dwarf case is the most applicable to supersoft X-ray binaries, the following overview will only consider column accretion onto the polecap of a white dwarf. Column accretion onto magnetized neutron stars has similarities to the white dwarf case, but extreme conditions on the neutron star surface makes a clear-cut analysis very challenging. More information on column accretion in neutron stars can be found in Frank et al. (2002, Section 6.5).

The main effect of the magnetic field on the column structure in the polecap region is to channel the accreting material onto the polecaps, and to confine electron transport processes (e.g. thermal conduction) to take place only along the direction of the fieldlines. As the flow is approximately radial, it is quite similar to spherically symmetric accretion. It has already been mentioned that the infalling material is

highly supersonic and virtually in free-fall in the latter case, with free fall velocity $v_{ff} = \sqrt{2GM/R}$. In order to accrete onto the white dwarf surface, the material has to be decelerated quite dramatically, and therefore the formation of a strong shock in the column is expected. Because $m_{\rm p} \gg m_{\rm e}$, the ions in the accretion stream carries essentially all the kinetic energy.

It can be shown that the ions are stopped above the white dwarf photosphere for all reasonable situations within a single accretion column. Therefore the material is slowed down by a strong shock before reaching the photosphere. In such a shock region, dissipative processes convert most of the ordered kinetic energy of the supersonic accretion flow into the random motion of the post-shock particles (i.e. into heat). For an adiabatic shock, the post-shock gas below it has a velocity

$$-v_2 = \frac{v_{ff}}{4} = 1.3 \times 10^8 m_1^{1/2} R_9^{-1/2} \text{ cm s}^{-1} \ . \tag{2.90}$$

The sound speed of the post-shock gas can be shown to be $\sqrt{5}v_{ff}/4 > v_2$, therefore v_2 is subsonic. The temperature of the shocked gas is given by Eq. (2.82), and can also be expressed as

$$T_{\rm S} = 3.7 \times 10^8 m_1 R_9^{-1} \text{ K} \ . \tag{2.91}$$

The processes by which this shock-heated gas is cooled must now be considered. The high temperature $T_{\rm S}$ of the gas suggests Bremsstrahlung to be the dominating radiative cooling mechanism, with subsequent emission in the form of hard X-rays. If the accretion column is "tall and thin", the cooling region below the shock front will be optically thick in the radial direction, but optically thin in the "horizontal" direction. However, if the accretion column is "short and fat", the optical thickness in the radial direction can be smaller than that in the "horizontal" direction. The absorption effects in different directions in the accretion column is therefore dependent on its geometry, which then determines the direction of X-ray beaming. The basic structure of an accretion column is shown in Fig. 2.9.

However, a substantial fraction of the radiation from the cooling region will be radiated or transported to the white dwarf photosphere at the base of the accretion column, where it will be absorbed and re-emitted. The re-emitted spectrum will probably closely resemble that of a blackbody because of the large optical depths below the white dwarf surface. The typical associated blackbody temperature is given by

$$T_b = \left(\frac{L_{\rm acc}}{4\pi R^2 f \sigma} \right)^{1/4} = 1 \times 10^5 \dot{m}_{16}^{1/4} f_{-2}^{-1/4} m_1^{1/4} R_9^{-3/4} \text{ K} \ , \tag{2.92}$$

where f is once again the fraction of the white dwarf surface that forms part of the accretion column base, and $f_{-2} = 10^2 f$. The typical value of T_b shows that the blackbody radiation will mainly consist of soft X-ray photons, with energies much

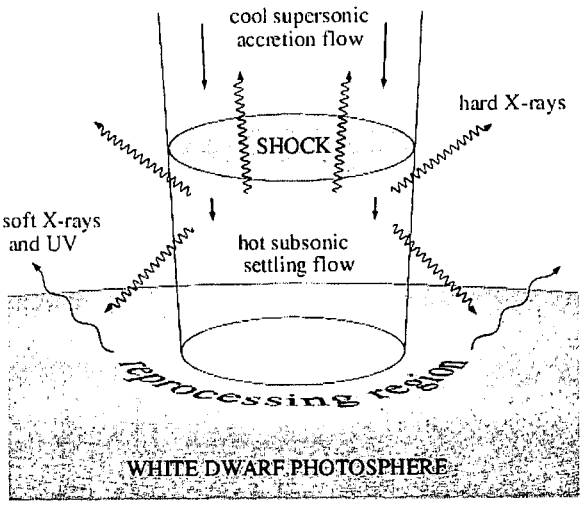

Fig. 2.9: Structure of a white dwarf accretion column. (Adopted from Frank et al. 2002, p. 178, Fig. 6.11.)

smaller than that of the hot accreting matter below the shock region.

This constitutes another possible cooling mechanism, as the electrons can interact with the soft photons through inverse Compton scattering — the photons are "up-scattered" to higher energy, while the electron gas will be cooled. Cyclotron emission will also be a cooling factor in the presence of a magnetic field, but will generally not be a major cooling mechanism, but rather an important signature process. Only at very low accretion rates or very large magnetic fields will it substantially contribute to the total accretion luminosity.

Theoretical considerations of this accretion column model leads us to expect most of the radiation to be in the form of hard X-rays. However, observations of such systems imply that the hard X-ray luminosity often constitutes only 10% of the system luminosity, with the spectrum being dominated by soft X-ray emission. It has therefore been suggested that in order to account for this discrepancy the accretion column model should be slightly adjusted to describe polecap accretion not in terms of a single large accretion column, but in terms of small accreting blobs, each creating their own small accretion column (Frank, King and Lasota, 1988). According to this revised model, the original flow is broken up into well-separated blobs above the white dwarf surface. Diffuse blobs will be shocked above the white dwarf surface, while dense blobs can penetrate into the photosphere before being shocked, enhancing the soft X-ray production.

Primary spin periods

We have seen that the accretion flow is directed onto only a small fraction of the surface of the primary star when the accretion process is controlled by the magnetic field of the primary. Half of the accretion luminosity is emitted from this small region, therefore any rotation of the accreting primary will bring about a periodic modulation in the observed flux from the system (usually in the X-ray band). This periodicity represents the spin period of the primary, $P_{\rm spin}$ (or, if the periodic signal is created by the directional emission from *both* polecaps, it represents $\frac{1}{2}P_{\rm spin}$). Typical observed values are 1 s $\lesssim P_{\rm spin} \lesssim 10^3$ s. It must be kept in mind, however, that there will be periodic variations (with the binary period P) of the spin frequency due to Doppler shifts during the binary rotation.

In many X-ray binaries, a steady decrease ("spin-up") in $P_{\rm spin}$ is observed, with occasional small increases ("spin-down"). The spin-up is probably caused by the torques resulting from accretion, and the spin-downs may be due to changes in the accretion torque or changes in the internal structure. From Eq. (2.87), it can be shown that for $P_{\rm spin} \gtrsim 1$ s, and for a typical Alfvén radius of $R_M \sim 10^8$ cm, the fastness $\omega_* \ll 1$ and we have a so-called "slow rotator". For such a slow rotator accreting from a disc, the dominant torque is the accretion of angular momentum at R_M. From the arguments in Section 2.5.2, it follows that the rate of angular momentum transfer from the disc to the primary is $\dot{m}(GMR_M)^{1/2}$, therefore, with I the moment of inertia of the primary star, the spin-up is expressed as

$$I\dot{\Omega}_* = \dot{m}(GMR_M)^{1/2} \ . \tag{2.93}$$

By using Eq. (2.86) and $\dot{m} = RL_{\rm acc}/GM$, the spin-up rate can also be written as

$$\dot{\Omega}_* \approx \begin{cases} 1.4 \times 10^{-17} m_1^{-3/7} R_9^{6/7} L_{33}^{6/7} \mu_{30}^{2/7} I_{50}^{-1} \ {\rm Hz \ s^{-1}} \\ 1.0 \times 10^{-11} m_1^{-3/7} R_6^{6/7} L_{37}^{6/7} \mu_{30}^{2/7} I_{45}^{-1} \ {\rm Hz \ s^{-1}} \end{cases} , \tag{2.94}$$

where $I_{45} = I/(10^{45}$ g cm$^2)$, etc. For a neutron star, $I_{45} \sim 1$, while $I_{50} \sim 1$ for a white dwarf, therefore it is much harder to spin up a white dwarf.

For faster rotators, for which $\omega_* \sim 1$, other effects may also play a more dominant role, e.g. the interaction of its magnetic field with disc regions at $R > R_M$, or angular momentum loss by blowing a wind of particles off the stellar surface along the fieldlines. Theoretically, any star that is spun-up for long enough will become a fast rotator, and $P_{\rm spin}$ reaches an equilibrium value, because of the additional effects just mentioned, and will only change significantly again if external conditions should change.

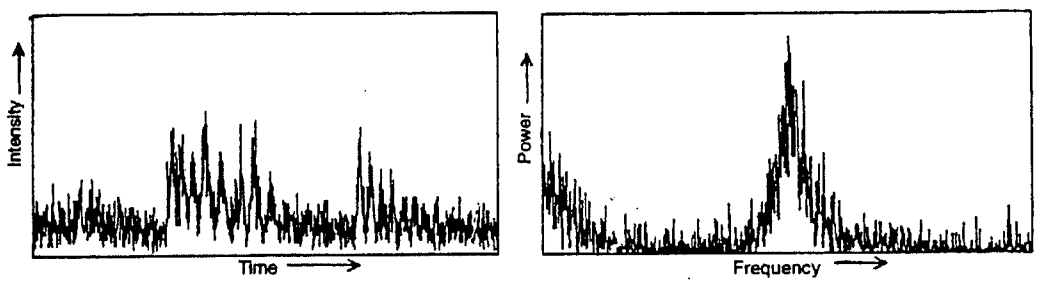

Fig. 2.10: A quasi-periodic light curve (left) and its corresponding power spectrum (right), showing the characteristic broadened peak due to the presence of a whole range of periods. (Compiled from sample data.) (Adopted from Seward and Charles 2010, p. 221, Fig. 11.65.)

The fastness of a rotator can also be regarded in terms of the *corotation radius*. The corotation radius, R_Ω, is the radius where the Keplerian angular velocity is equal to that of the primary star itself, and is given by

$$R_\Omega = \left(\frac{GMP_{\rm spin}^2}{4\pi^2} \right)^{1/3} = 1.5 \times 10^8 P_{\rm spin}^{2/3} m_1^{1/3} \text{ cm} . \tag{2.95}$$

The slow rotator condition $\omega_* < 1$ can also be expressed by the requirement that $R_\Omega > R_M$. At the equilibrium spin period $P_{\rm eq}$, $\omega_* \sim 1$ and $R_\Omega \sim R_M$, and comparison of Eq. (2.95) with Eq. (2.86) shows that

$$P_{\rm eq} \sim \begin{cases} 2.6 m_1^{-2/7} R_9^{-3/7} L_{33}^{-3/7} \mu_{30}^{6/7} \text{ s} \\ 1.0 m_1^{-2/7} R_6^{-3/7} L_{37}^{-3/7} \mu_{30}^{6/7} \text{ s} \end{cases} . \tag{2.96}$$

Quasi-periodic oscillations

Broad frequency peaks are sometimes detected in the power spectra of X-ray binaries and cataclysmic variables, representing what is known as quasi-periodic oscillations (QPO's). An example of a quasi-periodic signal and its corresponding power spectrum is shown in Fig. 2.10. It has been postulated that QPO's are caused by the interaction of a weak magnetic field of the primary star with changing, turbulent "blobs" orbiting the primary in the inner parts of the accretion disc. The magnitude of the corresponding QPO frequency possibly results from the beat between $P_{\rm spin}$ and the Keplerian period $P_{\rm K}$ of the blobs, according to

$$\frac{1}{P_{\rm QPO}} = \left| \frac{1}{P_{\rm spin}} - \frac{1}{P_{\rm K}} \right| . \tag{2.97}$$

The cataclysmic variable AE Aquarii also exhibits QPO's. However, this system does not have an accretion disc, but the QPO's arise from the beat period between the white dwarf spin period and the Keplerian period of blobs of material that are being ejected from the system. A power spectrum of AE Aqr is shown in Fig. 2.11

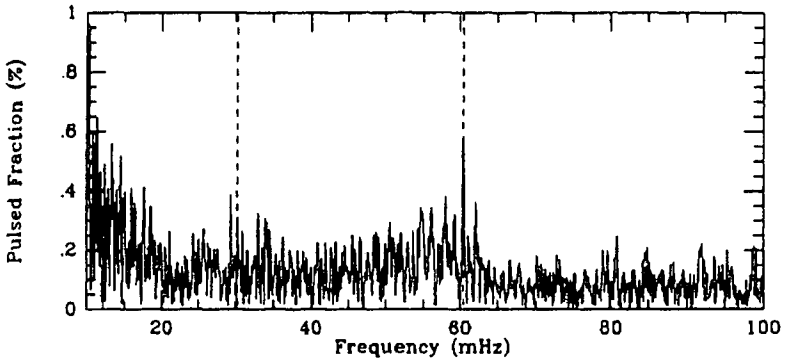

Fig. 2.11: Power spectrum of AE Aqr. The dotted lines indicate the positions of the spin period and its second harmonic. The broad structure at $\sim$ 56 mHz indicates a QPO. (Adopted from Meintjes et al. 1994, Fig. 3(d).)

(Meintjes et al., 1994).

2.7 Radiation processes

In the preceding discussions, there have been several references to different radiative processes and related quantities. In this section, an overview is provided of some concepts of radiative transport, whereafter the mechanisms of blackbody and thermal Bremsstrahlung radiation are briefly explained. A detailed account of radiative transfer, as well as other continuum radiation processes, can be found in Rybicki and Lightman (2004), Longair (1992) and Vietri (2008, Chapter 3).

2.7.1 Basic concepts

A radiation field can be quantified by its *specific intensity* I_ν, which has the units erg cm^{-2} s^{-1} Hz^{-1} sr^{-1} (e.g. Vietri 2008, Section 3.1). When considering all the radiation directed in a small cone of solid opening angle Ω about a reference direction, the total energy with frequency between ν and $d + d\nu$ transferred through the cone across a surface dA normal to the reference direction in a time dt is given by

$$dE = I_\nu dA dt d\Omega d\nu \ . \tag{2.98}$$

The *specific flux* F_ν (in erg cm^{-2} s^{-1} Hz^{-1}) is independent of direction and is related to the specific intensity by

$$F_\nu = \int I_\nu \cos\theta d\Omega \ . \tag{2.99}$$

If a certain fluid element with volume dV emits radiation with frequency between ν and $d + d\nu$, it will alter the local radiation field I_ν, as it emits an amount of energy given by

$$dE = j_\nu dV d\nu d\Omega dt \tag{2.100}$$

directed into a small solid angle $d\Omega$ in the reference direction. The parameter j_ν (in erg cm^{-3} s^{-1} Hz^{-1} sr^{-1}) is called the *coefficient of spontaneous emission*. The specific intensity of radiation passing through $dV = dA\ ds$ will therefore increase by

$$dI_\nu = j_\nu ds\ . \tag{2.101}$$

On the other hand, another fluid element with volume dV may absorb some of the radiation, and cause I_ν to decrease according to

$$dI_\nu = -\alpha_\nu I_\nu ds\ , \tag{2.102}$$

where α_ν is the *coefficient of absorption*, expressed as a fraction of the specific intensity that is absorbed from the incident radiation. It should be noted that there are two processes which can decrease I_ν, namely absorption (described by α_ν) during which photons are destroyed, and the scattering of photons into other directions, during which the number of photons is preserved. The latter effect is incorporated into j_ν, which is therefore also a function of I_ν. The equation of radiative transfer is

$$\frac{dI_\nu}{ds} = j_\nu - \alpha_\nu I_\nu\ . \tag{2.103}$$

The *optical depth* is defined as

$$\tau_\nu = \int \alpha_\nu ds\ , \tag{2.104}$$

and the *source function* as

$$S_\nu = \frac{j_\nu}{\alpha_\nu}\ . \tag{2.105}$$

Eq. (2.103) appears quite simple to solve, and indeed a formal solution of the form

$$I_\nu(\tau_\nu) = I_\nu(0)e^{-\tau_\nu} + \int_0^{\tau_\nu} S_\nu(\tau'_\nu)e^{-(\tau_\nu - \tau'_\nu)}d\tau'_\nu \tag{2.106}$$

can be obtained. However, because S_ν is a function of α_ν and therefore of I_ν if scattering effects are present, it is not practically possible to specify S_ν without referring to I_ν, except if scattering effects can be neglected.

When $\tau_\nu \ll 1$, the medium is said to be optically thin, and if $\tau_\nu \gg 1$, the medium is optically thick. For an optically thick medium, $S_\nu = I_\nu$. In the special case where the radiation itself is in thermal equilibrium, the thermal emission is in the form of blackbody radiation.

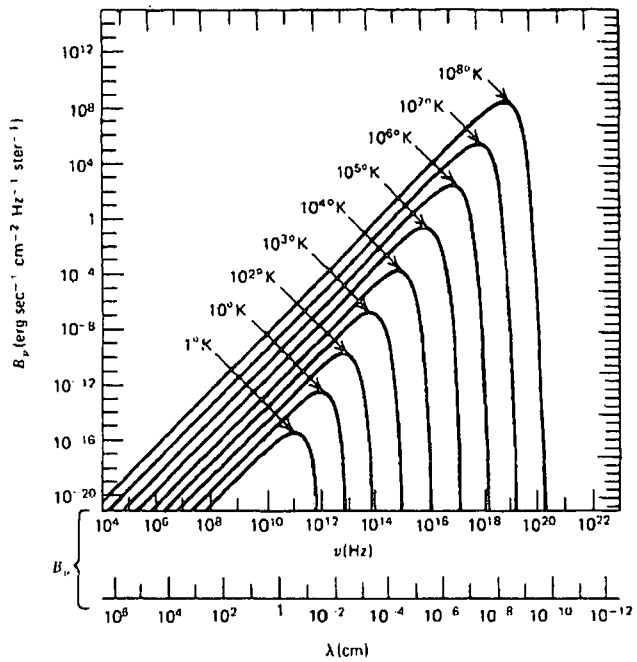

Fig. 2.12: Blackbody spectra at various temperatures. (Adopted from Rybicki and Lightman 2004, p. 22, Fig. 1.11.)

2.7.2 Blackbody radiation

In thermal equilibrium, the medium is spatially homogeneous and $dI_\nu/ds = 0$. The specific intensity I_ν is now only dependent on the frequency ν and the effective temperature T and is given by the Planck law:

$$I_\nu = B_\nu(T) = \frac{2h\nu^3/c^2}{e^{h\nu/kT} - 1} \ . \tag{2.107}$$

In the limit $h\nu \ll kT$, the exponential term can be approximated by $e^{h\nu/kT} - 1 \approx h\nu/kT$ and then we have the *Rayleigh-Jeans law*,

$$I_\nu^{RJ} = \frac{2\nu^2}{c^2} kT \ . \tag{2.108}$$

In the limit $h\nu \gg kT$, $e^{h\nu/kT} - 1 \approx e^{h\nu/kT}$, and the spectrum is described by the *Wien law*:

$$I_\nu^{W} = \frac{2h\nu^3}{c^2} e^{-h\nu/kT} \ . \tag{2.109}$$

Fig. 2.12 shows a series of blackbody curves for different temperatures. The bolometric (i.e. measured over all wavelengths) surface flux (in erg cm^{-2} s^{-1}) from a blackbody emitter is given in terms of the blackbody temperature by the Stefan-Boltzmann law,

$$F_{\rm bol} = \sigma T^4 \ , \tag{2.110}$$

where σ is the Stefan-Boltzmann constant. The flux can be expressed as $F_{\rm bol} =$

$L_{\rm bol}/4\pi R^2$, where $L_{\rm bol}$ is the emitter luminosity and R the emitter radius. Therefore the bolometric luminosity (i.e. the total power over all wavelengths) is given by

$$L_{\rm bol} = 4\pi R^2 \sigma T^4 \ . \tag{2.111}$$

Thus, if the bolometric luminosity and effective temperature of a source is known, the equation above can be used to calculate its radius. Solving Eq. (2.111) for the radius and expressing it in a more convenient form yields

$$R = 8.789 \times 10^{11} L_{37}^{1/2} \left(\frac{kT}{1 \text{ eV}} \right)^{-2} \text{ cm} \ , \tag{2.112}$$

where $L_{37} = L_{\rm bol}/10^{37}$ erg s^{-1}, and kT is the effective source temperature expressed in eV. The unabsorbed flux $F_{\rm u}$ measured by an observer is related to the bolometric source luminosity by $L_{\rm bol} = 4\pi D^2 F_{\rm u}$, where D is the distance from the (earthly) observer to the source.

2.7.3 Thermal Bremsstrahlung

Bremsstrahlung ("braking radiation") or free-free emission refers to the emission of radiation by an electric charge that is accelerated in the electric field of another charged particle (e.g. Rybicki and Lightman 2004, Chapter 5). No Bremsstrahlung takes place during the collision of two similar particles, as the dipole moment is proportional to the position of the centre of mass, which stays constant. In an ionized plasma, Bremsstrahlung due to the interactions between electrons and ions should therefore be considered. The acceleration of a particle is inversely proportional to its mass, therefore the electrons will be the primary radiators.

In thermal Bremsstrahlung, the thermal distribution of electron speeds is used to quantify the nature of the spectrum. Then the spectrum is given by

$$\frac{dE}{dV dt d\nu} = \frac{2^5 \pi e^6}{3 m_{\rm e} c^3} \left(\frac{2\pi}{3 k m_{\rm e}} \right)^{1/2} T^{-1/2} Z^2 N_e N_i e^{-h\nu/kT} \bar{g}_{ff} \ , \tag{2.113}$$

where $\bar{g}_{ff}$ is the velocity-averaged Gaunt factor. The Gaunt factor is a function of the electron energy and the emission frequency, and extensive tables for appropriate scenarios can be found in the literature, e.g. Karzas and Latter (1961). A schematic representation of the general form of a Bremsstrahlung spectrum is shown in Fig. 2.13. This spectrum is typical of dense ionised gas such as found in star formation regions. At low frequencies, self-absorption of the emitted spectrum by the emitting gas modifies the spectrum to the form of the Raleigh-Jeans component of the blackbody curve.

In this chapter, an overview of the basic properties of accreting binary systems and

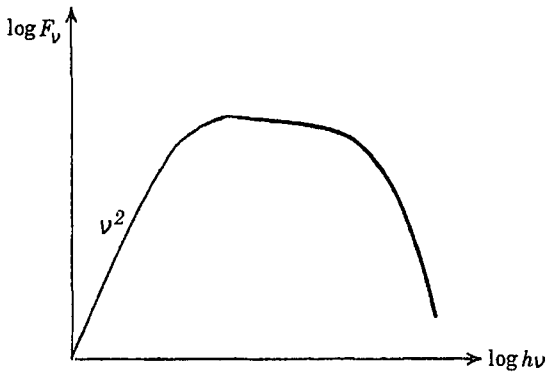

Fig. 2.13: Schematic representation of the form of a typical Bremsstrahlung spectrum, illustrating the Rayleig-Jeans tail at low freqencies. (Adapted from Rybicki and Lightman 2004, p. 166, Fig. 5.5.)

accretion discs has been provided. One of the most powerful techniques that can be used to infer the structure and properties of a binary system, is spectroscopy. This includes the analysis of the spectrum continuum, which may contain several components like the blackbody and Bremsstrahlung spectra discussed above. However, it also requires a closer look at the emission and absorption lines which originate from transitions between quantified energy states in atoms and ions in the optically thin regions of the system. The next chapter is devoted to a discussion of the origin of spectral lines, and how they can reveal an incredible amount of information related to the emitting regions.

Chapter 3

The Physics of Spectral Lines

The spectra of many astronomical sources are characterized by a series of "dips" and "peaks" superimposed on a continuum. They are known as absorption lines and emission lines respectively, and are caused by transitions between discrete energy levels in the atoms or ions in the source. These spectral lines contain a wealth of information related to numerous physical properties in the source, i.e. composition, temperature and pressure, as well as the dynamics of the material in the source.

In order to extract such information from the spectral lines, the structure and quantification of energy levels in an atom must first be understood, and also the transitions between the energy levels. This chapter provides a brief overview of these core principles, as well as the most relevant mechanisms responsible for the broadened line shapes and changing line positions that are often observed in astrophysical environments.

3.1 Origin of the quantum numbers

In this section, the origin and interpretation of the quantum numbers will be explored mainly in terms of the Bohr-Sommerfeld atomic model (Sommerfeld, 1928), supplemented with the contributions towards quantum theory by de Broglie and Schrödinger. The content of this section is largely based on the discussion of Kitchin (1995, chapter 2), supplemented with other sources where indicated.

3.1.1 The Bohr-Sommerfeld atomic model

In the Bohr-Sommerfeld model, the negatively charged electrons are considered as particles orbiting the small, compact, positive nucleus of the atom. In this model, the electrons in different orbits have different energies. The quantization of energy is therefore considered in terms of electrons that are only permitted in certain orbits. The Bohr-Sommerfeld model is, however, only successful in describing hydrogen atoms and other single-electron, "hydrogen-like" ions like He^+.

Bohr postulated that the angular momentum of an electron in any allowed orbit has to be an integer multiple of $h/2\pi$, i.e.

$$m_e v r = n\frac{h}{2\pi} , \tag{3.1}$$

with m_e the electron mass, v its velocity, r the orbital radius for a circular orbit, n an integer and h Planck's constant. In the assumed circular orbit, the Coulomb force attracting the electron to the nucleus acts as the centripetal force keeping the electron in orbit:

$$\frac{Ze^2}{r^2} = \frac{m_e v^2}{r} , \tag{3.2}$$

where e is the electron charge and Z the atomic number of the nucleus. Solving for the radius from Eq. (3.2) and eliminating v by using Eq. (3.1), the orbital radius r_n for the n^{th} Bohr orbit becomes

$$r = \frac{h^2 n^2}{4\pi^2 m_e e^2 Z} = a_0 \frac{n^2}{Z} , \tag{3.3}$$

where $a_0 = h^2/4\pi^2 m_e e^2 \approx 5.294 \times 10^{-9}$ cm represents the first Bohr orbit of hydrogen, for which $Z = 1$. The number n is called the *principal quantum number.*

The potential energy of an electron is considered to be zero when $r = \infty$, i.e. when the atom is ionized and the electron is free. For bounded electrons the potential energy function is negative, i.e.

$$E_{\text{pot}} = \frac{-Ze^2}{r} . \tag{3.4}$$

From this relation the potential energy decreases, i.e. becomes negative, for electron orbits closer to the nucleus.

From Eq. (3.2), the kinetic energy can be expressed as

$$E_{\text{kin}} = \frac{1}{2} m_e v^2 = \frac{Ze^2}{2r} . \tag{3.5}$$

The total energy, E, of the electron is then

$$E = E_{\text{pot}} + E_{\text{kin}} = \frac{-Ze^2}{2r} . \tag{3.6}$$

The negative sign indicates that the electron is in a bounded state, requiring work from an external force to detach it from the atomic nucleus.

Substituting r from Eq. (3.3) then yields

$$E = \frac{-2\pi^2 m_e e^4 Z^2}{h^2 n^2} \ . \tag{3.7}$$

Strictly speaking, the electron orbits the centre of mass of the combined electron-nucleus system rather than the centre of the nucleus itself. Thus, the electron mass m_e should be replaced by the reduced mass of the system, $\mu = m_e M/(m_e + M)$, with M the nuclear mass. Then Eq. (3.7) becomes

$$E = \frac{-2\pi^2 \mu e^4 Z^2}{h^2 n^2} \ . \tag{3.8}$$

According to the equation above, the energy of an electron for a certain atom is only dependent on n, the principal quantum number. When an electron makes a transition from one allowed orbit or "energy level" in the atom to a lower or a higher level, the difference in energy is emitted or absorbed in the form of a photon. More specifically, for a transition from energy level E_1, corresponding to principal quantum number n_1, to energy level E_2, corresponding to n_2, Eq. (3.8) can be applied to express the frequency (ν) of the associated photon as

$$\nu = \frac{|E_2 - E_1|}{h} = \frac{2\pi^2 \mu e^4 Z^2}{h^3} \left| \frac{1}{n_1^2} - \frac{1}{n_2^2} \right| = c R_M Z^2 \left| \frac{1}{n_1^2} - \frac{1}{n_2^2} \right| \ , \tag{3.9}$$

where c is the speed of light and

$$R_M = \frac{2\pi^2 \mu e^4}{c h^3} \tag{3.10}$$

is the Rydberg constant for an atom with nuclear mass M (after Tennyson 2005, p. 23-24). In the theoretical limit of an atom with infinite nuclear mass, the reduced mass μ becomes equal to m_e:

$$\mu = \frac{m_e M}{m_e + M} = \frac{m_e}{m_e/M + 1} \approx m_e \qquad \text{for } M \to \infty \ . \tag{3.11}$$

The Rydberg constant for a system with infinite nuclear mass is therefore

$$R_\infty = \frac{2\pi^2 m_e e^4}{c h^3} = 109737.32 \text{ cm}^{-1} \tag{3.12}$$

and R_M can be expressed in terms of R_∞ as follows:

$$R_M = \frac{\mu}{m_e} R_\infty \ . \tag{3.13}$$

Sommerfeld extended the concept of circular electron orbits by postulating the existence of elliptical electron orbits, where the integral of the electron's angular momentum associated with a specific orbit must be an integer multiple of h. In such

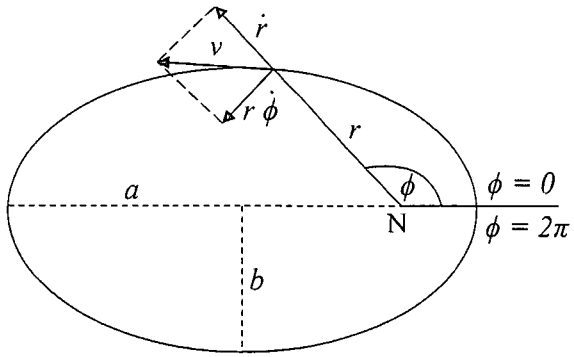

Fig. 3.1: Polar coordinates for an elliptical electron orbit. (Adapted from Sommerfeld 1928, p. 234, Fig. 70.)

an elliptical orbit, the position of the electron has two degrees of freedom: the distance from the nucleus, r, and the azimuthal angle, ϕ (i.e. in polar coordinates; see Fig. 3.1). The associated momentum components can be expressed as

$$p_\phi = m_e r^2 \dot{\phi} \qquad \text{and} \qquad p_r = m_e \dot{r} \ . \tag{3.14}$$

The momentum components are separately quantized, and according to Sommerfeld's postulate,

$$\int_{\phi=0}^{2\pi} p_\phi \, d\phi = kh \tag{3.15}$$

$$\int_{\phi=0}^{2\pi} p_r \, dr = zh \ , \tag{3.16}$$

where k and z are both integers, with k the azimuthal quantum number and z the radial quantum number.

According to Kepler's second law, angular momentum is constant for motion under the influence of inverse square attraction, therefore evaluating Eq. (3.15) yields

$$p_\phi = m_e r^2 \dot{\phi} = m_e v r = k \frac{h}{2\pi} \ , \tag{3.17}$$

which yields the same result as for Bohr's circular orbits in Eq. (3.1), but with k instead of n.

The evaluation of Eq. (3.16) is a bit more involved. The equation of an ellipse can be written as

$$\frac{1}{r} = \frac{1 + \varepsilon \cos\phi}{a(1 - \varepsilon^2)} \ , \tag{3.18}$$

where $\varepsilon = \sqrt{a^2 - b^2}/a$ is the eccentricity, a the semi-major axis and b the semi-minor

axis. Logarithmic differentiation of Eq. (3.18) with respect to ϕ yields (Sommerfeld 1928, p. 235)

$$\frac{1}{r}\frac{dr}{d\phi} = \frac{\varepsilon \sin\phi}{1+\varepsilon\cos\phi} \ , \tag{3.19}$$

which can be utilized together with Eq.'s (3.14) and (3.17) to show that Eq. (3.16) can be expressed as

$$\frac{\varepsilon^2}{2\pi}\int_{\phi=0}^{2\pi} \frac{\sin^2\phi \ d\phi}{(1+\varepsilon\cos\phi)^2} = \frac{z}{k} \ . \tag{3.20}$$

Evaluating the integral above yields (Sommerfeld, 1928, p. 550)

$$1-\varepsilon^2 = \frac{k^2}{(k+z)^2} \ , \tag{3.21}$$

showing that the eccentricity of the ellipse is also quantized. The kinetic energy of an electron in an elliptical orbit is given by

$$E_{\text{kin}} = \frac{m_{\text{e}}}{2}(\dot{r}^2 + r^2\dot{\phi}^2) \ , \tag{3.22}$$

which can be expressed as follows upon using Eq.'s (3.14), (3.18) and (3.19):

$$E_{\text{kin}} = \frac{p_\phi^2}{m_{\text{e}}a^2(1-\varepsilon^2)^2}\left(\frac{1+\varepsilon^2}{2} + \varepsilon\cos\phi\right) \ . \tag{3.23}$$

The potential energy is still given by Eq. (3.4), but can also be expressed as

$$E_{\text{pot}} = \frac{-Ze^2(1+\varepsilon\cos\phi)}{a(1-\varepsilon^2)} \tag{3.24}$$

by substituting from Eq. (3.18). By considering the fact that the total electron energy is independent of time (and therefore of ϕ), it can be shown that the total energy is

$$E = E_{\text{kin}} + E_{\text{pot}} = \frac{-2\pi^2 m_{\text{e}} e^4 Z^2}{h^2(k+z)^2} \ . \tag{3.25}$$

This is a quite remarkable result, as comparison with Eq. (3.7) shows that the quantum number n for a circular orbit corresponds to the quantum sum $k+z$ for an elliptical orbit. This means that each quantized ellipse has an amount of energy equal to that of a circular Bohr orbit.

If $z = 0$, Eq. (3.21) implies that the eccentricity is zero and we have Bohr's circular orbit once again. A value of $k = 0$ would be impossible, as it would reduce the orbit to a straight line and require the electron to pass straight through the nucleus, therefore the possible k-values start from 1. According to the above, $n = k + z$, therefore the upper limit for k is equal to n (corresponding to $z = 0$). The upper limit of z is $n-1$ (corresponding to $k = 1$). The Bohr-Sommerfeld atomic model can

therefore be described by two quantum numbers: $n = k + z$, (with possible values 1,2,3,4,...) and k (with possible values $1, 2, 3, ..., n$).

In the non-relativistic case, the energy is not dependent on k, and is simply given by Eq. (3.8). However, if relativistic effects are to be taken into account, the energy exhibits a weak dependence on k, causing a splitting of the spectral lines, known as their fine structure. The electron's energy with relativistic corrections introduced is then given by

$$E = \frac{-2\pi\mu e^4 Z^2}{h^2 n^2}\left[1 + \frac{\alpha^2 Z^2}{n}\left(\frac{1}{k} - \frac{3}{4n}\right)\right] , \tag{3.26}$$

where

$$\alpha = \frac{2\pi e^2}{hc} = 7.297 \times 10^{-3} \tag{3.27}$$

is known as the fine structure constant.

In the more refined general quantum-mechanical consideration (see Section 3.1.4), an *orbital angular momentum quantum number*, l, is introduced, which is analogous to the azimuthal quantum number k in the Bohr-Sommerfeld model. More specifically,

$$l = k - 1 (= 0, 1, 2, ..., n - 1). \tag{3.28}$$

3.1.2 Space quantization

Because an atom is three-dimensional, another quantum number is needed to describe the *orientation* of an electron orbit in three-dimensional space. If there is no reference direction in the system, identical orbits with different orientations will have the same energy, i.e. they will be degenerate. If there is a reference direction such as that introduced by a magnetic field, some or all of the orientations will have different associated energies (e.g. the Zeeman effect).

The orbital angular momentum of the electron is described by a vector $\mathbf{L}$ with magnitude $\sqrt{l(l+1)}\hbar$ which is perpendicular to the orbital plane (e.g. Beiser 2003, p. 209). The only allowed orientations of the electron orbit are those for which the projection of $\mathbf{L}$ onto the reference direction has the value $m_l\hbar$, where m_l is an integer called the *magnetic quantum number*. The space quantization for $l = 2$ is shown in Fig. 3.2, which also illustrates that m_l will be limited to values of

$$m_l = 0, \pm 1, ..., \pm l \ . \tag{3.29}$$

This result also follows more formally from quantum mechanics. There is no associated quantization in the other angular coordinate, as $\mathbf{L}$ will precess about the reference direction. In the presence of a magnetic field, the precession frequency will be the Larmor frequency $\nu_L = 1.400 \times 10^6 B$ Hz, with B the magnetic field strength

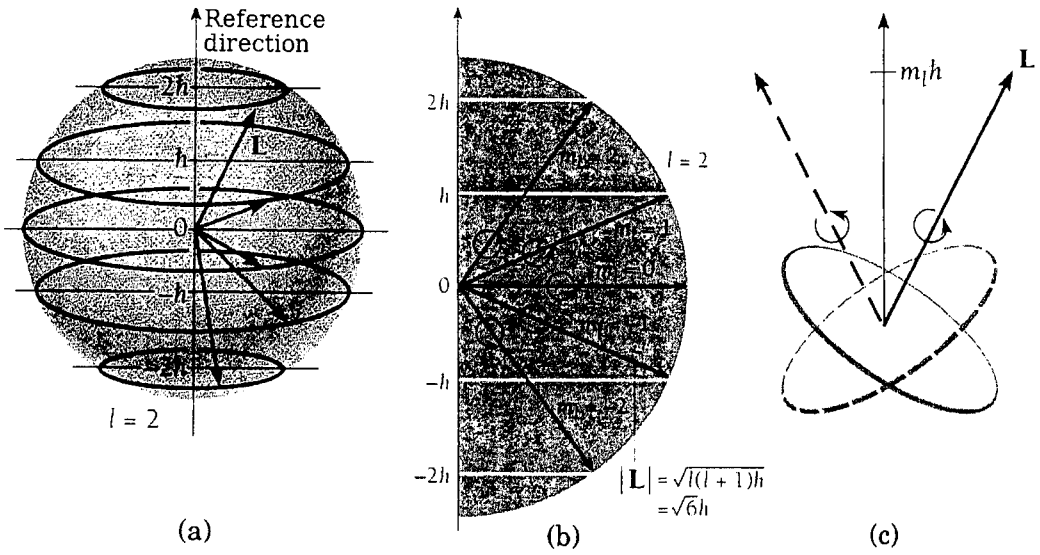

Fig. 3.2: (a) Allowed orientations of the orbital angular momentum vector **L** in 3 dimensions for $l = 2$. **L** constantly precesses about the reference direction. (b) Section in 2 dimensions, illustrating associated values of m_l. (c) The precession of the orbit with normal vector **L** about the reference direction. (Adopted from Beiser 2003, p. 211-212, Fig. 6.4, Fig. 6.5(b) and Fig. 6.6.)

in gauss.

3.1.3 Electron spin

In addition to orbital motion about the nucleus, the electron also spins about its axis. The spin angular momentum of the electron is also quantized and is described by a vector **S** with magnitude $\sqrt{s(s+1)}\hbar$ and direction parallel to the spin axis (e.g. Beiser 2003, p. 230), where $s = \frac{1}{2}$ for an electron. Analogous to the space quantization of the orbital angular momentum, the space quantization of the electron-spin is described by the condition that the projection of **S** onto the reference direction must have the value $m_s\hbar$, where m_s can be equal to either $+\frac{1}{2}$ (spin-up) or $-\frac{1}{2}$ (spin-down). The number m_s is called the *spin magnetic quantum number.*

3.1.4 Wave and Quantum Mechanics

The Bohr-Sommerfeld model is quite successful in describing hydrogen and hydrogen-like atoms, but it is not efficient in describing more complex, many-electron atoms. It became clear in the 1920's that the behaviour of an atom is better described by wave and quantum mechanics.

De Broglie suggested that particles could behave like waves. The wave nature of an electron orbiting the nucleus can thus be described by the de Broglie wavelength of

the electron, which is given by $\lambda = h/m_e v$, or, by substituting v from Eq. (3.2),

$$\lambda = \frac{h}{e}\sqrt{\frac{r}{Zm_e}} \ . \tag{3.30}$$

The only allowed electron orbits are those constituting of an integer number of de Broglie wavelengths (e.g. Beiser 2003, p. 132), creating a standing wave, i.e.

$$n\lambda = 2\pi r_n \ . \tag{3.31}$$

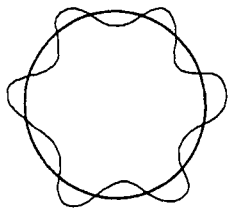

Fig. 3.3: The standing de Broglie wave of an electron in an allowed circular Bohr orbit. (Adapted from Kitchin 1995, Fig. 2.2.)

Remarkably, combining Eq.'s (3.30) and (3.31) yields exactly the same expression for r as the one predicted by Bohr, given in Eq. (3.3). The Bohr orbits can now be visualised as those containing a standing de Broglie wave, as illustrated in Fig. 3.3.

The quantum numbers discussed so far also arise quite naturally from a quantum-mechanical analysis, where Schrödinger's wave equation is solved for an electron in a hydrogen-like atom. The results are only summarized here; for a detailed discussion, see Beiser (2003, Chapter 6).

The Schrödinger wave equation for a particle with wave function $\Psi(\mathbf{r}, t)$ is given by

$$\frac{\partial^2\Psi(\mathbf{r},t)}{\partial x^2} + \frac{\partial^2\Psi(\mathbf{r},t)}{\partial y^2} + \frac{\partial^2\Psi(\mathbf{r},t)}{\partial z^2} = \frac{1}{v^2}\frac{\partial^2\Psi(\mathbf{r},t)}{\partial t^2} \ . \tag{3.32}$$

The square of the absolute magnitude of the wave function, i.e. $|\Psi|^2 = \Psi^*\Psi$, relates to the probability of finding the particle at the position $\mathbf{r} = (x, y, z)$ at time t (e.g. Beiser 2003, p. 162)[1]. Therefore, instead of the fixed orbits described by the Bohr-Sommerfeld model, we now have a function quantifying the electron's position in terms of a probability. The solution to Eq. (3.32) can be written in the form

$$\Psi(\mathbf{r}, t) = \psi e^{-2\pi i v t/\lambda} \ , \tag{3.33}$$

where ψ is time-independent and only depends on position. It can be shown that ψ is separately dependent on functions of each of the polar coordinates r, θ and ϕ, and can therefore be expressed as

$$\psi = R(r)\Theta(\theta)\Phi(\phi) \ . \tag{3.34}$$

[1]To be precise, the quantity $|\Psi|^2 = \Psi^*\Psi$ represents the probability density constraining the electron's position at (x, y, z, t).

The time-independent form of the Schrödinger equation for a hydrogen-like atom can then be written in the following form:

$$\frac{\sin^2\theta}{R}\frac{d}{dr}\left(r^2\frac{dR}{dr}\right)+\frac{\sin\theta}{\Theta}\frac{d}{d\theta}\left(\sin\theta\frac{d\Theta}{d\theta}\right)+\frac{2\mu r^2\sin^2\theta}{\hbar^2}\left(\frac{Ze^2}{r}+E\right)=-\frac{1}{\Phi}\frac{d^2\Phi}{d\phi^2}\ . \tag{3.35}$$

The two sides of Eq. (3.35) are functions of different variables and must therefore be equal to the same constant, which is called m_l^2. Therefore we have

$$\frac{d^2\Phi}{d\phi^2}+m_l^2\Phi=0\ . \tag{3.36}$$

Further separation of variables introduces another constant, called $l(l+1)$, and we obtain

$$\frac{1}{\sin\theta}\frac{d}{d\theta}\left(\sin\theta\frac{d\Theta}{d\theta}\right)+\left[l(l+1)-\frac{m_l^2}{\sin^2\theta}\right]\Theta=0 \tag{3.37}$$

and

$$\frac{1}{r^2}\frac{d}{dr}\left(r^2\frac{dR}{dr}\right)+\left[\frac{2\mu}{\hbar^2}\left(\frac{Ze^2}{r}+E\right)-\frac{l(l+1)}{r^2}\right]R=0\ . \tag{3.38}$$

The solutions to Eq. (3.36) has the form

$$\Phi(\phi)=Ae^{im_l\phi}\ , \tag{3.39}$$

provided that m_l is 0 or a positive or negative integer ($m_l=0,\pm1,\pm2,\pm3,...$).

The next equation, Eq. (3.37), has a solution only if l is an integer and $l\geq|m_l|$, implying that $m_l=0,\pm1,\pm2,...,\pm l$.

In order to solve Eq. (3.38), E must either be positive (a free electron) or negative (a bounded electron), specified by Eq. (3.7), which is identical to Bohr's result. Another condition for the solution of Eq. (3.38), is that $n\geq l+1$, which implies that $l=0,1,2,...,n-1$.

3.1.5 Many-electron atoms

For atoms with more than one electron, the solution of the Schrödinger equation is much more involved, and will not be considered here. See Beiser (2003, Chapter 7) and Tennyson (2005, Chapter 4) for more information. However, the basic principle of the quantization of electron energy according to the set of quantum numbers discussed above, still holds.

Description	Symbol	Allowed values	No. of allowed values
Principal	n	$1, 2, 3, ..., \infty$	∞
Orbital angular momentum	l	$0, 1, 2, ..., n-1$	n
Magnetic	m_l	$0, \pm 1, \pm 2, ... \pm l$	$2l+1$
Spin magnetic	m_s	$\pm \frac{1}{2}$	2

Table 3.1: Quantum numbers.

3.2 Quantum states and energy levels

3.2.1 The role of the quantum numbers

The four quantum numbers that have been discussed in the preceding sections are summarized in Table 3.1. The quantum state of any electron in an atom can be described by a set of specific quantum number values.

Instead of referring to the numerical value of the principal quantum number, the main shells are sometimes labelled with capital letters, i.e. K, L, M, N, O, etc. corresponding to n-values of 1, 2, 3, 4, 5, etc. (e.g. Kitchin 1995, Section 2.4).

By convention, different values of l are also usually indicated by a set of letters, with the subshells s, p, d, f, g, h, i, k, l, etc., corresponding to numerical l-values of 0, 1, 2, 3, 4, 5, 6, 7, 8, etc. For example, the quantum state corresponding to $n = 3$ and $l = 1$ is called the 3p state, or 3p orbital.

According to the Pauli Exclusion Principle (e.g. Beiser 2003, p. 233),
"No two electrons in an atom can exist in the same quantum state. Each electron must have a different set of quantum numbers n, l, m_l and m_s."

Therefore the quantum numbers describing a specific electron must be unique.

In the non-relativistic case, the energy of an orbital in a hydrogen-like atom is only determined by the principal quantum number n, and not by l, so that the energy ordering is as follows (Tennyson, 2005, p. 55):

$$E(1s) < E(2s) = E(2p) < E(3s) = E(3p) = E(3d) < E(4s)... \tag{3.40}$$

However, in many-electron atoms, the orbital energy does depend on l. This can be explained by the fact that electrons in orbits with low values of l penetrate into orbitals that are even closer to the nucleus. Because they spend more time closer to the nucleus, their energy is lowered relative to orbitals with higher l-values in the

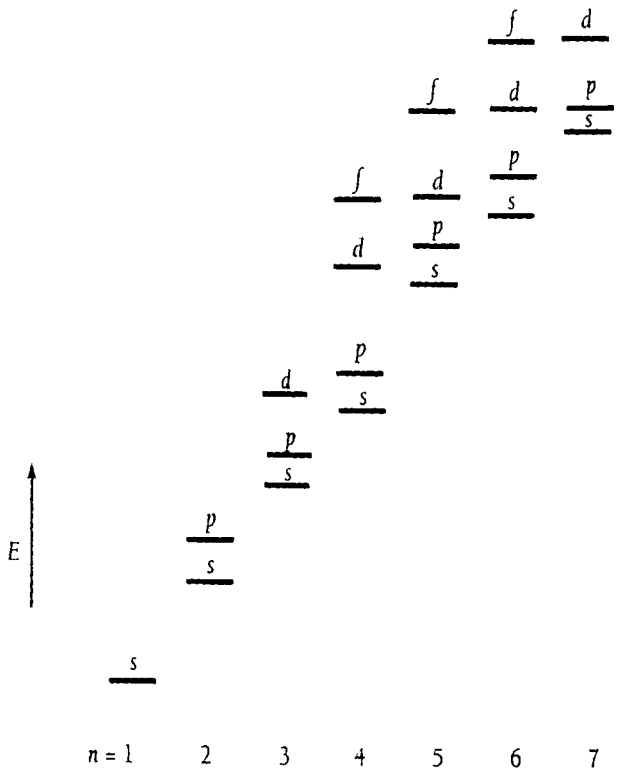

Fig. 3.4: The energy sequence of quantum states in a many-electron atom (not to scale). (Adopted from Beiser 2003, p. 246, Fig. 7.12.)

same shell, yielding a different energy ordering:

$$E(1s) < E(2s) < E(2p) < E(3s) < E(3p) < E(4s) < E(3d)... \tag{3.41}$$

This relative energy sequence of quantum states in a many-electron atom is illustrated in Fig. 3.4.

From Table 3.1, it is evident that an s subshell ($l = 0$) has only one allowed value of the magnetic quantum number, $m_l = 0$, and therefore contains only one orbital. Likewise, a p subshell has 3 orbitals ($m_l = -1, 0, 1$), a d subshell 5 orbitals, etc. Each orbital can contain 2 electrons with opposite spin, yielding $2(2l + 1)$ distinct quantum states for a subshell with orbital angular momentum quantum number l. In the ground state, the electrons in an atom will fill up the orbitals from lower to higher energy.

The distribution of electrons in an atom, referred to as the configuration, is often expressed in a notation in which the amount of electrons in a subshell is written as a superscript, with no superscript implying one electron. For example, carbon

contains 6 electrons, and the ground state configuration is

$$1s^2 2s^2 2p^2 \ ,$$

while in the excited state we have

$$1s^2 2s^2 \ 2p \ 3p \ .$$

3.2.2 Angular momentum coupling

As discussed in Sections 3.1.2 and 3.1.3, an electron in an atom has two momentum components: the electron orbital angular momentum described by l, and the electron spin angular momentum described by s. However, only the total angular momentum of the electron is a conserved quantity. The total electron angular momentum is denoted by j and is defined as the vector sum of l and s (Tennyson, 2005, p. 43), i.e.

$$\underline{j} = \underline{l} + \underline{s} \ . \tag{3.42}$$

Considering the triangulation condition for vector addition and the quantization conditions arising from quantum mechanics, Eq. (3.42) is equivalent to

$$j = |l - s|, |l - s| + 1, ..., l + s - 1, l + s \ . \tag{3.43}$$

In a hydrogen-like atom, the equations above are quite adequate in describing the "coupling" of the orbital and spin angular momenta to obtain the total angular momentum, as there is only one electron.

If, on the other hand, we have a complex atom containing more than one electron, the conserved quantity is the total angular momentum J for *all* the electrons in the atom. Evidently this requires that the angular momentum values of the individual electrons should be added together in some way. There are two quite logical ways to achieve this: either by $L - S$ coupling or by $j - j$ coupling (Tennyson, 2005, p. 59-62).

$L - S$ coupling

In this coupling scheme, the total orbital angular momentum, L, and the total spin angular momentum, S, are also assumed to be conserved quantities. They are first calculated separately, and then vector summed to obtain the total angular momentum, J, of the atom. If the orbital angular momentum of the i^{th} electron is l_i, and its spin angular momentum is s_i, then L and S are calculated from the

respective vector sums in the following way:

$$\underline{L} = \sum_i \underline{l}_i \tag{3.44}$$

and

$$\underline{S} = \sum_i \underline{s}_i \ . \tag{3.45}$$

The total angular momentum is then

$$\underline{J} = \underline{L} + \underline{S} \ . \tag{3.46}$$

For closed (i.e. filled) shells and subshells. $L = S = 0$, therefore it is only necessary to consider electrons in partially-filled shells, which are referred to as *active* electrons.

$j - j$ coupling

An alternative approach is to first calculate the total angular momentum for every separate electron according to

$$\underline{j}_i = \underline{l}_i + \underline{s}_i \tag{3.47}$$

and then to couple the j-values together to yield the total angular momentum for the atom:

$$\underline{J} = \sum_i \underline{j}_i \ . \tag{3.48}$$

Once again, $J = 0$ for closed shells and subshells.

Example

Consider the second ionized state of oxygen (O III) with configuration $1s^2 2s^2 2p3d$. The $1s^2$ and $2s^2$ orbitals are closed and only the 2p and 3d electrons contribute to the angular momentum:

$$\begin{array}{lllllll} \text{For the 2p electron:} & l_1 = 1 & ; & s_1 = \frac{1}{2} & ; & \underline{j}_1 = \underline{l}_1 + \underline{s}_1 & \Rightarrow \quad j_1 = \frac{1}{2}, \frac{3}{2} \ . \\ \text{For the 3d electron:} & l_2 = 2 & ; & s_2 = \frac{1}{2} & ; & \underline{j}_2 = \underline{l}_2 + \underline{s}_2 & \Rightarrow \quad j_2 = \frac{3}{2}, \frac{5}{2} \ . \end{array}$$

$$\begin{aligned} \underline{L} = \underline{l}_1 + \underline{l}_2 \quad &\Rightarrow \quad L = 1, 2, 3 \ , \\ \underline{S} = \underline{s}_1 + \underline{s}_2 \quad &\Rightarrow \quad S = 0, 1 \ . \end{aligned}$$

The values of J arising from combinations of the above according to the two different coupling schemes are shown in Table 3.2. It is evident from this table that the two approaches give rise to an identical set of twelve J-values. However, the $L - S$ coupling scheme is actually a non-relativistic approximation, and is only approximately accurate for atoms lighter than iron, for which relativistic effects are weak. As we

$L-S$ coupling ($\underline{J}=\underline{L}+\underline{S}$)				$j-j$ coupling ($\underline{J}=\underline{j}_1+\underline{j}_2$)		
L	S	J	Level	j_1	j_2	J
1	0	1	$^1P^o_1$	$\frac{1}{2}$	$\frac{3}{2}$	1,2
1	1	0,1,2	$^3P^o_0$, $^3P^o_1$, $^3P^o_2$	$\frac{1}{2}$	$\frac{5}{2}$	2,3
2	0	2	$^1D^o_2$	$\frac{3}{2}$	$\frac{3}{2}$	0,1,2,3
2	1	1,2,3	$^3D^o_1$, $^3D^o_2$, $^3D^o_3$	$\frac{3}{2}$	$\frac{5}{2}$	1,2,3,4
3	0	3	$^1F^o_3$			
3	1	2,3,4	$^3F^o_2$, $^3F^o_3$, $^3F^o_4$			

Table 3.2: Coupling of the angular momentum quantum numbers of the two active electrons in O III according to the $L-S$ and $j-j$ coupling schemes.

are mostly considering lighter atoms, the $L-S$ coupling scheme will suffice.

Every quantum state of an atom is identified by a specific combination of L, S and J, and each state defined as such is known as a *level*. The twelve levels of the O III atom are also listed in Table 3.2 by making use of spectroscopic notation, which is explained in the next section.

The consideration of the nuclear spin angular momentum i, and the associated hyperfine structure in the energy levels is not discussed here. More details can be found in Kitchin (1995, Section 3.7).

3.2.3 Spectroscopic notation

As illustrated above, atoms with many active electrons can have different energy levels associated with a single configuration. States arising from the $L-S$ coupling scheme are denoted by using the spectroscopic notation system (Tennyson, 2005, p. 62-65). According to this system, a state associated with a certain value of L and S is called a *term*, and has the format

$$^{2S+1}L^{(o)} .$$

The first superscript is known as the spin multiplicity — if the expression $2S+1$ equals 1, we have a singlet, 2 denotes a doublet, 3 a triplet, etc. In Table 3.2, there are six different terms: three singlets and three triplets. Special care must be taken of the Pauli Exclusion Principle when determining allowed terms when there are open shells containing multiple electrons.

The value of L is not given as a number, but as one of the letters corresponding to the orbital angular momentum as discussed in Section 3.2.1, only now we use an upper case letter. This is illustrated in Table 3.2, as L-values of 1,2, and 3 are

represented by the letters P, D and F respectively.

The final superscript "o" indicates the parity of the corresponding wave function. If the sum of the l-values of all the active electrons is odd, all the levels have odd parity and the "o" is present. If the sum is even, they will have even parity and the "o" is absent. It is only necessary to consider the active electrons, because closed shells and subshells always contain an even number of electrons. In our example, $l_1 + l_2 = 3$, which explains why all the levels have odd parity.

Terms are split into levels according to the value of J. For example, in Table 3.2, there are three values of J obtained from combining $L = 1$ and $S = 1$, yielding three different levels, each with a subscript denoting the J-value, according to the level notation format

$$^{2S+1}L_J^{(o)} \ .$$

In the non-relativistic case, a configuration is split into one or more terms with different energy levels as discussed, while the levels in each term with different values of J are degenerate. However, if relativistic effects are considered, the degeneracy on the levels in the term is lifted and fine structure splitting occurs. Also, each level contains $2J + 1$ sub-levels called *states*, described by the total magnetic quantum number, M_J, with allowed values

$$M_J = -J, -J+1, ..., J-1, J \ . \tag{3.49}$$

If an external magnetic field is present, these states have different energies (known as the Zeeman effect).

3.2.4 Hund's rules

The relative energy ordering of the different terms and levels according to $L - S$ coupling for a given configuration is governed by Hund's rules (Tennyson, 2005, p. 65-66):

1. The term with the largest spin multiplicity is lowest in energy.

2. For a given spin multiplicity, the term with the largest value of L is the lowest in energy.

3. The lowest energy is obtained for the lowest value of J in the normal case (atoms with less than half-filled shells) and for the highest value of J in the inverted case (atoms with more than half-filled shells).

While Hund's rules are only rigorous for ground states, they are also useful in describing the ordering of excited states.

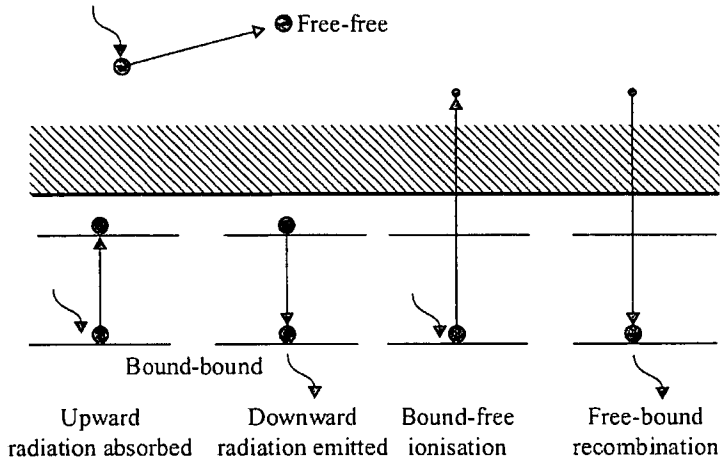

Fig. 3.5: Electron transitions. (Adopted from Robinson 2007, p. 28, Fig. 3.4.)

3.3 Transitions

An electron can transfer from one energy state to another, in what is called an electron transition. Four basic types of transitions can be distinguished, as illustrated in Fig. 3.5. They are the following (Robinson, 2007, p. 27):

- In a *free-free* transition, a free electron absorbs or emits energy, but remains free after the transition.
- In a *bound-free* transition, the electron absorbs sufficient energy to escape from the atom and to become a free electron. This is also known as *ionization*.
- In a *free-bound* transition, a free electron is "captured" by an atom and emits energy in the process. This is also known as *recombination*.
- In a *bound-bound* transition, the electron remains within the atom, but transfers from one quantized energy level to another.

3.3.1 Ionization potentials

As mentioned above, the process of ionization refers to the absorption of a photon by an electron bound to an atom, yielding a free electron and an ion. By convention, Roman numerals are used to indicate the degree of ionization. FeI refers to the neutral iron atom, FeII refers to Fe^{+} and FeXI is equivalent to Fe^{10+}, etc. The amount of energy (ϵ_i) required to ionize an atom from one ionized state to another, is known as the ionization potential. Table B.1 in Appendix B was adopted from Allen (1964, p. 37-40) and summarizes the ionization potentials for hydrogen to uranium up to XII, and for magnesium to zinc up to XX. The values are given in electronvolts (eV), where 1 eV = 1.602×10^{-12} erg.

For ionization to take place, photons with energy greater than or equal to the ionization energy is required. These photons are often associated with a local thermal radiation field. The ionization energy ϵ_i (in eV) can be converted to a temperature value by

$$T(\epsilon_i) = \epsilon_i \times \frac{1.602 \times 10^{-12} \text{ erg}}{1 \text{ eV}} \times \frac{1}{k} \approx 11600 \text{ K eV}^{-1} \times \epsilon_i \tag{3.50}$$

where k is now (and hereafter) Boltzmann's constant, not to be confused with the azimuthal quantum number k in the Bohr-Sommerfeld atomic model discussed earlier.

Suppose that a spectrum is observed that contains lines of FeII. From Table B.1, we see that a photon with minimum energy 7.87 eV is required to remove the outer electron of Fe. This can be converted to a temperature value by using Eq. (3.50):

$$T(\epsilon_i) = 11600 \text{ K eV}^{-1} \times 7.87 \text{ eV} \approx 91\ 000 \text{ K} , \tag{3.51}$$

which leads us to the conclusion that for thermal ionization of Fe I to Fe II, a temperature of at least $\sim 91\ 000$ K is required.

A rough estimate for the temperature of the emitting region can be obtained by equating the energy of the photons associated with the emission line to the average kinetic energy of particles in the gas, i.e.

$$\frac{hc}{\lambda} = \frac{3}{2}kT . \tag{3.52}$$

Substituting the constants and rearranging yields

$$T(\lambda) \sim \frac{9.590 \times 10^7 \text{ K Å}}{\lambda} . \tag{3.53}$$

For Hα photons, with a wavelength of 6563 Å, the corresponding temperature according to the equation above is $\sim 14\ 610$ K.

3.3.2 Bound-bound transitions

In a bound-bound transition, the amount of energy lost or gained by the electron is equal to the difference between the two energy levels involved. During *excitation*, the electron transfers from a lower energy level E_j to a higher energy level E_k by absorbing a photon with energy $h\nu = E_k - E_j$ from an external source, e.g. a radiation field. During the inverse process (*de-excitation*), the electron transfers from E_k to E_j and emits a photon with exactly the same energy $h\nu$ as the one absorbed originally.

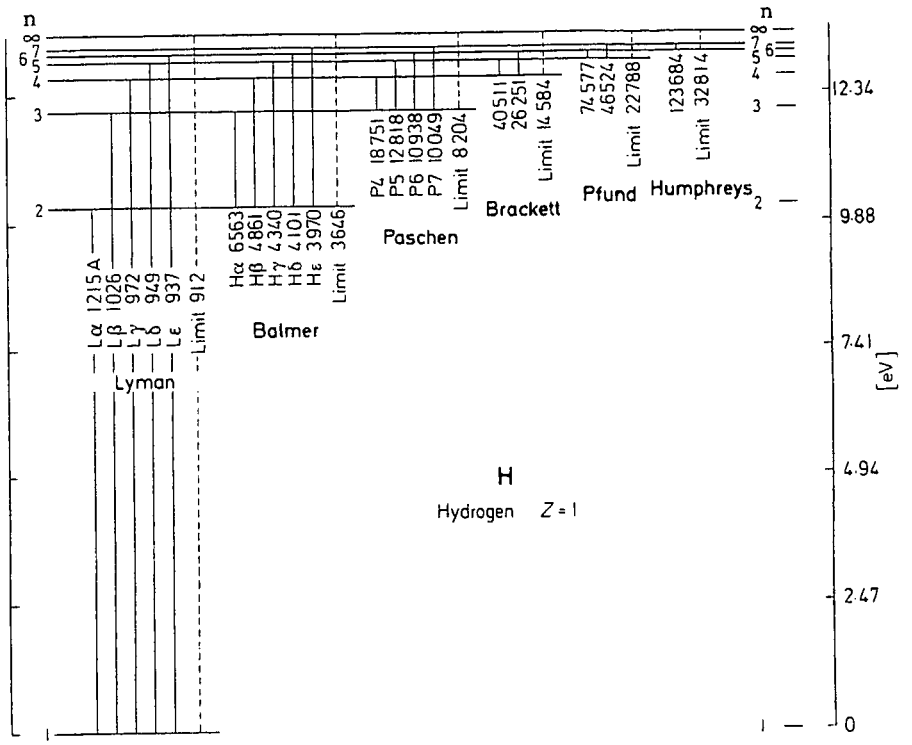

Fig. 3.6: Grotrian diagram for hydrogen, indicating the first lines of the first six spectral series, and the ionization limit of each. Wavelengths are given in Angstrom(Å), where 1 A = 10^{-10} m. The vertical axis represents the energy relative to the ground state. (Adopted from Lang 1999, p. 130, Fig. 2.4.)

The different atomic energy levels and the allowed transitions can be summarized in what is called a Grotrian diagram. It has already been mentioned that the orbital energy of a hydrogen-like atom only depends on the principal quantum number n, therefore such atoms will have the simplest Grotrian diagrams. Fig. 3.6 represents the Grotrian diagram for hydrogen — other hydrogen-like atoms will have similar Grotrian diagrams, but the energy level values will of course be different according to Eq. (3.7). For examples of more extended Grotrian diagrams related to many-electron atoms, see Lang (1999, p. 131-140).

The transitions in an atom are divided into different series based on the principal quantum number of the lower level. In the hydrogen atom, some of the series have special names. Transitions between the ground state ($n = 1$) and a higher level are called the Lyman series, between $n = 2$ and a higher level the Balmer series, and likewise for the Paschen ($n = 3$), Brackett ($n = 4$), Pfund ($n = 5$) and Humphreys ($n = 6$) series (see Fig. 3.6). Each series includes a number of transitions — in the optical waveband, the first five lines of the Balmer series of hydrogen, denoted by Hα, Hβ, Hγ, Hδ and Hϵ, are of considerable importance in most astrophysical environments.

The emission of a single photon in an astronomical source is unlikely to be noticed, but if many identical atoms are undergoing the same transitions, they will all emit photons of the same energy. This means that the intensity of emission at a certain wavelength will be enhanced relative to the surrounding continuum, and we see this as *emission lines* in the spectra of certain astronomical sources. Similarly, the absorption of photons with a certain wavelength from the local radiation field by many atoms will decrease the emission intensity at that wavelength, and this shows up as darker bands in the continuum spectra from stars, known as *absorption lines*.

Although it is conceptually easier to consider the bound-bound transitions simply in terms of electrons making a transition from one energy state to another, it is more correct to consider a transition as the *atom* changing from one energy state to another.

Selection rules

According to the above, one may be lead to expect that a bound-bound transition can take place between any two energy levels in an atom. However, even when considering the relatively simple case of a hydrogen atom, it can be seen that this is not the case (Kitchin, 1995, Section 4.2). In the hydrogen atom, the possible levels for $n = 2$ are

$$2\mathrm{s}\ {}^2\mathrm{S}_{1/2}\,, \quad 2\mathrm{p}\ {}^2\mathrm{P}^{\circ}_{1/2}\,, \quad 2\mathrm{p}\ {}^2\mathrm{P}^{\circ}_{3/2}$$

and the levels for $n = 3$ are

$$3\mathrm{s}\ {}^2\mathrm{S}_{1/2}\,, \quad 3\mathrm{p}\ {}^2\mathrm{P}^{\circ}_{1/2}\,, \quad 3\mathrm{p}\ {}^2\mathrm{P}^{\circ}_{3/2}\,, \quad 3\mathrm{d}\ {}^2\mathrm{D}_{3/2}\,, \quad 3\mathrm{p}\ {}^2\mathrm{D}_{5/2}\,.$$

It appears that there should be 15 different transitions for an electron transferring from $n = 3$ to $n = 2$ (i.e. for the Hα emission line). However, only 7 of these do occur in practice. The rules by which we can determine whether a transition is allowed or not, are called *selection rules*.

The strong transitions between levels are driven by electric dipoles. The electric dipole selection rules put limitations on the allowed changes of the quantum numbers during a transition, and they are the following (Tennyson, 2005, p. 71-74):

(1) $\Delta J = 0, \pm 1$, but transition from $J = 0$ to $J = 0$ is not allowed.

(2) $\Delta M_J = 0, \pm 1$.

(3) Parity must change (the Laporte rule).

(4) $\Delta S = 0$

(5) Only *one* electron jumps, and
Δn = any
$\Delta l = \pm 1$.

(6) $\Delta L = 0, \pm 1$ but transition from $L = 0$ to $L = 0$ is not allowed.

Rules (1) to (3) are rigorous, i.e. they must be obeyed by all electric dipole transitions. Transitions obeying *all* of the selection rules above, are called *allowed transitions.*

The 7 allowed transitions constituting Hα emission are:

$$
\begin{aligned}
&3s\ {}^2S_{1/2} \rightarrow 2p\ {}^2P^{\circ}_{1/2}\\
&3s\ {}^2S_{1/2} \rightarrow 2p\ {}^2P^{\circ}_{3/2}\\
&3p\ {}^2P^{\circ}_{1/2} \rightarrow 2s\ {}^2S_{1/2}\\
&3p\ {}^2P^{\circ}_{3/2} \rightarrow 2s\ {}^2S_{1/2}\\
&3d\ {}^2D_{3/2} \rightarrow 2p\ {}^2P^{\circ}_{1/2}\\
&3d\ {}^2D_{3/2} \rightarrow 2p\ {}^2P^{\circ}_{3/2}\\
&3p\ {}^2D_{5/2} \rightarrow 2p\ {}^2P^{\circ}_{3/2}
\end{aligned}
$$

Transitions that violate rules (4) to (6) are still possible, but much more unlikely. Transitions disobeying rule (4) are called *intercombination lines* and they arise from the mixing of spin states because of relativistic effects. Transitions disobeying rule (5) and/or (6) are called *forbidden transitions* and are usually weaker than the intercombination lines.

While not discussed in detail here, it should be noted that, apart from electric dipole transitions, weaker transitions driven by magnetic moments and higher electric multipoles are also possible. These are also known as forbidden transitions.

Einstein coefficients

According to the selection rules above, some transitions are allowed, some are forbidden and some are even "more forbidden". The allowability of a certain transition can be quantified in terms of the average *lifetime* of the transition (e.g. Kitchin 1995, Section 4.3). The *transition probability* (expressed in s^{-1}) is the inverse of the lifetime of the transition, and is given by the associated Einstein coefficients (e.g. Rybicki and Lightman 2004, p. 27-33).

The number of transitions per unit time per unit volume from a higher level j to a lower level i is given by

$$N_j A_{ji} + N_j B_{ji} I_{ji} \ . \tag{3.54}$$

The first term represents the contribution from spontaneous emission. N_j is the number of atoms per unit volume in state j and A_{ji} is the Einstein coefficient for spontaneous emission, which is the number of transitions per second from state j to state i.

The second term represents the contribution from stimulated emission. B_{ji} is the Einstein coefficient for stimulated emission, and I_{ji} is the intensity associated with the external radiation field with appropriate wavelength to induce the transition from state j to state i.

The number of transitions from level i to j caused by the absorption of photons with appropriate wavelength from the external radiation field, is given by

$$N_i B_{ij} I_{ji} \ , \tag{3.55}$$

where B_{ij} is the corresponding Einstein coefficient for photoabsorption. Therefore, for every possible transition in the different atoms and ions, there exists an Einstein coefficient describing the probability of that transition occurring. A database of transition probabilities is available on the website of the National Institute of Standards and Technology (NIST) at `http://physics.nist.gov/cgi-bin/ASBib1/TransProbBib.cgi` (Kramida and Fuhr, 2011). The NIST website also provides atomic and molecular energy levels and transition wavelengths.

3.4 The significance of the line profile

The preceding discussion of energy levels and transitions related to the formation of spectral lines, creates the perception that a certain spectral line will have a very specific wavelength and that it will in fact show up as an infinitely thin spike on an intensity versus wavelength diagram. However, it is quite obvious from any spectrum that each spectral line has a non-zero width, forming a more or less V-shaped structure, which is called the *line profile*. Such broadened profiles are shown in Fig. 3.7.

The *intensity* contained in a broadened spectral line is described by a convenient measure called the *equivalent width* which is defined as (e.g. Allen 1964, p. 164)

$$W_\lambda = \int \left(1 - \frac{I_\lambda}{C_\lambda}\right) d\lambda \ , \tag{3.56}$$

where I_λ is the line intensity and C_λ the continuum level at wavelength λ. According to this definition, the equivalent width will be positive for an absorption line and negative for an emission line. In a more practical sense, consider a rectangle with

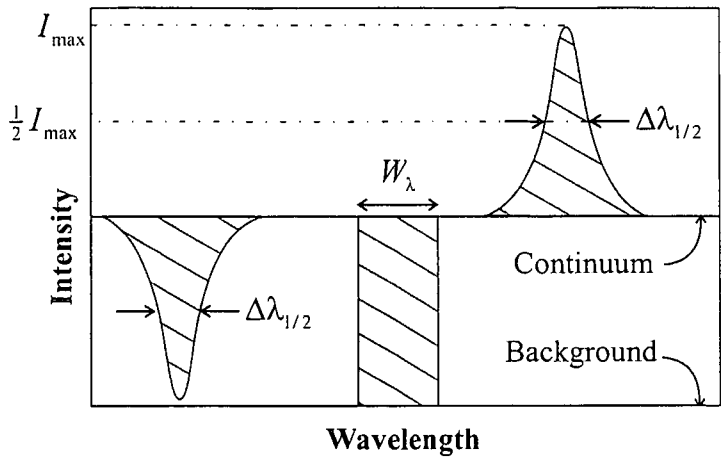

Fig. 3.7: The equivalent width and FWHM of an absorption line and an emission line. The shaded areas are all equal. (Adapted from Robinson 2007, p. 54, Fig. 5.3.)

height equal to the mean background-subtracted continuum at the line position. The width of this rectangle with area equal to the area contained in the spectral line itself, is the equivalent width of a spectral line. This concept is illustrated in Fig. 3.7.

Theoretically, the equivalent width is independent of exposure length and spectrograph properties, as it is normalized to the continuum, but practical considerations can lead to $\sim 10\%$ differences for different instruments (Kitchin, 1995, Section 13.4). The equivalent width is often expressed as the dimensionless quantity $W = W_\lambda/\lambda_0$.

The *width* of a spectral line is usually described by its width at half its peak intensity. This is called the *full width at half maximum* (FWHM) or the *half-width* ($\Delta\lambda_{1/2}$) of the line, and is indicated for both lines in Fig. 3.7.

The widened shape of the spectral line is primarily the result of processes taking place in the source itself. By analysing line profiles, a wealth of information can be extracted related to the fascinating physical processes inherent to the source. In this section the different broadening mechanisms contributing to the shape of a spectral line will be discussed.

3.4.1 Natural line broadening

In spite of (and not contradicting) the quantized nature of the energy levels in an atom, the energies associated with energy levels are not precisely determined, but spread over a small energy range ΔE (e.g. Peach 1975). This is explained by referring to the Heisenberg uncertainty principle, which can be written in terms of

energy and time as

$$\Delta E \Delta t \geq \frac{\hbar}{2} \,. \tag{3.57}$$

This means that the product of the uncertainty in energy and the lifetime of a energy level has a certain minimum value. Therefore, in a transition between two such "fuzzy" energy levels, the energy change will still be associated with a photon with precise wavelength, but photons arising from many of these transitions will have slightly different wavelengths, causing the spectral line to have a slightly widened profile.

Consider a collection of atoms in which the number of atoms in state j at time t is denoted by $N_j(t)$. The probability that a spontaneous transition from state j to another state will take place in a time dt is given by $\gamma_j dt$. The rate γ_j is often called the level's damping constant and represents the total number of transitions per unit time from state j to all available lower levels n and all available higher levels m, i.e.

$$\gamma_j = \sum_n A_{jn} + \sum_n B_{jn} I_{jn} + \sum_m B_{jm} I_{jm} \tag{3.58}$$

(refer to the discussion of Einstein coefficients in Section 3.3.2). It can be shown that the number of atoms in state j at time t relates to the number of atoms at $t = 0$ in the following way:

$$N_j(t) = N_j(0)\, e^{-\gamma_j t} \,. \tag{3.59}$$

In an atomic transition from level j to level i, an electromagnetic wave is emitted with amplitude

$$f(t) = f(0)\, e^{i\omega_{ji} t - (\gamma_{ji}/2)t} \,, \tag{3.60}$$

which represents a wave with decaying amplitude, where ω_{ji} is the associated angular frequency. Because two levels are involved during the transition, the effect of the damping constants of both levels are included by using the combined damping constant $\gamma_{ji} = \gamma_j + \gamma_i$.

The wave in Eq. (3.60) consists of a multitude of separate monochromatic waves with slightly different angular frequencies ω distributed about the central angular frequency, ω_{ji}, and this distribution can of course be described by the Fourier transform $F(\omega)$ of Eq. (3.60). The corresponding energy spectrum is given by $(1/2\pi)|F(\omega)|^2$. For an ensemble of atoms that are emitting photons at random phase, the spectrum of the ensemble is proportional to that of a single emitter. Then it can be shown that the line profile is

$$I_L(\nu) = \frac{1}{2\pi^2} \frac{\gamma_{ji}/4\pi}{(\nu - \nu_{ji})^2 + (\gamma_{ji}/4\pi)^2} \,, \tag{3.61}$$

which is in the form of a Lorentz profile describing the intensity spread for frequencies about the central frequency, ν_{ji}. It can be readily deduced from Eq. (3.61) that the FWHM of the line profile is given by

$$\Delta\nu_{1/2} = 2(\nu - \nu_{ji}) = \frac{\gamma_{ji}}{2\pi} \ . \tag{3.62}$$

In a classical approximation, the damping coefficient for a classical oscillator,

$$\gamma = \frac{8\pi^2 e^2 \nu_{ji}^2}{3m_e c^3} \tag{3.63}$$

can simply be substituted into Eq. (3.62) (e.g. Kitchin 1995, Section 4.4.1). Because $\Delta\lambda = -c/\nu^{-2}\Delta\nu$, the FWHM in wavelength terms is then

$$\text{FWHM} = \frac{4\pi e^2}{3m_e c^2} \approx 0.000118 \text{ Å} \ , \tag{3.64}$$

which is of course a constant, and this means that all naturally broadened lines have the same wavelength width, which is very small. Even though the more accurate quantum mechanical consideration introduces a dependence of the FWHM on the line identity, these values are also very small in most cases — in fact, natural broadening is usually completely overpowered by other broadening mechanisms and is often safely negligible in observational astronomical spectroscopy.

3.4.2 Pressure broadening

Because atoms consist of positive and negative charges, any atom will have an electric field associated with it. When there is a close encounter or "collision" between different atoms or ions, they will perturb each other's electric fields and the energy levels of the atoms will be disturbed. This can cause a transition between two energy levels to be associated with a wavelength that is slightly shifted from the expected value, and the spectral line arising from emission or absorption by many such disturbed atoms will have a broadened profile. This is known as *pressure broadening* (e.g. Robinson 2007, p. 61).

J. Stark suggested that the electronic vibrations of a radiating atom can be perturbed by the presence of neighbouring charges, and this was confirmed when the splitting of spectral lines into multiple components under the influence of a strong electric field was observed (see Struve 1929 and references therein). In a gas or plasma with many positive ions and free electrons, the distances from each perturbed atom to the neighbouring charged particles are randomly distributed. This implies that the wavelengths of the components produced by individual atoms will not be the same, and the combination of components from a population of atoms will blend into a continuously broadened line profile.

Pressure broadening is actually a very complex process with several possible contributing mechanisms, i.e. linear and quadratic Stark broadening, resonance broadening and Van der Waals interaction, but ion broadening by the linear Stark effect is the most important effect for hydrogen lines in the optical waveband (Lang, 1999, p. 188-196). However, electron broadening will also play a role, especially where the transitions involve levels with large principal quantum numbers.

When considering the influence of nearby charges on an atom, either the *quasi-static* or the *impact* approximation is often used. According to the quasi-static approximation, the charged particles move slowly and the electric field is therefore almost static. The impact approximation considers the atom as a radiating oscillator that is perturbed by close encounters with nearby particles and it is assumed that these collisions occur one at a time and are virtually instantaneous.

Vidal, Cooper and Smith (1973) provide tables of Stark broadening values for hydrogen. These are based on a "unified theory" for linear Stark broadening where ion broadening is considered in terms of a quasi-static approach, and electron broadening in terms of an impact approach near the central wavelength, and in terms of a quasi-static approach very far from the central wavelength. A selection of these tables, together with a description of how they should be used, are presented in Appendix C.

Consider an Hα emission line originating in a plasma with a temperature of 10 000 K. The amount of pressure broadening for this line will be determined by the density of the plasma. Tables C.1 to C.4 in Appendix C were used to calculate the pressure broadened profile for the Hα line at four different electron densities. These profiles are shown in Fig. 3.8. As can be expected, the width of the profile increases for larger densities.

3.4.3 Doppler broadening

When there is relative movement between a source of radiation and the observer, a phenomenon called the Doppler effect is introduced. When the source is moving towards the observer, the time between successive wave fronts decreases and the observer sees radiation with a shorter wavelength (called a "blue shift"). When the source is moving away from the observer, the time between successive wave fronts increases and the result is that the observed wavelength is longer (called a "red shift") (e.g. Robinson 2007, p. 46).

It is important to note that only motion directed along the line of sight — named *radial* motion — will introduce a Doppler effect, while motion perpendicular to the

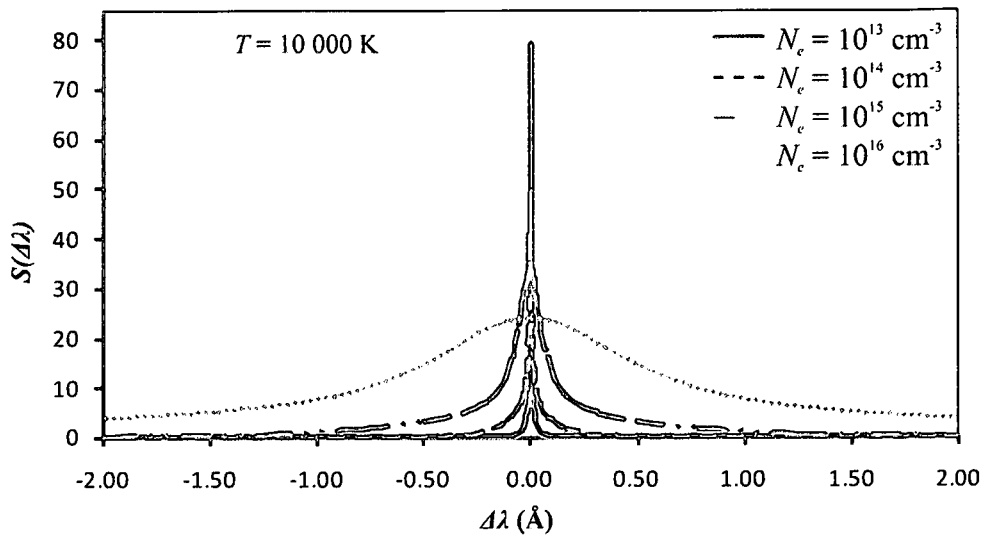

Fig. 3.8: The Hα line profiles for $T = 10\,000$ K at electron densities 10^{13} cm^{-3}, 10^{14} cm^{-3}, 10^{15} cm^{-3} and 10^{16} cm^{-3} respectively, compiled from the tables of Vidal et al. (1973). $\Delta\lambda$ represents the distance from the central wavelength, 6562.82 Å, while $S(\Delta\lambda)$ represents the intensity. For display purposes, the area under each curve is equal to the magnitude of its corresponding electric field strength F_0 (see Appendix C for more details).

line of sight will have no effect on the perceived wavelength. The Doppler formula relates the relative radial velocity v between the source and observer to the shift from the rest wavelength λ_0 or the rest frequency ν_0:

$$\frac{\Delta\lambda}{\lambda_0} = \frac{-\Delta\nu}{\nu} = \frac{v}{c} \tag{3.65}$$

where $\Delta\lambda = \lambda - \lambda_0$, with λ the apparent wavelength, $\Delta\nu = \nu - \nu_0$, with ν the apparent frequency, and c is the speed of light. For motion away from the observer, v is positive; for motion towards the observer, v is negative. The simple equation above is only valid for non-relativistic speeds; if v is comparable to c, the relativistic Doppler formula should be used:

$$\frac{\Delta\lambda}{\lambda_0} = \frac{1 + v/c}{\sqrt{1 + v^2/c^2}} - 1\ . \tag{3.66}$$

Analysis of the Doppler effect is an immensely powerful diagnostic tool in astronomical spectroscopy, as it relates to various physical phenomena in astronomical sources.

Thermal broadening

The atoms or ions in any emitting source with temperature above absolute zero are in constant thermal motion. Thermal broadening is one of the broadening mechanisms

contributing to the spectral line profile, and is caused by the radial components of the movement of the emitting atoms. The velocity distribution of a population of atoms with temperature T is described by the Maxwell distribution (e.g. Peach 1975),

$$f(v)dv = \left(\frac{m}{2\pi kT}\right)^{\frac{1}{2}} e^{-mv/2kT} dv \ , \tag{3.67}$$

with m the mass of a single particle with most probable speed $\sqrt{2kT/m}$. By means of Eq. (3.65), it is quite straightforward to rewrite Eq. (3.67) as a function of wavelength in the following way:

$$f(\lambda)d\lambda = \left(\frac{mc^2}{2\pi kT\lambda_0^2}\right)^{\frac{1}{2}} e^{-mc^2(\lambda-\lambda_0)^2/2kT\lambda_0^2} d\lambda \ . \tag{3.68}$$

This represents a Gaussian distribution (e.g. Kitchin 1995, Section 13.7.1) with intensity profile

$$I(\lambda) = I(\lambda_0) e^{-mc^2(\lambda-\lambda_0)^2/2kT\lambda_0^2} \tag{3.69}$$

and

$$\text{FWHM} = \sqrt{\frac{8kT\ln 2}{mc^2}}\ \lambda_0 \ . \tag{3.70}$$

If thermal broadening is the only broadening mechanism present, the associated spectral line will therefore have a Gaussian profile with a width dependent on the temperature of the emitting region and the rest wavelength of the line. The dependence on the mass (inertia) of the atoms implies that thermal broadening will be smaller for larger atoms.

To calculate the thermal broadening for an Hα line ($\lambda_0 = 6562.81$ Å) produced in a plasma with temperature 10 000 K, we substitute these values into Eq. (3.70) together with the mass of a hydrogen atom (i.e. the proton mass m_p), to obtain FWHM ≈ 0.47 Å. This can be verified by plotting the corresponding normalized gaussian profile, given by the dashed curve in Fig. 3.9.

By convolving this thermal profile with the Stark profile for $N_e = 10^{14}$ cm^{-3} in Fig. 3.8, the solid curve in Fig. 3.9 is obtained. The FWHM of the convolved profile is 0.52 Å, slightly larger than the 0.47 Å for the pure thermal profile. Temperature broadening is clearly much more prominent than pressure broadening if $N_e \sim 10^{14}$ cm^{-3} for the plasma described above.

The convolution of a 10 000 K thermal profile with Stark profiles at different electron densities for the Hα and Hβ lines were also obtained from the tables of Vidal et al. (1973) in Appendix C, and the resulting profiles are shown in Fig. 3.10. It is evident that pressure broadening is more pronounced for Hβ (and also for higher Balmer

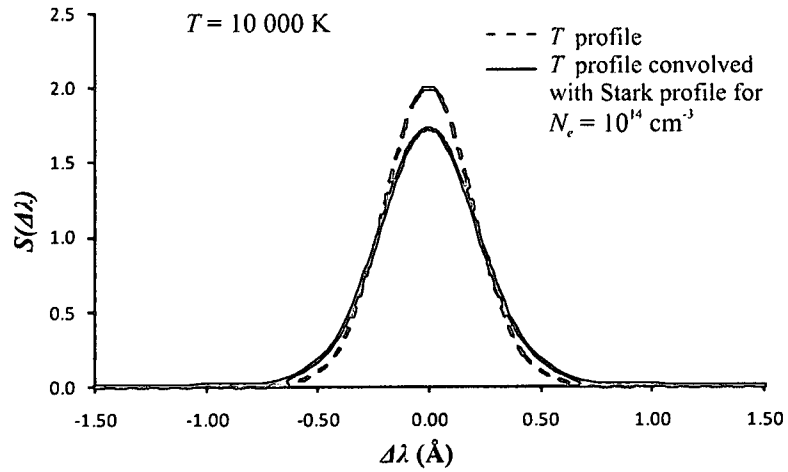

Fig. 3.9: Hα profiles for pure thermal broadening (dashed curve, FWHM $\approx$ 0.47 Å) and for thermal broadening convolved with Stark broadening for electron density 10^{14} cm^{-3} (solid curve, FWHM $\approx$ 0.52 Å) according to the tables of Vidal et al. (1973) (Table C.2). The area under each curve is normalized to 1.

lines) than for Hα.

Turbulent broadening

Large-scale motions of atoms arising from turbulence in the source, also causes Doppler broadening of spectral lines. This includes the movement of convective "blobs" inside the source. Like thermal broadening, turbulent broadening is also associated with a Gaussian profile (e.g. Kitchin 1995, Section 13.7.2), but the most probable speed of the thermal motion is replaced by an average turbulent velocity $v_{\rm T}$. The profile due to turbulence is then

$$I(\lambda) = I(\lambda_0) e^{-c^2(\lambda-\lambda_0)^2/v_{\rm T}^2\lambda_0^2} \ , \tag{3.71}$$

with

$$\mathrm{FWHM} = \sqrt{\frac{4v_{\rm T}^2 \ln 2}{c^2}}\ \lambda_0 \ . \tag{3.72}$$

For an average turbulent velocity of 2 km.s^{-1}, the FWHM of an Hα line will be 0.07 Å, and the FWHM of an Hβ line, 0.05 Å. The combined profile of the two Gaussian profiles arising from temperature and turbulent broadening is just a third Gaussian profile with

$$\mathrm{FWHM} = \sqrt{\frac{4(2kT/m + v_{\rm T}^2) \ln 2}{c^2}}\ \lambda_0 \ . \tag{3.73}$$

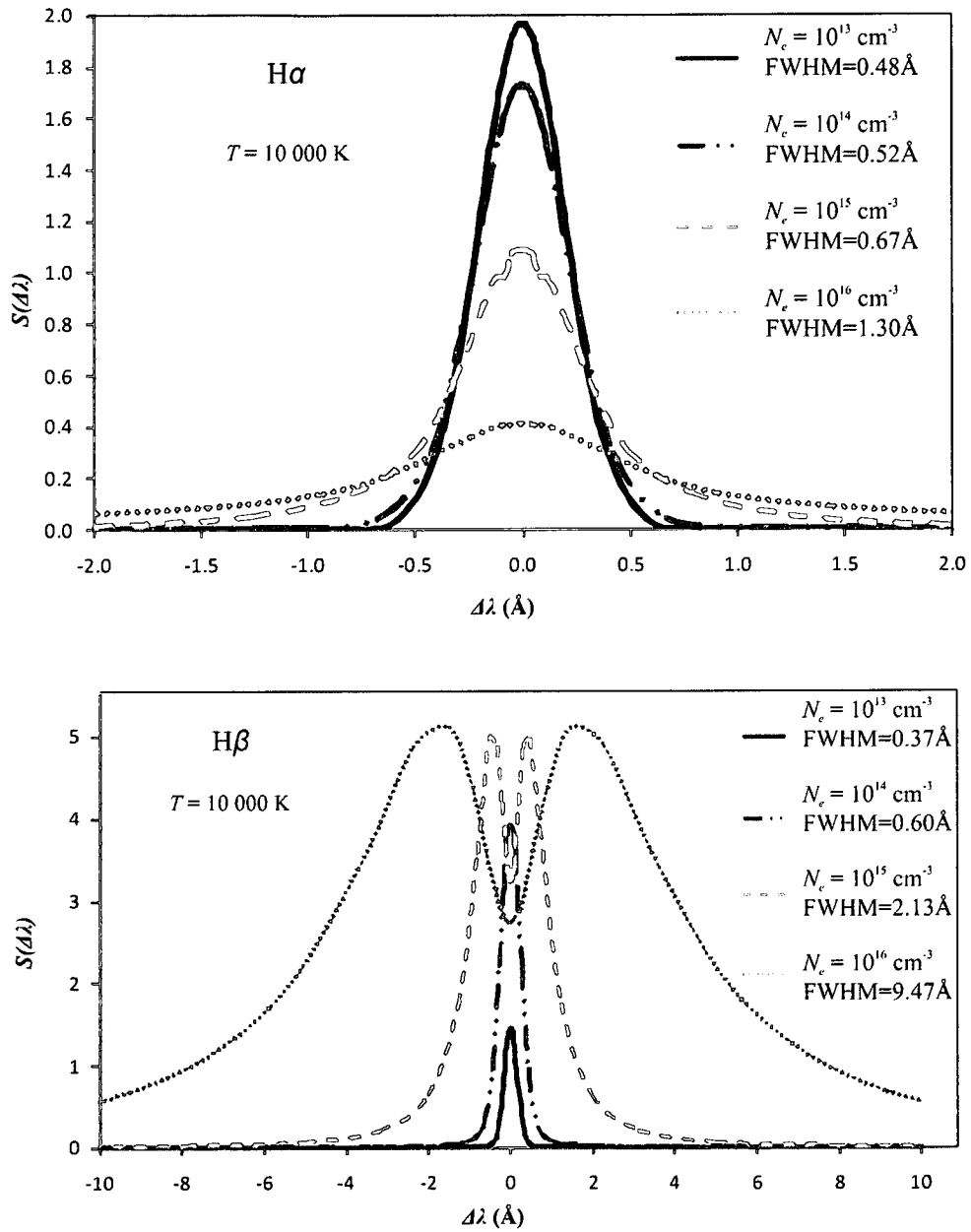

Fig. 3.10: A T =10 000 K thermal broadening profile convolved with pressure broadening profiles at different electron densities (10^{13} cm^{-3}, 10^{14} cm^{-3}, 10^{15} cm^{-3} and 10^{16} cm^{-3}) for Hα (top) and Hβ (bottom). For display purposes, the area under each Hα curve is normalized to 1, while the area under each Hβ curve is equal to the magnitude of the corresponding electric field strength F_0. The FWHM of each profile is also indicated. (Compiled from the tables of Vidal et al. 1973 in Appendix C.)

Stellar rotation

Rotation is an inherent property of many astrophysical environments, and photons emitted from different regions of the source will therefore be Doppler shifted by different amounts, depending on the radial component of the rotational velocity at every point. Because we usually observe a source as a point object, photons from different regions will be observed simultaneously, and the observed spectral line will have a broadened profile (e.g. Kitchin 1995, Section 13.7.4).

For example, a rotating star with equatorial velocity v_e will have a projected equatorial velocity of $v_e \sin i$ along the line of sight to the observer, where i is the inclination of the rotational axis, i.e. the angle between the axis and the line of sight. It can be shown that the radial velocity of any point on the star's surface is proportional to the distance of the point from the axis, and that the line profile is given by

$$I(\lambda) = I(\lambda_0) \left[1 - \frac{c^2(\lambda - \lambda_0)^2}{(v_e \sin i)^2 \lambda_0^2} \right]^{1/2} , \tag{3.74}$$

which is a semi-elliptical profile. The base width of the line is $2v_e\lambda_0 \sin i/c$, and the full width at half maximum is

$$\text{FWHM} = \frac{\sqrt{3} v_e \sin i}{c} \lambda_0 . \tag{3.75}$$

Expansion, contraction and stellar winds

The radial movement resulting from the radial expansion or contraction of a star can also result in Doppler-broadened spectral lines (e.g. Kitchin 1995, Section 13.7.5). For example, novae and supernovae have monotonically expanding surfaces during their explosive phases, while some protostars may have monotonically contracting surfaces. Cepheids, on the other hand, expand and contract continuously. Also, stars often lose mass in the form of stellar winds blowing from the surface. These processes can be very complex, and individual models should be used for an accurate description of the associated spectral lines. However, the spherically symmetric case is considered below as an idealized example.

In a shallow (i.e. very thin in comparison with its extent) absorbing or emitting region, the broadened spectral line can be described by the simple triangular profile

$$I(\lambda) = I(\lambda_0) \left[1 - C \frac{\lambda_0 - \lambda}{\lambda_0} \right] , \tag{3.76}$$

up to the maximum wavelength shift $\lambda_0 V/c$, where V is the expansion or contraction velocity. C is a constant appropriate to the star being considered. The full width

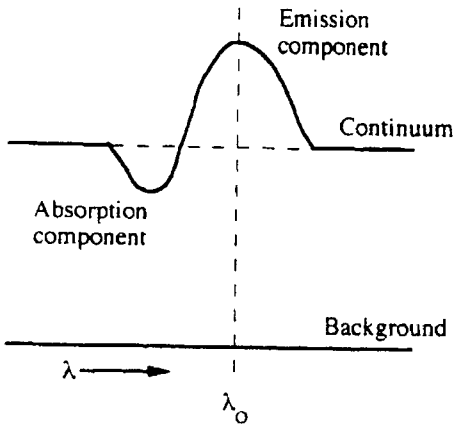

Fig. 3.11: P Cygni line profile. (Adopted from Kitchin 1995, Fig. 13.9.)

at half maximum of the profile is

$$\mathrm{FWHM} = \frac{\lambda_0}{C} \,. \tag{3.77}$$

However, for stellar winds and many other expanding sources, the thickness of the region is significant compared to its extent. The line shape is then still more or less triangular, but the wings now have a parabolic form, and the profile is now given by

$$I(\lambda) = I(\lambda_0) \begin{cases} \left\{1 - C\left(\frac{\lambda_0 - \lambda}{\lambda_0}\right)^2\right\} & \text{for } \lambda > \lambda_0\left(1 - \frac{V}{c}\sqrt{1 - \frac{r_0^2}{r_1^2}}\right) \\ \left\{1 - \left(\frac{r_1^2}{r_0^2} - 1\right)\left[1 - C\left(\frac{\lambda_0 - \lambda}{\lambda_0}\right)^2\right]\right\} & \text{for } \lambda \leq \lambda_0\left(1 - \frac{V}{c}\sqrt{1 - \frac{r_0^2}{r_1^2}}\right) \end{cases} , \tag{3.78}$$

where r_0 and r_1 are the inner and outer radii respectively of the absorbing or emitting region around the source.

In regions that accelerate as they are expanding, emission may come from the inner parts, while absorption takes place in the outer regions. This results in an absorption feature on the short wavelength side of the emission line, and this is known as a P Cygni profile (see Fig. 3.11).

Collimated outflows

Various astronomical objects, for example active galactic nuclei and other accreting compact objects, lose mass by collimated outflows or "jets", by which a collimated stream of material is ejected from the system. If such an outflow has a velocity component along the line of sight, emission or absorption associated with material in the jet will also be Doppler shifted. In order to predict the corresponding effect on the spectral line shape, various parameters of the individual object have to be considered first, e.g. the angle of the outflow to the line of sight, the opening angle

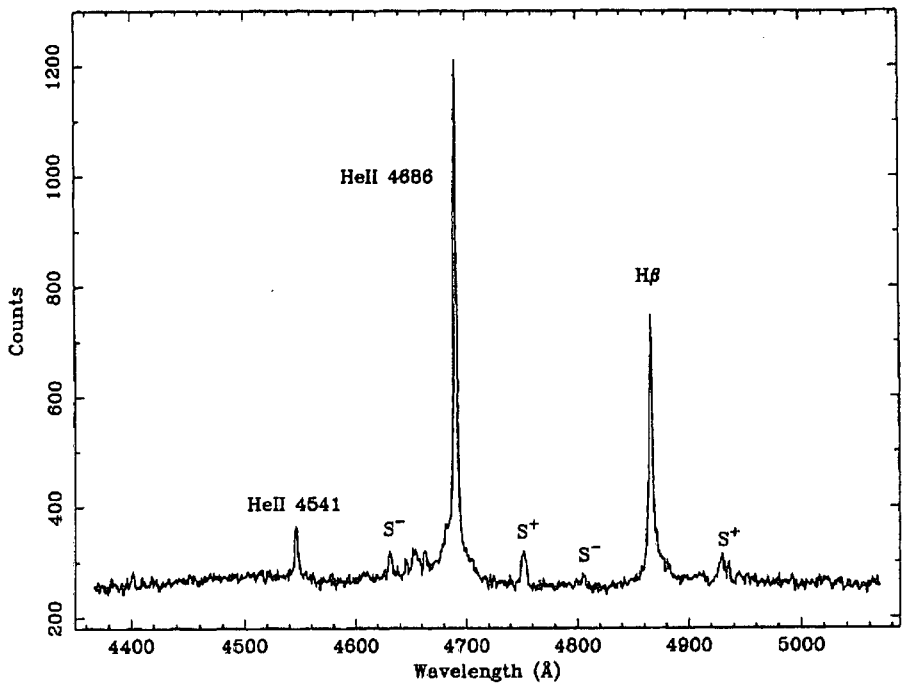

Fig. 3.12: The average blue spectrum of RX J0513.9-6951 at a resolution of 1.3 Å. (Adopted from Southwell et al. 1996, Fig. 1.)

and velocity distribution of the jet itself, and the possibility that part of the jet may be obscured by other parts of the system. If the radial component of the jet velocity is very small, one may expect a slight Doppler shift just contributing to the broadening of the spectral lines. For jet velocities with a large radial component, the emission or absorption features associated with the jets may be completely separated from the main or central emission line.

Evidence of bipolar outflows have been found in several supersoft sources (Cowley et al., 1998), one of them being the LMC supersoft source RX J0513.9-6951. Fig. 3.12 shows the average blue spectrum of this source, taken by the 3.9-m Anglo-Australian Telescope at Siding Spring at the end of November 1994 (Southwell et al., 1996). The presence of blueshifted (S^-) and redshifted (S^+) "satellite lines" on either side of the Hβ and He II λ4686 lines are interpreted as high-velocity components of the respective lines which are associated with bipolar jets in these systems. The inferred projected jet velocity for RX J0513.9-6951 is $\sim$ 3800 km.s^{-1}.

Accretion disc line profile

Another very interesting broadening mechanism associated with disc-accreting systems is the characteristic line profile arising from the Doppler shift of emission from a rotating accretion disc. In a previous section, the line broadening due to stellar

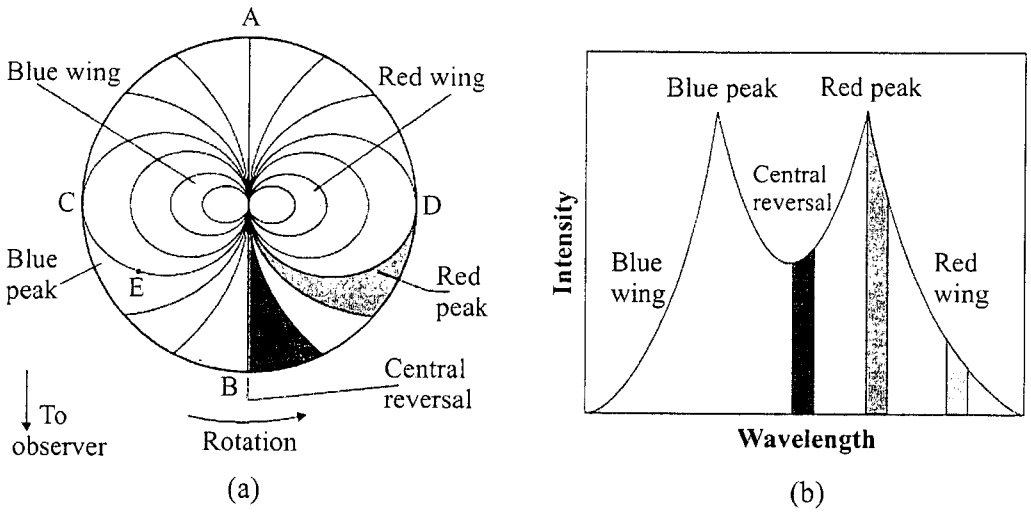

Fig. 3.13: (a) Top view of idealized rotating accretion disc, with constant radial velocity curves indicated. (b) The resulting double-peaked line profile. Shaded areas indicate which part of the disc produces which part of the profile. (Adapted from Robinson 2007, p. 112, Fig. 9.5, after Horne and Marsh 1986, Fig. 1.)

rotation was discussed, and by a similar argument, the emission from a revolving accretion disc should also yield a broadened spectral line. However, the geometry of a disc is very different from that of a star, so the broadened profile due to the disc can be expected to be very different from that associated with a rotating star.

In fact, apart from being considerably broadened, emission lines originating from accretion discs often have a double-peaked structure and quite broad wings (see Fig. 3.13(b)). Robinson (2007, p. 107-117) provides an overview of a basic model compiled by J. Smak which explains the structure of the double-peaked profile (Smak, 1969), and also mentions the refinements of K. Horne and T. Marsh on this model (Horne and Marsh, 1986).

In Smak's model, it is assumed that the accretion disc is optically thin and that emitting material is evenly distributed throughout the disc. It is also assumed that the orbital motion of the disc material about the primary object is Keplerian.

Consider an accretion disc that is being viewed at an inclination of 90°, i.e. "edge-on". For the moment, we will consider the rotational disc broadening to be the only relevant line broadening mechanism. Emission from disc material moving perpendicular across the line of sight (on line AB in Fig. 3.13) will of course not be Doppler shifted, and is represented by the central reversal region at the rest wavelength of the line. Emission from material moving towards or away from the observer (across CD) will be blue shifted or red shifted respectively.

However, the material crossing CD will not all have the same speeds; material towards the outer edge will move slower than material at the inner edge of the disc. In fact, the points on the disc's inner edge, closest to the primary star, will have the highest radial velocity and represent the outer wing limits of the line profile.

For such an optically thin disc, we can consider the intensity of the line profile at a certain Doppler shift from the rest wavelength as being proportional to the number of emitters in the disc material that are moving at the associated radial velocity. Therefore we can gain some insight in the form of the profile by investigating "contours" of constant radial velocity on the disc. If we should start at the point C and move counterclockwise, the Keplerian velocity will stay constant, but the *radial* component will decrease, therefore points with radial velocity equal to that of C, should be closer to the centre, like point E. In this fashion, a map containing an infinite amount of constant radial velocity curves can be created. Some of these curves are shown in Fig. 3.13(a), and the pattern created represents that of a dipole field.

Thus, emission from all particles along one of the curves will produce a single point on the line profile. The longest lines represent the blue and red peaks. Fig. 3.13 illustrates which parts of the disc produces what part of the profile.

However, the assumption of evenly distributed material is not entirely realistic, as the inward spiralling of material actually causes the density closer to the central star to be higher. This will cause the intensity in the wing regions of the profile to be enhanced.

Horne and Marsh refined Smak's model by considering the potential absorption of an emitted photon in an optically thick disc. For such a photon to be absorbed, the relative velocity of the absorbing atom relative to the emitting atom must be zero, otherwise the photon is "seen" to be at a wavelength differing from the rest wavelength. By simply considering the different relative velocities encountered by photons emitted at different angles, it is found that a photon has the greatest chance of escaping an optically thick disc if the angle of emission is 45° measured from the disc radius drawn through the emitting atom. The effect of this refinement to the line profile shape is to change the form of the central reversal more to a "V"-shape from the "U"-shape predicted by the Smak model.

So far, our discussion only considers a symmetrical disc, and therefore equal intensities of the two peaks. Asymmetrical features like one or more "hot spots" where the material transferred from the secondary hit the accretion disc rim, will obviously change the profile shape and the relative heights of the two peaks.

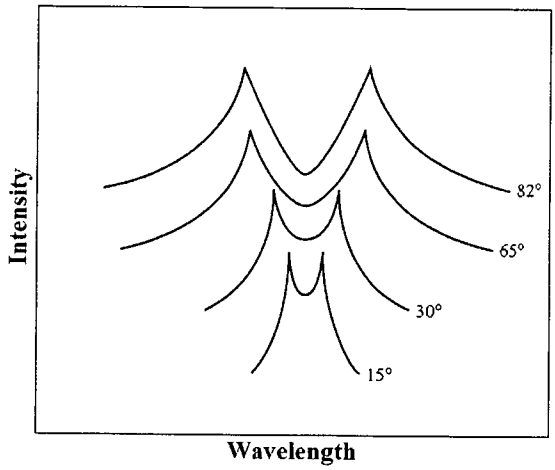

Fig. 3.14: Accretion disc emission line profiles for different inclination angles. (Adopted from Robinson 2007, p. 113, Fig. 9.6.)

For inclinations smaller than 90°, the rotational broadening effect will be similar but diminished, as the radial component of the disc rotation will be smaller. This is illustrated in Fig. 3.14. If we view the accretion disc face-on (at an inclination of 0°), the rotation will essentially have no radial component or broadening effect.

However, depending on the nature and inclination of the disc and of course the spectrograph resolution, an emission line from an accretion disc may not necessarily exhibit the double-peaked structure discussed above, but may just be considerably broadened about the central wavelength.

3.5 Doppler shift of central wavelength

Apart from the numerous phenomena that introduce *broadening* of a spectral line due to the Doppler effect, the movement of the source as a whole relative to an earthly observer will obviously cause a Doppler shift as well. This can be observed as a shift of the *whole* spectral line, and can be quantified in terms of the shift of the central wavelength of the line from the rest wavelength λ_0. The shift in the central wavelength depends on the radial velocity through the Doppler formula Eq. (3.65), regardless of any broadening that might also be present.

The radial velocity of the centre of mass of a system relative to the Sun is called its *systemic velocity*. Any astronomical system will thus have an associated systemic velocity V_0, causing the central wavelengths of all the spectral lines from that system to be shifted by $\Delta\lambda = \lambda_0 V_0/c$.

The significance of the radial velocities measured from central line wavelength shifts

for the two components of a binary system was already discussed in Section 2.1, where it has become evident that such measurement can play a key role in quantifying the characteristic parameters of a binary system.

Having reviewed the basic properties of accreting binary systems in the previous chapter and the fundamental principles applicable to spectroscopy in this chapter, we will now continue to a discussion of the general properties of supersoft X-ray sources as a class of objects.

Chapter 4

Supersoft X-ray Sources: General Characteristics

Supersoft X-ray sources (SSS) are a class of highly luminous astronomical sources, with bolometric luminosities $\sim 10^{36} - 10^{38}$ erg s^{-1}, which are near the Eddington limit for a solar-mass object. They are characterized by the emission of X-rays in the $0.1 - 2$ keV band; in fact, $\gtrsim 90\%$ of the source photons (without interstellar absorption) have energies below 0.5 keV (e.g. van Teeseling 1998), and effective temperatures range between $\sim 15 - 80$ eV. They were first discovered in the Magellanic Clouds due to the low interstellar absorption in the direction of these galaxies, and their proximity. The supersoft sources CAL83 and CAL87 in the Large Magellanic Cloud (LMC), and 1E 0035.4-7230 and 1E 0056.8-7154 in the Small Magellanic Cloud (SMC) were already discovered around 1980 with the *Einstein* satellite (Long, Helfand and Grabelsky, 1981; Seward and Mitchell, 1981). They were only established as a distinct class of objects during the all-sky survey of the ROSAT satellite in 1990-1991 (Trümper et al., 1991), during which several new SSS were discovered, and the subsequent pointed ROSAT observations.

The approximate known populations of SSS are as follows: ~ 15 in the Milky Way, 18 in the LMC (Kahabka et al., 2008), 6 in the SMC and 120-160 in about 20 external galaxies (Kahabka, 2006). The small number of observed SSS in the Milky Way is ascribed to the high degree of interstellar absorption of supersoft X-rays in the galactic plane.

4.1 The primary star — an accreting white dwarf?

Because of the similarities of their spectra to those of low-mass X-ray binaries, it has initially been suggested that SSS may be accreting black hole (Cowley et al., 1990; Smale et al., 1988) or neutron star systems (Greiner, Hasinger and Kahabka, 1991; Kylafis and Xilouris, 1993). However, these models present several problems, as pointed out by van den Heuvel et al. (1992).

Although black hole systems such as Cyg X-1 and LMC X-3 do have soft X-ray spectra, their effective temperatures are still in the range of a few keV, which is higher than required for SSS. Greiner et al. (1991) explained the supersoft emission as originating from a neutron star accreting matter at very high rates, yielding an accretion luminosity at or above the Eddington limit. This would cause the formation of a dense cocoon of ionized material around the neutron star, causing the X-ray spectrum to become softer as the photospheric radius expands. However, one of the difficulties of this model is that a column density high enough to quench the X-ray flux is expected to exist at super-Eddington accretion in a neutron star system.

The luminosity, radius and effective temperature of a star are related by the Stefan-Boltzmann law (see Section 2.7.2). Typical values of the intrinsic luminosity and effective temperature for SSS are $L \sim 3 \times 10^{37}$ erg s^{-1} and $kT_{\rm eff} \sim 40$ eV. Substituting these values into Eq. (2.112) yields radii that are typical for white dwarfs ($R \sim 10^9$ cm), leading to the conclusion that the X-rays are produced by accretion onto a white dwarf (e.g. Kahabka and van den Heuvel 1997).

A white dwarf (WD) would have to accrete matter at a rate of $\sim 2 \times 10^{-6} M_\odot$ yr^{-1} to produce such a high accretion luminosity. However, it can be shown that the nuclear fusion of an amount of material on a white dwarf yields about 30 times more energy than the accretion energy that is released when the same amount of material is accreted onto the white dwarf. Therefore, if nuclear fusion is present, the accretion rate required to produce the observed luminosity is substantially reduced.

Van den Heuvel et al. (1992) showed that the supersoft emission can be explained by steady nuclear burning of accreted hydrogen on the surface of a white dwarf with mass between $0.7 M_\odot$ and $1.2 M_\odot$ (see also Iben 1982). This requires mass transfer on a thermal time-scale by Roche lobe overflow from a close main-sequence companion that is more massive than the white dwarf ($1.5 - 2.0 M_\odot$), yielding $q > 1$. This is the close binary supersoft source or CBSS model. The accretion rate required to sustain the steady nuclear burning is $\sim 1 - 4 \times 10^{-7} M_\odot$ yr^{-1}.

There is evidently some similarities between the CBSS model and those of the cataclysmic variable (CV) class of objects, with the important difference being that, in CV's, the mass ratio $q < 1$, and the mass transfer rate will be too low to sustain steady hydrogen burning.

Although the high white dwarf masses inferred for many SSS seem to suggest that they contain O-Ne-Mg white dwarfs, this does not have to be the case; they may have started out as C-O white dwarfs, gaining mass through accretion (see Kahabka

and van den Heuvel (1997) and references therein).

4.2 Nuclear H-burning as a function of accretion rate

When an envelope of hydrogen-rich material is accreted onto a white dwarf, nuclear fusion can be ignited if the critical envelope mass $\Delta m_{\rm crit}$ is reached, which can sustain the temperature and pressure conditions that are required for nuclear burning by the CNO cycle (i.e. $T \sim 10^8$ K and $P \gtrsim 10^{18} - 10^{20}$ dyne cm^{-2}) (Fujimoto, 1982). The value of $\Delta m_{\rm crit}$ decreases with increasing WD mass and increasing accretion rate (Prialnik and Kovetz, 1995). The higher the accretion rate, the less violent the induced outburst will be, and steady nuclear burning can occur if the accretion rate is similar to the rate of nuclear burning, i.e. $\dot{m} \sim \dot{m}_{\rm nuc}$.

In fact, there are three different regimes when considering the response of a white dwarf to accretion — unstable nova shell outbursts for low accretion rates, steady nuclear burning for intermediate accretion rates, and some of the accreted matter blown off in an optically thick accretion wind for very high accretion rates. These three regimes are illustrated for different WD masses in Fig. 4.1, and in Fig. 4.2 the positions of the corresponding white dwarfs on the HR diagram are indicated.

4.2.1 Low accretion rate

For material consisting of 70% hydrogen ($X = 0.7$), the boundary between stable and unstable nuclear burning is given by (Hachisu and Kato, 2001)

$$\dot{m}_{\rm steady} = 3.7 \times 10^{-7} \left(\frac{M_{\rm WD}}{M_\odot} - 0.4 \right) M_\odot \ {\rm yr}^{-1} \ , \tag{4.1}$$

and is represented by the lower horizontal line in Fig. 4.1. No steady hydrogen burning takes place for $\dot{m} < \dot{m}_{\rm steady}$, but nova outbursts are triggered by unstable shell flashes. This is represented by the dotted lines in Fig. 4.2. For accretion rates below $0.25\dot{m}_{\rm steady}$, all accreted matter will be blown off during a nova outburst (Kahabka and van den Heuvel, 2006).

The basic evolutionary stages of a nova outburst are shown in Fig. 4.3. The timescale of the evolution is, however, very different for different novae, with a higher WD mass yielding faster evolution. In the presence of an optically thick wind, supersoft X-rays will not be observed due to absorption by the wind. Therefore, theoretically, all novae will become supersoft sources after the optically thick wind has ceased, up to when the hydrogen burning stops (Kato, 2010).

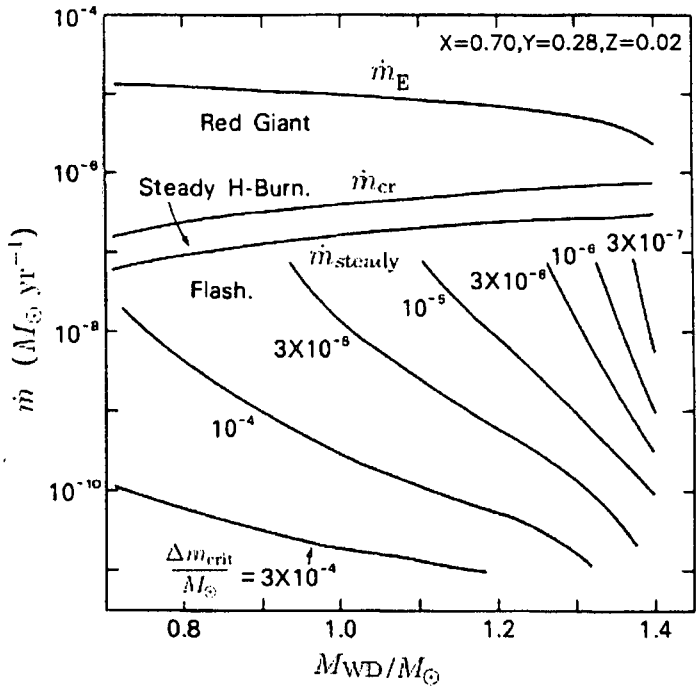

Fig. 4.1: The response of a WD to accretion rate, illustrating the regions of recurrent shell flashes, steady H-burning and optically thick accretion winds for different values of the WD mass M_{WD}. The Eddington-limited accretion rate for H is denoted by $\dot{m}_E$. The element abundance is indicated at the top, where X represents the fraction of H, Y the fraction of He and Z the fraction of other elements. The oblique lines at the bottom represent loci of constant ignition mass. (Adopted from Nomoto 1982, Fig. 9.)

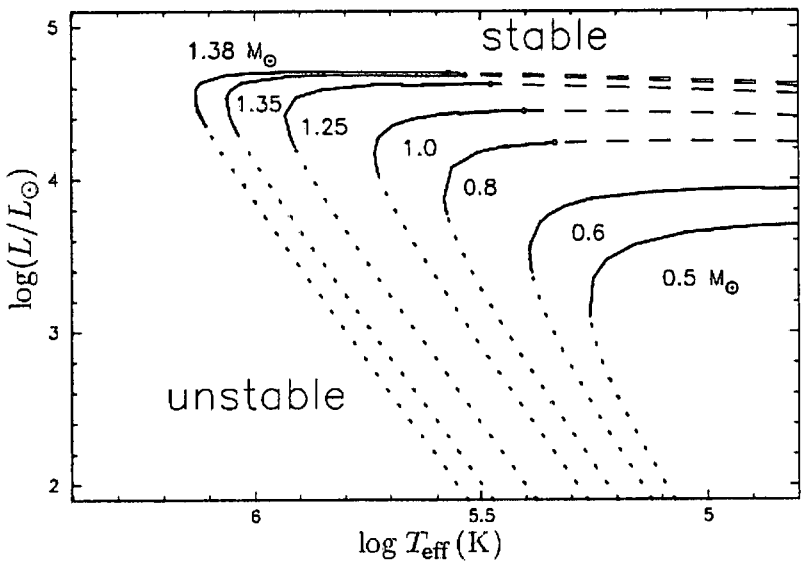

Fig. 4.2: An HR diagram with a number of loci ($M_\odot$ = constant) for accreting WD's, showing the luminosity L in terms of the effective surface temperature T_{eff}. The dotted portions represent unstable nuclear burning, and the solid and dashed fragments stable burning. The dashed portions represent the region of optically thick mass loss. The composition of accreted matter is the same as in Fig. 4.1. (Adapted from Kato 2010, Fig. 1.)

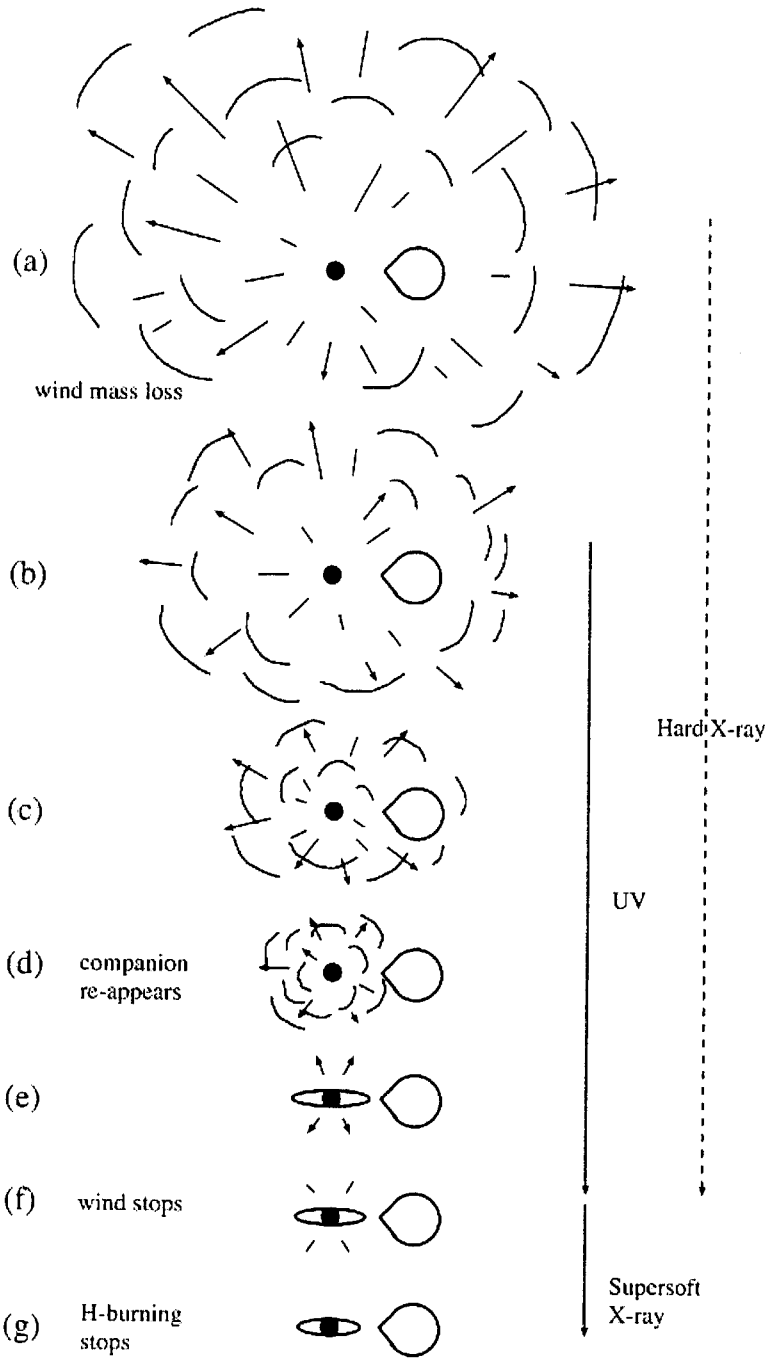

Fig. 4.3: The evolution of a nova outburst. (a) After the start of the nova explosion, the WD envelope greatly expands and wind mass loss sets in. (b)-(c) The photospheric radius shrinks with time while the photospheric temperature rises, and a large part of the envelope material is blown off. (d) The companion re-appears from the shrinking WD photosphere and (e) an accretion disc may form again. (f) The optically thick wind stops, (g) H burning stops and a cooling phase is entered. Internal shocks between the ejecta, or a bow shock formed between the ejecta and the companion, may cause the emission of hard X-rays from (a) to (f). The UV flux is the strongest from (b) to (f), and is replaced by supersoft X-ray emission from (f) to (g). (Adopted from Hachisu and Kato 2006, Fig. 1.)

4.2.2 Intermediate accretion rate

For $X = 0.7$, the onset of accretion winds is marked by the critical value (Hachisu and Kato, 2001)

$$\dot{m}_{\rm cr} = 7.6 \times 10^{-7} \left(\frac{M_{\rm WD}}{M_\odot} - 0.4 \right) M_\odot \ {\rm yr}^{-1} \ , \tag{4.2}$$

which is represented by the upper horizontal line in Fig. 4.1. For $\dot{m}_{\rm steady} < \dot{m} < \dot{m}_{\rm cr}$, steady hydrogen shell burning takes place without the formation of optically thick winds. This leads to the formation of a persistent SSS, represented by the solid lines in Fig. 4.2.

4.2.3 High accretion rate

When $\dot{m} > \dot{m}_{\rm cr}$, stable hydrogen burning can take place in a thin shell around the white dwarf, while the excess accreted matter piles up to form an extended envelope (a so-called *red giant envelope*) around the white dwarf, with part of the envelope being blown off in an optically thick wind. This is represented by the dashed lines in Fig. 4.2. Absorption of supersoft X-rays by the optically thick winds will prevent such a source from being observed as a SSS during such an extremely high mass accretion phase. However, a source with such a high accretion rate may still exhibit transient supersoft behaviour by a limit-cycle process such as that described by Reinsch et al. (2000).

4.3 White dwarf properties

The radius of a white dwarf is inversely related to its mass by (see Eracleous and Horne 1996; Hamada and Salpeter 1961)

$$R_{\rm WD} = 4.9 \times 10^8 \left(\frac{M_{\rm WD}}{M_\odot} \right)^{-0.8} \ , \tag{4.3}$$

according to which the white dwarf radius decreases with increasing mass.

However, the accretion of material onto the WD surface will cause the formation of a hydrogen burning shell on the WD, and this will mean that the effective photosphere of the X-ray source will have a larger radius than the radius of the degenerate core. Therefore the radius inferred from a measured luminosity and effective temperature by using the relationship in Eq. (2.112) will also include the contribution of a hydrogen burning shell. Using this radius to calculate the WD mass with Eq. (4.3) will therefore lead to an underestimation of the WD mass. For SSS with stable nuclear burning, the photospheric radius will be $\sim 2-3$ times larger than the radius of the white dwarf alone (see Ibragimov et al. 2003 and references therein).

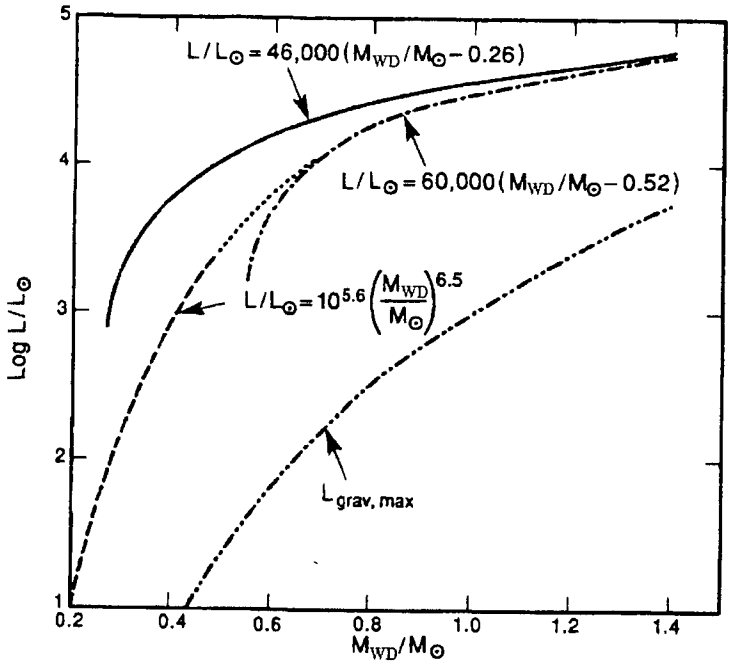

Fig. 4.4: Relationship between mass and luminosity for degenerate dwarfs with H-burning shells. The solid curve at the top is the plateau luminosity curve for cool WD's. The dashed curve is applicable to He WD's, and the dash-dotted curve to hot C-O WD's. $L_{\rm grav,max}$ is the maximum accreting WD luminosity that can be reached by the release of gravitational potential energy. (Adapted from Iben and Tutukov 1996, Fig. 5.)

The relationship between the luminosity and mass of a hot, degenerate C-O white dwarf core powered by a shell of burning hydrogen can be estimated by:

$$\frac{L}{L_\odot} = 60000 \left(\frac{M_{\rm WD}}{M_\odot} - 0.52 \right) \tag{4.4}$$

and is illustrated by the dash-dotted curve in Fig. 4.4 (see Iben and Tutukov 1996 and references therein). This luminosity represents the "plateau" luminosity, i.e. the luminosity at the horizontal track for a specific WD mass in the HR diagram (Fig. 4.2). For a He white dwarf, the relationship is described by

$$\frac{L}{L_\odot} = 10^{5.6} \left(\frac{M_{\rm WD}}{M_\odot} \right)^{6.5} \tag{4.5}$$

during the plateau H-burning phase after its departure from the first giant branch. This relation is represented by the dashed curve in Fig. 4.4. For thermonuclear burning of hydrogen on a zero-temperature WD consisting of He, C and O, or O and Ne, the following estimate (given by the solid curve in Fig. 4.4) can be used during the shell H-burning phase after a shell flash:

$$\frac{L}{L_\odot} = 46000 \left(\frac{M_{\rm WD}}{M_\odot} - 0.26 \right) \tag{4.6}$$

According to Iben and Tutukov (1996), SSS that are undergoing stable burning normally have hot cores and are described quite well by Eq. (4.4). On the other hand, white dwarfs in CV's and symbiotic sources undergoing nova outbursts are more likely to be old, and the approximation for a cool WD in Eq. (4.6) is more valid.

Suleimanov and Ibragimov (2003) approximated the mass-radius relation for a white dwarf by a third-order polonomial,

$$R_9 = 1.90 - 2.90\left(\frac{M_{\rm WD}}{M_\odot}\right) + 2.53\left(\frac{M_{\rm WD}}{M_\odot}\right)^2 - 0.960\left(\frac{M_{\rm WD}}{M_\odot}\right)^3 , \qquad (4.7)$$

where $R_9 = R_{\rm WD}/10^9$ cm. They analysed the effective temperature of supersoft sources in the region of stable nuclear burning, and suggested the following estimate of the relationship between the effective temperature and the WD mass for a SSS:

$$kT_{\rm eff} = 26 \text{ eV} \times \frac{m_1\,(m_1 - 0.26)^{0.25}}{\left[1 - 1.53m_1 + 1.33m_1^2 - 0.51m_1^3\right]^{0.5}} , \qquad (4.8)$$

where $m_1 = M_{\rm WD}/M_\odot$. The equation was derived assuming that the WD luminosity is equal to one half of the plateau luminosity, and that the photospheric radius is larger than the radius of the WD by a factor of $2(M_\odot/M_{\rm WD})^2$. However, they note that the appropriate relation for sources accreting below the steady-burning rate may be more complex than the above.

Another quantity that is of importance is the surface gravity of the WD, given by

$$g = \frac{GM_{\rm WD}}{R_{\rm WD}^2} , \qquad (4.9)$$

under the assumption that the WD can be regarded as a point mass.

4.4 SSS subclasses

Apart from the classical CBSS model of van den Heuvel et al. (1992), there are also other classes of systems that can produce supersoft X-ray emission. Di Stefano and Nelson (1996) considered hydrogen burning on accreting white dwarfs, and distinguished four basic classes: CV's, CBSS's, WBSS's (wide-binary supersoft sources) and SySS's (symbiotic supersoft sources). This classification scheme is shown in Table 4.1.

Even though CV's can not be steady SSS, nova outbursts in such systems can still bring about supersoft emission as explained in the previous section. Classical novae (CN) are defined as systems for which only one eruption is observed. Recurrent

Type	Mass transfer mechanism	$\dot{m}$ ($M_\odot$ yr^{-1})	$P_{\rm orb}$ (days)	Steady (S) / Recurrent (R)	Mass ejection	Well-known examples
CV	Magnetic braking/ gravitational radiation	$<\sim 10^{-8}$	$<\sim 0.2$	R	Nova	Nova LMC 1995 (CN) U Sco (RN) SMC 13?[a]
CBSS	Thermal time-scale readjustment of donor	$>\sim 10^{-7}$	$\sim 0.2 - 3.0$	S	Winds (for $\dot{m} > \dot{m}_{\rm cr}$)	CAL 83 CAL 87 RX J0925.7-4758
		$<\sim 10^{-7}$	$\sim 0.2 \times 10^2$	R	Nova	
WBSS	Nuclear evolution of donor	$>\sim 10^{-7}$	$\sim 3.0 \times 10^2$	S	Winds (for $\dot{m} > \dot{m}_{\rm cr}$)	
		$<\sim 10^{-7}$	$\sim 3.0 \times 10^2$	R	Nova	
SySS	Stellar winds or Roche lobe overflow from evolved donor	$>\sim 10^{-7}$	$\sim 10^2$	S	Winds	RR Tel AG Dra RX J0048.4-7332
		$<\sim 10^{-7}$	$\sim 10^2$	R	Nova	

Table 4.1: The SSS classification scheme of Di Stefano and Nelson (1996) for hydrogen-burning C-O white dwarfs. (Adapted from Di Stefano and Nelson 1996, Table 1.)
[a]SMC 13 has previously been classified as a CBSS, but is now thought that this source may be a CV with supersoft emission from a slowly evolving nova outburst.

novae (RN), on the other hand, are defined as systems that were first classified as CN, but were later found to repeat their eruptions (e.g. Warner 1995). Examples of SSS exhibiting such behaviour are the CN Nova LMC 1995, and the RN U Sco.

Systems in which the donor star is initially more evolved than the donor in a CBSS, and in which the nuclear evolution of the donor can then sustain mass transfer by Roche lobe overflow with $\dot{m}$ in the steady burning range, are referred to as wide-binary supersoft sources or WBSS by Di Stefano (1996), who suggests that such a system may also exhibit SSS behaviour.

Some SSS have been identified as symbiotic systems. Symbiotic stars are interacting binary stars with very long periods that usually consist of a hot white dwarf and a red giant donor embedded in an ionized nebula. The nebula is produced by the excitation of the atmosphere/wind of the giant by radiation from the hot white dwarf (Mürset, Schild and Vogel, 1996). Material from the red giant is accreted onto the white dwarf, and when a critical mass is reached, this can lead to a nova outburst. However, nuclear outbursts in symbiotic novae last much longer than those in classical novae (McKenna et al., 1997). Symbiotic systems that have been observed as SSS are RR Telescopii and AG Draconis in our galaxy, and the SMC source RX J0048.4-7332 (SMC 3).

Other possible scenarios for the production of supersoft X-rays include the luminous

nuclei of planetary nebulae (PN) — like the SMC SSS 1E 0056.8-7154 — and He shell flashes (Kato, 1996). Before eventually becoming the nucleus of a PN, a star can undergo a final He shell flash during the course of its evolution. Also, if part of the accreted matter remains on the surface of an accreting WD after a nova outburst, a layer of He "ash" can develop under the H-burning zone, and this will grow with every H flash. Once the mass of the He layer is large enough, it can be ignited and a He nova outburst follows. Both a "final He flash" and a He nova can produce supersoft X-rays. Yungelson et al. (1996) also mentions systems with He donors, as well as double degenerate systems, as SSS candidates. The LMC SSS RX J0439.8-6809 is possibly a double degenerate source (van Teeseling et al., 1997).

4.5 The nature of the secondary star

As previously discussed, the CBSS model requires a secondary star more massive than the WD. Such an appropriate donor should have a radiative envelope, and should be a slightly evolved main-sequence star with a spectral type earlier than about F5 (Kahabka and van den Heuvel, 1997). This is explained as follows: With $q > 1$, the mass transfer will shrink the binary separation and also the Roche lobe of the donor. Also, the thermal equilibrium radius of an evolved star with a He-rich core will not shrink when mass is removed from its envelope. Therefore the Roche lobe shrinkage will yield the donor thermally unstable, and mass will be transferred on its thermal time-scale until it becomes less massive than the primary.

When considering SySS, there are two possibilities. Roche lobe overflow from a red giant with a lower mass than the WD can take place due to the nuclear evolution of the red giant. In wide symbiotic systems where the red giant is on the asymptotic giant branch and does not fill its Roche lobe, a strong stellar wind from the red giant can still drive mass transfer rates high enough for the system to be a SSS.

However, because the optical spectra of CBSS are completely dominated by emission from a bright, irradiated accretion disc, the donor itself makes only a minor ($\sim 10\%$) contribution to the optical spectrum, therefore the spectral type of the secondary can not be directly determined (see Kahabka and van den Heuvel (2006) and references therein). (It does appear that the donor star is strongly heated by the X-ray emission from the WD, and therefore contributes to the reprocessing of X-ray emission to optical flux). The exceptions on this limitation are SSS that can also be observed in their optically faint states, like recurrent novae, where irradiation of the disc is greatly reduced and the spectrum is dominated by the secondary. For example, the donor of the recurrent nova U Sco has been found to be of spectral type K2 V.

4.6 The accretion disc

Observational evidence suggests that many SSS may contain accretion discs. However, the WD luminosity due to nuclear burning is much larger than the accretion luminosity of the disc, and some of the X-ray energy emitted by the luminous white dwarf irradiates the surface of the disc. Therefore the main role of the disc in terms of radiation is the reprocessing of X-rays from the white dwarf, and this greatly exceeds the accretion energy released in the disc (Popham and Di Stefano, 1996).

Popham and Di Stefano (1996) calculated disc models and spectra for steady-burning sources by using the so-called "slim disc" equations, which are more sophisticated than the simple thin disc models. They included the spectrum of the white dwarf, the spectrum of the disc with reprocessing and flaring, and also the contribution of the heated donor (see Fig. 4.5 for some of their results). They compared the combined model to the observed optical and UV fluxes for three LMC sources, CAL 83, CAL 87 and RX J0513.9-6951, and it was found that the fluxes for CAL 83 is described quite well with such a model. The low inclination of RX J0513.9-6951, and the high inclination of the eclipsing source CAL 87 can explain the differences between their observed fluxes and that of the model, for which $i = 60°$ was used.

According to Meyer-Hofmeister, Schandl and Meyer (1997), the impact of the accreting stream of material impinging on the disc probably leads to a high rim structure at the outer edge of the accretion disc, with a height of up to $z/r = 0.4$, which corresponds to an accretion rate of $\sim 2 \times 10^{-7} M_{\odot}$ yr^{-1}. This elevated rim structure is like a huge screen, and is strongly irradiated by the white dwarf. It is thought that the reprocessed radiation from the accretion disc rim can then become the strongest source of optical light from the system, and this is confirmed by e.g. the light curves of the eclipsing source CAL 87.

In cases of super-Eddington accretion, the standard disc model of Shakura and Sunyaev (1973) no longer provides an accurate solution, and a supercritical accretion disc or "superdisc" is formed (Fukue, 2000; Fukue and Matsumoto, 2001). In superdiscs, the effects of self-irradiation and self-occultation are important, and the double-peaked profiles become asymmetric. The superdisc luminosity is also close to the Eddington limit. The accretion rate required to create a superdisc is $\dot{m}_{\rm out} \sim 10^{-5} M_{\odot}$ yr^{-1} at the outer edge of the disc, while the typical accretion rate at the inner disc edge in SSS is $\dot{m}_{\rm in} \sim 10^{-7} - 10^{-6}$ (Kitabatake, Fukue and Matsumoto, 2002). Kitabatake et al. (2002) suggested that a radiation-driven "superwind" may be blowing from the superdisc, in which most of the accreting material is blown away without being accreted onto the white dwarf.

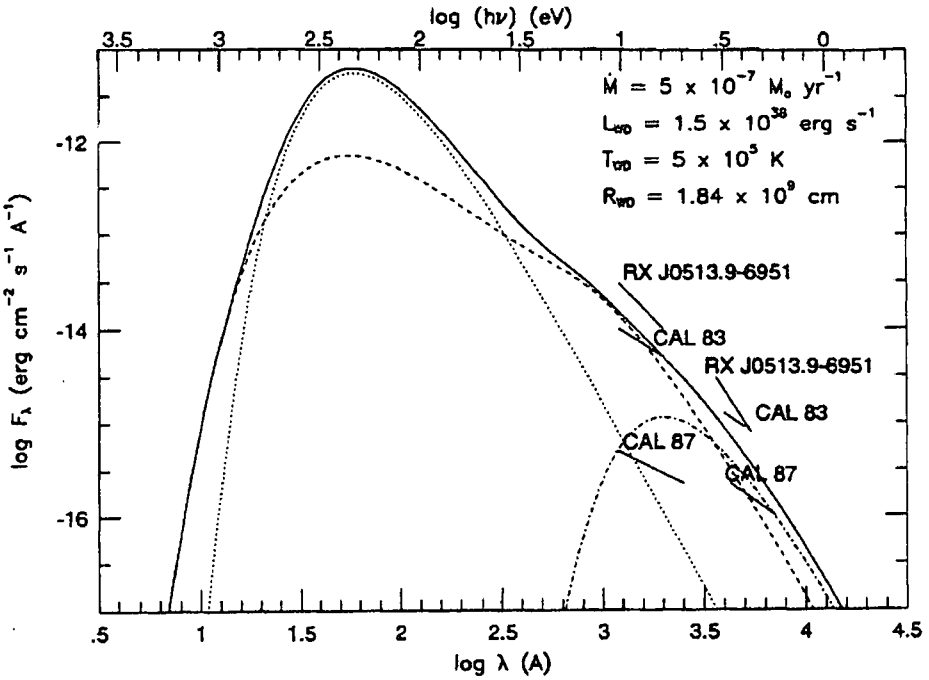

Fig. 4.5: Comparison of model spectra with those of 3 LMC sources. The model spectra shown are the WD spectrum (dotted curve), the disc spectrum with reprocessing and flaring (dashed curve), the spectrum of the heated donor (dash-dotted curve) and the combination of all 3 (solid line). The WD mass is $1.2M_{\odot}$, and an inclination of $i = 60°$ is assumed. The other parameters for the solution are listed at the top. (Adopted from Popham and Di Stefano 1996, Fig. 4.)

4.7 Bipolar jets

The He II λ4686, Hα and Hβ emission lines in the optical spectra of the sources RX J0019.8+2156, RX J0513.9-6951 and RX J0925.7-4758 were found to have blueshifted and redshifted satellite features (varying on time-scales of months) at Doppler shifts of $\sim$ 885 km s^{-1}, $\sim$ 3800 km s^{-1} and $\sim$ 5200 km s^{-1} respectively (see Kahabka and van den Heuvel 2006 and references therein). The satellites for the Hβ and He II λ4686 lines of RX J0513.9-6951 were shown in Fig. 3.12 of Chapter 3. These satellite components are interpreted as bipolar jets from these systems.

The observed Doppler velocities can be compared with the escape velocity from a white dwarf,

$$v_{\rm esc} \approx 5160 \sqrt{\frac{M_{\rm WD}}{M_{\odot}} \left(\frac{R}{10^9 \text{ cm}} \right)^{-1}} \text{ km s}^{-1} , \qquad (4.10)$$

and the terminal velocities $v_{\infty}^{\rm ld} = 3v_{\rm esc}$ of a line driven wind, and $v_{\infty}^{\rm rd} = 0.42v_{\rm esc}$ of a radiation driven wind from the inner part of the disc. The observed bipolar jets are explained quite well by radiation driven winds originating from the inner accretion disc region close to a white dwarf. This is confirmed by absorption velocities from

P Cygni structures found in the X-ray spectrum of RX J0925.7-4758. The observed velocities also serve as further justification for the white dwarf model for SSS.

4.8 Spectral properties

4.8.1 X-rays

SSS are often approximated as optically thick blackbody emitters. However, the blackbody fits to the X-ray spectra often predict luminosities that are above the Eddington limit. Heise, van Teeseling and Kahabka (1994) showed that H- and He-rich local thermal equilibrium (LTE) white dwarf atmosphere models yield bolometric luminosities below the Eddington limit, and that the predicted radii are closer to what is expected for white dwarfs. However, for a truly adequate interpretation, deviations from LTE has to be taken into account, and fully metal-line blanketed non-LTE model atmospheres should be fitted to the spectra (e.g. Rauch and Werner 2010).

Apart from possible long-term transient behaviour, the soft X-ray light curves of some SSS exhibits an asymmetric modulation that is in phase with the optical orbital light curve (Kahabka, 1996a). The observed X-ray light curves may indicate a WD with a strong magnetic field.

4.8.2 Ultraviolet and optical

As mentioned previously, the strong UV and optical fluxes detected in SSS is ascribed to a strongly irradiated accretion disc, with the heated side of the companion also contributing to the optical flux (see Fig. 4.5). Balmer and He II λ4686 emission lines from the accretion disc are quite common in the spectra of SSS, and high-excitation emission lines of e.g. C, N, O, S and Si are also observed (e.g. van Teeseling 1998). Quasi-sinusoidal variations in the optical flux with the orbital period is observed in most systems, while long-term variations are also detected in transient sources. More details on the individual spectra will be provided in the next chapter, where the characteristics of specific sources are discussed.

4.8.3 Radio

Radio emission and X-ray emission are often found together in high-energy astrophysical environments. While the X-ray spectrum represents thermal emission from material at very high temperatures, non-thermal radio emission can originate from the spiralling of electrons around magnetic field lines in the system. If the electrons are relativistic, synchrotron emission takes place, while cyclotron emission is associated with non-relativistic electrons (e.g. Rybicki and Lightman 2004, Chapter 6).

Source	Point-source flux density (mJy)			
	3.5 cm	6.3 cm	12.7 cm	21.7 cm
LMC				
RX J0513-69	< 0.09	< 0.09	< 0.15	< 0.18
RX J0528-69	< 0.09	< 0.09		
CAL 83	< 0.12	< 0.12		
CAL 87	< 0.12	< 0.12		
RX J0550-71	< 0.15	< 0.15		
SMC				
1E 0035-72	< 0.12	< 0.12		
RX J0059-71	< 0.12	< 0.15		

Table 4.2: 3σ upper limits on radio emission from Magellanic Cloud SSS from ATCA observations. (Extracted from Fender et al. 1998, Table 1.)

The high accretion rates in SSS imply that the accretion disc in magnetized systems exerts a large torque on the magnetosphere of the white dwarf, which opens up the possibility for transient non-thermal behaviour. Magneto-hydrodynamic (MHD) instabilities can be expected to produce non-thermal radio outbursts as a result of magnetospheric flares.

A radio survey of X-ray sources in the LMC and SMC (including a sample of SSS) was performed during the period of 30 June – 13 July 1997 with the Australia Telescope Compact Array (ATCA) (Fender, Southwell and Tzioumis, 1998). None of the targets were detected as radio sources, but upper limits on possible radio emission from these sources could be reduced. These results of Fender et al. (1998) are shown in Table 4.2.

During radio observations with the VLA and MERLIN telescopes during 2000, two components with a combined flux of ~ 1 mJy [1] were detected in the galactic symbiotic SSS AG Dra — the radio emission possibly originates from the ionized nebula surrounding the source (Ogley et al., 2002). The galactic supersoft sources T Pyxis, Nova Cygni 1992 and QR Andromedae were not detected.

Meroghetti et al. (2011) reported the first radio detection of the planetary nebula N67 with ATCA on 30 November 2010.

The availability of MeerKAT and eventually the SKA will be extremely valuable in studying accretion in SSS, as the high sensitivity will enable the detection of much fainter radio signals that may originate from non-thermal emission in these sources. The detection of non-thermal radio emission from other SSS will greatly enhance our understanding of the role of magnetic fields in this class of objects.

[1] 1 mJy = 10^{-26} erg s^{-1} cm^{-2} Hz^{-1}

4.9 Origin and evolution of SSS

The origin of CBSS is closely related to that of CV's, the difference being that the eventual donor is more massive than the WD (Kahabka and van den Heuvel, 1997). A schematic illustration of CBSS formation is shown in Fig. 4.6. They initially form through common envelope (CE) evolution of wide binary systems consisting of a red giant (on the asymptotic giant branch) with a degenerate C-O or O-Ne-Mg core and a main-sequence star with $M_2 \leq 2.5 M_\odot$. After the red giant engulfs the lower-mass companion in its envelope, the frictional drag on the orbital motion of the two stars in the CE causes the stars to spiral in rapidly, while the envelope is expelled due to the heat produced by friction. The binary will become a CBSS when the companion fills its Roche lobe at a later stage.

The origin of symbiotic systems is similar, but the initial orbit is so wide that the envelope ejection and white dwarf formation of the initially more massive red giant takes place without noticeable interaction with the companion star. Mass transfer only starts when the companion evolves into a red giant.

Apart from the thermal time-scale evolution associated with the CBSS model of van den Heuvel et al. (1992), an alternative evolutionary scenario has been suggested by van Teeseling and King (1998), i.e. the wind-driven evolution of SSS with low-mass secondary stars. They propose that the strong irradiation of the secondary star by the white dwarf excites strong winds from the secondary, and that the considerable loss of angular momentum in the wind can drive Roche lobe overflow at a high enough rate to sustain steady or recurrent hydrogen burning in systems with $q \lesssim 0.7$. Such a self-sustained wind-driven model is proposed for SMC 13, and also for the LMC SSS RX J0537.7-7034 (Greiner, Orio and Schwarz, 2000).

A white dwarf is supported against its own gravitation by electron degeneracy pressure. The maximum mass for an object supported by electron degeneracy is the *Chandrasekhar limit*, which is $M_C \approx 1.4 M_\odot$. When a massive accreting white dwarf approaches the Chandrasekhar limit, the ignition of nuclear fuel in its core can cause the white dwarf to be destroyed in a runaway explosive event called a Type Ia supernova (SN Ia). In some other cases, the degenerate electrons of the massive white dwarf are captured by the ionized nuclei through a process known as inverse beta decay, which involves the combination of a proton and an electron to yield a neutron and a neutrino. The white dwarf is therefore robbed of its electron degeneracy support before a supernova explosion commences, and it collapses to a neutron degeneracy supported core (i.e. a neutron star). This process is referred to as accretion-induced collapse (AIC) (e.g. Metzger et al. 2009). Explosive nuclear burning and electron captures are therefore two "competing" processes, and the fate

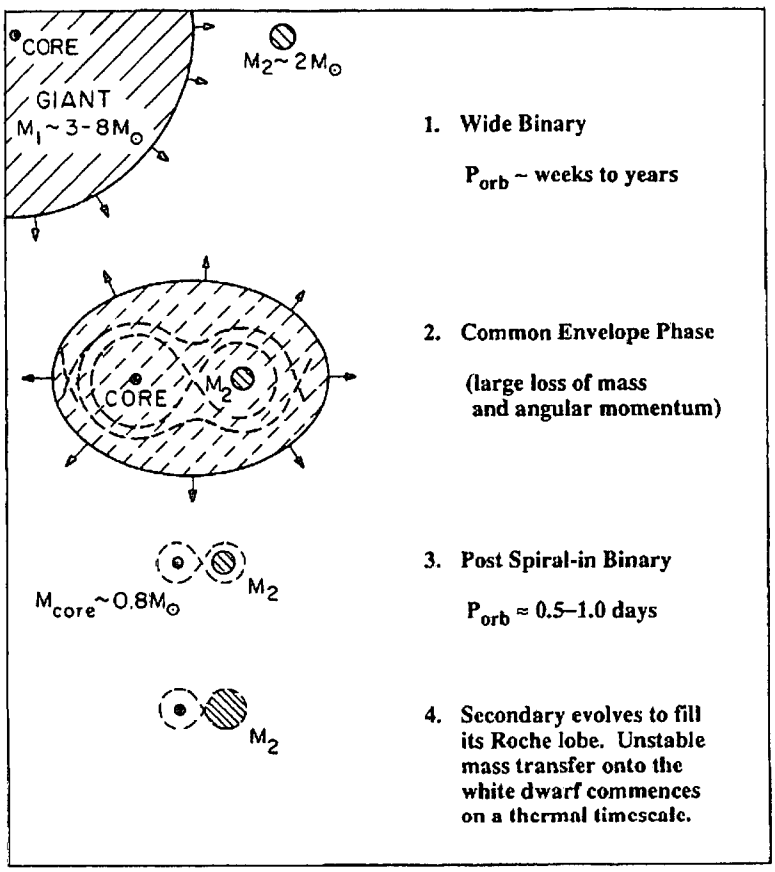

Fig. 4.6: The formation of a CBSS through CE evolution. (Adopted from Rappaport and Di Stefano 1996, Fig. 1.)

of the white dwarf will depend on which of the two processes commences first.

Although the exact nature of the progenitor systems of SNe Ia are not yet clear, the most popular model for SNe Ia is an accreting C-O white dwarf in a binary system, either as part of a single-degenerate or a double-degenerate binary. In the single-degenerate case, the white dwarf is believed to accrete mass from the companion star until it reaches the Chandrasekhar limit and a SN Ia takes place. However, the problem with this model is that it is not as easy as may be expected to increase the mass of a white dwarf through accretion. For a low accretion rate, nova explosions may eject most of the accreted material, while for a high accretion rate, most of the transferred material can be lost through winds. For this reason, the intermediate accretion rates in steady-burning CBSS make these objects a very promising class as possible progenitors of SNe Ia (see the reviews of Kahabka and van den Heuvel (1997); Podsiadlowski (2010) and references therein). The possibility also exists that off-centre ignitions of He on sub-Chandrasekhar C-O white dwarfs (with masses in the range $0.6 - 0.9M_\odot$) can create explosions that are similar to SNe Ia. This can occur after the accumulation of $0.15 - 0.20M_\odot$ of He through hydrogen burning —

this is the so-called double-detonation model.

Another possibility is that supersoft sources may evolve to become cataclysmic variables. Meintjes (2002) and Schenker et al. (2002) explain the long orbital period and short white dwarf spin period ($\sim$ 33 s) of the CV AE Aqr by the possibility that the source has passed through a supersoft phase in its recent past. It is thought that a significant fraction of the current cataclysmic variables may have formed in this way. Examples of other CVs with such short spin periods indicative of extensive spin-up of the white dwarf are V533 Her (63.633 s) and DQ Her (142 s)[2] (Norton, Wynn and Somerscales, 2004).

The purpose of the basic discussion of supersoft X-ray sources in this chapter is not to provide a comprehensive account of all the aspects of this highly multi-dimensional class of sources, but only to provide an overview of their general properties, especially those related to binary characteristics and accretion-related phenomena. The individual properties of the different targets that form part of this study are discussed in the next chapter.

[2]Originally thought to be 71 s, but shown by Zhang et al. (1995) to be twice this value, i.e. 142 s.

Chapter 5

Supersoft X-ray Sources: Review of Target Sample

The supersoft sources included in the observational part of this study are the supersoft X-ray binaries CAL 83 in the LMC and SMC 13 in the SMC, the luminous single nucleus 1E 0056.8-7154 of the SMC planetary nebula N67, as well as the galactic supersoft symbiotic nova RR Tel. The coordinates of these sources are given in Table. 5.1. In this chapter, a literature review of each source is presented, focusing only on those aspects that are considered the most relevant to the current study. These include the nature of the compact object, as well as the binary parameters and accretion-related phenomena as related to observable properties in different wavelength regions.

5.1 CAL 83

5.1.1 X-ray spectra

The Large Magellanic Cloud supersoft X-ray source CAL 83 was one of the first SSS discovered by the *Einstein X-ray Observatory* (Brown et al., 1994; Long et al., 1981), and since then it has been observed by several other X-ray satellites. The soft nature of its spectrum was confirmed by an EXOSAT observation on 18 December 1985 (Crampton et al., 1987).

Target	Galaxy	RA	Dec
CAL 83	LMC	05:43:34.5	-68:22:18
1E 0035.4-7230 (SMC 13)	SMC	00:37:19.0	-72:14:14
1E 0056.8-7154 (N67)	SMC	00:58:37.1	-71:35:50
RR Telescopii	Milky Way	20:04:18.5	-55:43:33

Table 5.1: Celestial coordinates of SSS that formed part of this study (epoch=J2000, equinox=2000).

Parameter	LTE	NLTE
$kT_{\rm eff}$ (eV)	$44.4^{+1.1}_{-1.0}$	$\lesssim 34.7$
$N_{\rm H}$ (10^{20} cm^{-2})	$8.87^{+1.55}_{-1.30}$	$6.07^{+\gtrsim 0.33}_{-\gtrsim 0.47}$
$\log g$	9.0	9.0
$L_{\rm bol}$ (10^{37} erg s^{-1})	$5.81^{+0.13}_{-0.20}$	$\gtrsim 2.0$
R (10^9 cm)	$1.00 - 1.14$	$\gtrsim 1.03$
χ^2/DOF	1.18	1.48

Table 5.2: CAL 83 LTE and NLTE white dwarf atmosphere fit parameters for a ROSAT PSPC observation. DOF is the degrees of freedom for the fit. (Adopted from Kahabka 1998, Table 3.)

Parameter	Blackbody		LTE	NLTE
$kT_{\rm eff}$ (eV)	41 ± 6	46.4 ± 1.4	$44.0\pm^{6.3}_{0.6}$	32.6 ± 0.7
$N_{\rm H}$ (10^{20} cm^{-2})	$8.2\pm^{1.9}_{1.1}$	6.5[a]	$9.5\pm^{0.3}_{5.2}$	6.5[a]
$\log g$			9.0	8.45
$L_{\rm bol}$ (10^{37} erg s^{-1})	$6.4\pm^{21.1}_{3.0}$	2.49 ± 0.19	$5.4\pm^{0.6}_{4.7}$	$2.30\pm^{0.10}_{0.05}$
R (10^9 cm)	$1.33\pm^{1.41}_{0.36}$	0.826 ± 0.030	$1.05\pm^{0.08}_{0.76}$	$1.25\pm^{0.08}_{0.05}$
χ^2/DOF	0.71	0.76	1.02	0.76

Table 5.3: Results of spectral fits to BeppoSAX LECS data for CAL 83. An LMC distance of 50 kpc (kiloparsec) was adopted. (Adopted from Parmar et al. 1998, Tables 1-3.)
[a]Fixed at the value of 6.5×10^{20} cm^{-2} determined by Gänsicke et al. (1998a).

CAL 83 has been observed several times by ROSAT — during the ROSAT calibration phase, during the ROSAT all-sky survey, as well as during subsequent pointed observations (Greiner et al., 1991; Kahabka, 1998; Trümper et al., 1991). Kahabka (1998) performed fits of LTE (local thermal equilibrium) and NLTE (non-LTE) white dwarf atmosphere models to the ROSAT PSPC (Position Sensitive Proportional Counters) data, and obtained the parameters shown in Table 5.2. The parameter $N_{\rm H}$ is the hydrogen absorbing column density along the line of sight, g is the white dwarf surface gravity and $L_{\rm bol}$ the inferred bolometric luminosity. By using their derived value of $N_{\rm H} = 6.5 \times 10^{20}$ cm^{-2}, Gänsicke et al. (1998a) constrained the WD luminosity to $L_{\rm bol} = (0.7-2)\times 10^{37}$ erg s^{-1} by fitting LTE models to the ROSAT PSPC data. with $R = (3-8)\times 10^8$ cm and $R = (2-6)\times 10^8$ cm for $\log g = 8$ and $\log g = 9$ respectively.

Observations with the BeppoSAX LECS (Low-Energy Concentrator Spectrometer) on 7-8 March 1997 were fitted with blackbody, LTE and NLTE models by Parmar et al. (1998). The derived fit parameters are shown in Table 5.3. CAL 83 was also observed with ASCA on 21-22 June 1997, and an effective temperature of 29 ± 8 eV was derived (Dotani et al., 2000).

From a re-analysis of ROSAT data with line-blanketed LTE white dwarf atmosphere models, and a comparison to theoretical relationships between the properties of white dwarfs with hydrogen shell burning (see discussion in Section 4.3), Suleimanov and

Parameter	LTE
$kT_{\rm eff}$ (eV)	43.4 ± 1.5
$N_{\rm H}$ (10^{20} cm^{-2})	6.33[a]
$\log g$	$8.0 - 8.25$
$L_{\rm bol}$ (10^{37} erg s^{-1})	$2.8 - 3.1$
R (10^9 cm)	$0.7 - 0.9$
$M_{\rm WD}/M_\odot$ (for $R_{\rm WD} = R$)	$\sim 0.6 - 0.8$
$M_{\rm WD}/M_\odot$ (for $R_{\rm WD} = \frac{1}{2}R$)	$\sim 1.2 - 1.3$

Table 5.4: Physical parameters of CAL 83 based on a re-analysis of ROSAT data. The first mass estimate was calculated by assuming that the photospheric radius is equal to that of the WD core (more applicable to a cool WD), and the second by assuming that it is twice that of the WD core (more applicable to a warm WD). (Adopted from Suleimanov and Ibragimov 2003.)
[a]Fixed at the galactic value in the direction of the LMC.

Ibragimov (2003) estimated the source parameters for 10 known supersoft sources, including CAL 83, SMC 13 and 1E 0056.8-7154. Their estimates for the physical parameters of CAL 83 are shown in Table 5.4.

The higher spectral resolution of the modern X-ray telescopes *Chandra* and XMM-Newton, has opened up the possibility of more detailed spectral fits to SSS spectra. CAL 83 was observed by XMM-Newton on 23 April 2000, and an initial comparison of the spectrum by Paerels et al. (2001) to various line-blanketed models pointed to an effective temperature of $\sim$ 45 eV, for a WD surface gravity of $\log g \sim 8.5$. A combined analysis of the XMM-Newton RGS (Reflection Grating Spectrometer) spectrum, as well as a spectrum recorded with *Chandra* on 15-16 August 2001 using the HRC (High Resolution Camera) and the LETG (Low Energy Transmission Grating), is presented by Lanz et al. (2005). They used detailed line-blanketed NLTE models to characterize the spectra, and their results are shown in Table 5.5. Their fits provided spectral evidence that the white dwarf in CAL 83 is massive. i.e. $M_{\rm WD} \gtrsim 1 M_\odot$. This implies that the white dwarf mass is just below the Chandrasekhar limit (i.e. $M_{\rm C} \approx 1.4 M_\odot$), where hydrostatic equilibrium is achieved by electron degeneracy pressure.

5.1.2 Ultraviolet spectra

IUE spectra of CAL 83 taken during November 1984, February 1985 and May 1986 contained two emission lines, N V λ1240 and He II λ1640, an unidentified emission feature near 1670 Å and also possible absorption features near 1260, 1300 and 1335 Å (Crampton et al., 1987). Gänsicke et al. (1998a) considered the possibility that the unidentified feature, which they placed at $\sim$ 1666 Å, may represent redshifted emission of the He II λ1640 line, which would imply a high velocity shift of

Parameter	NLTE
$kT_{\rm eff}$ (eV)	47 ± 2
$\log g$	8.5 ± 0.1
$L_{\rm bol}$ (10^{37} erg s^{-1})	3.4 ± 1.1
R (10^9 cm)	0.7 ± 0.07
$M_{\rm WD}/M_\odot$	1.3 ± 0.3

Table 5.5: Results of NLTE spectral analysis of XMM-Newton RGS and *Chandra* HRC-S/LETG data for CAL 83. The adopted LMC distance is 50 ± 3 kpc. (Adapted from Lanz et al. 2005, Table 3.)

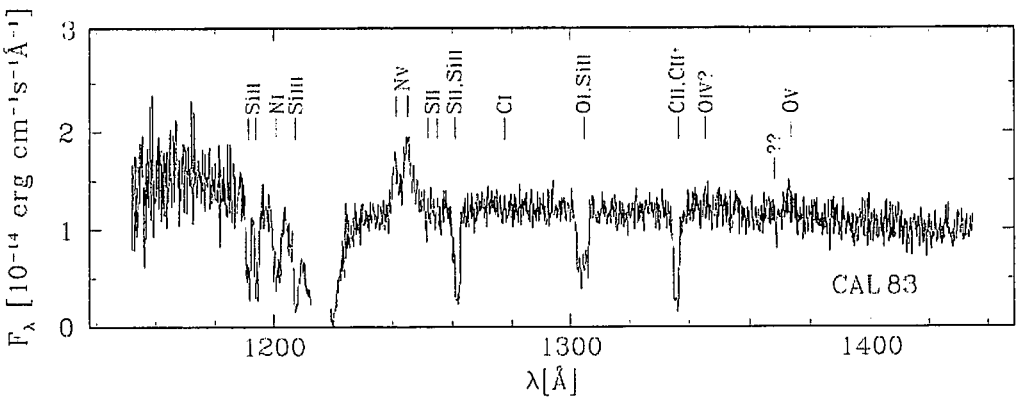

Fig. 5.1: HST GHRS spectrum of CAL 83 recorded on 10 November 1996. The geocoronal Lα emission line is truncated. (Adopted from Gänsicke et al. 1998a, Fig. 1.)

~ 4000 km s^{-1}.

A spectrum of CAL 83 recorded with the HST GHRS (Hubble Space Telescope Goddard High Resolution Spectrograph) on 10 November 1996 is shown in Fig. 5.1 (Gänsicke et al., 1998a). From the broad Lα absorption profile, these authors derive an upper limit of $N_{\rm H} = (6.5 \pm 1.0) \times 10^{20}$ cm^{-2} for the neutral hydrogen absorbing column density along the line of sight to CAL 83. The three absorption features detected in the IUE spectra are also present here, along with several others. All the absorption lines are probably due to interstellar absorption.

Several emission lines were also observed (see Fig. 5.1), most probably originating from an accretion disc. The N V doublet lines exhibit a complicated structure, with the red wings extending to about 800 km s^{-1} from the line centre. Gänsicke et al. (1998a) noted that if the N V lines originate from an accretion disc, their small width indicate a low inclination for CAL 83. It was also indicated that the UV flux is variable, and the detected UV bright state coincides with an optically bright state (refer to the discussion in Section 5.1.4).

Schmidtke et al. (2004) presented a UV spectrum of CAL 83, recorded with FUSE

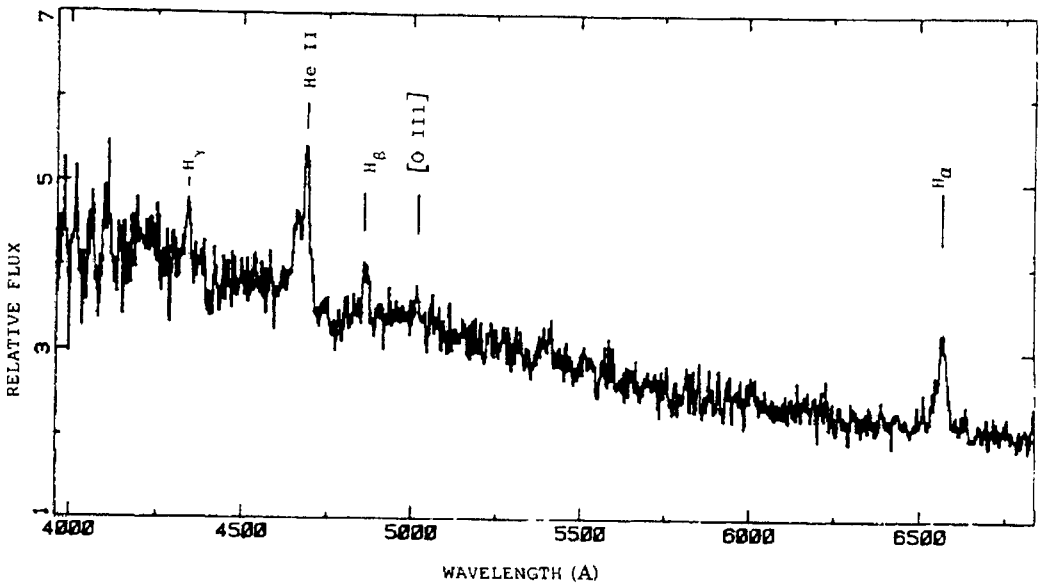

Fig. 5.2: ESO 3.6-m spectrum of CAL 83 (May 1984). The resolution is $\sim 9 - 12$ Å. (Adopted from Pakull et al. 1985, Fig. 1.)

(Far Ultraviolet Spectroscopic Explorer) in September 2001. The only stellar feature in the FUSE spectrum is O VI λ1031.9 emission. This emission line also shows an extension to longer wavelengths, similar to what has been observed in He II lines. However, the phasing of the O VI line, with a maximum velocity at $\phi \sim 0.23$, is different from that of He II, which may indicate that the O VI and He II emission originate from different locations. The parameter ϕ refers to the orbital phase, ranging from 0 to 1.

5.1.3 Optical photometry and spectroscopy

CAL 83 was identified with a blue star ($B \sim 16.8$) with variable He II emission (Cowley et al., 1984). An optical spectrum of CAL 83 recorded with the ESO (European Southern Observatory) 3.6-m telescope at La Silla during May 1984 is shown in Fig. 5.2 (Pakull, Ilovaisky and Chevalier, 1985). From various spectroscopic observations during 1980 and 1983-1984. they find that the emission ratio of He II λ4686 to Hβ is always larger than 5, and that the equivalent width of Hβ does not exceed 6 Å. A weak emission feature at $\sim$ 4660 Å was also observed. They suggest that the emission feature may represent blueshifted He II emission, indicating Doppler motion of $\sim 1500 - 2300$ km s^{-1} towards the observer.

Several spectroscopic observations of CAL 83 were performed at CTIO (Cerro Tololo Inter-American Observatory) and the Las Campanas Observatory during 1982-1985 (Crampton et al., 1987). The average spectrum is shown in Fig. 5.3. The spectra exhibit a blue continuum ($U - B = -1.1$) mainly characterized by strong He II and weaker Balmer emission.

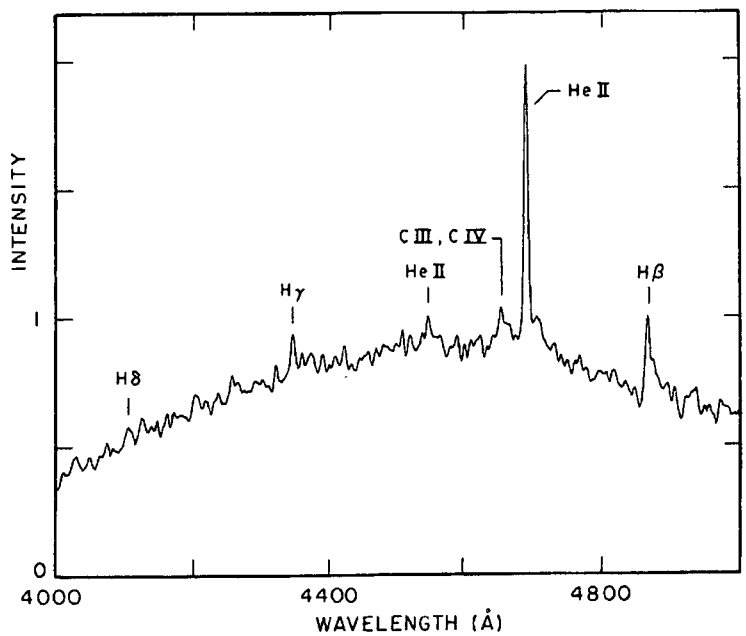

Fig. 5.3: Average spectrum of CAL 83 taken with the Las Campanas "2D-Frutti" detector during December 1985. (Adopted from Crampton et al. 1987, Fig. 1.)

Epoch	Hδ	Hγ	Hβ	Hα	C III/IV	He II	O VI
1982 Feb	...	...	...	...	...	10.9	...
1982 Nov.....	...	...	2.4	...	...	10.0	1.2
1984 Jan	...	...	...	...	2.5	5.0	1.8
1985 Mar.....	2.6	2.3	6.4	...	2.8	12.8	0.7
1985 Dec	1.5	1.8	5.3	18	2.2	12.2	...

Table 5.6: Equivalent widths (in Ä) of CAL 83 emission lines detected during observations at CTIO and Las Campanas. (Adopted from Crampton et al. 1987, Table 2.)

The He II λ4686 emission line has a very broad, variable wing structure with a velocity range $\sim 10^3$ km s^{-1} which is usually on the violet side, but then shifted to the red side of the line during the 1985 observations. A similar structure was detected in the Hβ emission line during 1985 (see Fig. 5.4). The weak emission feature at $\sim$ 4660 Å, also identified by Pakull et al. (1985), is still present in the 1985 spectrum where the He II wing has shifted to longer wavelengths. Therefore these authors interpret this $\sim$ 4660 Å feature to be the result of C III and C IV emission. The identification of highly ionized O VI emission at 3911 Å and 3834 Å supports the presence of highly ionized C. The only feature identified in the red spectrum is Hα. The equivalent widths of the detected emission lines are given in Table 5.6.

A possible interpretation of the slowly changing He II λ4686 structure is the slow precession (with a period $\sim$ 69 days) of an accretion disc which exhibits outflow through either a wind or a jet with a large collimation angle. This possibility is

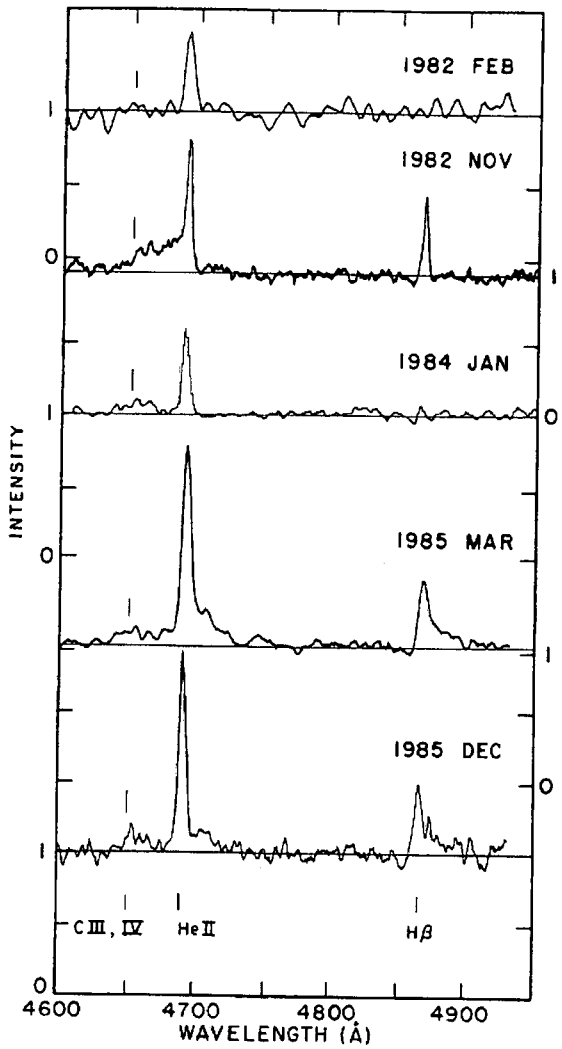

Fig. 5.4: Extracts from the average spectra of CAL 83 from 5 different observing runs at the CTIO and Las Campanas. Note the changing wing structure of He II λ4686, as well as the Hβ wing in the last 2 spectra. (Adopted from Crampton et al. 1987, Fig. 2.)

supported by the arguments of Southwell, Livio and Pringle (1997), who showed that irradiation-induced accretion disc warping in CAL 83 can cause disc precession on these time-scales. Based on the variation in velocity of the He II emission line, Crampton et al. (1987) also showed that, for any value of the compact primary star mass, the secondary star must be less massive, i.e. $q < 1$. This is in contradiction with the mass ratio $q > 1$ predicted for CAL 83 by van den Heuvel et al. (1992).

The low intensity of the Balmer emission lines relative to the CNO lines indicate that the accreting matter from the envelope of the secondary is H-poor. This may indicate that the WD is accreting from an evolved secondary star that has lost its outer envelope as a result of high mass transfer. This corresponds to the situation in AE Aqr where the line ratios of C and N relative to H shows that the $0.6M_{\odot}$

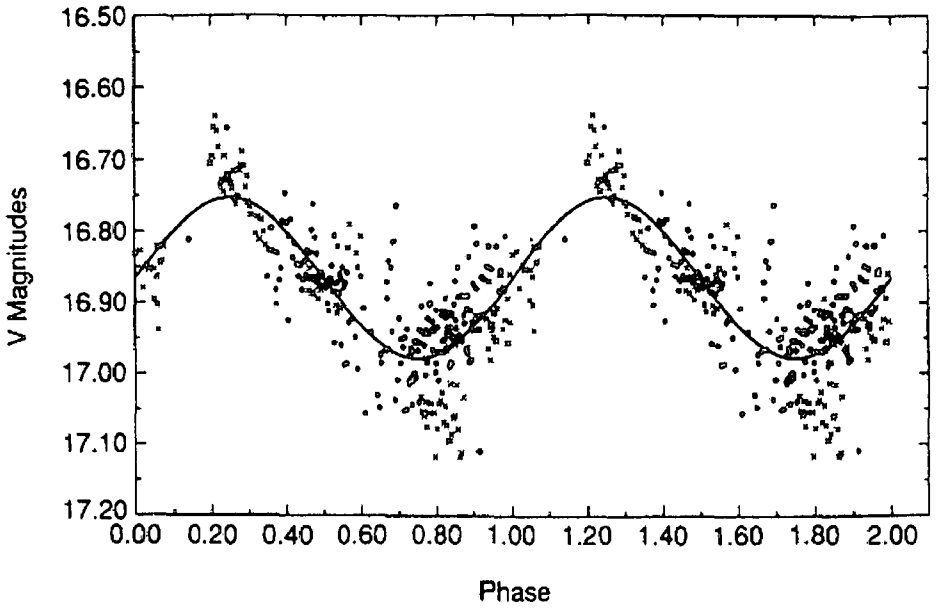

Fig. 5.5: Photometric light curve of CAL 83 from December 1984 data, folded on an orbital period of 1.0436 d. (Adopted from Smale et al. 1988, Fig. 3.)

		He II λ4686			Hβ		
Date U T	**Obs**	**Velocity (km/sec)**	**FWHM (km/sec)**	**Eq.Width (Å)**	**Velocity (km/sec)**	**FWHM (km/sec)**	**Eq.Width (Å)**
1983 Jan (Sum)	**ESO**	326±16	376±37	8.2±1.1	326±16	376±37	8.2±1.1
1983 Jan/Feb (Sum)	**AAT**	260±20	340±33	7.3±0.9	255±19	160±40	1.8±0.5
1983 Dec (Sum)	**SAAO**	233±23	279±52	2.4±0.4	402±40	93±10	1.4±0.3
1985 Dec 16 (Sum)	**SAAO**	235±23	407±52	12.5±2.3	229±34	362±74	4.2±1.7

Table 5.7: Emission line parameters for He II λ4686 and Hβ, showing the velocity shift in the central wavelength, the FWHM and the equivalent width for the summed spectra. (Adopted from Smale et al. 1988, Table 4.)

secondary is rather evolved for its mass (Jameson, King and Sherrington, 1980; Mauche, Lee and Kallman, 1997).

An orbital period of 1.0436 ± 0.0044 d (days), with a variation amplitude of $\Delta V = 0.22$, was determined from V-band photometry obtained during an international campaign in December 1984 (Smale et al., 1988). Shown in Fig. 5.5 is their folded light curve. Their data also show evidence of occasional short time-scale ($\sim$ 2 hr) variability. Smale et al. (1988) also obtained optical spectra of CAL 83 with ESO 3.6-m telescope, the 3.9-m AAT (Anglo-Australian Telescope) and the SAAO 1.9-m Telescope. He II λ4686 and Hβ emission is detected, with the He II line exhibiting a broad wing towards the violet side. Their measured line parameters are given in Table 5.7.

Spectra obtained with the CTIO 4-m telescope during November 1996 exhibit several

Emission line	Average equivalent width (Å)	FWHM (Å)
He II λ4686	-12.1	5.4
He II λ4541	-0.8	
He II λ5411	-1.8	
Hα λ6563	-21.9	
Hβ λ4861	-4.8	
Hγ λ4340	-1.9	
O VI λ5290	-1.3	
O VI λ3811	-1.6	

Table 5.8: Emission line parameters for CAL 83 recorded with the CTIO 4-m telescope. (Values from Cowley et al. 1998, Table 5.)

emission lines of H, He II and O VI. The lines and their equivalent widths are listed in Table 5.8 (Cowley et al., 1998). It is noticeable that the ratio of He II λ4686 to Hβ emission from the values in Tables 5.6, 5.7 and 5.8 is smaller than 5 and even equal to 1 for the Jan 1983 ESO observations, contrary to the findings of Pakull et al. (1985).

Considering the optical light curve and emission-line widths, the inclination of CAL 83 should be in the range $i = 20 - 30°$ (see Cowley et al. (1998) and references therein). If $M_{\rm WD} = 1.3 M_{\odot}$, then the secondary should have a mass of $\sim 0.5 M_{\odot}$. Such a low secondary mass, as well as the H-poor envelope discussed earlier, supports the scenario of the evolution of cataclysmic variables from supersoft sources, as proposed for AE Aqr (Meintjes, 2002; Schenker et al., 2002).

Schmidtke et al. (2004) derived the following orbital ephemeris from MACHO Project photometry:

$$T_0 = \text{JD } 2451500.953 \pm 0.004 \quad + \quad 1.047568E \pm 0.000003 \text{ d} .$$

Oliveira and Steiner (2006) reported an optical observation obtained with the GMOS-IFU (Gemini Multi-Object Spectrograph Integral Field Unit). They found the [FeX] λ6375 coronal line in emission, and also evidence of absorption and emission components of H and He II that may be associated with bipolar jets. Emission near 6548 Å may be due to [N II], but may also be associated with blueshifted Hα emission from a jet with a radial velocity of ~ -600 km s^{-1}. Such a blueshifted feature is observed with the same velocity near Hβ.

Optical evidence has been found that CAL 83 is surrounded by a large ionization nebula (Chiang and Rappaport, 1996; Remillard et al., 1995). Remillard et al. (1995) derived a time-averaged ionizing luminosity of $\sim (1 - 4) \times 10^{37}$ erg s^{-1} for CAL 83 from the nebular Hα and [O III] emission.

5.1.4 X-ray off-states and variability

Although there has been several X-ray detections of CAL 83 at nearly the same effective temperature and X-ray luminosity, several X-ray "off-states" have also been documented. The first observed X-ray off-state was on 28 April 1996, and off-states have also been observed on 29-30 November 1999, 3-4 October 2001 and 2 January 2008 (Alcock et al. 1997; Greiner et al. 2008; Greiner and Di Stefano 2002; Kahabka 1998; Lanz et al. 2005; Lanz, Audard and Walter 2008). The inferred duration of such an off-state is $\lesssim 100$ days. Greiner and Di Stefano (2002) investigated optical light curves recorded by MACHO, and found that CAL 83 exhibits long-term variations between a low, intermediate and high optical state and that the X-ray off-states and optical low states are anti-correllated. These observed X-ray off-states contradict the initial description of CAL 83 as a prototypical CBSS undergoing steady nuclear burning.

The exact nature of these long-term variations is still not quite clear, but various models have been put forward. Alcock et al. (1997) explained the first X-ray off-state by a model where a decrease in the accretion rate causes a cessation of hydrogen burning on the WD, and where the short time-scale of the off-state implies a massive WD. Kahabka (1998), on the other hand, ascribed the off-state to an increase in accretion rate that results in the expansion and cooling of the WD photosphere. Greiner and Di Stefano (2002) considered both photospheric radius changes and absorption by circumstellar material, but concluded that the situation is much more complex than these simple models and that the interaction between the changing photosphere and the irradiated disc also has to be taken into account.

Lanz et al. (2005) report short time-scale variations (less than 10% of the orbital period of 1.04 d) in the *Chandra* and XMM-Newton X-ray light curves of CAL 83. Schmidtke and Cowley (2006) performed period analysis on these data, and found a periodic signal of 38.4-minutes in the *Chandra* LETG data, but no statistically significant periodicity in the XMM-Newton data. These authors ascribe the periodicity to possible non-radial pulsations in the accreting WD, similar to those observed in some novae.

According to our knowledge, no white dwarf spin period has been detected for CAL 83 so far.

In summary, the observational evidence suggests that CAL 83 consists of a massive ($\sim 1.3 M_{\odot}$) white dwarf accreting from a less massive ($\sim 0.5 M_{\odot}$) companion. This yields $q \sim 0.38$, which is in contradiction with the $q > 1$ model of van den Heuvel et al. (1992). According to Eq. (2.27), mass transfer will cause the Roche lobe of

the secondary to expand if $q < \frac{5}{6}$, while any loss of angular momentum from the system will tend to shrink the Roche lobe. *If* the white dwarf in CAL 83 has a substantial magnetic field, the magnetic propelling of accreting material with high angular momentum from the binary system will tend to shrink the secondary Roche lobe. Also, a main sequence star with a mass of $\sim 0.5 M_{\odot}$ will have a convective envelope, and the removal of material from a convective envelope by Roche lobe overflow will cause the star to expand. This effect can contribute to a mass transfer rate high enough to cause nuclear shell burning of hydrogen on the white dwarf surface, even though $q < 1$.

5.1.5 Radio emission

Upper limits for possible radio emission from CAL 83 are given in Table 4.2, i.e. < 0.12 mJy at both 3.5 cm and 6.3 cm wavelengths.

5.2 1E 0035.4-7230 (SMC 13)

5.2.1 X-ray spectra

SMC 13 is one of the sources discovered by the *Einstein* IPC (Imaging Proportional Counter), and Seward and Mitchell (1981) considered the source as extended, possibly a supernova remnant (SNR). However, the source was detected as a point source with the *Einstein* HRI (High Resolution Imager), as reported by Jones et al. (1985). The *Einstein* observations imply a low effective temperature, $kT_{\rm eff} \lesssim 35$ eV, a luminosity of $L_{\rm X} \sim 10^{37}$ erg s^{-1} in the *Einstein* band and a high X-ray-to-optical luminosity ratio of $\sim 10^2$ (Wang and Wu, 1992).

SMC 13 was also detected during the ROSAT All-Sky Survey (RASS) and a subsequent deep pointed observation. The results of a blackbody fit to a pointed observation spectrum yielded $kT_{\rm eff} = 41 \pm 9$ eV and a bolometric white dwarf luminosity of $L_{\rm bol} = 2.4 \times 10^{37}$ erg s^{-1} for an absorbing hydrogen column density of $N_{\rm H} = 5.0^{+3.0}_{-1.5} \times 10^{20}$ cm^{-2} (Kahabka, Pietsch and Hasinger, 1994). The adopted distance to the SMC is 65 kpc.

The source was observed with the BeppoSAX LECS (Low-Energy Concentrator Spectrometer) during January 1998 (Kahabka, Parmar and Hartmann, 1999b). Combined spectral fits of the BeppoSAX and ROSAT PSPC data were performed, using first a simple blackbody model, and then a blackbody combined with an absorption edge. The position of the fitted edge (~ 0.44 keV) suggested that a C edge may be present, and a blackbody model with CV and CVI edges fixed at their respective energies was applied. LTE and NLTE white dwarf atmosphere models were also fitted. Their results are shown in Table 5.9. The possible presence of a C edge sup-

Model	BeppoSAX LECS + ROSAT PSPC							
	N_H	kT_{eff}	$E_{C\,V}$	$E_{C\,VI}$	$\tau_{C\,V}$ Edge	$\tau_{C\,VI}$	L_{36}[b] (0.1–2.4 keV) (bolometric)	χ^2/DOF
	(10^{20} cm^{-2})	(eV; 10^5 K)	(keV)					
bbody	$4.8\pm^{1.1}_{0.8}$	$43\pm^{4}$ $5.0\pm^{0.5}_{0.5}$					$9.3\pm^{11}_{4.2}$ $12\pm^{42}_{9}$	0.68
bbody+edge	$3.8\pm^{1.1}_{0.8}$	$63\pm^{13}_{15}$ $7.3\pm^{1.5}_{1.7}$	$0.44\pm^{0.03}_{0.08}$		$5.4\pm^{3.6}_{2.7}$[a]		$4.2\pm^{3.8}_{1.5}$ $5.2\pm^{0.9}_{2.0}$	0.62
bbody+Cv+CvI edge	$3.9\pm^{1.2}_{0.8}$	$65\pm^{16}_{15}$ $7.5\pm^{1.5}_{1.7}$	0.391	0.487	$1.6\pm^{1.0}_{0.7}$[a]	$3.9\pm^{3.6}_{2.8}$[a]	$4.2\pm^{3.3}_{1.4}$ $5.4\pm^{3.6}_{3.5}$	0.63
LTE WD atm.[a]	$3.6\pm^{0.4}_{0.4}$	$47\pm^{1}$ $5.5\pm^{0.1}_{0.1}$					$2.0\pm^{1.4}_{0.8}$ $4.8\pm^{1.1}_{0.8}$	0.80
Non-LTE WD atm.[a]	$4.1\pm^{0.4}_{0.3}$	$28\pm^{0.6}_{0.8}$ $3.25\pm^{0.07}_{0.09}$					$9.8\pm^{4.0}_{1.4}$ $10.9\pm^{0.3}_{0.3}$	0.77

Table 5.9: Results for combined spectral fitting of BeppoSAX LECS and ROSAT PSPC spectra of SMC 13. 90% confidence errors are given, except where otherwise indicated. The adopted SMC distance is 60 kpc. (Extracted from Kahabka et al. 1999b, Table 1.)
[a]68% confidence errors are given.
[b]Luminosity for the BeppoSAX spectrum ($L_{36} = L/10^{36}$ erg s^{-1}).

Parameter	LTE
kT_{eff} (eV)	40.0 ± 0.9
N_H (10^{20} cm^{-2})	6.94[a]
$\log g$	$7.7 - 7.9$
L_{bol} (10^{37} erg s^{-1})	$3.0 - 3.3$
R (10^9 cm)	$0.8 - 1.0$
$M_{WD}/M_\odot$ (for $R_{WD} = R$)	$\sim 0.65 - 0.85$
$M_{WD}/M_\odot$ (for $R_{WD} = \frac{1}{2}R$)	~ 1.25

Table 5.10: Physical parameters of SMC 13 based on re-analysis of ROSAT data. (Adopted from Suleimanov and Ibragimov 2003.)
[a]Fixed at the galactic value in the direction of the SMC.

ports the WD model. Under the assumption that the source is on the stability line for nuclear burning, they constrain the WD mass to $\sim 1.1M_\odot$ and $\sim 0.9M_\odot$ with the LTE and NLTE fits respectively, but they also note that the temperature and luminosity values derived from the NLTE fit actually indicates $M_{WD} \sim 0.6 - 0.7M_\odot$.

Table 5.10 gives the parameters of SMC 13 derived by Suleimanov and Ibragimov (2003).

5.2.2 Optical photometry and spectroscopy

Jones et al. (1985) proposed a star with $V \sim 21$ as the probable optical candidate for SMC 13. This was confirmed by Orio et al. (1994), who reported an optical counterpart with $V = 20.25 \pm 0.05$.

Schmidtke et al. (1994) initially reported an orbital period of 0.1719 ± 0.0004 d for SMC 13 from optical CTIO (Cerro Tololo Interamerican Observatory) data, with minimum light at an epoch Nov. 3.105 1994. From a detailed analysis of photometric observations from the CTIO 0.9-m telescope during December 1993 and November 1994, Schmidtke et al. (1996) determined the maximum V-magnitude of SMC 13 to be 20.2, with a smooth light curve modulated over a range of $\Delta V \sim 0.3$. Their period analysis of these photometric observations and comparison with ROSAT light curves, yielded the following photometric orbital ephemeris for SMC 13:

$$T_0 = \text{HJD } 2449659.6001 \pm 0.0002 \quad + \quad 0.1719256E \pm 0.0000005 \text{ d} ,$$

where T_0 is the midpoint of minimum V light. Their optical light curve is shown in Fig. 5.6, together with the ROSAT light curve of SMC 13, both folded on the orbital ephemeris above. The rounded maximum and sharper minimum of the optical light curve are similar to the light curves of systems where the "inner" side of the secondary star undergoes strong heating by the primary. However, the amplitude of the optical variation is smaller in SMC 13 than in these systems. This can be accounted for if an accretion disc is the dominant source of optical light in SMC 13. Due to the short orbital period, the spectral type of the donor star should be G or K.

Crampton et al. (1997) considered the 1993 and 1994 data, as well as new photometric data taken with the CTIO 0.9-m telescope during November 1995 and November 1996, and derived a new orbital ephemeris. Their folded V-magnitude light curve is shown in Fig. 5.7. Because of the flat maximum and quite sharp, asymmetric minimum, these authors consider SMC 13 to be an eclipsing system, where the minimum is due to a partial eclipse of the accretion disk by the donor star, viewed at $i \sim 75°$. Considered together with the He II emission line velocities, this implies a primary mass between $\sim 1.3 - 1.5 M_{\odot}$.

Additional photometric observations with EFOSC-2 at the ESO/MPI 2.2-m telescope at La Silla during December 1996, lead van Teeseling et al. (1998) to yet another revised orbital ephemeris of

$$T_0 = \text{HJD } 2450434.1320 \pm 0.0006 \quad + \quad 0.1719260E \pm 0.0000007 \text{ d} .$$

They also reported a significant variability in the $B - V$ index, with the source appearing to be bluest at orbital phase $\phi \sim 0.7 - 0.8$. Their optical V-band light curve folded on the orbital ephemeris above is shown in Fig. 5.8, and exhibits an almost perfectly sinusoidal form without the sharp minima reported by Schmidtke

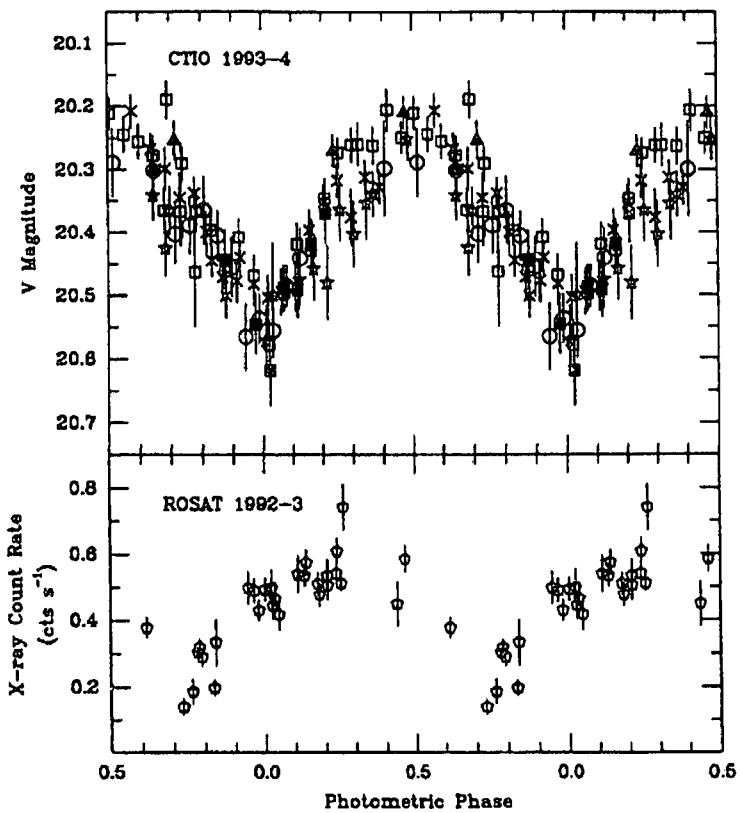

Fig. 5.6: Optical CTIO light curve (top) and ROSAT X-ray light curve (bottom) folded on the orbital ephemeris of Schmidtke et al. (1996). (Extracted from Schmidtke et al. 1996, Fig. 3.)

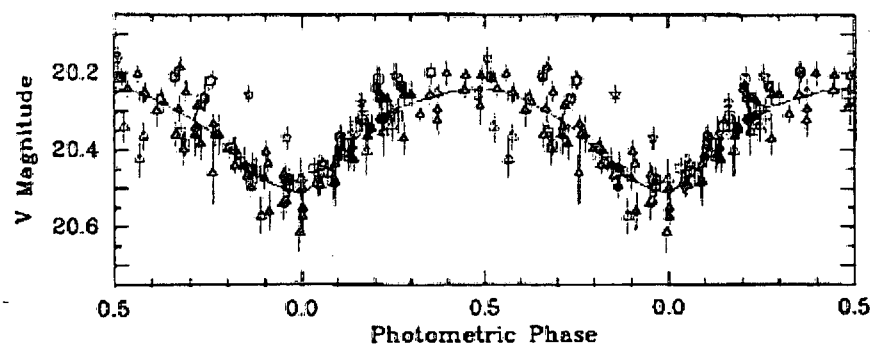

Fig. 5.7: V-band folded light curve of SMC 13. (Extracted from Crampton et al. 1997, Fig. 2.)

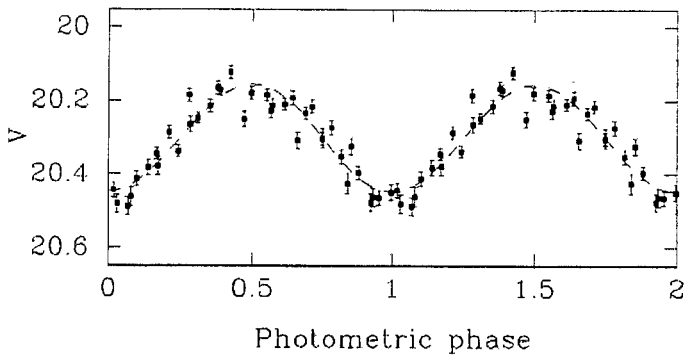

Fig. 5.8: Optical light curve of SMC 13 obtained with EFOSC-2 at the ESO/MPI 2.2-m telescope, folded on the orbital ephemeris of van Teeseling et al. (1998). (Extracted from van Teeseling et al. 1998, Fig. 1.)

et al. (1996) and Crampton et al. (1997). Therefore van Teeseling et al. (1998) prefer a model with a moderate inclination of $i = 20 - 50°$, with $q > 0.33$, but they do not exclude the possibility of a higher inclination, where $i \sim 70°$. The effective temperature of the heated side of the companion is that of an O or a B star, but the inferred intrinsic temperature of the companion is that of an (unobservable) type M star. These findings are consistent with the scenario of wind-driven evolution suggested by van Teeseling and King (1998). As discussed in Section 4.9, these authors consider SMC 13 as a system with a low-mass companion ($q \lesssim 0.7$) in which mass transfer is sustained by an irradiation-driven wind from the donor.

Several optical spectra of SMC 13 have been recorded, and are found to exhibit a very blue continuum with various weak emission lines, with the only well pronounced feature being the He II λ4686 emission line, with signs of Balmer absorption (e.g. Orio et al. 1994; Schmidtke et al. 1996).

A series of spectra taken with EFOSC-1 at the La Silla 3.6-m telescope during October 1995 also show He II emission and Hβ absorption, with some spectra also showing the other Balmer lines (including Hα) in absorption (van Teeseling et al., 1998). The average flux-calibrated spectrum is shown in Fig. 5.9. Part of the Balmer absorption may originate from the companion star.

Spectroscopic data, taken with the CTIO 4-m telescope on the same nights as the photometric data in November 1996, show quite strong emission lines of He II and also Hα (which is also blended with He II emission) that was not present in previous spectra (Cowley et al., 1998; Crampton et al., 1997). Broad absorption features appear on both sides of the Balmer emission cores, with only the absorption component visible for Balmer lines higher than Hβ. Hγ absorption appears to the strongest when the companion star is closest to the observer. O VI emission from the inner

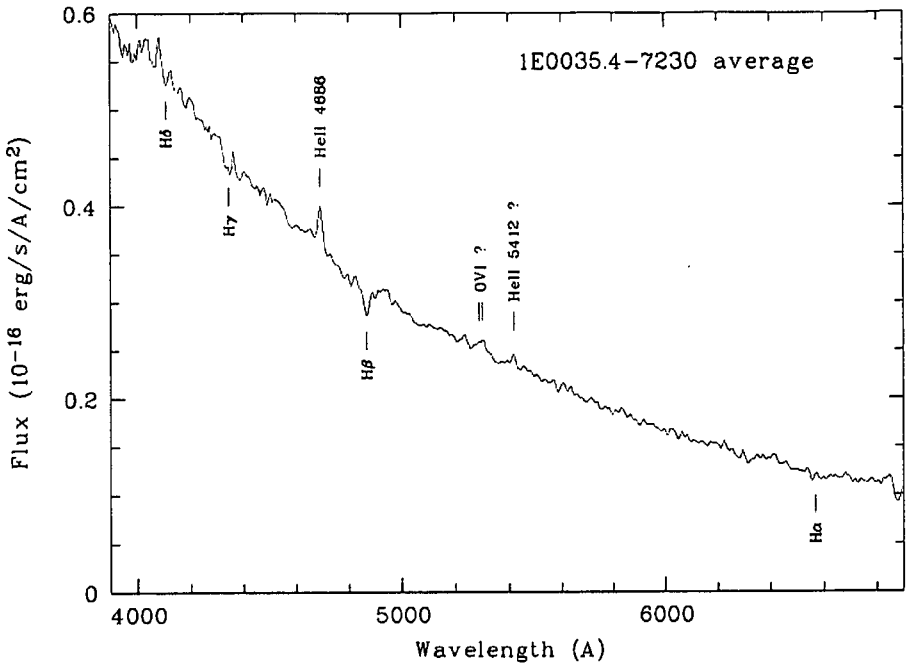

Fig. 5.9: Average flux-calibrated EFOSC-1 spectrum of SMC 13, taken during October 1995. The resolution is $\sim$ 15Å. (Adopted from van Teeseling et al. 1998, Fig. 7.)

parts of the disc is also detected. The relative weakness of the H and He II lines relative to O VI is ascribed to the presumably small size of the accretion disc inferred from the very short orbital period. The average spectrum is shown in Fig. 5.10.

The velocity curve of the He II λ4686 emission line confirms an orbital period of $\sim$ 0.1719 d, even though its maximum occurs at phase $\phi \sim 0.8$. The phasing suggests that the He II lines originate near the compact star and reveal its orbital motion. An orbital inclination of $i \sim 75°$ is inferred for SMC 13 from light curve models of eclipsing systems by Meyer-Hofmeister et al. (1997). When using the radial velocity semi-amplitude for He II λ4686 ($K \sim 100$ km s^{-1}) to calculate the mass function, it is found that the component masses should be $M_1 \sim 1.3 M_\odot$ and $M_2 \sim 0.4 M_\odot$.

On the other hand, it has been suggested that SMC 13 is actually a cataclysmic variable driven by magnetic braking, with a low mass WD ($\sim 0.6 M_\odot$) accreting from a low mass ($\sim 0.4 M_\odot$) donor at a rate ($\sim 10^{-8} - 10^{-9} M_\odot$ yr^{-1}) below the steady burning limit and that the supersoft emission may be due to a nova outburst that is evolving very slowly (Kahabka and Ergma, 1997; Kato, 2010). Such a model with a low mass WD is favoured by the value of $M_{\rm WD}$ inferred from the NLTE BeppoSAX temperature and luminosity discussed in Section 5.2.1.

Clearly, there is still some uncertainty about the inclination and component masses of SMC 13. In order to determine the masses from the mass function, the incli-

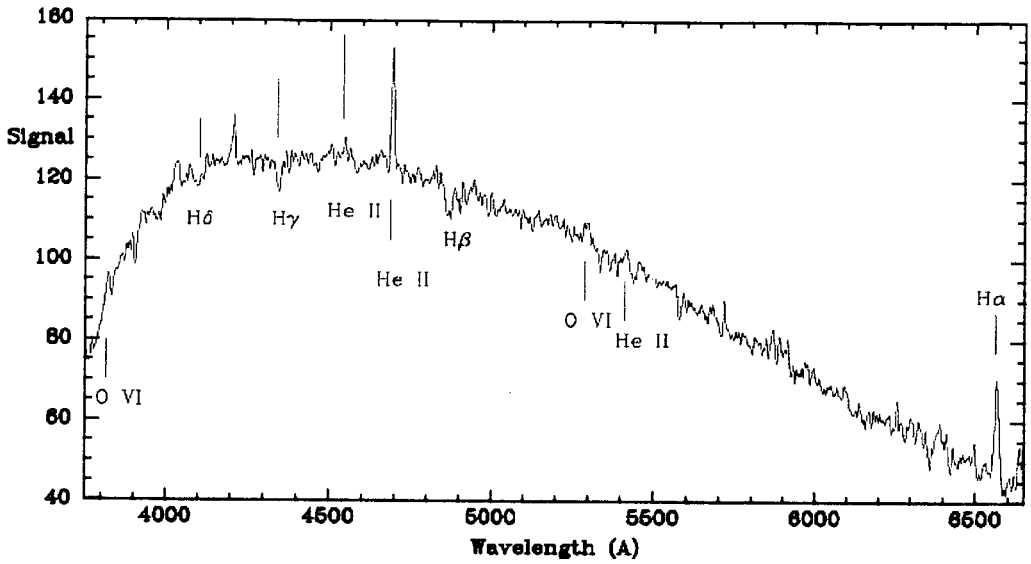

Fig. 5.10: Average CTIO 4-m telescope spectrum of SMC 13, taken during November 1996. The resolution is $\sim$ 3Å. (Adopted from Crampton et al. 1997, Fig. 3.)

nation should be known and vice versa, and without any additional independent information, this makes it very difficult to obtain these variables.

5.2.3 Orbital modulation in X-rays

Orbital modulation in X-rays has been found in the ROSAT PSPC data of SMC 13 (Kahabka, 1995, 1996a). The intensity at the X-ray minimum is $\sim$ 77% of the intensity at phases $\phi = 0.5 - 0.95$. Kahabka (1996a) searched for periodicity in the ROSAT data around the period of Schmidtke et al. (1994), and found a period of 0.1718 d in X-rays. The ROSAT light curve in the $0.1 - 0.5$ keV band is shown in Fig. 5.11, which also illustrates the separate light curves in the soft ($0.1 - 0.25$ keV) and hard ($0.26 - 0.50$ keV) energy bands. These light curves are folded on the ephemeris of Schmidtke et al. (1994).

In addition to the main minimum at $\phi \sim 0.9 - 1.1$, there seems to be a second dip at $\phi = 0.6$, but this is only detected in the $0.1 - 0.25$ keV band. This minor dip, as well as the main dip, is coupled with an increase in the hardness ratio (HR). It is also interesting to note that the count rate in the hard energy band correllates with the variations in HR. This can be explained by temperature variations from $\sim (4 - 5) \times 10^5$ K, caused by the changing aspect of an accretion column structure above the polecaps of a magnetic WD. An alternative interpretation of the HR variations is that it is caused by the presence of an additional, varying absorbing column of $N_{\rm H} \lesssim 4 \times 10^{20}$ cm^{-2}, which may originate in the binary system, e.g. a wind driven from the secondary star.

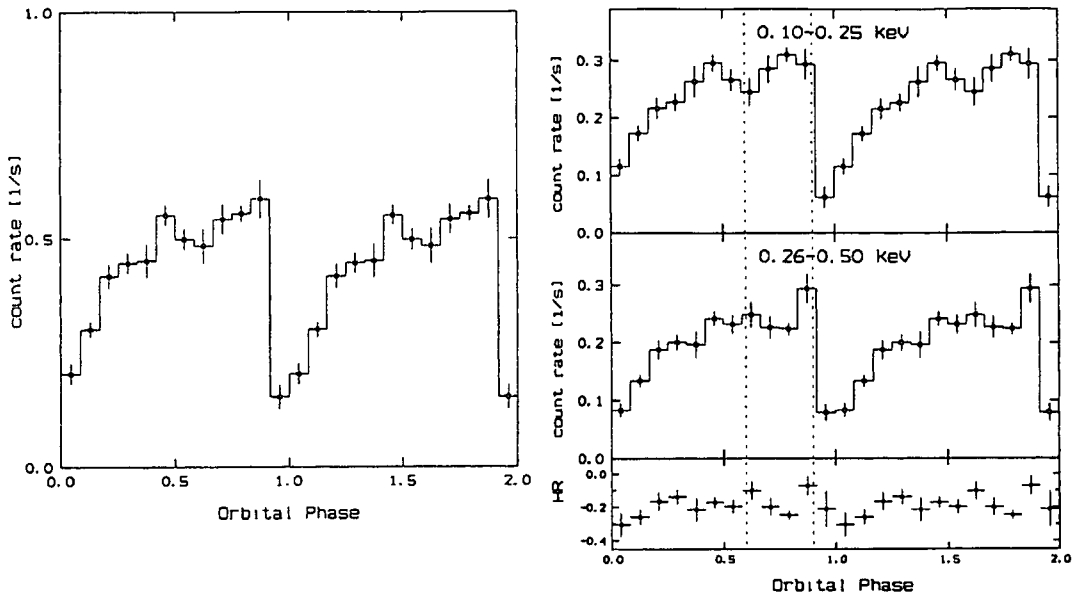

Fig. 5.11: Phase-binned ROSAT PSPC light curves of SMC 13, with an orbital period of 0.1718 d folded with respect to the epoch Nov. 3.105, 1994. Two cycles are shown for clarity. (a) Light curve in the $0.1 - 0.5$ keV band. (b) Light curves in the soft ($0.1 - 0.25$ keV) and hard ($0.26 - 0.50$ keV) bands. The panel at the bottom shows the variations in the hardness ratio, defined as HR=(H–S)/(H+S), where S is the number of counts in the soft band and H the number of counts in the hard band. (Adopted from Kahabka 1996a, Fig. 2 and Fig. 3.)

From Fig. 5.11, it appears that the X-ray modulation is synchronous with the orbital motion. However, Schmidtke et al. (1996) found that, according to their derived ephemeris, the optical minimum occurs about a quarter of an orbital cycle earlier than the X-ray minimum (see Fig. 5.6 in the previous section). This may be explained by a small difference between the optical and X-ray periods due to disc precession or the presence of a third body. However, the preferred interpretation of these authors is that X-rays are scattered in an accretion disc corona, and that the X-ray minima can occur when the corona is partially occulted by an extended accretion disc rim, slightly before mid-eclipse.

5.2.4 Radio emission

Upper limits for possible radio emission from SMC 13 are given in Table 4.2, i.e. < 0.12 mJy at both 3.5 cm and 6.3 cm wavelengths.

As remarked by Kahabka and Ergma (1997), SMC 13 "is possibly one of the most puzzling supersoft sources", and many riddles regarding the nature of this source still have to be solved.

Parameter	Blackbody	LTE (H-rich)	LTE (He-rich)
$kT_{\rm eff}$ (eV)	31	39	37
$N_{\rm H}$ (10^{20} cm^{-2})	8	5	5
$L_{\rm bol}$ (10^{37} erg s^{-1})	30	2	2
R (10^{9} cm)	5	0.8	0.9
χ^2/DOF	0.82	0.69	0.70

Table 5.11: Best-fit parameters of 3 different models for the ROSAT PSPC spectrum of 1E 0056.8-7154. (Adopted from Heise et al. 1994, Table 1.)

5.3 1E 0056.8-7154 (SMC N67, SMP 22)

5.3.1 X-ray spectra

The supersoft X-ray source 1E 0056.8-7154 was discovered with the *Einstein Observatory*, and was also detected with EXOSAT (Jones et al., 1985; Seward and Mitchell, 1981). Wang (1991) shows that the observed X-ray spectrum of this source is consistent with that of a single nucleus of a planetary nebula (PN) collapsing to a white dwarf, and identifies this X-ray source with the bright (V=16.6) planetary nebula N67 in the SMC (also known as SMP 22). N67 has the hottest nucleus among all the known planetary nebulae in the SMC, and its previously known characteristics confirms its ability to produce the observed soft X-ray emission. Wang (1991) derives a blackbody temperature of $kT_{\rm eff} \sim 26 \pm 9$ eV and a bolometric luminosity of $L_{\rm bol} \sim (2-40) \times 10^{37}$ erg s^{-1} for the nucleus from the *Einstein* IPC data, and this corresponds to an effective radius of $R \sim 4 \times 10^{9}$ cm.

Heise et al. (1994) fitted blackbody and LTE models (H-rich and He-rich) to the ROSAT PSPC spectrum of 1E 0056.8-7154, and their results are shown in Table 5.11. It is noted that, unlike the blackbody fit, the LTE fits yield luminosities under the Eddington limit for a white dwarf.

Table 5.12 gives the parameters of 1E 0056.8-7154 derived by Suleimanov and Ibragimov (2003). Because this source is most likely to be a hot WD, the mass estimate of $0.9 - 1.1 M_{\odot}$ is probably the correct one.

More recent observations by XMM-Newton (2007 and 2009) were modelled with an NLTE white dwarf model atmosphere, composed of H, He, C, N and O with abundances derived from studies of the nebular lines (Mereghetti et al., 2010). Results of the NLTE fit, as well as those of a simple blackbody fit, are shown in Table 5.13. It appears that the white dwarf is quite massive, which is in good agreement with its other observational properties.

Parameter	LTE
$kT_{\rm eff}$ (eV)	34.5 ± 8.6
$N_{\rm H}$ (10^{20} cm^{-2})	$3.71^{21.29}_{-2.38}$
$\log g$	7.7 – 8.5
$L_{\rm bol}$ (10^{37} erg s^{-1})	2.4 – 8.0
R (10^9 cm)	1.0 – 2.8
$M_{\rm WD}/M_\odot$ (for $R_{\rm WD} = R$)	$\sim 0.5 - 0.8$
$M_{\rm WD}/M_\odot$ (for $R_{\rm WD} = \frac{1}{2}R$)	$\sim 0.9 - 1.1$

Table 5.12: Physical parameters of 1E 0056.8-7154 based on re-analysis of ROSAT data. (Adopted from Suleimanov and Ibragimov 2003.)

Parameter	Blackbody	NLTE
$kT_{\rm eff}$ (eV)	$27.0^{+4.0}_{-2.0}$	13.3 ± 0.09
$N_{\rm H}$ (10^{20} cm^{-2})	$5.2^{+1.3}_{-1.9}$	2.8 ± 0.4
$\log g$		6.0
$L_{\rm bol}$ (10^{37} erg s^{-1})	8	6
R (10^9 cm)	3.5	13 ± 1
$M_{\rm WD}/M_\odot$		1.2 ± 0.1
χ^2/DOF	0.98	1.17

Table 5.13: Blackbody and NLTE fit parameters for XMM-Newton data of 1E 0056.8-7154. The adopted SMC distance is 60 kpc. (Values from Mereghetti et al. 2010.)

5.3.2 Ultraviolet spectra

Spectra obtained with the IUE (International Ultraviolet Explorer) during April 1984 exhibit several emission lines of C, N, O and He (Aller et al., 1987). N67 has the highest N/O abundance ratio ($\sim$ 1) of the known SMC planetary nebulae and is classified as a type I PN. Nebular modelling of the IUE observations yields the following stellar parameters for the nucleus of N67: $\log g \sim 5.15$, $kT_{\rm eff} \sim 9.91$ eV and $R \sim 8 \times 10^9$ cm. Kaler and Jacoby (1990) provided an estimate of $kT_{\rm eff} \sim 17.7$ eV based on the He II λ4686 to Hβ ratio. However, according to Stasińska and Tylenda (1986) these temperatures most probably represent lower limits.

N67 has formed part of an extensive Hubble Space Telescope survey of Magellanic Cloud Planetary Nebulae. Full details are not presented here, but can be found in e.g. Stanghellini et al. (1999, 2003); Vassiliadis, Dopita, Bohlin, Harrington, Ford, Meatheringham, Wood, Stecher and Maran (1998); Vassiliadis, Dopita, Meatheringham, Bohlin, Ford, Harrington, Wood, Stecher and Maran (1998). An HST spectrum for N67 is shown in Fig. 5.12. No P Cygni profiles are detected in the emission lines. According to Stanghellini et al. (1999), the nebular expansion velocity of N67 is $V_{\rm exp} = 27.9$ km s^{-1}. Vassiliadis, Dopita, Meatheringham, Bohlin, Ford, Harrington, Wood, Stecher and Maran (1998) calculated the temperature and luminosity of the nucleus to be $kT_{\rm eff} \sim 18$ eV and $L_{\rm bol} \sim 10^{37}$ erg s^{-1} respectively,

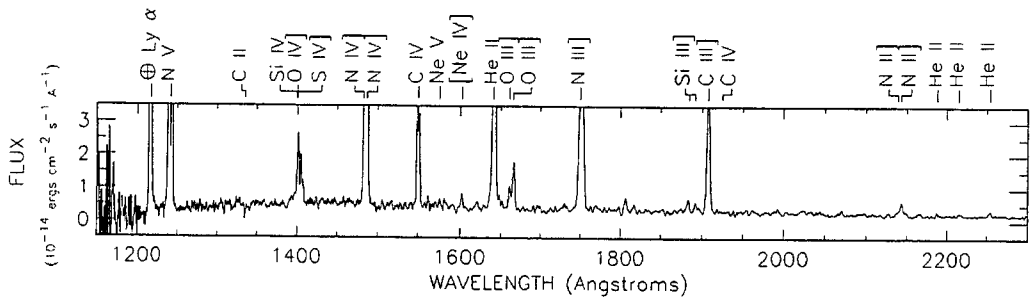

Fig. 5.12: HST spectrum of N67. The crossed circle denotes geocoronal emission. (Extracted from Vassiliadis, Dopita, Bohlin, Harrington, Ford, Meatheringham, Wood, Stecher and Maran 1998, Fig. 1.)

corresponding to a mass of $M_{\rm WD} \sim 0.7 M_{\odot}$.

5.3.3 Optical spectra

Meatheringham and Dopita (1991) performed a detailed optical spectrophotometric study of planetary nebulae in the Magellanic Clouds, during several observations in 1983, 1986 and 1988. They provide a list of spectral lines for N67 covering the range of 3340 – 7330 Å. The spectral lines exhibit a broad range of ionization, from [O I] to [Ne V]. The high abundance of N and lower abundance of C and O is probably coupled to the high temperature of N67, as C and O are important cooling agents through the collisional excitation of their lower energy levels. The nebula has a very high electron temperature: $T_{\rm e}$([O III]) = 26 600 K and $T_{\rm e}$([N II]) = 11 600 K. Derived electron densities are N_e([O II]) = 5510 cm^{-3} and N_e([S II]) = 2330 cm^{-3}. Photo-ionization modelling of these data yields $kT_{\rm eff} \sim 17$ eV and $L \sim 10^{37}$ erg s^{-1} for the nucleus of N67 (Dopita and Meatheringham, 1991).

5.3.4 Radio emission

Mereghetti et al. (2011) reports the first radio detection of N67 with the ATCA (Australian Telescope Compact Array) on 30 November 2010. It was detected with a flux of 0.36 mJy at 6 cm and a flux of 0.31 mJy at 3 cm.

5.4 RR Telescopii

RR Tel is a galactic symbiotic nova that started its last nova outburst in 1944, with the outburst lasting for many decades (Kahabka and van den Heuvel, 1997). It is a very wide, interacting binary system with an orbital period of 387 days. It consists of a hot compact star (presumed to be a white dwarf) and a cool Mira variable with spectral type around M5 (McKenna et al., 1997; Whitelock, 2003). The systemic velocity of RR Tel is ~ -62.3 km s^{-1}.

Pointed ROSAT PSPC observations of RR Tel were carried out during April 1992, and exhibited a soft spectrum, with a small hard component that is thought to originate from a collisional shock between a fast wind from the hot white dwarf and a slow wind from the cool companion (Jordan, Murset and Werner, 1994). The soft end of the spectrum can be described by a NLTE atmosphere model with $kT_{\rm eff} = 12.2$ eV, $L_{\rm bol} = 1.3 \times 10^{37}$ erg s^{-1}, $\log g \gtrsim 6.5$ and $R = 6.3 \times 10^9$ cm, yielding $M_{\rm WD} = 0.9 M_{\odot}$. A blackbody fit yields $kT_{\rm eff} = 11.6 \pm 0.4$ eV, $L_{\rm bol} = 9.5 \pm 0.8 \times 10^{36}$ erg s^{-1} and $R = 6.3 \times 10^9$ cm.

The binary components are embedded in an extended nebular envelope caused by the ionization of the wind from the secondary star by the luminous primary star. RR Tel exhibits an extremely rich optical spectrum, dominated by nebular emission lines. With increasing time, the spectrum is evolving towards higher ionization states. Spectral line lists of RR Tel are available in the literature (e.g. Kotnik-Karuza, Friedjung and Exter 2009; McKenna et al. 1997). RR Tel is a well-known source that has been studied extensively with a variety of instruments. In this discussion, the focus will be the Raman scattering of emission lines in RR Tel and how they provide evidence of an accretion disc in the source.

5.4.1 Raman scattering of O VI emission lines

Broad emission features at $\sim$ 6830 Å and $\sim$ 7088 Å were found in the spectrum of RR Tel, and in fact they are observed in more than 50% of symbiotic stars. Schmid (1989) identified these features as Raman-scattered emission features of the O VI $\lambda\lambda$1032 and 1038 resonance doublet.

Raman scattering is the process by which a photon is inelastically scattered by an atom or molecule, as opposed to Rayleigh scattering, which involves elastic photon scattering (e.g. Loudon 2000). Usually, this means that a photon is absorbed by an atom, which is then excited from its initial state to an intermediate state, whereafter a photon with a lower energy is emitted by the atom (in a random direction). The atom is then de-excited to its final energy state, which is still higher than its initial state. In some (rare) cases, the photon may gain energy from the atom (which may happen if the atom was already in an excited state).

Schmid (1989) showed that the observed emission features can be produced by the Raman scattering of the O VI doublet by neutral hydrogen. The initial photon with frequency ν_i excites hydrogen from its ground state, 1s ^{2}S, to an intermediate state, from where the Raman-scattered photon with frequency ν_f is emitted, leaving the atom in the excited state 2s ^{2}S. From the conservation of energy, the frequency of

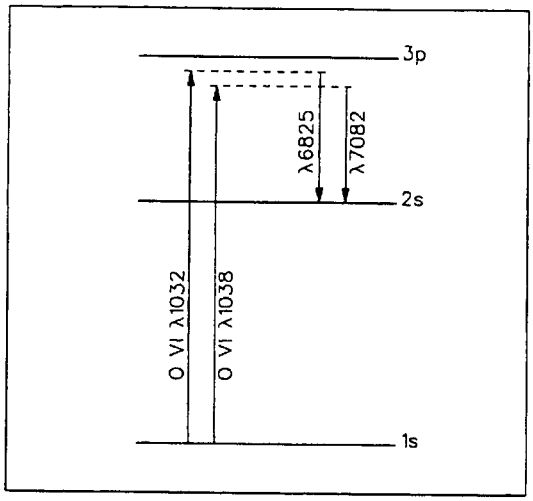

Fig. 5.13: Energy levels involved during the Raman scattering of O VI photons by H I. (Adopted from Schmid 1989, Fig. 2.)

the scattered photon is given by

$$\nu_f = \nu_i - \nu_{if} \ , \tag{5.1}$$

where ν_{if} represents the frequency difference between the initial and final atomic states. For such a scattering scenario, wavelengths of 6825.44 Å and 7082.40 Å are obtained for the Raman scattered components of O VI λ1032 and O VI λ1038 respectively. Such emission can be strongly polarized (Schmid and Schild, 1990). A schematic representation of the energy levels involved is given in Fig. 5.13.

The wavelengths of the O VI doublet is close to that of Lβ λ1026, therefore the intermediate state lies close to 3p ^{2}P^o. The size of the scattering cross-section increases strongly when the energy of the intermediate state approaches that of a bound state, therefore the scattering cross-section for λ1032 should be larger than for λ1038. This is indeed observed in symbiotic star spectra, where the intensity of the $\sim$ 6830 Å feature is about 4 times larger than that of the $\sim$ 7088 Å feature.

During the Raman scattering process described above, the wavelength shift of an incident O VI photon is amplified by the wavelength ratio between the scattered and initial photons, which is $\sim$ 6.7. According to Friedjung, Stencel and Viotti (1983), radiative transfer can be responsible for red shifts in the resonance lines of C IV, N V and Si IV. This can also explain the $\sim$ 5 Å difference between the predicted and observed wavelengths of the Raman scattered O VI lines, which would require a shift of 0.11 Å in the original O VI lines.

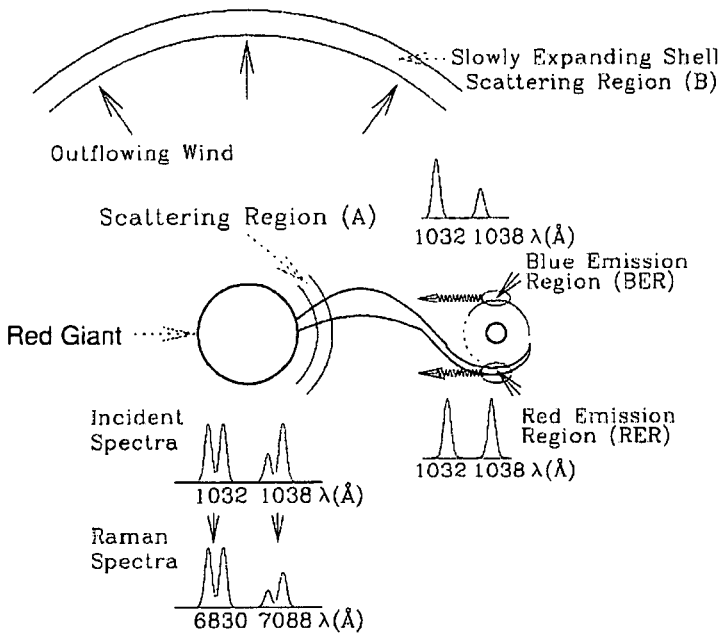

Fig. 5.14: Schematic illustration of the production of double-peaked Raman-scattered O VI emission lines in RR Tel. (Adopted from Lee and Park 1999, Fig. 1.)

5.4.2 Evidence of an accretion disc in RR Tel

Lee and Park (1999) showed that the double-peaked structures and high degrees of polarization of the Raman-scattered O VI lines in RR Tel provide strong evidence for the presence of an accretion disc around the primary star. The fact that the Raman-scattered lines are double-peaked, while the other emission lines are single-peaked, is interpreted in terms of line-of-sight effects. Fig. 5.14 provides a schematic diagram of their model.

The neutral hydrogen atoms responsible for the scattering are believed to be mainly located near the secondary star (Scattering Region (A)), with a small (but non-negligible) amount of scatterers located in a shell expanding at $V_{\rm exp} = 30$ km s^{-1} (Scattering Region (B)). While an observer viewing the accretion disc at a low inclination angle i will only see single-peak profiles, the H I scatterers near the secondary will "see" double-peaked profiles from an accretion disc. The emission regions in the accretion disc can be divided into the red emission region (RER) rotating away from the secondary, and the blue emission region (BER) rotating toward the secondary. Together, they produce the Doppler-broadened, double-peaked emission profile "seen" by the scatterers in region A, which scatter this double-peaked profile to longer wavelengths.

A higher mass concentration in the RER relative to the BER can cause the blue peak of the emission line profile to be weaker than the red peak. It is noted that, in

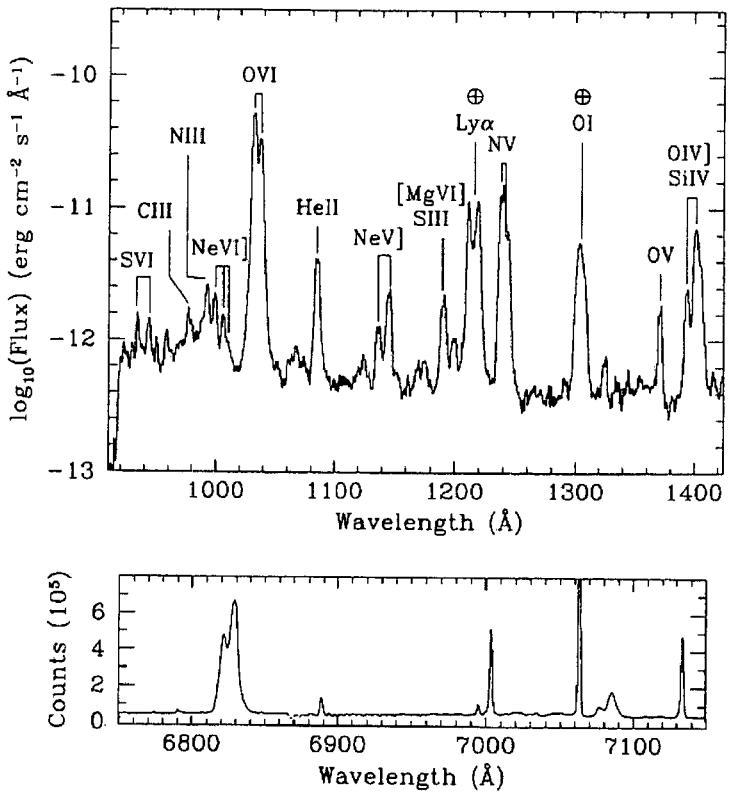

Fig. 5.15: Top: HUT spectrum of RR Tel, showing the O VI $\lambda\lambda$1032 and 1038 doublet. Bottom: The optical AAT spectrum, showing the double-peaked, Raman-scattered components at $\sim$ 6830 Å and $\sim$ 7088 Å. The crossed circles denote geocoronal emission. (Adopted from Espey et al. 1995, Fig. 1 and Fig. 2.)

the illustration of Lee and Park (1999) in Fig. 5.14, the double-peaked O VI λ1038 emission line is depicted with asymmetric peaks (red stronger than blue), while the O VI λ1032 emission is not. However, according to our interpretation, the O VI λ1032 line and its Raman-scattered component should also have the same asymmetric profile as O VI λ1038, and this is confirmed by observations of the 6830 Å component.

Simultaneous observations of the direct O VI lines and their Raman-scattered components during March 1995 are presented by Espey et al. (1995). The optical spectrum, obtained with the AAT, and the UV spectrum, obtained with the HUT (Hopkins Ultraviolet Telescope), are shown in Fig. 5.15. The presence of the blended O VI $\lambda\lambda$1032 and 1038 doublet (with each component having a single peak) and the double-peaked Raman-scattered components are clearly visible.

The discovery of Raman-scattered lines other than O VI in spectra recorded with the ESO 3.6-m telescope during September 1988 are also reported (van Groningen, 1993). These lines are identified as the Raman-scattered components of He II $\lambda\lambda$972 and 949, and C III λ977 that are scattered by neutral hydrogen to wavelengths of

4851 A, 4332 Å and 4977 Å respectively. The presumably Raman-scattered C III feature is actually observed as a double-peaked structure with peaks at 4977.0 and 4979.8 Å, which is compatible with the velocity spread of the scattered O VI lines.

Schmid et al. (1999) found the shift in the line centre of the Raman-scattered component at $\sim$ 6830 Å to be +28 km s^{-1}, and its FWHM = 10.7 Å. The broad wings of Hα are probably due to the Raman scattering of Lβ photons by H I (Lee, 2000).

This concludes the literature review of the target sample for this study. Various aspects of binary characteristics and accretion have been discussed in relation to the spectral and temporal behaviour of the sources in different wavebands. The next chapter is devoted to a discussion of the new optical spectra that were obtained for the sources CAL 83, N67 and RR Tel. Observational results for SMC 13 will only be presented in the chapter on X-ray spectroscopy (Chapter 7).

Chapter 6

Optical Spectroscopy

The main focus of this chapter is to apply the technique of optical spectroscopy to a few selected sources, which were discussed in the previous chapter. The purpose of this is to utilize the properties of the spectral lines to constrain the location of the line-emitting regions within these sources, as well as the kinematical properties of the line-emitting plasma. Of special interest is possible differentiation between the line emission from possible disc outflow, outflow driven by radiation pressure from a hot white dwarf, or possible magnetospheric propelling.

The chapter is structured as follows: An introductory discussion is presented, first focusing on the instrumentation that was utilized (Section 6.1). Sections 6.2 and 6.3 focus on the observations and data reduction techniques respectively. Sections 6.4 and 6.5 present a very brief discussion related to spectral calibration and analysis methods. In the last three sections, the results and accompanying discussion of the selected sources, i.e. CAL 83 (Section 6.6), N67 (Section 6.7) and RR Telescopii (Section 6.8) are presented separately.

6.1 Instrumentation

Optical spectra of the three supersoft sources were obtained at the South African Astronomical Observatory (SAAO) in 2011. The observatory is located approximately 18 km east of Sutherland in the Northern Cape, with coordinates 20° 48′ 38.5″ E; 32° 22′ 46″ S, at an altitude of 1798 m. The instruments that were used to record the spectra are the Robert Stobie Spectrograph (RSS) on the Southern African Large Telescope (SALT), and the Grating Spectrograph on the SAAO 1.9-m (Radcliffe) Telescope.

6.1.1 The Robert Stobie Spectrograph (RSS)

Relevant information related to SALT and the RSS was obtained from the SALT website[1]. The RSS Observer's Guide (Burgh and Nordsieck, 2009) and the technical documents of Burgh et al. (2003), Kobulnicky et al. (2003) and Nordsieck and Babler (2011) were consulted as well. Links to these documents can also be found on the SALT website.

SALT

SALT is the largest single optical telescope in the southern hemisphere. The primary mirror has a diameter of about 11 m and consists of 91 hexagonal mirror segments, each 1 m wide. This compound primary mirror is spherical in shape. SALT operates at a fixed altitude of 53° (with observable altitude range 47° to 59°) and can only rotate in the azimuthal direction to acquire astronomical targets. Target tracking is achieved by moving the tracker and optical payload over the mirror on a virtual spherical focal surface, enabling the payload to track targets as the earth rotates without adjusting the azimuth angle for up to 2 hours. The payload also contains the Spherical Aberration Corrector (SAC).

RSS

The RSS is mounted at the prime focus of SALT. The SAC provides an f/4.2 beam and an 8 arcminute field of view at the focal plane, with a plate scale of 4.5″/mm. The RSS has three basic observing modes, i.e. Imaging, Grating Spectroscopy and Fabry-Perot Imaging Spectroscopy. Polarization optics also introduces a polarimetric sub-mode for each of these three main modes.

The optical layout of the RSS is shown in Fig. 6.1. A variety of longslits can be inserted in the focal plane (see Table 6.1), as well as custom-designed masks for multi-object spectroscopy (MOS). The field lens is 10 mm beyond the focal plane. Behind this lens, waveplates for polarimetry can be inserted. Then follows the collimator system, with a 90° fold mirror before the last collimator doublet. A shutter is situated in the collimated beam, just before the dispersers. The disperser area contains either a double-etalon Fabry-Perot system, or one of six diffraction gratings.

There is one regular transmission grating and five volume-phase-holographic (VPH) gratings. Where a regular diffraction grating diffracts light by means of a periodic surface structure, a VPH grating diffracts light by means of refractive index variations within its volume (Barden et al., 2000). The advantages of VPH gratings include their high diffractive efficiency, low induced polarization effects and a re-

[1] `http://www.salt.ac.za`

	Longslit	Width (arcsec)	Height (arcmin)
Standard longslits	PL0060N001	0.6	8
	PL0100N002	1	8
	PL0120N001	1.2	8
	PL0125N001	1.25	8
	PL0150N001	1.5	8
	PL0200N001	2	8
	PL0300N001	3	8
	PL0400N001	4	8
Polarimetric longslits	PL0060P001	0.6	4
	PL0125P001	1.25	4
	PL0150P001	1.5	4
	PL0400P001	4	4

Table 6.1: Longslits available on the RSS. (According to the PIPT 1.98 SALT software.)

Grating	Wavelength coverage (Å)	Usable angles (°)	Bandpass per tilt (Å)	Resolving Power (1.25″ slit)
pg0300	3700-9000		3900/4400	250-600
pg0900	3200-9000	12-20	$\sim$ 3000	600-2000
pg1300	3900-9000	19-32	$\sim$ 2000	1000-3200
pg1800	4500-9000	28.5-50	1500-1000	2000-5500
pg2300	3800-7000	30.5-50	1000-800	2200-5500
pg3000	3200-5400	32-50	800-600	2200-5500

Table 6.2: RSS gratings (Adopted from Burgh and Nordsieck 2009, p. 6.)

duction of scattered light. Their efficiency also varies with the angle of incidence, therefore a large wavelength range can be accessed with a single grating by changing the angle between the beam and the grating normal. This is achieved by using a rotating grating stage. The VPH efficiency is usually at a maximum at the Littrow condition (where the angle of incidence is equal to the angle of diffraction), therefore the RSS camera angle has to be adjusted to two times the grating angle. For a given slit width, a larger grating tilt will also enhance the spectral resolution. The available gratings, with their wavelength, angle and resolution ranges are listed in Table 6.2. The efficiencies of the VPH gratings in at different wavelengths and resolution values are illustrated in Fig. 6.2.

The gratings are only used in first order. Second order transmission is removed by an appropriate order-blocking filter: in addition to a clear filter, there are 4 "cut-off" filters for order-blocking. There are also 40 different narrow-band interferometric filters for Fabry-Perot imaging spectroscopy.

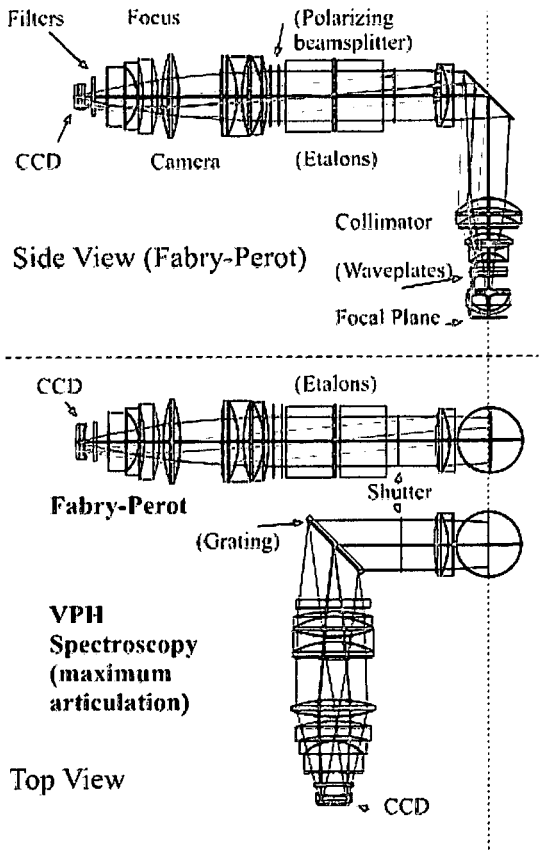

Fig. 6.1: The optical layout of the Robert Stobie Spectrograph (RSS). (Adopted from Burgh et al. 2003, Fig. 1.)

The science camera (f/2.2) has a plate scale of 8.6″/mm. The detector subsystem consists of a mosaic of three E2V 44-82 CCD chips. This mosaic is cooled by a Cryotiger, and as a result the inherent dark current is insignificant.

A variety of arc lamps are available for wavelength calibration: Ar, Ne, Xe, CuAr, ThAr and HgAr. See the technical discussion of Nordsieck and Babler (2011) for more information.

6.1.2 The SAAO 1.9-m Telescope Grating Spectrograph

The information on this instrument was obtained from the SAAO website[2], primarily from the user manual by Kilkenny and Worters (2011) which is also available on the website.

[2] `http://www.saao.ac.za`

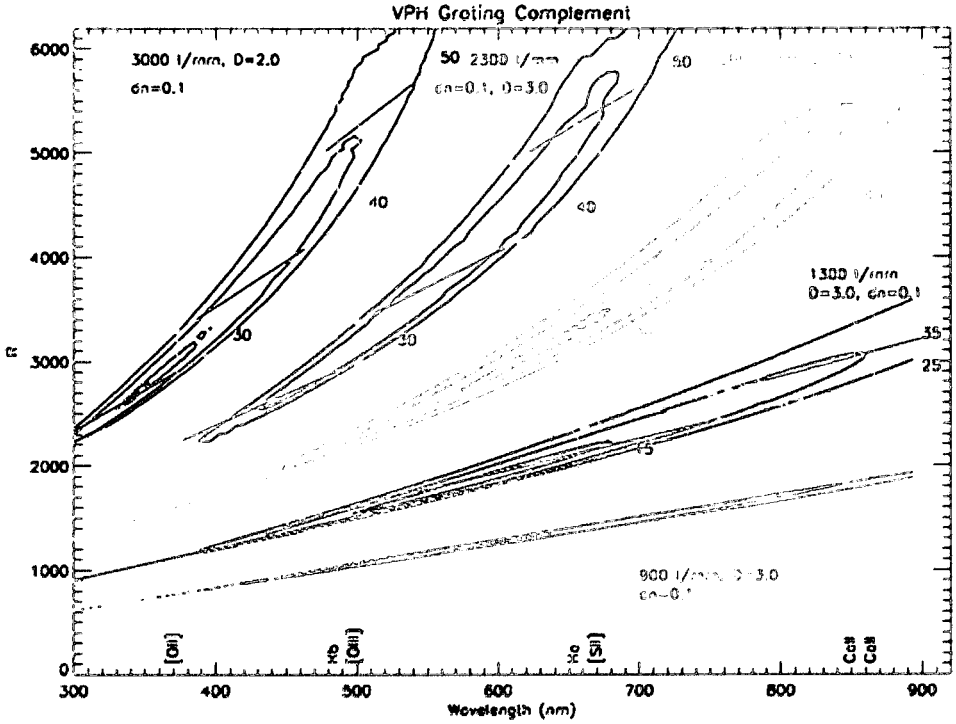

Fig. 6.2: The efficiencies of the VPH gratings of the RSS versus resolution (R) and wavelength. The contours indicate efficiencies of 50%, 70% and 90%. "D" indicates the grating thickness in microns and "dn" the modulation in the refractive index. Most of the VPH grating efficiencies peak at > 90%, which is appreciably higher than e.g. the efficiencies of the regular diffraction gratings of the 1.9-m Telescope Grating Spectrograph shown in Fig. 6.4. (Adopted from Burgh and Nordsieck 2009, p. 6, Fig. 4.)

The SAAO 1.9-m (Radcliffe) Telescope

The Radcliffe Telescope has a primary mirror with diameter 1.9-m. It has an equatorial mount and all observations are carried out with the telescope on the eastern side of the polar axis. It has an f/4.85, 22.49″/mm Newtonian focus which is rarely used, and an f/18, 6″/mm Cassegrain focus which can be used with the following science instruments: the Grating Spectrograph, the GIRAFFE Echelle Spectrograph, the HIPPO (High speed Photo-Polarimeter), the SAAO CCD (STE3/STE4) and the UCT CCD Photometer.

1.9-m Grating Spectrograph

The optical layout of the spectrograph is shown in Fig. 6.3. The guide mirror is a plane mirror oriented at 45° to the incident beam. It has an elliptical hole in the centre, effectively creating a circular 6.5′ aperture to incident light. During acquisition, the mirror is moved to an off-centre position, and the light that would have been focused at the slit, is reflected from the guide mirror and reaches the acquisition

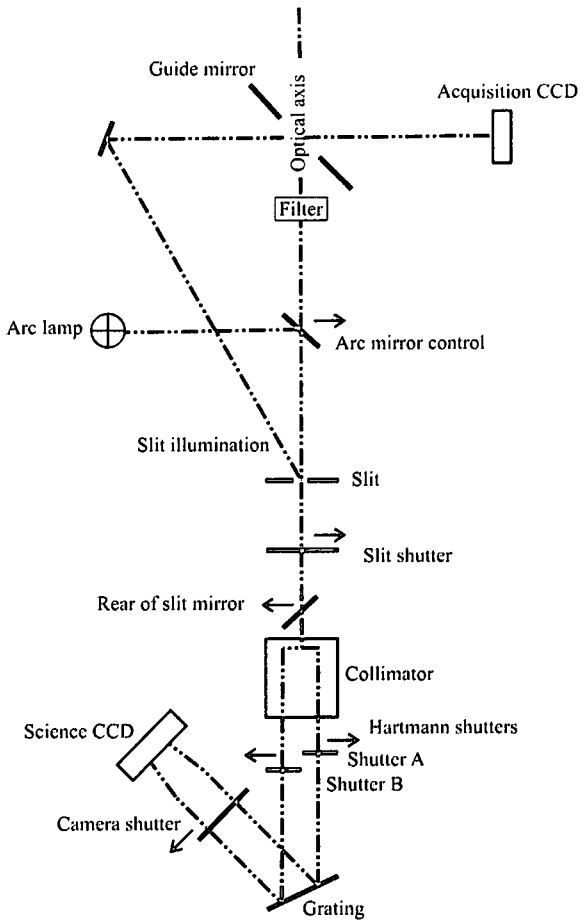

Fig. 6.3: The optical layout of the 1.9-m Grating Spectrograph. (Adopted from Kilkenny and Worters 2011, p. 31, Fig. 4.3.)

CCD. This enables the observer to point the telescope to the exact target position. After acquisition, the guide mirror is centred, and the target beam can reach the spectrograph slit. A guide star near to the target has to be selected so that the light from the guide star is reflected from a $\sim 4'$ annulus on the guide mirror just outside the circular aperture. The acquisition camera is then moved to an appropriate position (on an XY slides system) to intercept the guide star image, which is then used for autoguiding.

The observer can choose one of a number of different filters which are contained in the filter wheel. There are the different colour filters (BG38, BG39 and GG495) for order separation, as well as a number of neutral density filters that may be required for the observation of extremely bright stars.

Two types of arc lamps are available: CuAr and CuNe. When taking an arc expo-

Grating	Lines (mm^{-1})	Order	Dispersion (Å/mm)	Bandpass (Å)	Blaze wavelength (Å)	Resolution (Å)
4*	1200	1	50	800	4600	1
5	1200	1	50	800	6800	1
		2	20	350	3400	0.5
6*	600	1	100	1600	4600	2
7	300	1	210	4200	4600	5
8*	400	1	155	2300	7800	4
		2	75	1150	3900	2
9	830	1	65	960	7800	1.5
		2	30	480	3900	0.7
10	1200	1	50	800	10000	1
11	600	1	100	1600	10000	2
12	300	1	210	4200	10000	5

Table 6.3: Available gratings of the 1.9-m Grating Spectrograph (Adopted from Kilkenny and Worters 2011, p. 73.)
*Gratings 4, 6 and 8 have been severely scratched.

sure, the arc mirror is moved into the beam; the light from the target is blocked and the light from the arc lamp reaches the slit. If a colour filter is inserted in the sky beam, the same type of filter should be used in the arc beam.

The focal point of the Cassegrain configuration is on the entrance slit. The slit width can be set to one of 28 possible values, ranging from 0.15″ to 4.19″. The slit illumination lamp is used to illuminate the slit, and consequently an image of the slit is formed on the acquisition CCD. Whenever this lamp is on, the slit shutter should be closed to protect the science CCD. Slit illumination is used to determine the position of the slit on the acquisition image, or to focus the acquisition camera. Behind the slit and its shutter is the rear of slit mirror, that can be used for "knife-edge" telescope focusing.

The Hartmann shutters (A and B) are situated just after the collimator system. Shutter A can be used to block one half of the collimated beam, while shutter B can be used to block the other half. A focus test of the spectrograph camera is carried out by recording two arc spectra — the first with shutter A in the beam and the second with shutter B in the beam.

Several diffraction gratings with different resolutions and accessible wavelength ranges are available, and are listed in Table 6.3. The *blaze wavelength* of a grating represents the wavelength for which the grating has the maximum efficiency for a given order. The wavelength range accessed by a grating will vary with the grating angle. The viability of using a grating in a certain wavelength range also depends on the

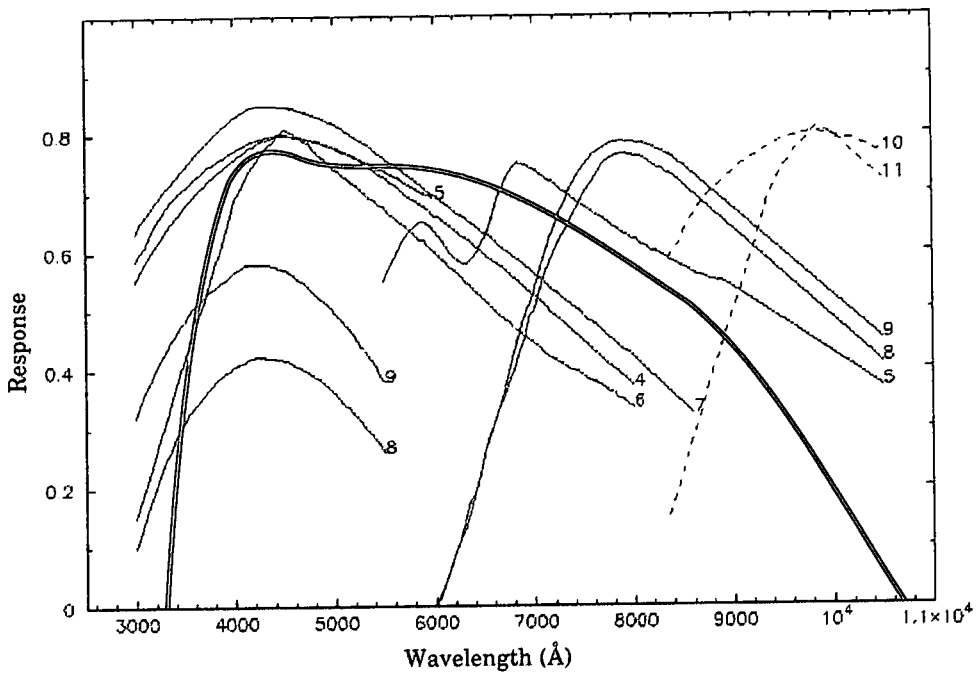

Fig. 6.4: Efficiency curves for the gratings of the 1.9-m Grating Spectrograph. For gratings 5, 8 and 9, second-order efficiency curves are shown as well (on the left). The thick red curve extending from $\sim$ 3250 – 10700 Å represents the efficiency of the science CCD. (Adopted from Kilkenny and Worters 2011, p. 83, Fig. 9.15.)

efficiency of the grating in that range. The efficiency curves for the different gratings are shown in Fig. 6.4.

The science CCD is a SITe1 1798 × 266 pixel chip with a linearity maximum of $\sim$ 40 000 counts per pixel, a gain of 1 and readout noise equal to 6.7 electrons. The dark current associated with this chip is negligible.

6.2 Observations

6.2.1 RSS

The galactic symbiotic nova RR Tel was observed with the RSS on 27 June 2011, and the close binary supersoft source CAL83 in the LMC was observed on 26 November 2011. All the different instrumental configurations that were used are shown in Table 6.4. A list of the target exposures are provided in Table 6.5. An arc lamp spectrum was recorded after each iteration sequence. (Wavelength calibration by means of arc spectra is discussed in Section 6.4.)

Setup	Longslit width (″)	Grating	Grating angle (°)	Range (Å)	Resolution (Å)	Filter	Arc lamp
A	1	pg0900	12.88	3342-6453	~ 3.8	pc03200	ThAr(0.36Å)
B	1	pg3000	43.62	4216-4925	~ 0.8	pc00000	CuAr(0.062Å)
C	0.6	pg0900	12.13	3057-6175	~ 2.3	pc00000	ThAr(0.24Å)
D	0.6	pg0900	19.62	5882-8891	~ 2.3	pc04600	Xe (0.12Å)

Table 6.4: Different RSS configurations used for the observations in Table 6.5. The values in brackets after the arc lamp specifications indicate the approximate uncertainty in the wavelength calibration.

Target	Setup[a]	Start date and time (UT)	Exposures
RR Tel	A	2011-06-27 21:28:02	4 × 60 s = 240 s
	B	2011-06-27 21:40:38	6 × 150 s = 900 s
CAL 83	C	2011-11-26 01:31:20	6 × 37 s = 222 s
	D	2011-11-26 01:55:47	6 × 37 s = 222 s

Table 6.5: RSS target exposures.
[a]Refer to the different instrument configurations in Table 6.4.

6.2.2 1.9-m Grating Spectrograph

During an observing run in September 2011, optical spectra of the SMC planetary nebula N67 and the galactic source RR Tel were obtained. The different instrumental configurations that were used are presented in Table 6.6, and the target exposures are listed in Table 6.7.

A set of 20 to 40 dome flat field exposures were taken at the start of each observing night. A set of bias frames were also recorded —15 per night during the April observing run, and 20 per night in September, except for the nights of 14 and 19 September, for which the bias frames of 15 and 20 September respectively were used. An arc spectrum was recorded before each target spectrum.

6.3 Basic CCD data reduction

Every raw CCD image not only contains photons from the program star collected by the spectrograph, but also unwanted signal, or noise. Such noise can originate from

Setup	Slit width (″)	Grating	Grating angle (°)	Range (Å)	Resolution (Å)	Filter	Arc lamp
E	1.5	4	5.4	4040-4904	~ 1	None	CuAr(0.09Å)
F	1.5	5	-2.9	6220-6968	~ 1	GG495	CuNe(0.02Å)

Table 6.6: Different 1.9-m Grating Spectrograph configurations used for the observations in Table 6.7. The values in brackets after the arc lamp specifications indicate the approximate uncertainty in the wavelength calibration.

Target	Setup[a]	Start date and time (UT)	Exposures
RRTel	E	2011-09-14 18:15:07	2×900 s = 1800 s
RRTel		2011-09-15 19:43:42	4×900 s = 3600 s
RRTel		2011-09-16 21:43:46	2×900 s = 1800 s
			4×600 s = 2400 s
RRTel	F	2011-09-17 21:11:47	4×180 s = 720 s
N67		2011-09-18 00:05:05	2×1800 s = 3600 s
RRTel		2011-09-19 21:04:08	4×180 s = 720 s
RRTel		2011-09-20 21:00:29	2×180 s = 360 s

Table 6.7: 1.9-m Grating Spectrograph target exposures.
[a]Refer to the different instrument configurations in Table 6.6.

various sources, such as readout noise, cosmic rays, thermal current and hot pixels, dust or internal reflections in the telescope. In order to produce a CCD spectrum of good quality, these artefacts have to be removed.

Each CCD exposure was stored in FITS (Flexible Image Transport System) format, which can handle tables and multi-dimensional arrays very effectively. The reduction and analysis of these CCD spectra were carried out by making use of the software program IRAF V2.15.1a (Image Reduction and Analysis Facility). This section provides an overview of the most basic reductions that are required, and concludes with a brief summary of how the data sets were reduced with IRAF. A detailed discussion of CCD reductions with IRAF can be found in Massey (1997).

6.3.1 Overscan, bias correction and trimming

The first step is to calibrate the signal on each CCD frame to the zero noise level (e.g. Howell 2006, p. 52-54). Consider an unexposed CCD pixel, i.e. one with zero collected photoelectrons. The digital count value of such a pixel (i.e. value stored on computer) after readout and analog-to-digital (A/D) conversion can be expected to have a mean value of zero, with a small distribution about zero due to readout noise and computer noise. Therefore, CCD electronics are configured to provide a positive offset value for each image in order to avoid negative count values in the raw image. This offset is known as the *bias level* and represents a "pedestal" on top of which science and other detected counts accumulate.

Most CCD images contain an *overscan region*, which is created by an extra number of empty readout cycles that do not contain any of the charge accumulated on the CCD. The overscan region of an image is used to obtain the mean bias level for the image (or for each row separately if, the bias level varies significantly over the different rows), and this is then subtracted from every pixel.

A *bias frame* is a zero-second exposure of the CCD, which simply consists of a read-out of the pixels and an A/D conversion to produce a digital image on computer. Bias frames contain more information than the overscan regions, as they reveal two-dimensional structure that may be present in the bias level. After applying overscan corrections to all the CCD frames (including the bias frames), several bias frames can be combined to obtain a master bias frame, and, if necessary, this can then be subtracted from the science frames (and any other calibration frames like dark frames and flat frames) to correct for structure in the bias level.

As soon as this is done, the area of the CCD chip that contains the science data can be determined, and the strips at the edges that do not contain useful data can be trimmed off.

6.3.2 Dark current correction

Any material above 0 K will be affected by thermal noise (e.g. Howell 2006, p. 47-50). In a CCD, thermal energy can free electrons from the valence band, and these "dark current" electrons become part of the signal when the CCD is read out. Science CCD's are cooled by making use of a liquid nitrogen dewar, or thermo-electric cooling methods. The significance of the dark current depends primarily on the operating temperature, and also on the characteristics of the CCD. The necessity of correcting for dark current will therefore depend on the situation at hand. A *dark frame* is simply an exposure taken with no light reaching the CCD (i.e. with a closed shutter). This will contain only thermal noise and contributions from hot pixels, and by subtracting an appropriate master dark frame (created from several dark frames) from the science images, these effects can be removed.

6.3.3 Flat field correction

A *flat field* exposure involves exposing the CCD to a uniformly illuminated calibration source, such as an illuminated dome screen or the twilight sky. Such a flat field contains information about the pixel-to-pixel variations in the response of the CCD, as well as the effect of dust, vignetting and internal reflections in the telescope (e.g. Wodaski 2002, p. 238-244). After bias and dark correction, the science images can be divided by a combined master flat field to compensate for these artefacts. A separate master flat field should be used for different instrumental configurations, as it characterizes the system sensitivity and behaviour under specific conditions.

Clearly, a flat field exposure should be uniformly illuminated. However, this is often not the case in practice, for example the flat lamp used to illuminate a dome screen for dome flats may illuminate the central part of the screen more strongly than the edges. To remove the large-scale gradients from such a flat field exposure, the

flat is divided by a heavily smoothed version of itself. This removes the illumination pattern, and only the small scale response effects are retained. Therefore, if necessary and applicable, the master flat field can first be illumination corrected before it is used to calibrate the target exposures.

6.3.4 RSS data reduction summary

Fidelity checking and pre-calibration were already performed on the RSS data obtained from SALT by a semi-automated SALT PyRAF pipeline. This pipeline performed gain corrections depending on readout and gain modes, as well as overscan subtraction and cross-talk corrections. There are six amplifiers in the detector, and the data from each is originally stored in a separate Header/Data Unit (HDU) in the FITS file for each exposure. The pipeline also mosaicked the data from the six amplifiers into a single two-dimensional image. Finally, we trimmed all the pre-calibrated two-dimensional images with the IRAF task **ccdproc**, keeping the region [1:3162,60:1900]. As the science CCD dark current is negligible, no master dark correction was performed, and also no master bias or master flat correction.

6.3.5 1.9-m Grating Spectrograph data reduction summary

By examining a sample of the data frames with the IRAF task **implot**, the area of the CCD chip that contains useful data was determined to be [26:1774,1:133] (known to IRAF as the "TRIMSEC"). The appropriate overscan region (known to IRAF as the "BIASSEC") was noted to be [4:21,1:133], and these regions were specified to the task **ccdproc**. The task **ccdproc**, as well as the tasks **zerocombine** and **flatcombine** mentioned below, is part of the **noao.imred.ccdred** package.

The bias frames were combined with **zerocombine**, yielding one master bias for every observing night. The master bias for every night was subtracted from all the target and flat field frames of that night with the **ccdproc** task, which also applied the overscan corrections and trimmed the images. One master flat was created from the set of flat frames for each night with **flatcombine**, and an illumination correction was applied to each master flat frame. Consequently, the science images for each night were divided by the corresponding illumination corrected master flat frame with a second pass through **ccdproc**. Because the dark current in the science CCD is negligible, no dark frame calibration was carried out.

6.4 Spectral calibration and extraction

After these basic reductions, a set of noise-corrected CCD images were obtained. On the target images, the target spectrum can be seen as an elongated trace in the dispersion direction. Shown in Fig. 6.5 is an example of such a two-dimensional

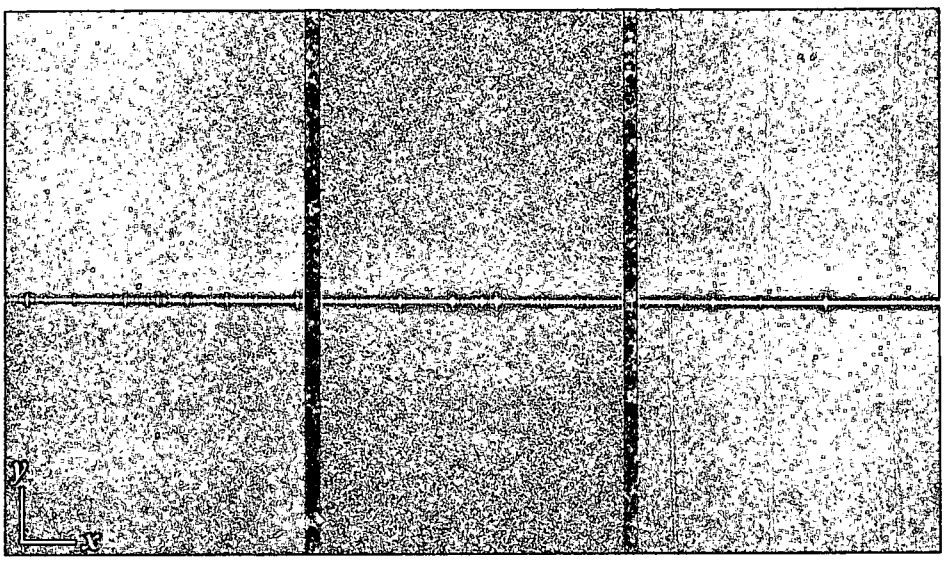

Fig. 6.5: An exposure of RR Tel recorded with the RSS, with basic reductions performed. The bright trace in the x-direction (dispersion direction) represents the spectrum of RR Tel, with its strong emission lines clearly visible as the bright points on this trace. On the right, several sky lines are visible as elongated structures covering the whole CCD in the y-direction (cross-dispersion direction). The two black strips correspond to the gaps between the CCD chips.

target image: an exposure recorded of RR Tel with the RSS, using configuration A in Table 6.4. The dispersion direction will be referred to as the x-direction, with the cross-dispersion direction as the y-direction. In this section, the procedures that were carried out to obtain the final spectrum from such two-dimensional target images will be outlined. For a detailed discussion of spectral calibration and extraction with IRAF, see Massey, Valdes and Barnes (1992).

6.4.1 Wavelength calibration

The next step is to transform the CCD pixel coordinates in the dispersion direction to wavelength coordinates (in Å). This is achieved by using *comparison arcs* (e.g. Massey and Hanson 2010, p. 33). Such a comparison arc is obtained by recording a spectrum of a discharge tube (e.g. CuNe or ThAr) at exactly the same instrumental configuration as the science exposure. Arc spectra have strong emission lines at known wavelengths, and thus enable the transformation of a pixel scale in the x-direction to a wavelength scale. Because the discharge tube illuminate the whole slit, the arc emission lines extend over the whole CCD in the y-direction.

The wavelength calibration was accomplished by utilizing various tasks in the **noao** IRAF package. For each arc exposure, the tasks **identify** and **reidentify** were used to assign the correct wavelength values to the arc emission lines at intervals

of 5 pixels in the y-direction, in other words a dispersion solution was obtained at every fifth "horizontal" row in the two-dimensional arc image. The task **fitcoords** was consequently used to fit a two-dimensional polynomial (with order 4 in both dimensions) to the assigned coordinates, and a transformation function was created for mapping the [x,y] pixel coordinates to a [λ,y] coordinate system. The **transform** task was used to perform the actual transformation of the target frames to [λ,y] coordinates, using each target frame's corresponding arc's transformation function.

6.4.2 Background/sky subtraction

After performing the wavelength calibration, background subtraction was performed on the two-dimensional images. The background includes spectral lines originating from the atmosphere ("sky lines") superimposed on the target spectrum. It is therefore crucial to subtract the background correctly to get rid of the contribution from sky lines.

Because the whole slit is illuminated by the sky, the sky lines extend over the whole CCD image, while the target spectrum is only contained in a few adjacent rows corresponding to the target position on the slit. As seen in Fig. 6.5, the sky lines on the [x,y] image have a curved form because of geometrical distortions. However, these distortions are accounted for by the wavelength calibration described in the previous section, and in the resulting [λ,y] images the sky lines are perfectly aligned in the y-direction.

The two-dimensional background subtraction for each target image was performed by utilizing the **background** task. This task was used to fit a polynomial function to each column in the y-direction, excluding the pixels containing the target spectrum from the fit. For each image column, this fitted function was subtracted from the column, effectively removing the background from the image and yielding a background subtracted target image.

6.4.3 Extraction of target spectra

The extraction of each spectrum in the form of an intensity versus wavelength plot was accomplished by using the task **apall**. Appropriate aperture regions containing the target counts in each spectrum image were first determined. An aperture region encompassing 50 rows centred on the target trace was used for the RSS data, while a region of 13 rows was used for the 1.9-m Grating Spectrograph data. A cleaning algorithm was also applied by **apall** to get rid of cosmic rays. The final spectra were examined with **ds9** and **spectool** for residual cosmic ray hits not cleaned by the algorithm, and these were fixed by interpolating across the bad pixels.

6.4.4 Stacking of spectra

In order to increase the signal-to-noise ratio of a spectrum, a number of spectra of the same target over the same wavelength range can be averaged or "stacked". This was done by using the task **scombine**. Prior to applying this task, it was verified that the spectra that are going to be stacked, all have the same shape.

No absolute flux calibration was performed on these data.

6.5 Spectral analysis methods

The IRAF task **spectool** was used to perform the measurements described in this section. The first step was to identify the spectral features for each target. The target spectra were first deredshifted by using the previously determined heliocentric systemic velocity for each target. This brought the line positions quite close to their laboratory wavelengths, enabling easier identification. The wavelength positions of the line centres were determined with a gaussian centering algorithm. After the lines were identified, the actual velocity shifts of the individual lines were calculated with the Doppler formula (see Eq. (3.65)), and heliocentric corrections were performed. An approximate 1σ error level was determined for each spectrum by using **spectool**.

In order to determine the FWHM (full width at half maximum), FWZI (full width at zero intensity) and equivalent width of certain spectral lines, a Gaussian profile was fit to each line. The FWHM and FWZI measurements (in A) were corrected for instrumental broadening by using the following basic formula:

$$\text{Corrected width} = \sqrt{\text{Uncorrected width}^2 - \delta^2}\ , \tag{6.1}$$

where δ is the wavelength resolution.

The laboratory air wavelengths of the spectral lines were obtained from the NIST Atomic Spectra Database[3] (NIST, 2011).

Now that the scientific instrumentation used for this study, as well as the data reduction procedures have been reviewed, the results of the spectroscopic study of CAL 83, N67 and RR Tel will be presented consecutively. After the presentation of the results related to each individual source, a brief discussion will follow immediately.

[3] `http://www.nist.gov/pml/data/asd.cfm`

6.6 CAL 83

6.6.1 Results

The RSS spectra taken on 26 November 2011 were combined into two averaged spectra: one in the blue and one in the red, and these are shown in Fig. 6.6. The only strong emission features discernible above the noise level are the He II λ4686 and Hα λ6563 emission lines. The weak feature at 4863.78 Å is concluded to be Hβ λ4861 emission, while the weak feature superimposed on the blue wing of He II may be C III and C IV emission, as suggested by Crampton et al. (1997). Fig. 6.7 provides plots of the He II and Hα lines in terms of velocity, illustrating their broad structure.

The profile measurements are presented in Table 6.8. The velocity shift of the centroid of each spectral line from its laboratory wavelengths after heliocentric corrections is given as Δv. Also included in the table is the conversion (by means of Eq. (3.50)) of the ionization energy obtained from Table B.1 to a temperature, $T(\epsilon_i)$, for each of the line-emitting species identified in the spectrum. The thermal energy $T(\lambda)$ associated with the line wavelength according to $h\nu \sim \frac{3}{2}kT$ (see Eq. (3.53)) is also shown.

The average heliocentric velocity displacement of the emission lines from their laboratory wavelengths is 190 km s^{-1}. According to Eq. (3.65), the spectral resolution of $\sim$ 2.3 Å corresponds to a velocity resolution of $\sim$ 100 km s^{-1} in the vicinity of Hα λ6563, and $\sim$ 150 km s^{-1} in the vicinity of He II λ4686.

The FWZI of 1380 km s^{-1} presented in Table 6.8 for the He II λ4686 line represents the range from 4678 to 4700 Å, as determined from the wing limits of the Gaussian profile fit. However, when inspecting the line profile (see Fig. 6.6 and Fig. 6.7), it seems that the blue wing of the He II emission actually extends to $\sim$ 4600 Å,

ID	Lab λ (Å)	$T(\epsilon_i)$ K	$T(\lambda)$ K	Δv (km/s)	W_λ (Å)	FWHM (Å)	FWHM (km/s)	FWZI (Å)	FWZI (km/s)
C III, C IV?	$\sim$ 4650 – 4660	282 800 555 300	$\sim$ 20 600						
He II	4685.68	285 100	20 470	200	-6.19	5.57	356	21.5	1380
Hβ	4861.35	–	19 730	$\sim$ 150	~ -2	$\sim$ 5	$\sim$ 300	$\sim$ 21	$\sim$ 1300
Hα	6562.82	–	14 610	224	-13.6	9.75	445	35.9	1640

Table 6.8: CAL 83 emission lines detected with the RSS. The parameters were derived by fitting a Gaussian profile to each emission line. Δv represents the heliocentric velocity shift of the measured line from its laboratory wavelength. The FWHM and FWZI values were corrected for the effect of instrumental broadening with Eq. (6.1), using $\delta = 2.3$ Å. As the Hβ emission is barely discernible above the noise level, its profile measurements only provide a rough estimate.

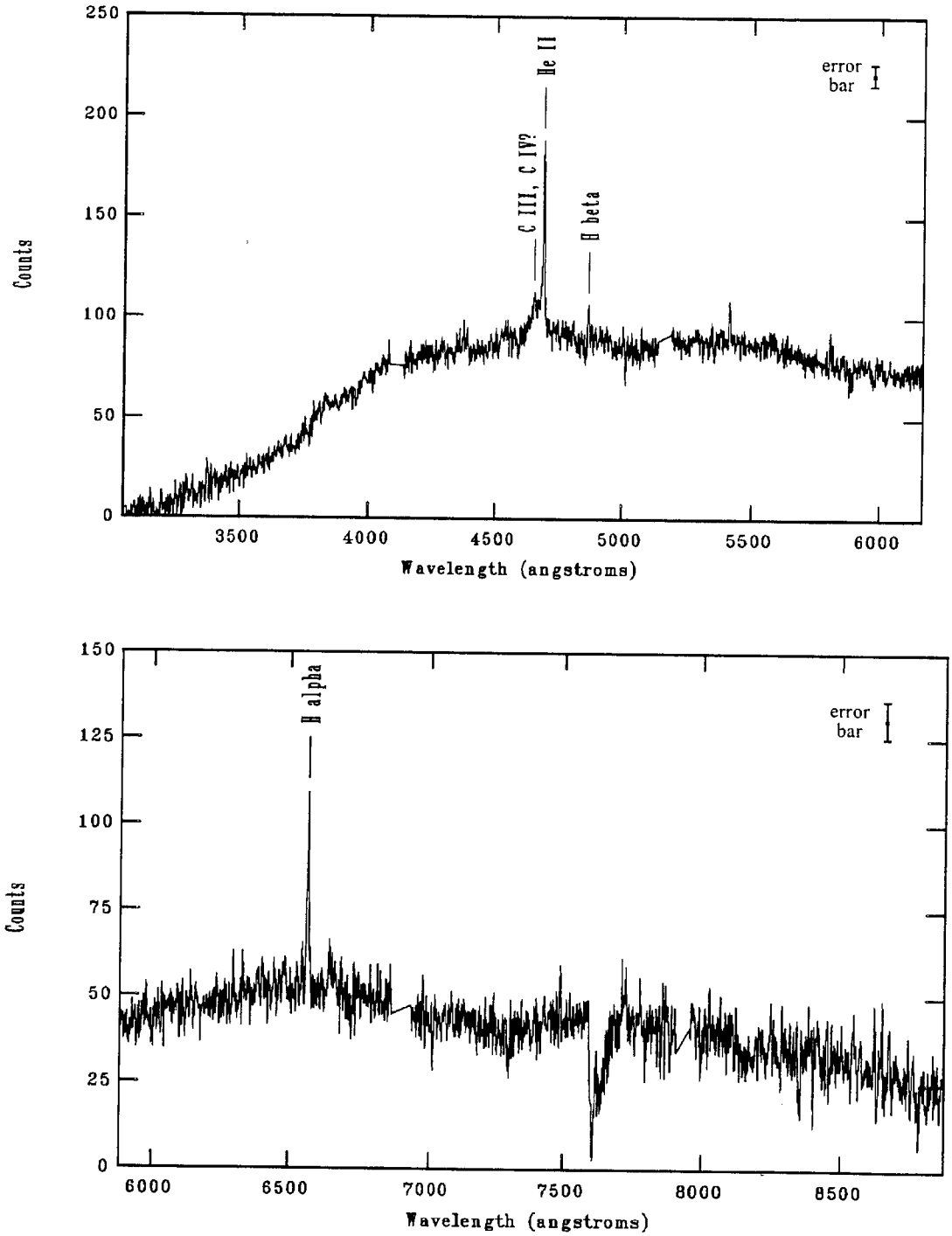

Fig. 6.6: The average CAL 83 spectrum recorded with the RSS. The resolution is ~ 2.3 Å. The spectrum was smoothed with a box size of 3 data points for display purposes. The error bar indicates a typical 1σ error level on either side of a data point.

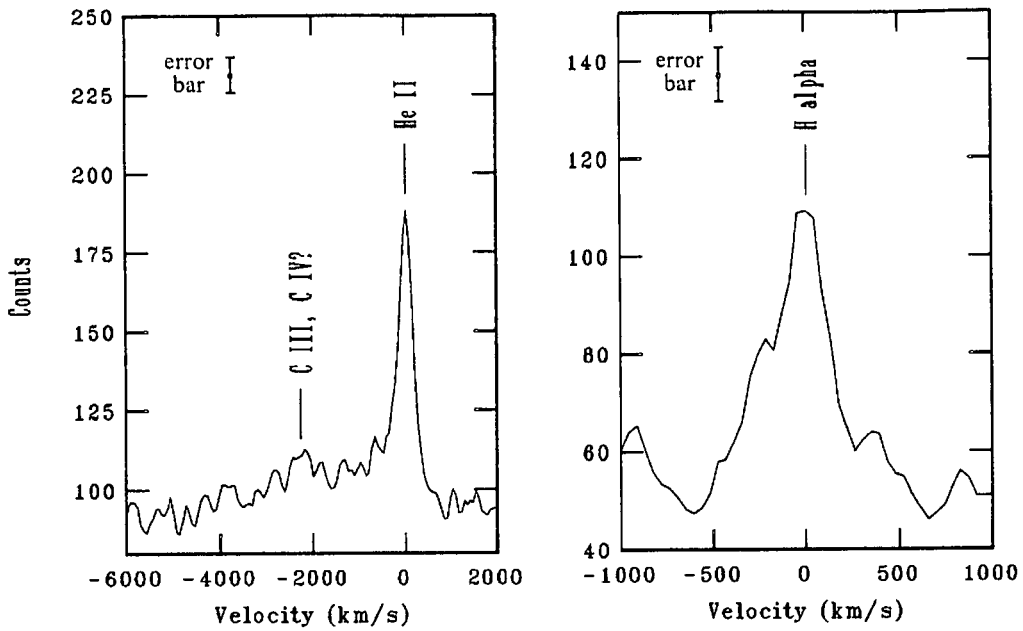

Fig. 6.7: The He II λ4686 and Hα λ6563 emission lines of CAL 83 detected with the RSS, plotted in terms of velocity relative to the centres of these lines. The resolution is $\sim$ 150 km s^{-1} for the left panel and $\sim$ 100 km s^{-1} for the right panel. The spectrum was smoothed with a box size of 3 data points for display purposes. The error bar indicates a typical 1σ error level on either side of a data point.

representing a ~ -5500 km s^{-1} shift from the rest wavelength.

6.6.2 Discussion

The observed emission lines are expected to originate from an accretion disc around the primary white dwarf. The He II λ4686 emission line exhibits a very broad wing structure to the shorter wavelength side, similar to what has been observed before (e.g. Fig. 5.4). While the FWZI of the "main component" is $\sim$ 1380 km s^{-1}, the blue wing extends to ~ -5500 km s^{-1} from the peak value. The presence of this extended emission component is in favour of the presence of a wind or jet with a large collimation angle from the accretion disc in CAL 83.

The presence of a possible outflow or jet from the disc may in fact be a distinct possibility if the compact object in CAL 83 is a rapidly rotating magnetized white dwarf accreting from an accretion disc. For white dwarf magnetosphere-disc interaction outside the corotation radius, magnetospheric propelling of the plasma may result in an outflow of material from the accretion disc along open magnetospheric field lines.

No similar wing structure is observed in the Hβ line. However, the possibility of such structure in Hβ can not be excluded, as the Hβ emission in our spectrum is

just discernible above the noise level.

Comparison of the FWHM and equivalent widths (W_λ) of the emission lines in Table 6.8 with the previously measured values in Tables 5.6, 5.7 and 5.8, shows the following: The values of W_λ and the FWHM for the He II λ4686 line are within the range of the (variable) values measured previously, although the central wavelength shift is somewhat smaller than the values in Table 5.7. The equivalent width of the Hβ line (~ -2 Å), is close to the lowest values in Table 5.7, but the new FWHM is $\gtrsim 2$ times larger than the corresponding FWHM values. However, the weakness of Hβ emission in our spectrum introduces significant uncertainty related to the current profile measurements.

The W_λ values given for Hα in Tables 5.6 and 5.8 (-18 Å and -21.9 Å) are somewhat larger than the newly measured value of -13.6 Å. While this still requires further investigation, this may be related to the transient nature of CAL 83, as the equivalent width is a measure of the line intensity.

In order to determine the orbital phase at which our spectra were recorded, the mid-exposure UT times of the combined spectra were determined and converted to Barycentric Julian Dates (BJD). All conversions in this work involving BJD were carried out with the Time Utilities of the Ohio State University[4] (Eastman, Siverd and Gaudi, 2010). All BJD values determined from here on are expressed in the Barycentric Dynamical Time system (TDB).

For the CAL 83 spectra, BJD 2455891.566 was obtained at mid-exposure for the blue spectrum and BJD 2455891.583 at mid-exposure for the red spectrum. Converting the time of minimum light of the orbital ephemeris of Schmidtke et al. (2004) to BJD yields the following orbital ephemeris:

$$T_0 = \text{BJD } 2451500.954 \pm 0.004 \quad + \quad 1.047568E \pm 0.000003 \text{ d} .$$

Relative to this ephemeris, the blue spectrum was recorded at $\phi = 0.24$ and the red spectrum at $\phi = 0.26$, yielding, by approximation, $\phi \sim 0.25$ for our observation. By the definition of orbital phase, the primary and secondary stars pass through a plane perpendicular to our line of sight at $\phi = 0.25$, with the primary moving towards us and the secondary away from us. This means that the maximum possible radial velocity components associated with the orbital motion can be measured at $\phi = 0.25$ for both the primary and the secondary star.

To put the velocity shifts measured for the emission lines into context, we need

[4] `http://astroutils.astronomy.ohio-state.edu/time`

to determine the expected velocity shifts due to the orbital motion of the system and the systemic velocity of the source. The systemic velocity of CAL 83 will be assumed to be more or less equal to the systemic velocity of the LMC, which is 262.2 ± 3.4 km s^{-1} according to van der Marel et al. (2002). Because the orbital phase relative to the above ephemeris is known, one may be able to determine from what part of the system the emission originates. The velocity shifts expected from the system were calculated in the following way:

Based on the literature review in Section 5.1, the following parameters were adopted for CAL 83: $M_1 \sim 1.3 M_\odot$, $M_2 \sim 0.5 M_\odot$, $i \sim 25°$ and $P_{\rm orb} = 1.047568$ d. The WD temperature is $\sim$ 47 eV, corresponding to $\sim$ 550 000 K. The given masses yield $q \sim 0.38$. From Eq. (4.3), the radius of the WD is

$$R_{\rm WD} = 4.9 \times 10^8 \left(\frac{M_{\rm WD}}{M_\odot}\right)^{-0.8} \text{ cm} = 4.0 \times 10^8 \left(\frac{M_1}{1.3 M_\odot}\right)^{-0.8} \text{ cm} . \qquad (6.2)$$

The *photospheric* radius reported for the white dwarf with hydrogen burning in a shell on its surface is $R \sim 8.0 \times 10^8$ cm, about twice the size of the white dwarf core itself.

Substituting the necessary values into Eq. (2.1) yields a binary separation of the order

$$a = \left[\frac{G(M_1 + M_2)P_{\rm orb}^2}{4\pi^2}\right]^{1/3} = 5.4 \times 10^{11} \left(\frac{M_1 + M_2}{1.8 M_\odot}\right)^{1/3} \left(\frac{P_{\rm orb}}{1.047568 \text{ d}}\right)^{2/3} \text{ cm} . \qquad (6.3)$$

From the definition of the centre of mass in Eq. (2.3), and since $a = a_1 + a_2$, the following is obtained:

$$a_1 = \frac{M_2}{M_1 + M_2} a = 1.5 \times 10^{11} \left(\frac{M_2}{0.5 M_\odot}\right) \left(\frac{M_1 + M_2}{1.8 M_\odot}\right)^{-1} \left(\frac{a}{5.4 \times 10^{11} \text{ cm}}\right) \text{ cm} \qquad (6.4)$$

and

$$a_2 = a - a_1 = (5.4 - 1.5) \times 10^{11} \text{ cm} = 3.9 \times 10^{11} \text{ cm}. \qquad (6.5)$$

By using Eq. (2.2) and Eq. (2.5), the binary parameters presented above can be used to show that the maximum value of the heliocentric velocity displacement (Δv) from the systemic velocity of a spectral line originating from near the primary due to orbital motion is

$$K_1 = \frac{2\pi a_1}{P_{\rm orb}} \sin i \sim 44 \left(\frac{a_1}{1.5 \times 10^{11} \text{ cm}}\right) \left(\frac{P_{\rm orb}}{1.047568 \text{ d}}\right)^{-1} \left(\frac{\sin i}{\sin 25°}\right) \text{ km s}^{-1} , \qquad (6.6)$$

yielding $\Delta v = -44$ km s^{-1} at $\phi = 0.25$ and $\Delta v = +44$ km s^{-1} at $\phi = 0.75$. The

corresponding value for a spectral line originating near the secondary yields

$$K_2 = \frac{2\pi a_2}{P_{\rm orb}} \sin i \sim 110 \left(\frac{a_2}{3.9 \times 10^{11}\ {\rm cm}}\right) \left(\frac{P_{\rm orb}}{1.047568\ {\rm d}}\right)^{-1} \left(\frac{\sin i}{\sin 25^\circ}\right)\ {\rm km\ s^{-1}}\ , \tag{6.7}$$

i.e. $\Delta v = +110$ km s^{-1} at $\phi = 0.25$ and $\Delta v = -110$ km s^{-1} at $\phi = 0.75$.

Referring the above to the systemic velocity of 262.2 km s^{-1} shows that, at $\phi = 0.25$, $\Delta v = (262.2 - 44)$ km s^{-1} ~ 218 km s^{-1} would be expected for spectral lines that originate near the WD and thereby follow the orbital motion of the WD. On the other hand, $\Delta v = (262.2 + 110)$ km s^{-1} ~ 372 km s^{-1} would be expected for lines originating near the secondary star at $\phi = 0.25$. As the velocity shifts of He II λ4686, Hβ and Hα are 200 km s^{-1}, ~ 150 km s^{-1} and 224 km s^{-1} respectively, our data provides evidence that the emission originate from near the WD, assuming that CAL 83 has the same systemic velocity as reported for the LMC. This supports the scenario of emission from an accretion disc around the WD. (Although the velocity resolution of ~ 150 km s^{-1} in the blue region of the spectrum, as well as the uncertainty in the measurement of Hβ may compromise a conclusive statement for the blue lines in this regard, the ~ 100 km s^{-1} resolution in the vicinity of Hα is considered adequate to distinguish between 218 km s^{-1} and 372 km s^{-1}.)

A thermal ionization temperature of at least $\sim$ 285 100 K would be required for the initial ionization of He I to He II. Given the WD temperature of approximately 550 000 K, it is entirely possible for He II ions to be produced in the system. The most probable temperature associated with Balmer emission is $\sim$ 10 000 K. At lower temperatures, most atoms are in their ground states, while Balmer emission involves transitions to the $n = 2$ level. The temperature associated with the Balmer emission is consistent with the temperatures associated with an accretion disc.

Comparison of the profile widths of Hα and Hβ with the combined thermal and pressure broadened profiles in Fig. 3.10 corresponding to a gas with $T = 10\ 000$ K, shows that the T- and P-broadening for Hα, even for relatively high electron densities, is much smaller than the measured broadening, therefore the measured Hα broadening is mainly ascribed to Doppler broadening due to rotation in the system. For Hβ, the same argument holds for electron densities up to $N_e \sim 10^{15}$ cm^{-3}, but for larger densities, pressure constitutes a major broadening mechanism.

The WD temperature of $\sim$ 550 000 K can be considered as an upper limit to the temperature of the accretion disc, as the disc temperature will decrease with increasing radius (see Eq. (2.65)). The FWHM for thermal broadening can be calculated from Eq. (3.70), with the mass of the He atom being $m \approx 4m_{\rm p}$. Even for temperatures

up to $\sim$ 550 000 K, the thermal broadening FWHM of the He II λ4686 emission line is less than 1.3 Å. For larger atoms and ions, the thermal broadening effect will be even smaller.

Although a detailed study of pressure broadening for atoms heavier than hydrogen has not been performed as part of the current investigation, the Stark effect is known to be less pronounced for larger atoms, and also weaker for ions than for the corresponding neutral atoms (Struve, 1929). It is therefore assumed that pressure broadening effects for He II contribute even less to the broadened profile than in Hα, and that the broadening of the He II λ4686 line is mainly due to the radial velocity of orbiting material in the system.

However, when inferring radial velocities directly from the profile widths, it should be noted that these values represent upper limits, because, strictly speaking, other broadening mechanisms (even though they may be negligibly small in some cases), still contribute to the line profile. The contribution of the broadening effect of turbulence to the line profiles was not quantified in our current discussion. In cases where a high degree of turbulence is expected in the plasma, meticulous modelling should also account for its broadening effect.

Another factor to keep in mind during the subsequent discussion is that any particular emission line will only contain photons from regions in the system where the particular emitting species are present. The ability of certain atoms or ions to exist at certain radii in the accretion disc is evidently related to the temperature profile of the disc. For instance, the Balmer emission lines typically occur at $\sim$ 10 000 – 15 000 K, with more and more of the H atoms being ionized at higher temperatures closer to the WD. Balmer emission from regions very close to the hot WD is therefore very unlikely. As a result of this consideration, the Keplerian velocity derived from the wing limits of an emission line will correspond to the maximum Keplerian velocity in the accretion disc for *the region in the disc from where the particular emission line originates.*

The FWZI for the "main component" of He II λ4686 is $\sim$ 1380 km s^{-1}. This implies radial velocities of $\sim$ 690 km s^{-1} towards and away from the observer for the He II emission regions in the accretion disc that are rotating at the highest speeds. Compensating for the inclination of the system by dividing by $\sin 25°$, yields an azimuthal speed of $\sim$ 1630 km s^{-1} in the accretion disc. Substituting this value into

Eq. (2.34) yields

$$R = \frac{GM_1}{v_K^2} = 6.49 \times 10^9 \left(\frac{M_1}{1.3M_\odot}\right) \left(\frac{v_K}{1.630 \times 10^8 \text{ cm s}^{-1}}\right)^{-2} \text{ cm} = 16.2R_{WD} \ , \tag{6.8}$$

where R_{WD} is the radius of the degenerate white dwarf core as determined from its mass. Therefore the measured radial velocity corresponds to a Keplerian orbit at a radius of $16.2R_{WD}$. Because larger radii imply smaller Keplerian velocities, this value represents a lower limit to the He II emission region of the accretion disc.

A similar analysis for the Hβ line yields $R \sim 18R_{WD}$. For the Hα profile, $R = 11.5R_{WD}$.

From Eq. (2.32), the circularization radius is

$$\begin{aligned} R_{circ} &= a(1+q)(0.500 - 0.227 \log q)^4 \\ &= (5.4 \times 10^{11} \text{ cm})(1 + 0.38)(0.500 - 0.227 \log 0.38)^4 \\ &= 9.4 \times 10^{10} \text{ cm} \\ &= 235R_{WD} \ , \end{aligned} \tag{6.9}$$

and Eq. (2.21) yields

$$\begin{aligned} R_{L,1} &= a\frac{0.49q^{-2/3}}{0.6q^{-2/3} + \ln\left(1 + q^{-1/3}\right)} \\ &= (5.4 \times 10^{11} \text{ cm})\frac{0.49(0.38)^{-2/3}}{0.6(0.38)^{-2/3} + \ln\left(1 + (0.38)^{-1/3}\right)} \\ &= 2.5 \times 10^{11} \text{ cm} \\ &= 630R_{WD} \end{aligned} \tag{6.10}$$

for the radius of the Roche lobe of the primary WD. The Keplerian radii calculated above can now be compared to the values of R_{circ} and $R_{L,1}$ in order to construct an idea of whether the calculated Keplerian radii are compatible with the approximate regions in the system where an accretion disc can be expected.

The Keplerian radii exceed the radius of the white dwarf by a factor of > 10, and are much smaller than the circularization radius and Roche lobe radius of the WD. The calculated Keplerian radii are therefore consistent with emission from an accretion disc around a white dwarf in CAL 83.

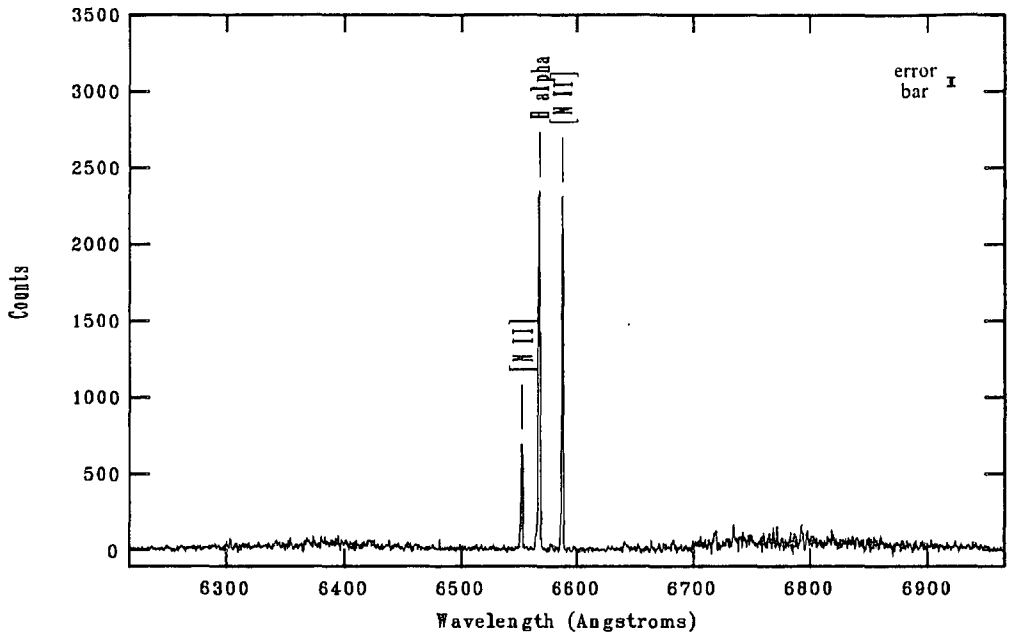

Fig. 6.8: Average N67 spectrum recorded with the 1.9-m Grating Spectrograph. The spectral resolution is $\sim$ 1 Å. The error bar indicates a typical 1σ error level on either side of a data point.

ID	Lab λ	$T(\epsilon_i)$	$T(\lambda)$	Δv	W_λ	FWHM		FWZI	
	(Å)	(K)	(K)	(km/s)	(Å)	(Å)	(km/s)	(Å)	(km/s)
[N II]	6548.05	168 500	14 650	158	-87.7	1.21	55.4	5.50	251
Hα	6562.82	-	14 610	155	-344.3	1.46	66.7	6.25	286
[N II]	6583.45	168 500	14 570	156	-316.6	1.13	51.5	5.31	242

Table 6.9: N67 emission lines detected with the 1.9-m Grating Spectrograph. The parameters were derived by fitting a Gaussian profile to each emission line. Δv represents the heliocentric velocity shift of the measured line from its laboratory wavelength. The FWHM and FWZI values were corrected for the effect of instrumental broadening with Eq. (6.1), using $\delta = 1$ Å.

6.7 N67

6.7.1 Results

The two N67 spectra obtained on 18 September 2011 were averaged to a single spectrum. Three strong emission lines are present. The lines were identified as Hα and two [N II] lines by consulting the line identification table for this source compiled by Meatheringham and Dopita (1991). The average spectrum is shown in Fig. 6.8, and the lines are plotted in terms of velocity in Fig. 6.9. The measurements of the line profiles are given in Table 6.9. The spectral resolution is $\sim$ 1 Å, which corresponds to $\sim$ 46 km s^{-1}.

The average shift of the lines from their laboratory wavelengths, after heliocentric

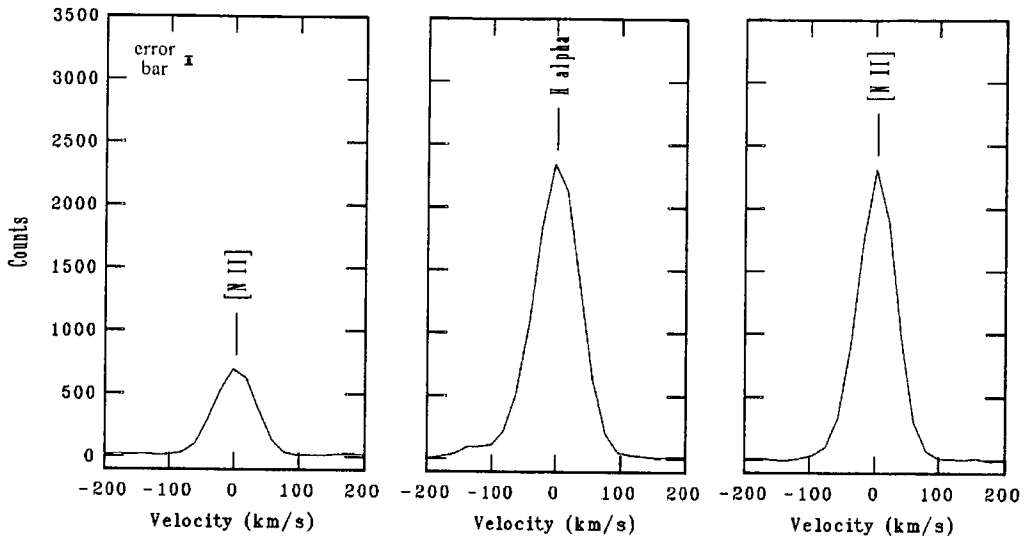

Fig. 6.9: The [N II] λ6548, Hα λ6563 and [N II] λ6583 emission lines (from left to right) of N67 detected with the 1.9-m Grating Spectrograph, plotted in terms of velocity relative to the centres of these lines. The spectral resolution is $\sim$ 46 km s^{-1}. The error bar indicates a typical 1σ error level on either side of a data point.

corrections, is 156 km s^{-1}, and considering the velocity resolution of our spectra ($\sim$ 46 km s^{-1}), this is in good agreement with the value of 145.6 $\pm$ 0.6 km s^{-1} obtained by Harris and Zaritsky (2006) for the heliocentric radial velocity of the SMC.

6.7.2 Discussion

These emission lines are thought to originate in the expanding nebular region. Pressure broadening of the Hα emission line is not expected to be important here, due to the low densities in the nebula. The thermal broadening FWHM for Hα at 10 000 K is 0.47 Å, and at 15 000 K the FWHM is 0.57 Å.

The temperature required for the initial ionization of N I to N II is $\sim$ 168 700 K. In Section 5.3, a range of different possible temperatures were quoted for the nucleus of N67, e.g. $\sim$ 13.3 eV ($\sim$ 154 000 K) derived from XMM-Newton data, and $\sim$ 34.5 eV ($\sim$ 400 000 K) derived from ROSAT data. These temperatures show that the ionization of N I to N II by radiation from the nucleus is therefore quite plausible.

The nebular electron temperature derived from the [N II] and [O III] lines by Meatheringham and Dopita (1991) is $\sim (1-3) \times 10^4$ K, which yields a thermal broadening FWHM of $\sim$ 0.2 Å for [N II]. The thermal broadening FWHM for [N II] at much higher temperatures of up to $\sim$ 343 600 K, at which ionization to N III will commence, is $\sim$ 0.8 Å. Pressure broadening is assumed to be negligible due to the low density of the nebula and the large atomic mass of N atoms.

Emission line	Thermal FWHM (Å)	Corrected FWHM (Å)[a]	V_{exp} (km/s)[b]
[N II] λ6548	$\sim 0.2 - 0.8$	$\sim 0.91 - 1.19$	$\sim 21 - 27$
Hα λ6563	$\sim 0.47 - 0.57$	$\sim 1.34 - 1.38$	$\sim 31 - 32$
[N II] λ6583	$\sim 0.2 - 0.8$	$\sim 0.80 - 1.11$	$\sim 18 - 25$

Table 6.10: Calculation of N67 expansion velocity from FWHM values measured with the 1.9-m Grating Spectrograph.
[a] Corrected for instrumental and thermal broadening.
[b] $V_{exp} = 0.5$ FWHM

Based on theoretical considerations, the expansion velocity of an unresolved nebula can be expressed in terms of the FWHM corrected for instrumental and thermal broadening by $V_{exp} = 0.5$ FWHM (see Stanghellini et al. 1999 and references therein). In order to calculate expansion velocities, the estimated thermal broadening was subtracted from the instrumental broadening corrected FWHM values in Table 6.9 by utilizing Eq. (6.1) again, this time substituting the thermal broadening FWHM into δ. V_{exp} was consequently calculated from the final corrected FWHM for each emission line. The results are presented in Table 6.10. The calculated values of V_{exp} are relatively close to the previously reported nebular expansion velocity of 27.9 km s^{-1}.

6.8 RR Telescopii

6.8.1 Results

A broadband medium-resolution and a blue high-resolution spectrum of RR Tel were obtained by combining the RSS pg0900 and pg3000 spectra of 27 June 2011 respectively, and the average spectra are shown in Fig. 6.10. Another blue spectrum and a red spectrum were obtained by combining the blue and red spectra recorded with the 1.9-m Grating Spectrograph on 18 September 2011, and these are shown in Fig. 6.11 and Fig. 6.12.

All the spectra exhibit a collection of strong nebular emission lines that are characteristic of RR Tel. The spectra were searched for the Raman-scattered emission components discussed in Section 5.4.2, i.e. the scattered components of the O VI λ1032 and λ1038 doublet at ~6830 Å and ~7088 Å, the scattered components of He II λ972 and λ949 at 4851 Å and 4332 Å, and the scattered component of C III λ977 at 4977 Å.

The Raman-scattered components of He II and C III were not detected in our spectra. However, the strong, double-peaked Raman-scattered component of the O VI λ1032 line is present at 6828 Å in the red spectrum recorded with the 1.9-m

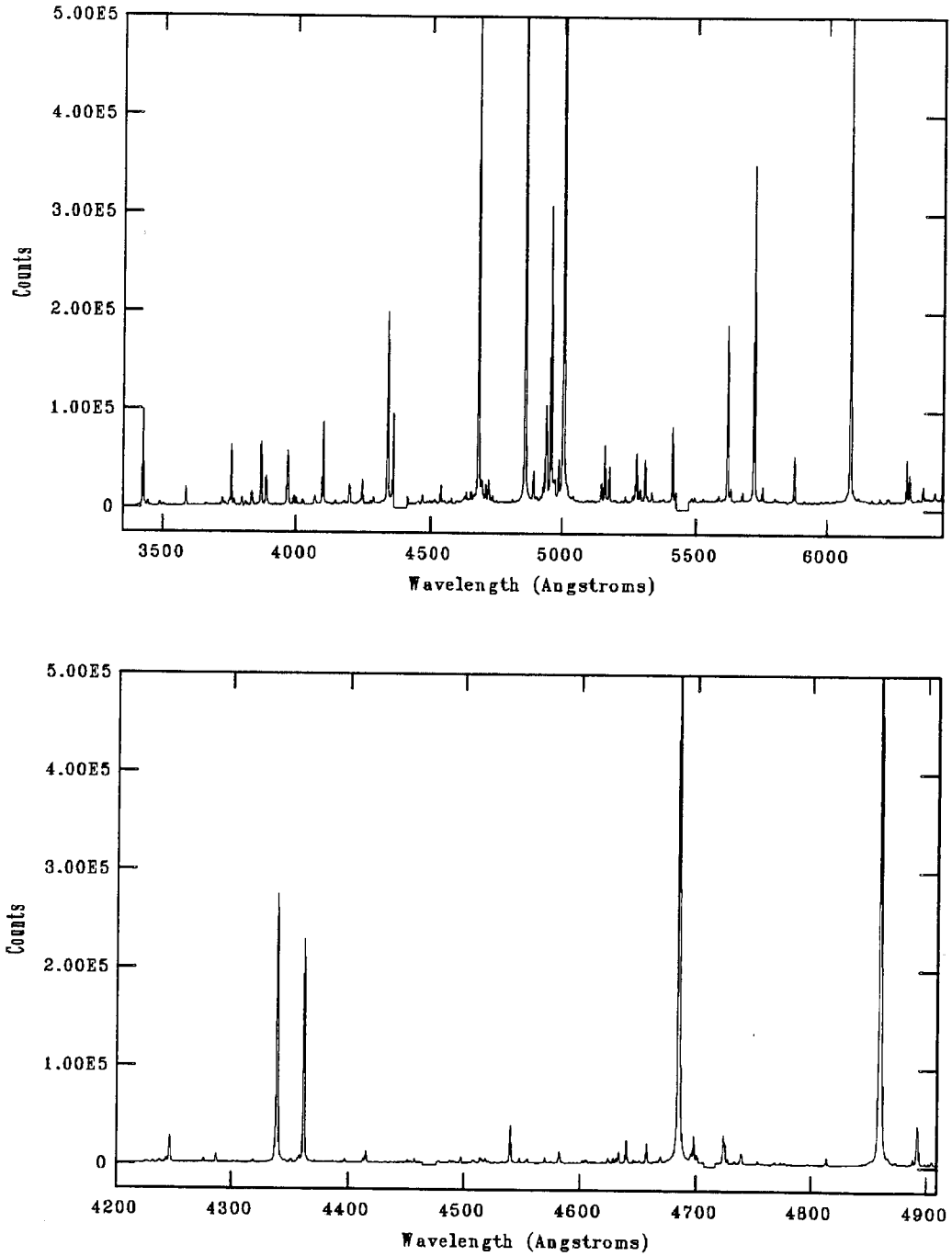

Fig. 6.10: Average spectra of RR Tel recorded with the RSS. Top: pg0900 spectrum (spectral resolution ~ 3.8 Å). Bottom: pg3000 spectrum (spectral resolution ~ 0.8 Å). The strongest emission lines have been truncated.

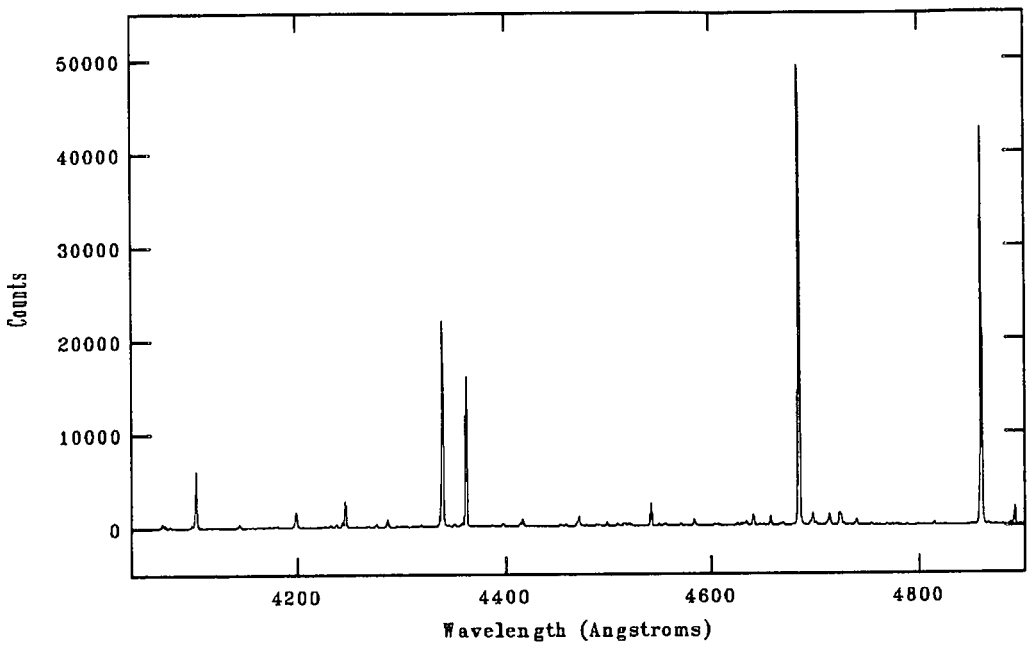

Fig. 6.11: Average blue spectrum of RR Tel recorded with the 1.9-m Grating Spectrograph. The spectral resolution is ~ 1 Å.

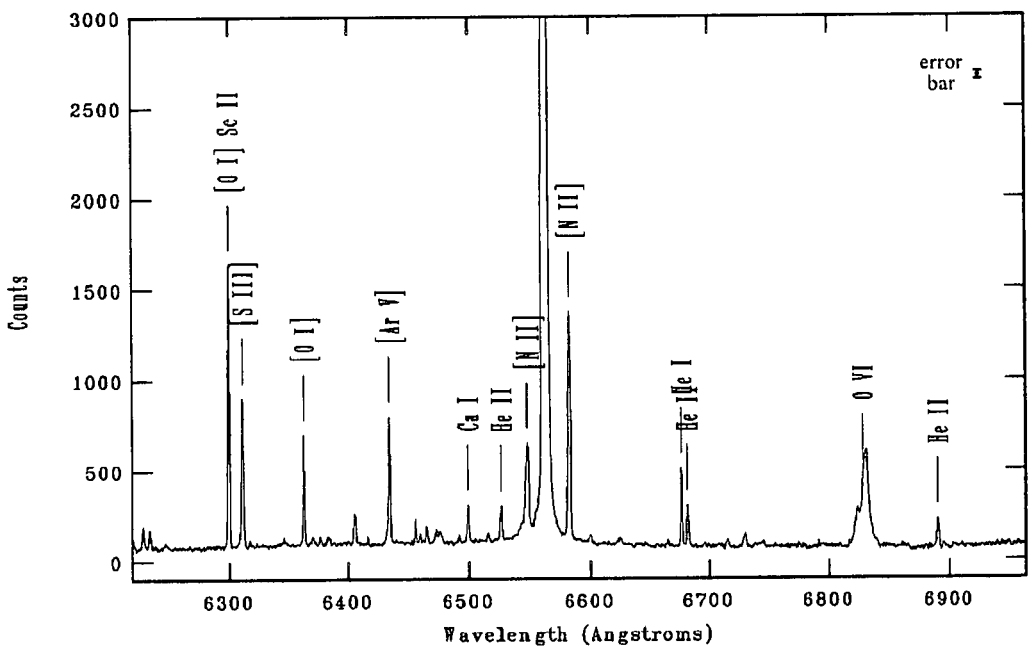

Fig. 6.12: Average red spectrum of RR Tel recorded with the 1.9-m Grating Spectrograph, with the identities of the strongest emission lines indicated. The spectral resolution is ~ 1 Å. The Hα emission line has been truncated. The error bar indicates a typical 1σ error level on either side of a data point.

ID	Lab λ (Å)	$T(\epsilon_i)$ (K)	$T(\lambda)$ (K)	Δv (km/s)
[O I]	~ 6300 [a]	–	15 220	
Sc II		75 900		
[S III]	6312.06	271 400	15 190	-64.6
[O I]	6363.88	–	15 070	-66.4
[Ar V]	6435.10	693 600	14 900	-66.5
Ca I	6499.65	–	14 750	-37.8
He II	6527.12	285 100	14 690	-66.7
[N II]	6548.05	168 500	14 650	-66.1
Hα	6562.82	–	14 610	-65.5
[N II]	6583.45	168 500	14 570	-67.8
He I	6678.15	–	14 360	-66.0
He II	6683.23	285 100	14 350	-88.7
O VI (Raman)		1 321 000	92 930[b]	
He II	6890.88	285 100	13 920	-60.3

Table 6.11: Identification of the strongest emission lines in the red 1.9-m Grating Spectrograph spectrum of RR Tel.
[a]Blend.
[b]Temperature corresponding to wavelength of 1032 Å unscattered photons.

Grating Spectrograph (Fig. 6.12). The discussion in this section will therefore focus on the analysis of this spectrum, in particular on the double-peaked O VI line, which is the main feature of interest. Our spectra did not extend to 7088 Å, therefore we were unable to verify whether the scattered component of O VI λ1038 was present.

For the current purposes, only the strongest emission lines in the red spectrum were identified by comparing our spectrum to the line lists of McKenna et al. (1997) and Kotnik-Karuza et al. (2009). The identified lines are listed in Table 6.11. The mean heliocentric velocity shift of the emission lines is -65.1 km s^{-1}, which is close to the value of -62.3 km s^{-1} quoted in Section 5.4. The resolution of the red spectrum is ~ 1 Å, corresponding to ~ 46 km s^{-1}. The FWZI values for the emission lines (except for Hα and O VI) range between $\sim 100 - 200$ km s^{-1}.

A blend of two Gaussian profiles was fit to the double-peaked, Raman-scattered O VI feature at 6828 Å, and from the fit the FWZI (corrected for instrumental broadening) was determined to be ~ 26.9 Å, corresponding to ~ 1180 km s^{-1}. Because the wavelength shift of each photon is amplified by a factor of ~ 6.7 during the scattering process, the FWZI of the original O VI λ1032 line was ~ 4.0 Å (still corresponding to ~ 1180 km s^{-1}). The red peak is considerably stronger than the blue peak.

In Fig. 6.13, the [O I] λ6364 line and the Raman-scattered O VI line are plotted in terms of velocity dispersion, and the broad structure of the O VI line relative to the

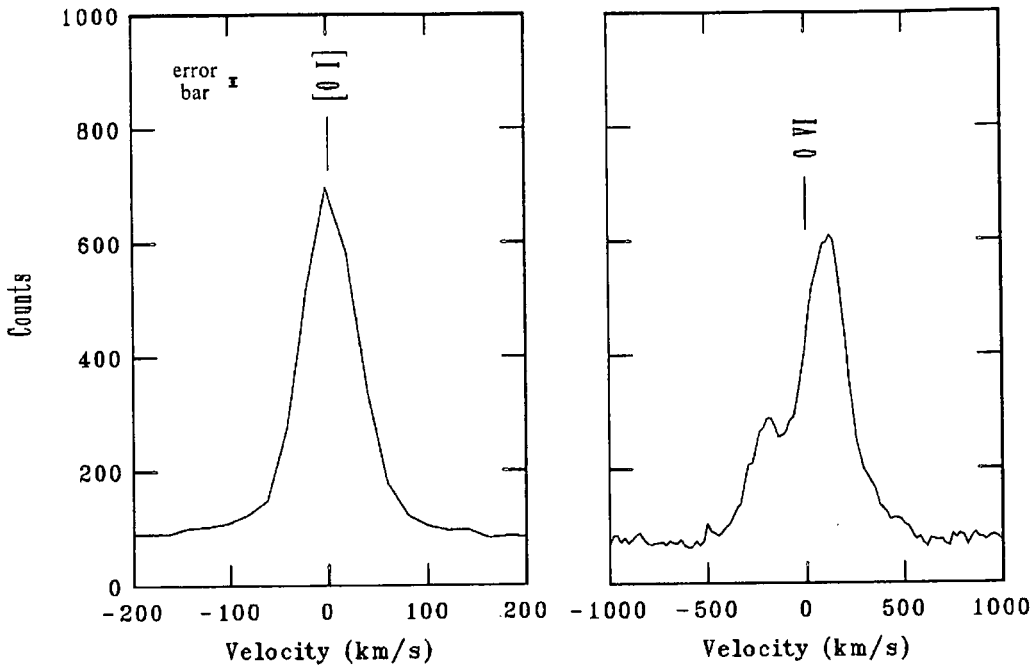

Fig. 6.13: The nebular [O I] λ6364 emission line (left) and the Raman-scattered O VI λ6828 emission line (right) of RR Tel. Note the wide, double-peaked structure of the O VI line compared to the typical width of a nebular line. The spectral resolution is ~ 46 km s^{-1}. The error bar indicates a typical 1σ error level on either side of a data point.

nebular [O I] line becomes evident. By fitting a Gaussian profile to the [O I] line, it was determined that the FWHM is 0.97 Å (corrected for instrumental broadening).

The Hα emission line has very broad wings, extending to ~ 1000 km s^{-1} to either side of the central wavelength. This was ascribed to Raman scattering of Lβ photons by H I (Lee, 2000).

6.8.2 Discussion

The presence of the double-peaked Raman-scattered O VI feature provides strong evidence for the presence of an accretion disc in RR Tel, as explained by Lee and Park (1999). The high strength of the red peak relative to the blue peak can be explained by the higher mass concentration in the red emission region (RER) compared to the blue emission region (BER), possibly due to the ballistic accretion stream impinging on the RER segment of the disc (see Fig. 5.14). Because the Raman-scattered O VI line provides us with a view of the system from the perspective of the secondary star, regardless of the orbital phase, such a configuration will always cause an enhancement in the strength of the red peak relative to the blue peak. The velocity width of the Raman-scattered O VI line associated with the high Keplerian speeds in the accretion disc is notably larger than the width of the other emission lines that

originate in the expanding nebular "shell" around the source (refer to Fig. 5.14).

The ionization temperature required for initially ionizing O V to O VI is $\sim$ 1 321 000 K, implying that there is or must have been a hot X-ray component in the emission from the WD, even though the soft spectrum dominates. Jordan et al. (1994) did find a hard component in the X-ray spectrum, which they ascribed to collisional shocks. Even at such high temperatures, the thermal broadening FWHM of O VI is < 0.25 Å. Thermal and pressure broadening is now assumed to be negligible compared to rotational broadening in the accretion disc, which is expected to introduce the dominant broadening effect.

The expansion velocity of the nebular region can be estimated from the FWHM of the [O I] λ6364 line in Fig. 6.13. The thermal broadening FWHM of this line at $T(\lambda) = 15\ 070$ K is 0.14 Å, and near the limit of 13.614 eV ($\sim$ 158 000 K) for ionization to O II, the thermal FWHM is 0.45 Å. Subtracting these values from the FWHM of 0.97 Å by means of Eq. (6.1) yields a corrected FWHM range of $0.86 - 0.96$ Å, which corresponds to an expansion velocity range of $20 - 23$ km s^{-1} according to $V_{\rm exp} = 0.5$ FWHM, which is comparable to the known expansion velocity of $V_{\rm exp} = 30$ km s^{-1} for RR Tel, given the current velocity resolution.

In analogy to the analysis that was performed for CAL 83, we will now proceed to estimate the relevant dimensions in the binary system that would constrain the size of an accretion disc. The Keplerian radius corresponding to the velocity width of the O VI line will be compared to these dimensions to evaluate the possible presence of an accretion disc in terms of the distances involved.

According to the literature review in Section 5.4, the mass of the WD in RR Tel is $M_1 \sim 0.9 M_\odot$, and the orbital period $P_{\rm orb} = 387$ d. The WD temperature is estimated to be $\sim$ 12.2 eV, corresponding to $\sim$ 142 000 K. The radius of the WD according to Eq.(4.3) is

$$R_{\rm WD} = 4.9 \times 10^8 \left(\frac{M_{\rm WD}}{M_\odot}\right)^{-0.8} \text{cm} = 5.3 \times 10^8 \left(\frac{M_1}{0.9 M_\odot}\right)^{-0.8} \text{cm} . \qquad (6.11)$$

The *photospheric* radius reported for the WD and its shell is 6.3×10^9 cm. As the secondary star is thought to be a Mira variable, a typical mass estimate of the secondary will be $M_2 \sim 1 - 2 M_\odot$ (e.g. Wyatt and Cahn 1983). Adopting $M_2 \sim 1.5 M_\odot$ (implying $q \sim 1.7$), the binary separation is of the order

$$a = \left[\frac{G(M_1 + M_2) P_{\rm orb}^2}{4\pi^2}\right]^{1/3} = 2.1 \times 10^{13} \left(\frac{M_1 + M_2}{2.4 M_\odot}\right)^{1/3} \left(\frac{P_{\rm orb}}{387\ \text{d}}\right)^{2/3} \text{cm} , \quad (6.12)$$

using Eq. (2.1). It follows that

$$a_1 = \frac{M_2}{M_1 + M_2} a = 1.3 \times 10^{13} \left(\frac{M_2}{1.5 M_\odot}\right) \left(\frac{M_1 + M_2}{2.4 M_\odot}\right)^{-1} \left(\frac{a}{2.1 \times 10^{13}\ \mathrm{cm}}\right) \ \mathrm{cm} \tag{6.13}$$

and hence

$$a_2 = a - a_1 = (2.1 - 1.3) \times 10^{13}\ \mathrm{cm} = 8 \times 10^{12}\ \mathrm{cm}. \tag{6.14}$$

From Eq. (2.32), the circularization radius is

$$\begin{aligned} R_{\mathrm{circ}} &= a(1+q)(0.500 - 0.227 \log q)^4 \\ &= (2.1 \times 10^{13}\ \mathrm{cm})(1 + 1.7)(0.500 - 0.227 \log 1.7)^4 \\ &= 2.3 \times 10^{12}\ \mathrm{cm} \\ &= 4300 R_{\mathrm{WD}}\ , \end{aligned} \tag{6.15}$$

and using Eq. (2.21) yields

$$\begin{aligned} R_{\mathrm{L},1} &= a \frac{0.49 q^{-2/3}}{0.6 q^{-2/3} + \ln\left(1 + q^{-1/3}\right)} \\ &= (2.1 \times 10^{13}\ \mathrm{cm}) \frac{0.49 (1.7)^{-2/3}}{0.6 (1.7)^{-2/3} + \ln\left(1 + (1.7)^{-1/3}\right)} \\ &= 7.0 \times 10^{12}\ \mathrm{cm} \\ &= 13000 R_{\mathrm{WD}} \end{aligned} \tag{6.16}$$

for the radius of the Roche lobe of the primary WD.

Because the double-peaked Raman-scattered O VI emission feature at 6828 Å is thought to be the result of scattering by neutral hydrogen close to the companion star, it will be assumed that these scatterers are viewing the disc at an inclination angle of 90°.

From the FWZI of $\sim$ 1180 km s^{-1}, the upper limit for the Keplerian velocity in the disc is therefore $\sim$ 590 km s^{-1}, yielding a lower limit for the radius of the O VI emitting region of

$$R = \frac{G M_1}{v_{\mathrm{K}}^2} = 3.4 \times 10^{10} \left(\frac{M_1}{0.9 M_\odot}\right) \left(\frac{v_{\mathrm{K}}}{5.90 \times 10^7\ \mathrm{cm\ s^{-1}}}\right)^{-2} \ \mathrm{cm} = 64 R_{\mathrm{WD}}\ . \tag{6.17}$$

Once again the calculated Keplerian radius can be compared to the values of R_{circ} and $R_{\mathrm{L},1}$ to get a qualitative indication of whether the Keplerian radius is in the range of what can be expected for an accretion disc in RR Tel. The Keplerian radius is significantly larger than the radius of the WD, but orders of magnitude smaller than the circularization radius and the Roche lobe radius of the WD. The broad-

ened. double-peaked profile of the detected O VI line is therefore consistent with emission from an accretion disc well inside the Roche lobe of the white dwarf.

In addition to the analysis of optical spectra that was discussed in this chapter, spectral and timing analysis of archived *Chandra* and XMM-Newton data were also performed. In the next chapter, the X-ray component of our observational investigation is presented for two sources: SMC 13 and CAL 83.

Chapter 7

X-ray data analysis

In this chapter, the results of the analysis of archived X-ray data of the supersoft X-ray sources SMC 13 and CAL 83 are presented. The nature of the soft X-ray spectrum of SMC 13 is investigated by fitting a simple model to *Chandra* data, and the strong variations in the X-ray light curve is also considered. For CAL 83, the results of a systematic search for short time-scale periodicity in archived X-ray data is presented. The chapter is therefore divided into two main sections: in Section 7.1, the X-ray data analysis for SMC 13 is discussed, while the timing analysis of XMM-Newton data of CAL 83 is presented in Section 7.2. Each of these two sections are structured as follows: A brief overview of the relevant X-ray telescope is provided, followed by a summary of the observations and the data calibration procedures. The last part of each section consists of an overview of the relevant data analysis methods, directly followed by the results and discussion for each source.

7.1 *Chandra* observations of SMC 13

7.1.1 The *Chandra* X-ray Observatory

The *Chandra* X-ray Observatory was launched by NASA in 1999. It is in a high Earth orbit, completing one orbit in 63.5 hours. This makes uninterrupted observations of up to $\sim$ 47 hours possible. *Chandra* consists of a spacecraft, a telescope and a science instrument payload with high sensitivity and resolution. Detailed information can be found on the *Chandra* website[1], and The *Chandra* Proposers' Observatory Guide (*Chandra* X-ray Center, 2011).

The main components of *Chandra* are illustrated in Fig. 7.1. The High Resolution Mirror Assembly (HRMA) consists of a set of four nested grazing-incidence Wolter Type-I mirrors. The Pointing Control and Aspect Determination System (PCAD) controls the pointing and dithering of the telescope during observations. The focal plane science instruments are the Advanced CCD Imaging Spectrometer (ACIS) and

[1] `http://chandra.si.edu`

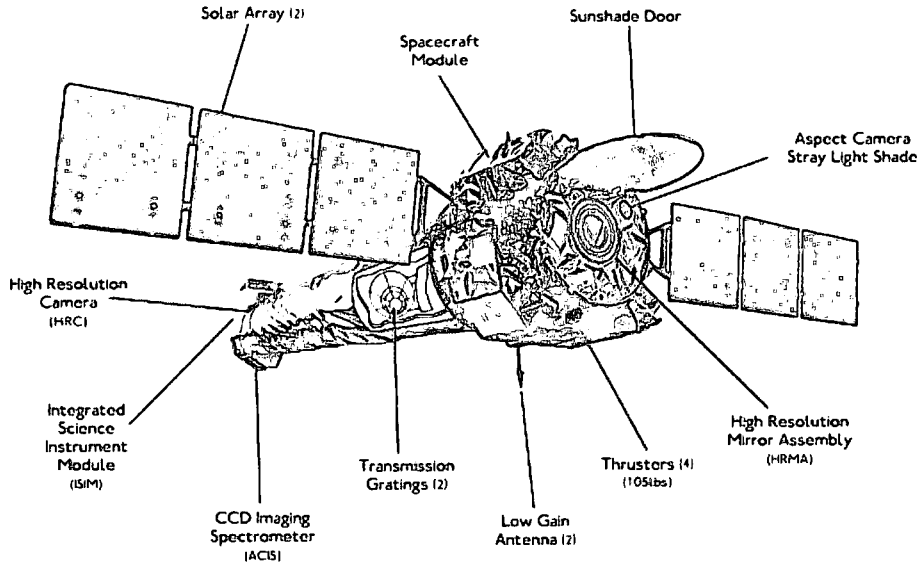

Fig. 7.1: The *Chandra* X-ray Observatory. (Adopted from `http://www-xray.ast.cam.ac.uk/xray_introduction/Chandra.html`, Cambridge X-ray Astronomy 2005.)

the High Resolution Camera (HRC). Two transmission gratings are available for use with these CCD's, namely the LETG (Low Energy Transmission Grating) and the HETG (High Energy Transmission Grating).

The intrinsic energy resolution of the ACIS detectors provides the ability to obtain high-resolution images and medium-resolution spectra simultaneously. ACIS consists of two CCD arrays. Four chips arranged in a 2x2 array comprise ACIS-I, which is used for imaging, and another six chips in a 1x6 array comprise ACIS-S, which is used for either imaging or with the HETG (or LETG) for high-resolution spectroscopy. Any combination of up to 6 of the CCD's can be used simultaneously. There are two different operating modes for ACIS. The first is Timed Exposure (TE) mode, which enables the readout of a full CCD chip at a nominal frame time of 3.2 s, or only a sub-array of a CCD chip at a higher time resolution. The second operating mode is Continuous Clocking (CC) mode, which provides a time resolution of 3 ms at the expense of one dimension of spatial resolution. Several telemetry formats are also available.

The HRC also has two components: HRC-I which is used for wide-field imaging, and HRC-S which is used with the LETG for grating spectroscopy at low energies.

Only ACIS-S, HRC-S and the LETG were used in the observations discussed in this chapter, and more technical information on these instruments are provided in the tables in Appendix D.

Obs ID	Instrument	Start date and time (UT)	Mode	Exposure time (ks)	PI[a]
4535	ACIS-S3	2005-01-30 16:56:17	VFAINT TE	40.14	J. Greiner
7456	HRC-S+LETG	2007-02-12 18:25:16		40.19	T. Lanz
8519	HRC-S+LETG	2007-02-18 00:42:08		42.67	T. Lanz

Table 7.1: *Chandra* observations of SMC 13.
[a]Principal Investigator.

7.1.2 Observations

In this chapter, three archived *Chandra* observations of the supersoft source SMC 13 will be discussed. One observation used ACIS-S (more specifically, the ACIS-S3 chip), without a grating, in TE mode, with the telemetry format being VFAINT (Very Faint), which is appropriate for observing very faint sources. The other two observations were performed with HRC-S+LETG. A summary of the observations is provided in Table 7.1. According to our knowledge, no results have so far been published on these observations.

7.1.3 Data calibration

The calibration of the data was carried out by following standard data calibration procedures with the CIAO (*Chandra* Interactive Analysis of Observations) software, Version 4.3, using Version 4.4.5 of the CALDB (CIAO Calibration Database). The CIAO website[2] and Fruscione et al. (2006) can be consulted for more detail.

The initial reduction of the data sets were performed by using the **chandra_repro** script, which produces a new level=2 event file with the latest available calibrations applied, as well as a new level=2 Type II PHA file for grating data.

7.1.4 Spectral analysis

Spectral extraction

The source region for the ACIS-S data was defined as a circle with a radius of 4.92″ centred on the source position, which is expected to contain $\sim$ 98% of the source photons. A concentric annulus with an inner radius of 9.84″ pixels and an outer radius of 18.4″ was defined as a background region. The area of the background annulus is therefore 10 times the area of the source region, and the background level derived from the annulus was scaled by a factor of $\frac{1}{10}$ during all further analysis procedures. The CIAO task **specextract** was used to extract a source spectrum (including background) and a background spectrum, as well as the necessary response-files necessary to translate detector counts to an absolute flux level: an ARF

[2]`http://cxc.harvard.edu/ciao4.4/index.html`

(Ancillary Response File) and an RMF (Response Matrix File).

For the LETG observations, a standard extraction region in the form of a bow-tie was used to extract the source spectrum (including background) from the dispersed spectrum recorded with the HRC-S. The intrinsic energy resolution of the HRC-S detector is not sufficient to distinguish between first-order and higher-order diffracted photons, therefore only two source spectra were extracted for each LETG observation: one containing all the negative orders and one containing all the positive orders. Background counts were obtained from regions on the detector on the outer sides ("top" and "bottom") of the bow-tie source region, and one background spectrum was created for the negative orders and one for the positive orders. The tasks **mkgrmf** and **mkgarf** were utilized to create RMF's and ARF's for the first three positive and negative orders of the grating data.

Blackbody model fitting

A simple absorbed blackbody model was fitted to observations 7456 and 8519 with the spectral fitting program ISIS (Interactive Spectral Interpretation System), Version 1.6.1-26. Relevant information related to this software can be found on the ISIS website[3] and also in the ISIS 1.0 Technical Manual (Houck, 2010). Some of the functions in the custom S-lang scripts[4] of Nowak (2011) were also used in conjunction with ISIS.

Each observation was analysed separately. For each of them, the source+background and the background spectra in the positive and negative orders, as well as the response files for the first three positive and negative orders, were loaded into ISIS, and the positive and negative orders were fitted simultaneously. Although the first and higher orders can not be separated with the HRC-S energy resolution, higher orders can still be accounted for by using higher-order response files during the fitting procedure.

The spectral range extends from 0.08 to 10 keV, but the source spectrum was only detected in the $0.165 - 0.827$ keV ($15 - 75$ Å) range, and only this interval was considered during the fitting procedure. There are two plate gaps in the HRC-S detector, yielding zero counts for two intervals positioned near -50 Å and 60 Å. Electrical field-fringing effects in the few bins bordering on a plate gap can lead to high background in these regions. Therefore the gap regions, as well as a few channels on both sides of each gap, were ignored during the fitting procedure. The spectra were rebinned by a factor of 50, i.e. the channels were added together in groups of 50 each

[3] `http://space.mit.edu/cxc/isis/`

[4] `http://space.mit.edu/home/mnowak/isis_vs_xspec/download.html`

to increase the S/N. This lowered the spectral resolution to ~ 2.5 Å.

The fits were performed with the **lmdif** fitting algorithm, which is a variant of the Levenberg-Marquardt minimization algorithm. This algorithm is based on the minimization of the χ^2 fit statistic, which is given by (e.g. Arnaud, Dorman and Gordon 2011)

$$\chi^2 = \sum_I \frac{[C(I) - C_{\rm p}(I)]^2}{[\sigma(I)]^2} \ . \tag{7.1}$$

The parameter I depicts a certain instrument channel, with $C(I)$ representing the measured counts in channel I and $C_{\rm p}(I)$ the predicted model counts in channel I. The error for channel I is given by $\sigma(I)$. The degrees of freedom (DOF) of the fit is defined as the number of channels minus the number of model parameters, and the "reduced χ^2" is defined as $\chi^2/{\rm DOF}$. A reduced χ^2 value close to 1 indicates a good fit, although the validity of the model also depends, of course, on whether it provides a scientifically feasible interpretation.

Two fits were performed for each observation: one with the column density $N_{\rm H}$ as a free parameter, and one with $N_{\rm H}$ fixed at the galactic value of 6.94×10^{20} cm^{-2} quoted in Section 5.2. The background level was not *subtracted* prior to the fitting, but was incorporated and accounted for during the fitting procedure.

Because the response of the ACIS-S detector can only be calibrated down to 0.245 keV (50.6 Å), conclusive fit parameters were not obtained for observation 4535. Therefore the spectral fitting of observation 4535 is not discussed here.

Results

The spectra of observations 7456 and 8519 are shown in Fig. 7.2, with the best-fit absorbed blackbody models overplotted (for the fits with $N_{\rm H}$ fixed at 6.94×10^{20} cm^{-2}). The best-fitting parameters are shown in Table 7.2.

The parameters $kT_{\rm eff}$, $N_{\rm H}$ and $F_{\rm u}$ were measured from the data, while $L_{\rm bol}$, R and $M_{\rm WD}$ were obtained from further calculations. The bolometric luminosity is related to the bolometric flux by $L_{\rm bol} = 4\pi D^2 F_{\rm u}$. Hilditch, Howarth and Harries (2005) determined the mean distance to the SMC to be $D = 60.6 \pm 2.8$ kpc. Therefore, for SMC 13,

$$L_{\rm bol} = 4.39 \times 10^{47} \ {\rm cm}^2 \left(\frac{D}{60.6 \ {\rm kpc}} \right)^2 \times F_{\rm u} \ , \tag{7.2}$$

where 1 pc $= 3.086 \times 10^{18}$ cm, yielding the values presented in Table 7.2. The photospheric radius R corresponding to each fit was calculated from the bolometric luminosity and effective temperature by means of Eq. (2.112).

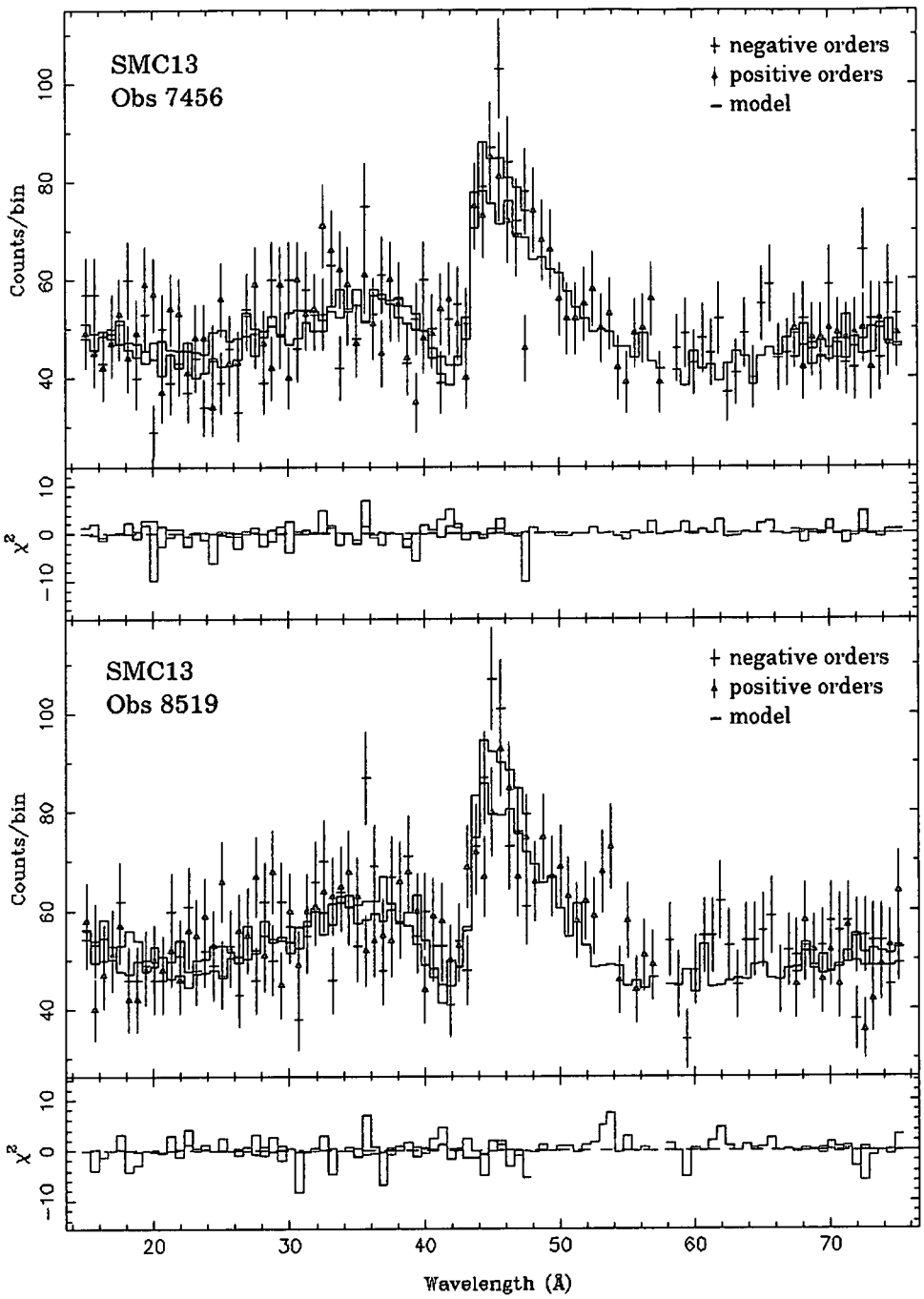

Fig. 7.2: *Chandra* LETG spectra of SMC 13: observation 7456 (top) and 8519 (bottom). For each observation, the best-fitting absorbed blackbody model with $N_{\rm H}$ fixed at 6.94×10^{20} cm^{-2} is overplotted. The fit parameters are presented in columns (2) and (4) respectively in Table 7.2. A single model produces two slightly different count profiles when folded through the responses of the different grating orders, which are seen as the two slightly different model curves for each spectrum. The gap in each of the spectra is due to the spaces between the HRC-S detectors.

Parameter	Obs 7456		Obs 8519	
	$N_{\rm H}$ free	$N_{\rm H}$ fixed	$N_{\rm H}$ free	$N_{\rm H}$ fixed
	(1)	(2)	(3)	(4)
$kT_{\rm eff}$ (eV)	$34.4\ ^{+5.2}_{-4.5}$	$32.5\ \pm 1.8$	$44.8\ ^{+5.2}_{-4.8}$	$35.0\ ^{+1.9}_{-1.8}$
$N_{\rm H}$ (10^{20} cm^{-2})	$6.12\ ^{+1.89}_{-1.54}$	6.94	$3.81\ ^{+1.17}_{-0.95}$	6.94
$F_{\rm u}$ [a] (10^{-10} erg cm^{-2} s^{-1})	$1.24\ ^{+3.34}_{-0.79}$	$2.15\ ^{+0.77}_{-0.49}$	$0.24\ ^{+0.25}_{-0.10}$	$1.56\ ^{+0.47}_{-0.32}$
$L_{\rm bol}$ (10^{37} erg s^{-1})	$5.44\ ^{+14.68}_{-3.45}$	$9.42\ ^{+3.38}_{-2.14}$	$1.05\ ^{+1.08}_{-0.44}$	$6.83\ ^{+2.08}_{-1.41}$
R (10^9 cm)	$1.73\ ^{+2.38}_{-0.76}$	$2.55\ ^{+0.54}_{-0.41}$	$0.45\ ^{+0.25}_{-0.14}$	$1.88\ ^{+0.34}_{-0.28}$
$M_{\rm WD}/M_\odot$ (for $R_{\rm WD} = R$)	$0.21\ ^{+0.23}_{-0.13}$	$0.13\ ^{+0.16}_{-0.10}$	$1.12\ ^{+1.77}_{-0.64}$	$0.18\ ^{+0.23}_{-0.15}$
$M_{\rm WD}/M_\odot$ (for $R_{\rm WD} = \frac{1}{2}R$)	$0.49\ ^{+1.01}_{-0.17}$	$0.30\ ^{+0.38}_{-0.24}$	$2.65\ ^{+4.22}_{-1.52}$ [b]	$0.44\ ^{+0.54}_{-0.36}$
χ^2/DOF	181.2045/159	181.743/160	181.6378/159	194.4119/160
	= 1.140	= 1.136	= 1.142	= 1.215

Table 7.2: Results of absorbed blackbody fits to *Chandra* HRC-S+LETG spectra of SMC 13. An SMC distance of 60.6 kpc was adopted. 90% confidence errors are given.
[a]Unabsorbed bolometric flux.
[b]Impossible for a WD, as it is way above the Chandrasekhar limit of $1.4M_\odot$.

Estimates of the WD mass were obtained with Eq. (4.3) for two cases: first by assuming that the WD radius is equal to the calculated photospheric radius ($R_{\rm WD} = R$), and then by assuming that the WD radius is half the photospheric radius ($R_{\rm WD} = \frac{1}{2}R$).

The determined masses for observation 8519 with $N_{\rm H}$ as a free parameter (data column (3) in Table 7.2) are obviously much larger than for the other fits, and for ($R_{\rm WD} = \frac{1}{2}R$) a mass of $2.65M_\odot$ is obtained, which significantly exceeds the Chandrasekhar mass. It is also noted that the value of $N_{\rm H}$ for this spectral fit is much smaller than the galactic value in the direction of the SMC, while the 7456 fit with $N_{\rm H}$ as a free parameter does yield a more credible value for $N_{\rm H}$ (column (1)). However, the fact that a blackbody model is only a crude estimate for the underlying spectrum, leads us to the conclusion that the fits where $N_{\rm H}$ is fixed to the known value of 6.94×10^{20} cm^{-2} will yield more credible results than those where $N_{\rm H}$ is allowed to vary as a free parameter. Therefore the fit results for $N_{\rm H} = 6.94 \times 10^{20}$ cm^{-2} in columns (2) and (4) are considered to be more appropriate.

Discussion

The average temperature of $\sim$ 34 eV derived from the blackbody fits in columns (2) and (4) of Table 7.2 is within the range of previously determined temperatures

reported in Section 5.2.

From the various considerations in Section 5.2, it seems that the mass of the WD in SMC 13 may be $\sim 0.6 M_{\odot}$. However, the values of $M_{\rm WD}$ in columns (2) and (4) seem to indicate a lower WD mass, even though the upper error limits for the masses corresponding to $R_{\rm WD} = \frac{1}{2}R$ do include $0.6 M_{\odot}$. If the size of the hydrogen burning shell contributes more than half of the photospheric radius, even smaller values of $R_{\rm WD}$ will obviously be obtained, yielding larger WD masses for our fit parameters.

The adopted test values for the WD radius ($R_{\rm WD} = R$ and $R_{\rm WD} = \frac{1}{2}R$) are only useful as estimations, because the exact contribution of the hydrogen burning layer to the photospheric radius is not known. However, the fact that Suleimanov and Ibragimov (2003) found $M_{\rm WD} \sim 0.65 - 0.85 M_{\odot}$ for $R_{\rm WD} = R$ implies that, if the mass of the WD is indeed $\sim 0.6 M_{\odot}$, the WD radius is very close to the photospheric radius.

When comparing the $L_{\rm bol}$ values determined from our blackbody fits to those in Section 5.2 (e.g. in Tables 5.9 and 5.10), it becomes evident that our $L_{\rm bol}$ values are larger than the previously reported values, especially when compared to the luminosities derived from the more sophisticated LTE and NLTE models. This confirms the issue that was mentioned earlier, namely that blackbody fits tend to overestimate the WD luminosity, because actual WD atmospheres are more efficient emitters of soft X-rays than blackbody emitters. The overestimation of $L_{\rm bol}$ translates to an underestimation of the WD mass.

Our spectra therefore await fitting with more sophisticated WD atmosphere models, and it is expected that these will yield more accurate parameters for the WD and the surrounding hydrogen burning region, including a slightly higher WD mass. At this stage, it can be concluded that the derived blackbody radii are compatible with emission from a hydrogen burning WD. Also, a WD mass of $0.6 M_{\odot}$ is not excluded by our fits and is quite plausible when considering the complications involved with a blackbody approximation.

7.1.5 Timing analysis

Procedure

The arrival times in the level=2 event files of the three observations were corrected to the solar system barycentre (in the TDB system) by using the CIAO task **axbary** with appropriate information on the orbit of the satellite and the position of the target. Consequently, **dmextract** was used to create a background-subtracted light curve from the corrected event file of each observation.

For the ACIS observation (4535), the source and background regions described in the previous section were used. For the LETG observations (7456 and 8519), a source region with a radius of 5″ was defined, centred on the position of the zero-order grating image. A concentric annulus with an inner radius of 6.6″ and an outer radius of 13″ were used for the background, yielding an area equal to 5 times the source area, and the background values were scaled by a factor of $\frac{1}{5}$ in the extraction procedure.

The very weak intrinsic energy resolution of the HRC-S complicated defining clear-cut wavebands for light curves in different energy ranges. Therefore, for observations 7456 and 8519, the created light curves contain all the detected zero-order source photons in the range of the HRC-S ($\sim 0.08-10$ keV). For observation 4535, a similar light curve was created, containing all source photons in the range $\sim 0.14-10$ keV. However, as mentioned previously, the source spectrum is actually only detected in the $\sim 0.165-0.827$ keV range, therefore the three "broad-band" light curves mentioned above encompass essentially the same (complete) source spectrum.

The intrinsic energy resolution of the ACIS-S detector was used to create two additional light curves: one in the "soft" band ($0.100-0.250$ keV) and one in the "hard" band ($0.251-0.500$ keV), in order to compare the form of these light curves to that of the ROSAT light curves in Fig. 5.11. However, the hardness ratio was calculated in a different way than the ROSAT hardness ratio in Fig. 5.11, in order to suit the detectable energy range of SMC 13 covered by *Chandra* somewhat better. The hardness ratio was defined as HR=H/(H+S), where H is the number of counts above 0.5 keV and S is the number of counts below 0.5 keV.

Two different software packages were used for the timing analysis reported in this chapter. One is the Xronos Timing Analysis Software Package, which is part of the HEAsoft software distribution. Detailed discussions on the different Xronos tasks can be found in the Xronos User's Guide (HEASARC, 2009). The other is the Starlink PERIOD timing analysis package[5]. In this section, the software was used to search for an orbital period in the *Chandra* X-ray data around the period of 0.1718 d (4.123 h) found by Kahabka (1996a) in the ROSAT data.

The Xronos task **powspec** makes use of a discrete fourier transform (DFT) algorithm to create a power spectrum from binned light curves or from event files containing arrival times. The task **efsearch** can be used to search for periodicities around a given period P. The task folds the data over a range of periods and determines the χ^2 value for the folded light curve for each test period. The intrinsic

[5]http://www.starlink.rl.ac.uk/star/docs/sun167.htx/sun167.html

Fourier frequency resolution of a power spectrum is given by $\Delta f = 1/T$, where T is the total length of the data set. This translates to an uncertainty in the period over a range of

$$\Delta P = \frac{P^2}{T} \ , \tag{7.3}$$

or $\frac{1}{2}\Delta P$ to either side of P. The default spacing between consecutive **efsearch** test periods is $\frac{1}{2}\Delta P$. When the position of the strongest peak has been identified, the search period spacing can be made even smaller to determine the exact position of the peak centroid. However, doing this will of course not change the amount of uncertainty in the peak position, as the latter only depends on the total length of the data set.

The PERIOD task SCARGLE creates a Lomb-Scargle periodogram, which is designed for finding periodicities in unevenly sampled data (Lomb, 1976; Scargle, 1982).

A broad-band light curve with a binning of 100 s was created for each SMC 13 observation. Each separate light curve was detrended by normalizing to the mean, and then subtracting 1 to obtain a light curve varying about zero. Initially, **powspec** was used to create a power spectrum from each detrended light curve for each observation separately. Each of the power spectra exhibits a frequency peak at the approximate position of the orbital period. However, the uncertainty in the peak positions is very high, as Eq. (7.3) yields a very poor resolution of $\Delta P \sim 5500$ s when searching for periods around 0.1718 d in a data set with a length of ~ 40 ks (which is the approximate length of the observations discussed here).

In order to obtain a higher period resolution, the normalized broad-band X-ray light curves of observations 4535, 7456 and 8519 were joined together to form one long combined data set (with binning 100 s). The combined light curve was detrended by using the PERIOD task DETREND to subtract the mean and divide by the standard deviation to obtain a data set with a zero mean and a standard deviation of 1. The task SCARGLE was consequently applied to the combined data set to yield a Lomb-Scargle periodogram in order to determine the period more accurately. Due to the $\sim$ 2-year gap between the first two data sets and the $\sim$ 1-week gap between the last two, the aliasing effects made it difficult to decide which one of the peaks represents the true periodicity in the data.

Consequently, a combined broad-band light curve was created using only the observations of February 2007 (Obs 7456 and 8519), and a similar Lomb-Scargle periodogram was created. The PERIOD task PEAKS was utilized to determine the peak with maximum power in the 2007 periodogram. The position of this (relatively broad) peak was used to choose the appropriate peak on the high time-resolution

periodogram obtained by combining all three data sets, and the PEAKS task was used to determine its position.

The soft, hard and HR light curves of observation 4535 were folded on the newly determined period by making use of the Xronos task **efold**, using the time of minimum light of the third minimum of the 4535 light curve. This was done to enable easier comparison to the phase-binned ROSAT light curves in Fig. 5.11.

The orbital ephemeris of van Teeseling et al. (1998) quoted in Section 5.2 can be rewritten in BJD terms as

$$T_0 = \text{BJD } 2450434.1327 \pm 0.0006 \quad + \quad 0.1719260E \pm 0.0000007 \text{ d} . \qquad (7.4)$$

Expressing the orbital period above in terms of hours yields $P_{\rm orb} = 4.126224 \pm 0.000017$ h. The three broad-band light curves were folded on the orbital ephemeris above to investigate the phasing of the X-ray eclipses compared to the previous data.

Results

The broad-band X-ray light curves of the three SMC 13 observations are shown in Fig. 7.3. For easier comparison, each light curve was normalized to its mean count rate.

The power spectra for the three separate observations are presented in Fig. 7.4. All three exhibit a strong frequency peak at $\sim 6.25 \times 10^{-5}$ Hz, corresponding to 4.44 ± 0.89 h. This period is compatible with the known orbital period of the system, but the peak position is obviously very weakly resolved.

The Lomb-Scargle periodograms obtained from the combined data sets are shown in Fig. 7.5. The strongest power peak obtained from the combination of the 2007 data sets is at a period of 4.12 ± 0.06 h. By using the position of this broad peak to choose the correct peak from the high time-resolution periodogram, a final period of 4.1214 ± 0.0005 h is obtained.

The "soft" and "hard" X-ray light curves extracted from observation 4535, as well as the hardness ratio, are provided in Fig. 7.6. These light curves are folded with the newly determined orbital period of $P_{\rm orb} = 4.1214$ h with respect to the epoch of the third minimum of the data set itself, which is positioned at BJD 2453401.5682.

The broad-band light curves of the three observations folded through the orbital ephemeris of van Teeseling et al. (1998) are shown in Fig. 7.7.

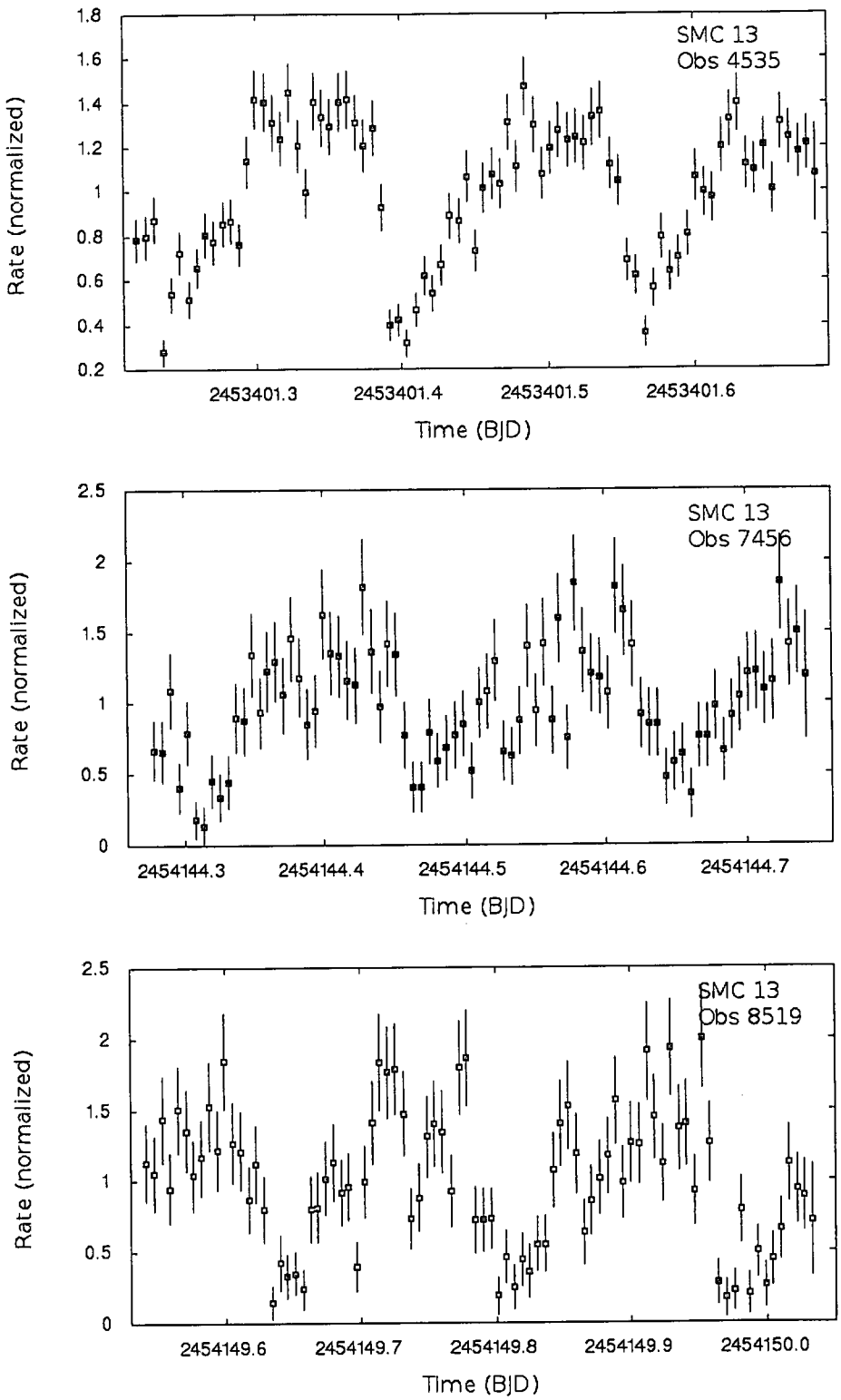

Fig. 7.3: *Chandra* light curves of SMC 13. The binning is 500 s, and the vertical lines denote the error bars. Photons with energies < 10 keV are included. The RATE axes have been normalized to the mean count rate for each observation, which are: 0.1877 counts/s for Obs 4535, 0.0355 counts/s for Obs 7456 and 0.0357 counts/s for Obs 8519.

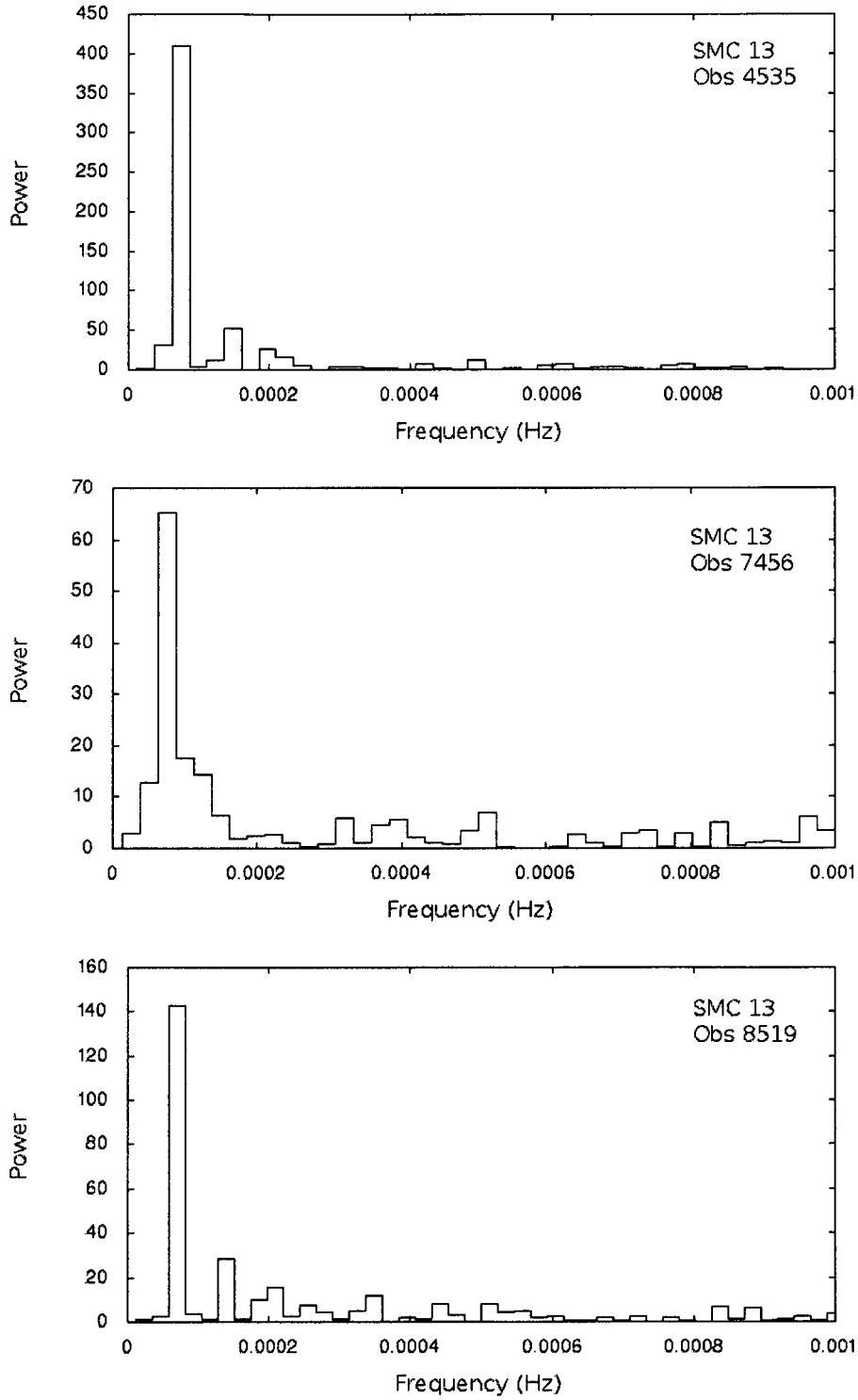

Fig. 7.4: Power spectra of SMC 13 from *Chandra* data.

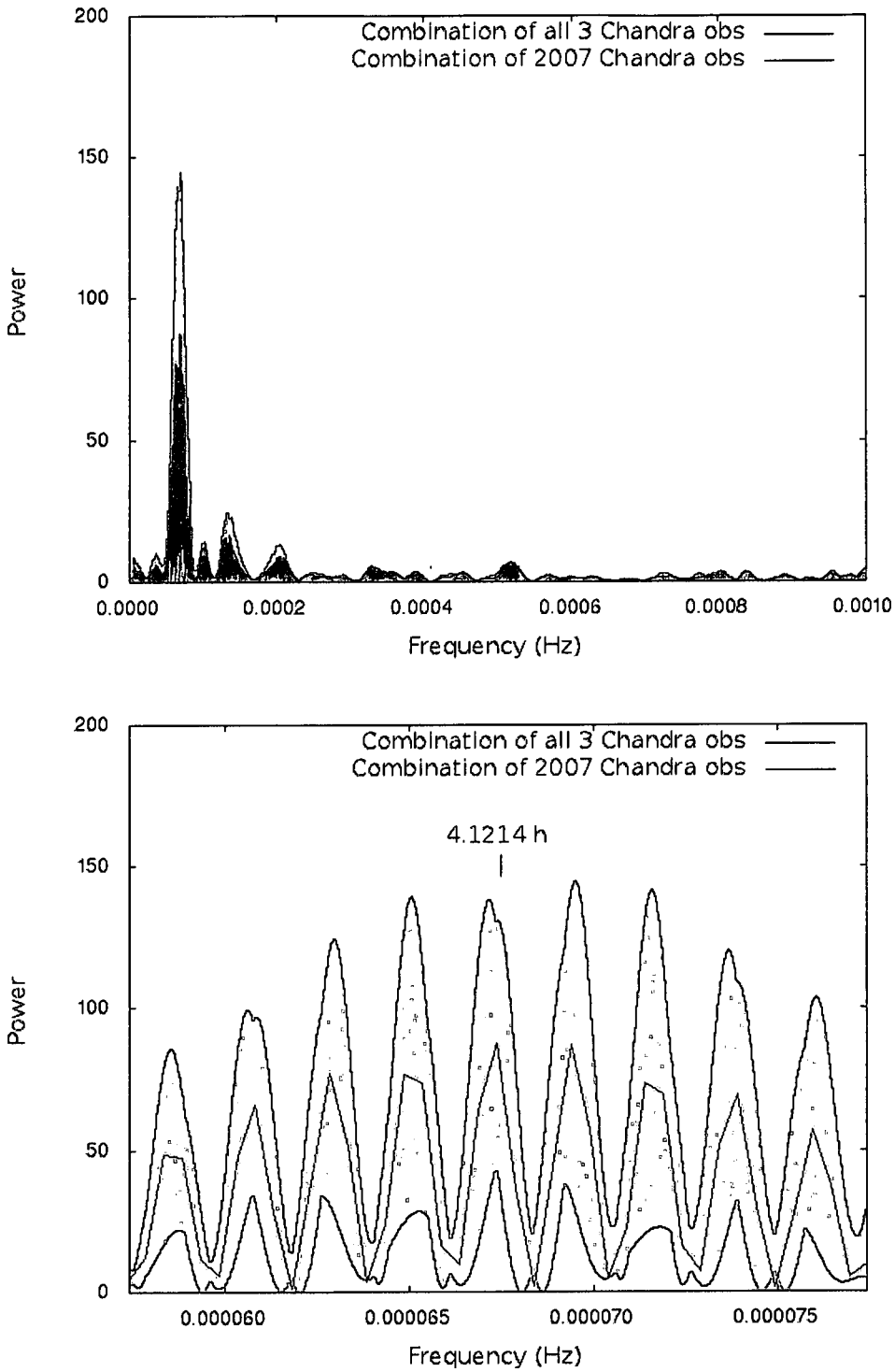

Fig. 7.5: Lomb-Scargle periodograms of combined *Chandra* light curves of SMC 13. Top: showing the frequency range up to 0.001 Hz. Bottom: zooming in on the chosen peak (see text) at 4.1214 h.

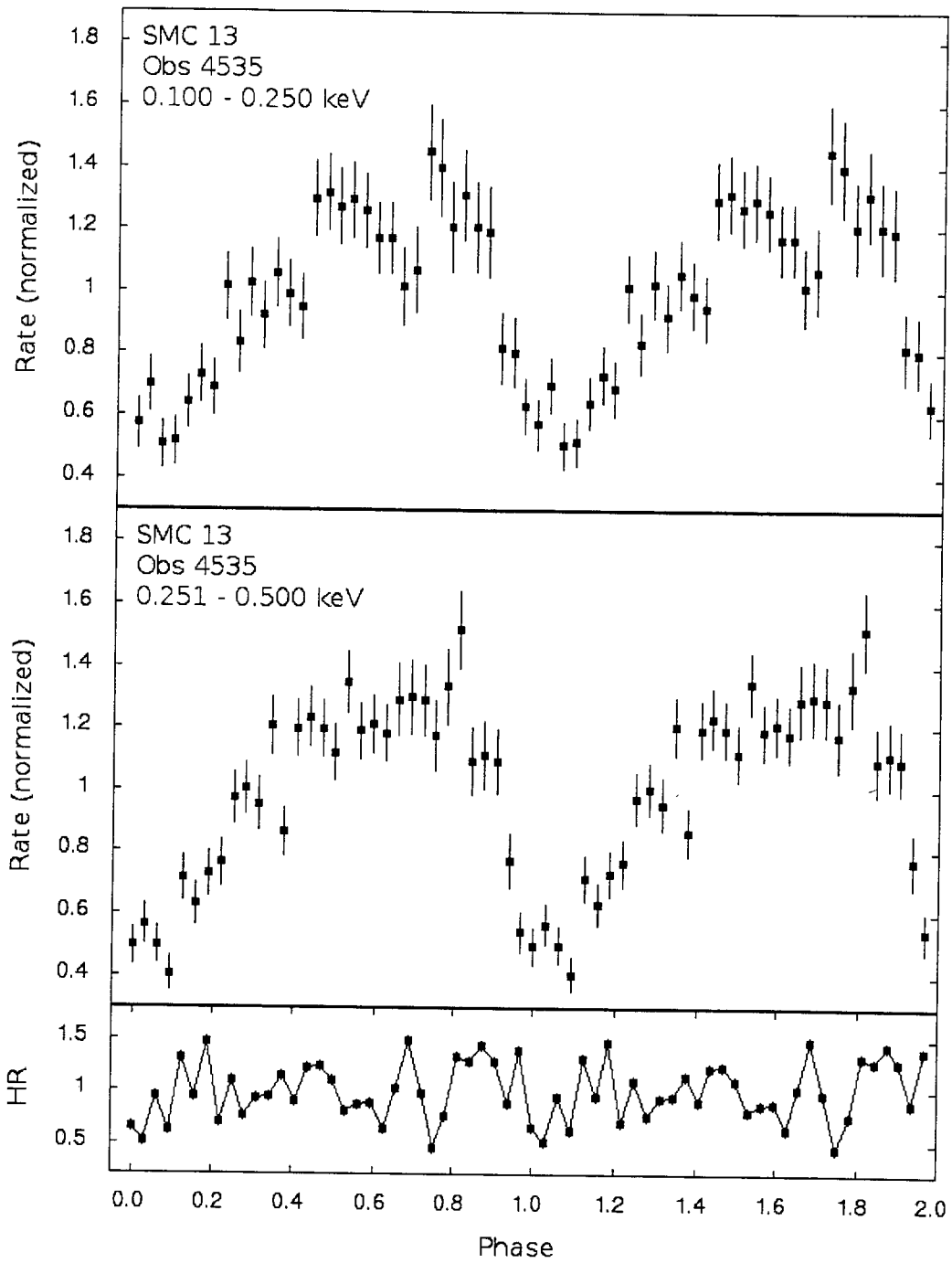

Fig. 7.6: *Chandra* ACIS-S Obs 4535 phase-binned light curves for SMC 13, folded on $P_{\rm orb}$ = 4.1214 h with respect to the third minimum in the data set (see top panel in Fig. 7.3). Two cycles are shown. The count rate in the "soft" band (0.100 – 0.250 keV) (top), the count rate in the "hard" band (0.251 – 0.500 keV) (middle) and the hardness ratio (bottom) are shown. The hardness ratio is given by HR=H/(H+S), where H is the number of counts above 0.5 keV and S is the number of counts below 0.5 keV. The number of phase bins per period is 32.

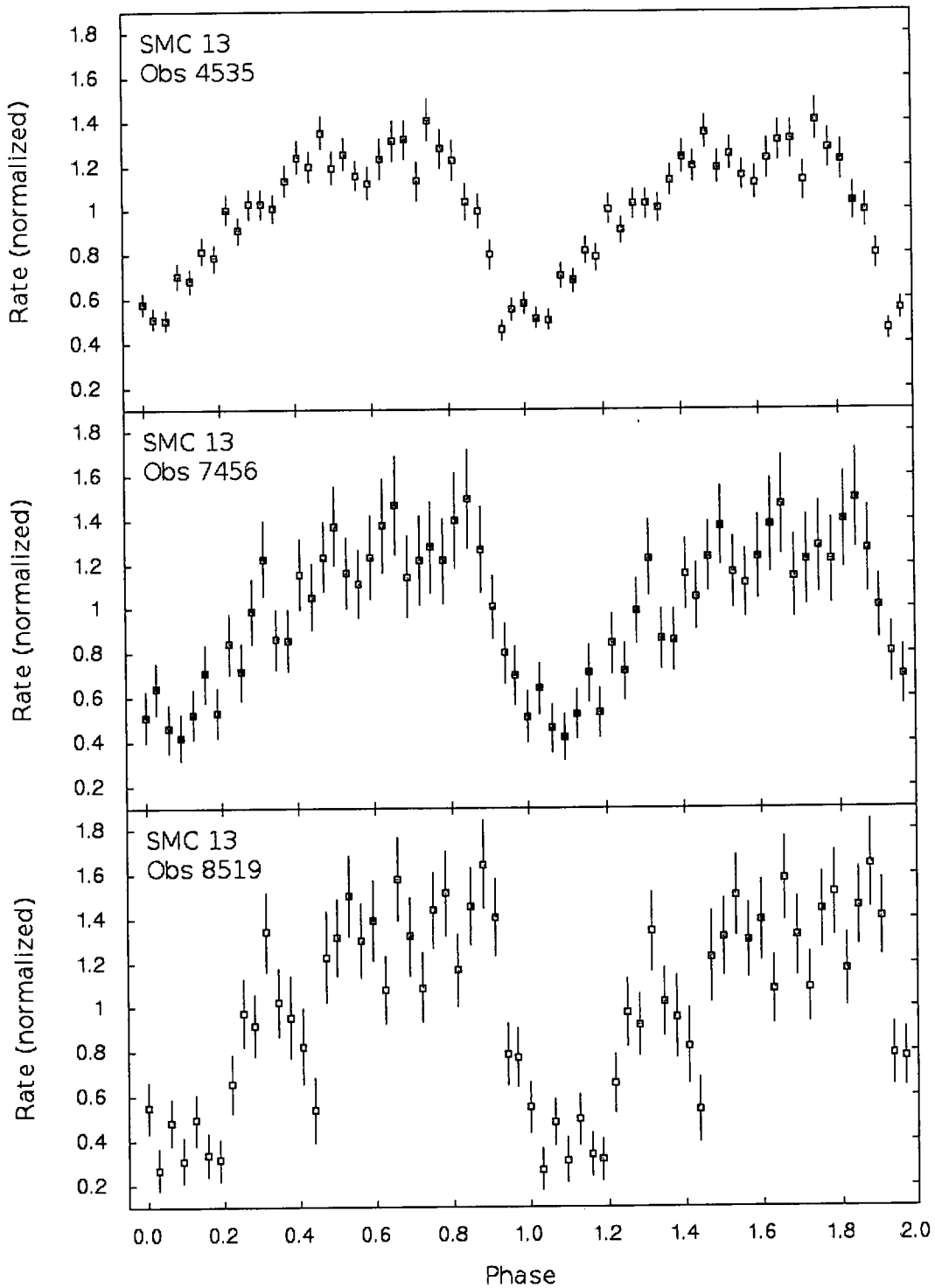

Fig. 7.7: SMC 13 broad-band *Chandra* light curves folded on the orbital ephemeris of van Teeseling et al. (1998), i.e. $P_{\rm orb} = 4.126224$ and an epoch of BJD 2450434.1327. The number of phase bins per period is 32.

Discussion

The light curves from the three analysed *Chandra* observations provide evidence that the X-ray emission from SMC 13 is strongly modulated by the orbital period. The same result was found by Kahabka (1996a) from ROSAT data. Because the time of minimum in the ROSAT light curve is largely defined by only three data points, Crampton et al. (1997) mentioned the possibility that these few minima might be caused by the system being in a low state at some epochs, rather than by orbital modulation. However, each of the *Chandra* data sets constitutes an uninterrupted observation of the source for a duration of ~ 2.7 full orbital periods, and the orbital modulation is clearly evident. As suggested by Kahabka (1996a), the shape of the X-ray light curve may indicate that the WD possesses a substantial magnetic field.

The orbital period of 4.1214 ± 0.0005 h determined from the combined data set is very close to $P_{\rm orb} = 4.126224 \pm 0.000017$ h determined by van Teeseling et al. (1998), although not included in its error ranges.

The folded light curves in the soft and hard X-ray bands in Fig. 7.6 can now be compared with the ROSAT light curves in Fig. 5.11. Our light curves exhibit the same sharp, asymmetric form as the ROSAT light curves. In addition to the main minimum, both the ROSAT and *Chandra* soft bands show a secondary minimum between phase values of 0.6 and 0.7. However, for both satellites, this secondary minimum is not observed in the hard band.

The HR values can not be compared directly, as they were defined differently and are also dependent on the response functions of the different satellites. In the ROSAT light curve, both the minor and major dips are coupled with an increase in the hardness ratio. The trend of the HR to increase during the secondary minimum in the soft band is also observed in the *Chandra* data. However, the relative value of the *Chandra* HR is quite low during the main eclipse.

As discussed in Section 5.2, Schmidtke et al. (1996) found from their ephemeris that the X-ray minimum occurs about 0.25 of a cycle after the optical minimum. However, when folding the *Chandra* light curves through the improved orbital ephemeris of van Teeseling et al. (1998), the phasing illustrated in Fig. 7.7 is obtained, with the X-ray minimum nearly coinciding with the optical minimum. This is similar to the phasing obtained by Kahabka (1996a) after folding the ROSAT light curves through the orbital ephemeris of Schmidtke et al. (1994). A qualitative evaluation of our folded light curves might even suggest that the X-ray minimum occurs at a higher phase value for observation 7456 than for observation 4535, and still higher for observation 8519.

Therefore a more in-depth analysis of the orbital period and ephemeris need to be carried out by the timing analysis of these data in conjunction with previous observations of SMC 13. In particular, simultaneous optical and X-ray observations are needed to clarify the relative phasing of the minima in these wavebands. High-resolution optical spectroscopy of SMC 13 with the RSS is also planned for the future in order to investigate the activity of the accretion disc that may be present in the system.

7.2 XMM-Newton observations of CAL 83

The optical spectra of CAL 83 revealed strong evidence for a disc and some associated outflow. The outflow can only be readily explained in terms of propeller driven outflow. This could possibly imply the presence of a spun-up white dwarf. Therefore a search was carried out for periodicities on time-scales of tens to hundreds of seconds. All the CAL 83 data in the public archives of *Chandra* and XMM-Newton were included in this search. While no significant periodic signals on these time-scales were found in the *Chandra* power spectra, the XMM-Newton data yielded some interesting results.

Before the results of the search for periodicity are presented, a qualitative discussion focusing on the observations and relevant data calibration procedures are presented briefly.

7.2.1 The X-ray Multi-Mirror Mission (XMM-Newton)

XMM-Newton was launched by the European Space Agency (ESA) in December 1999, and to date it is the X-ray telescope with the largest effective area. It is in a 48-hour, high Earth orbit, enabling uninterrupted observations of up to ~ 40 hours. The scientific payload includes three Wolter Type-I X-ray telescopes, as well as a 30 cm optical/UV telescope (see Fig. 7.8).

XMM-Newton contains six science instruments. There are two Reflection Grating Spectrometers (RGS) for high-resolution spectroscopy. There are three EPIC (European Photon Imaging Camera) detectors for X-ray imaging and medium-resolution spectroscopy: MOS1, MOS2 and pn. The Optical Monitor (OM) provides capability for optical and UV imaging and grism spectroscopy. The available filters for OM photometry are V, B, U, UVW1, UVM2 and UVW2. The six instruments can be operated at the same time, enabling simultaneous multi-wavelength observations. The basic properties of the instruments are summarized in Table 7.3. For a detailed discussion of the instruments and different observing modes, refer to the

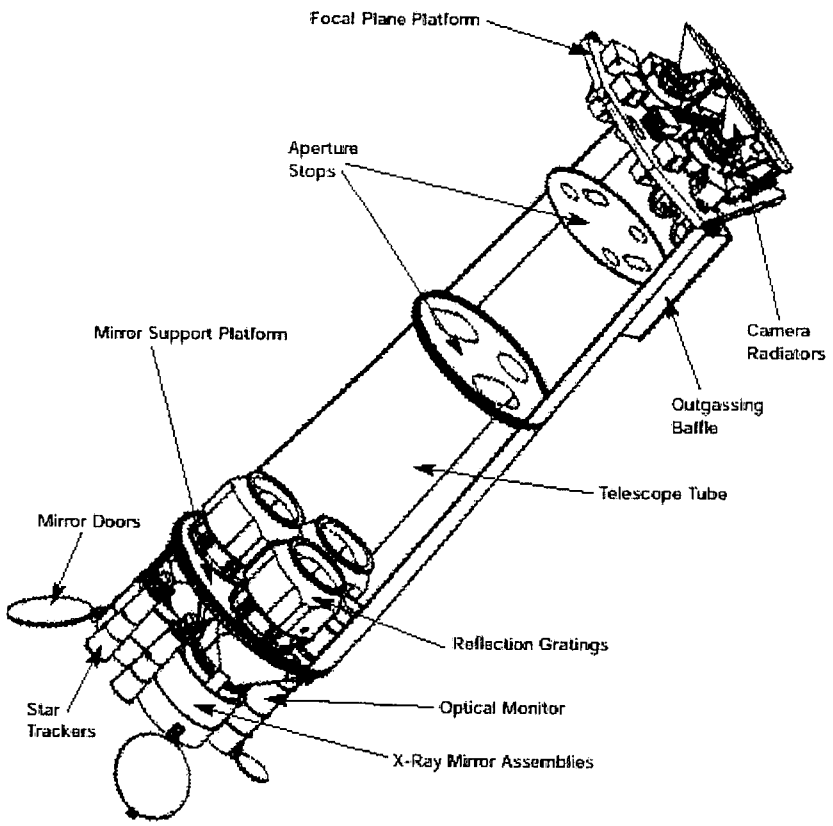

Fig. 7.8: The XMM-Newton payload. (Adopted from `http://xmm.esac.esa.int/external/xmm_user_support/documentation/technical/Spacecraft/index.shtml`.)

XMM-Newton website[6], and the XMM-Newton Users Handbook (ESA, 2011).

7.2.2 Observations

The five XMM-Newton data sets in which the periodic signals were found are summarized in Table 7.4.

7.2.3 Data calibration

Initial reductions and extraction

All the data from the different science instruments for each observation were calibrated by following standard data reduction procedures with the XMM-Newton SAS (Science Analysis System) software, Version 11.0 (see the Users Guide (XMM-Newton Science Operations Centre Team, 2011) for a detailed discussion). The arrival times in the calibrated event files were corrected to the solar system barycentre (in the TDB system) by using the SAS task **barycen**. Because we will primarily report on the results of the EPIC pn data, the extraction procedures used for the

[6] `http://xmm.esac.esa.int/`

Instrument	EPIC MOS	EPIC pn	RGS	OM
Bandpass	0.15-12 keV	0.15-12 keV	0.35-2.5 keV [a]	180-600 nm
Target visibility	5-135 ks	5-135 ks	5-135 ks	5-145 ks
Sensitivity	$\sim 10^{-14}$ [b]	$\sim 10^{-14}$ [b]	$\sim 8 \times 10^{-5}$ [c]	20.7 mag
Field of view	30′	30′	$\sim 5'$	17′
PSF (FWHM/HEW)	5″/14″	6″/15″	N/A	$1.4 - 2.0''$
Pixel size	40 μm (1.1″)	150 μm (4.1″)	81 μm (0.009 Å)	0.476513″
Timing resolution	1.75 ms	0.03 ms	0.6 s	0.5 s
Spectral resolution	~ 70 eV	~ 80 eV	0.04/0.025 Å	350 [d]

Table 7.3: XMM-Newton instrumentation summary. (Adopted from the XMM-Newton Users Handbook (ESA, 2011, p. 8, Table 1).)
[a]For grating order -1.
[b]In erg s^{-1} cm^{-2}.
[c]O VII 0.57 keV line flux in photons cm^{-2} s^{-1}.
[d]With UV and optical grism.

other detectors will not be described here.

For each EPIC pn exposure, a circular source region with a radius of 40″, centred at the source position, was defined. A rectangular background region with twice the area of the source region was defined on the same chip, but as far as possible from the source region. By using these regions, two filtered event files were created for each exposure: one containing only events from the source region and another containing only events from the background region. The energy range used in both cases is $0.15 - 2.5$ keV.

7.2.4 Timing analysis

Procedure

The Xronos task **powspec** was used to create a power spectrum from each of the 5 corrected datasets. The presence of a periodic signal just below 0.015 Hz (corresponding to ~ 67 s) is evident, especially in observation 0506531501 (see Fig. 7.9). A light curve binning of 20 s was used during the creation of these power spectra. Smaller and larger bin sizes were also tested and yielded the same peak at ~ 67 s.

The task **efsearch** was consequently used to search for the best-fitting period around 67 s in each data set. A light curve binning of 16.75 s was used, but, once again, testing different bin sizes did not change the results. A period of 67 s was used as a starting point and a range of periods to either side were tested (50 intrinsic fourier resolution elements to each side). As soon as the position of the strongest peak in each **efsearch** periodogram was obtained, its position was refined obtained by decreasing the increment between the consecutive test periods to 0.0001 s.

Obs ID	Instruments and exposures	Start date and time (UT)	Exposure time (ks)	PI[a]
0123510101	EPN EFF(3), MOS1 FF(3), MOS2 FF(3), RGS1 SES(1), RGS2 SES(1)	2000/04/23 07:34:01	45.021	F. Jansen
0500860301	EPN SW(1), MOS1 SW2(1), MOS2 SW2(1), RGS1 SES(1), RGS2 SES(1), OM U(3)	2007/07/06 23:31:52	10.920	T. Lanz
0500860601	EPN SW(1), MOS1 SW2(1), MOS2 SW2(1), RGS1 SES(1), RGS2 SES(1), OM U(5)	2007/11/24 21:10:14	23.173	T. Lanz
0506531501	EPN SW(1), MOS1 SW2(1), MOS2 SW2(1), RGS1 SES(1), RGS2 SES(1), OM B(1), OM UVW1(1), OM UVM2(1), OM UVW2(1)	2008/08/12 14:50:27	6.918	R. Schwarz
0506531701	EPN SW(1), MOS1 SW2(1), MOS2 SW2(1), RGS1 SES(1), RGS2 SES(1), OM UVW1(1), OM UVM2(6), OM UVW2(3)	2009/05/30 08:00:48	46.115	R. Schwarz

Table 7.4: XMM-Newton observations of CAL 83. EPN denotes EPIC pn. The different data modes are FF=Full Frame, EFF=Extended FF, SW=Small Window, SES=Spectroscopy. The OM filters that were used are also indicated. The numbers in brackets indicate the number of exposures.
[a]Principal Investigator.

A similar analysis was performed on the events in the background regions. The EPIC pn chip in Small Window mode provides a very small exposed detector area. Although we defined the background region as far away from the source region as possible, we expected that the "contamination" of the background region by marginal amounts of source counts from CAL 83 can not be excluded, and that there is a possibility that this might show up as a weak periodic signal in the background. The weak feature in the background power spectrum of observation 0500860601 may be ascribed to such an effect. However, no power peaks that are statistically significant are present at ~ 67 s in the background power spectra (see Fig. 7.10).

In addition to analysing the defined background regions, we also investigated possible contamination by counts from other sources by performing timing analysis on all the detected *off-source* photons in the EPIC pn, MOS1 and MOS2 event files. No 67 s periodicity were found in the off-source counts of any of the observations.

We especially considered contamination from the accreting pulsar XMMU J054134.7-682550, which is situated $\sim 4'$ away from CAL 83. Although its position is outside

of the small sky region covered by the EPIC pn chip in Small Window mode, its position is included in the MOS1 and MOS2 detector windows. Manousakis et al. (2009) found pulsed emission from this source at a period of $\sim$ 61 s in XMM-Newton observations 0500860301, 0500860401, 0500860501 and 0500860601, during which the source was observed in outburst. These authors also report that the detected spin period of XMMU J054134.7-682550 decreased with 1.54 s during $\sim$ 50 days as a result of spin-up effects. By careful investigation we have excluded the possibility that the $\sim$ 67 s modulation arises from contamination by XMMU J054134.7-682550 photons, because

- the power spectra of this pulsar calculated from the observations under consideration do not exhibit a peak corresponding to $\sim$ 67 s, and
- the $\sim$ 61 s period (which is decreasing due to spin-up effects) reported for the pulsar is removed from the $\sim$ 67 s peaks in our data by a substantial amount of resolution elements in all cases.

Frank Haberl (personal communication) and the XMM-Newton Science Operations Centre Team were also contacted to inquire whether such a power peak may arise from instrumental effects, and this does not seem to be the case. We therefore conclude that the periodic signal originates from CAL 83.

Results

The periodic signal was detected in the EPIC pn exposures of all 5 of the observations listed in Table 7.4. The power spectra of the MOS exposures of observations 0123510101, 0506531501 and 0506531701 exhibit a very weak feature near $\sim$ 0.015 Hz. The periodicity was not detected in the power spectra of the RGS and the OM.

The EPIC pn power spectra for the CAL 83 source region are presented in Fig. 7.9. The corresponding power spectra for the background regions are shown in Fig. 7.10. The results of the period searches with **efsearch** for each separate data set are shown in the periodograms in Fig. 7.11. The period with the highest chi-squared value is also indicated on the periodograms. A periodic signal between 65.1832 s and 67.6720 s was found in all the data sets.

These periods and the corresponding error ranges, as determined by the total length of each data set, are summarized in Table 7.5. By considering the source power spectra in Fig. 7.9, a rough estimation of the 1σ noise level yields a power of $\sim$ 8. The statistical significance of the strongest peak in each power spectrum expressed in terms of the estimated σ-value is also presented in Table 7.5.

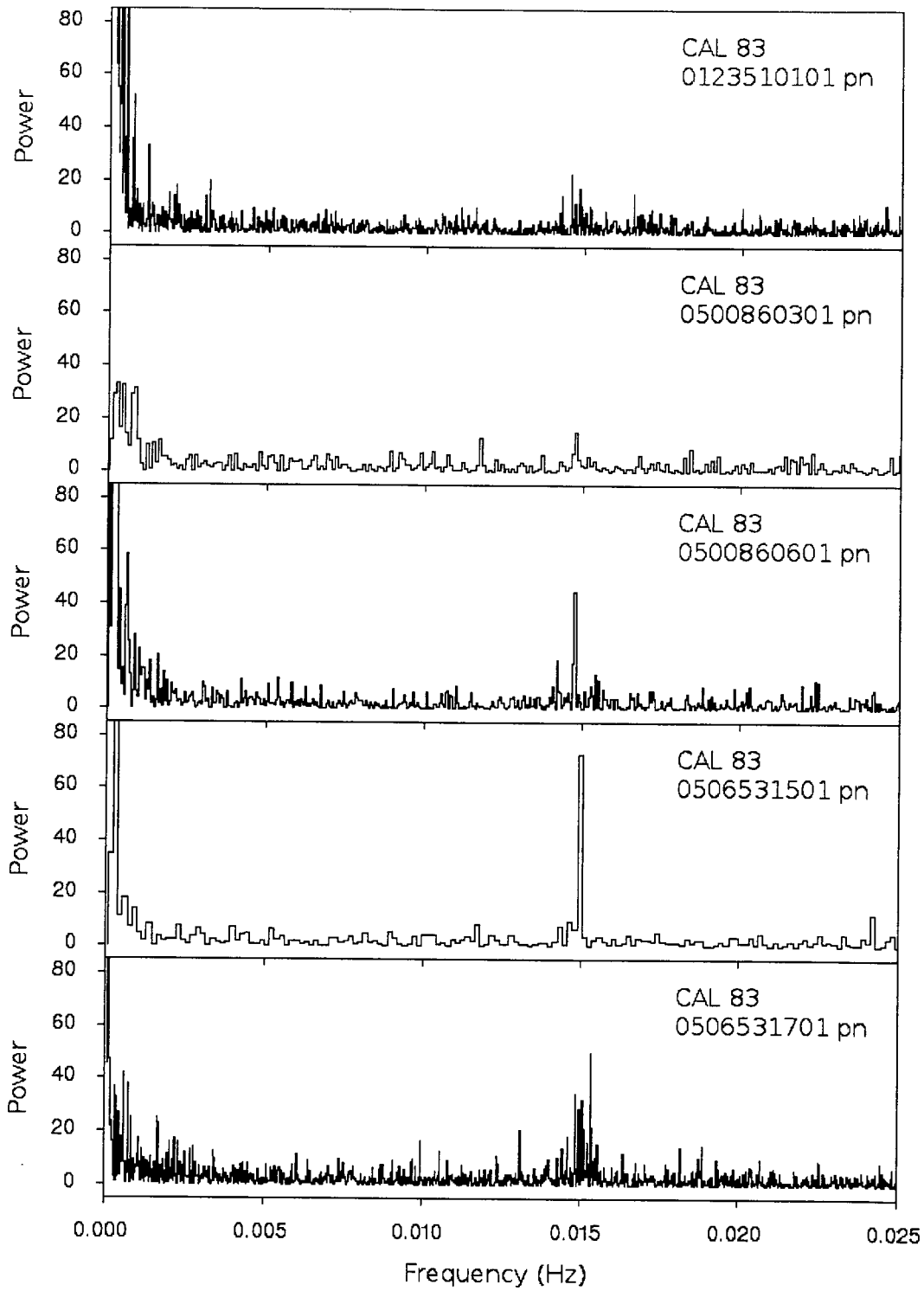

Fig. 7.9: CAL 83 power spectra from 5 XMM-Newton EPIC pn data sets, created with **powspec**. Energy range: 0.15 – 2.5 keV.

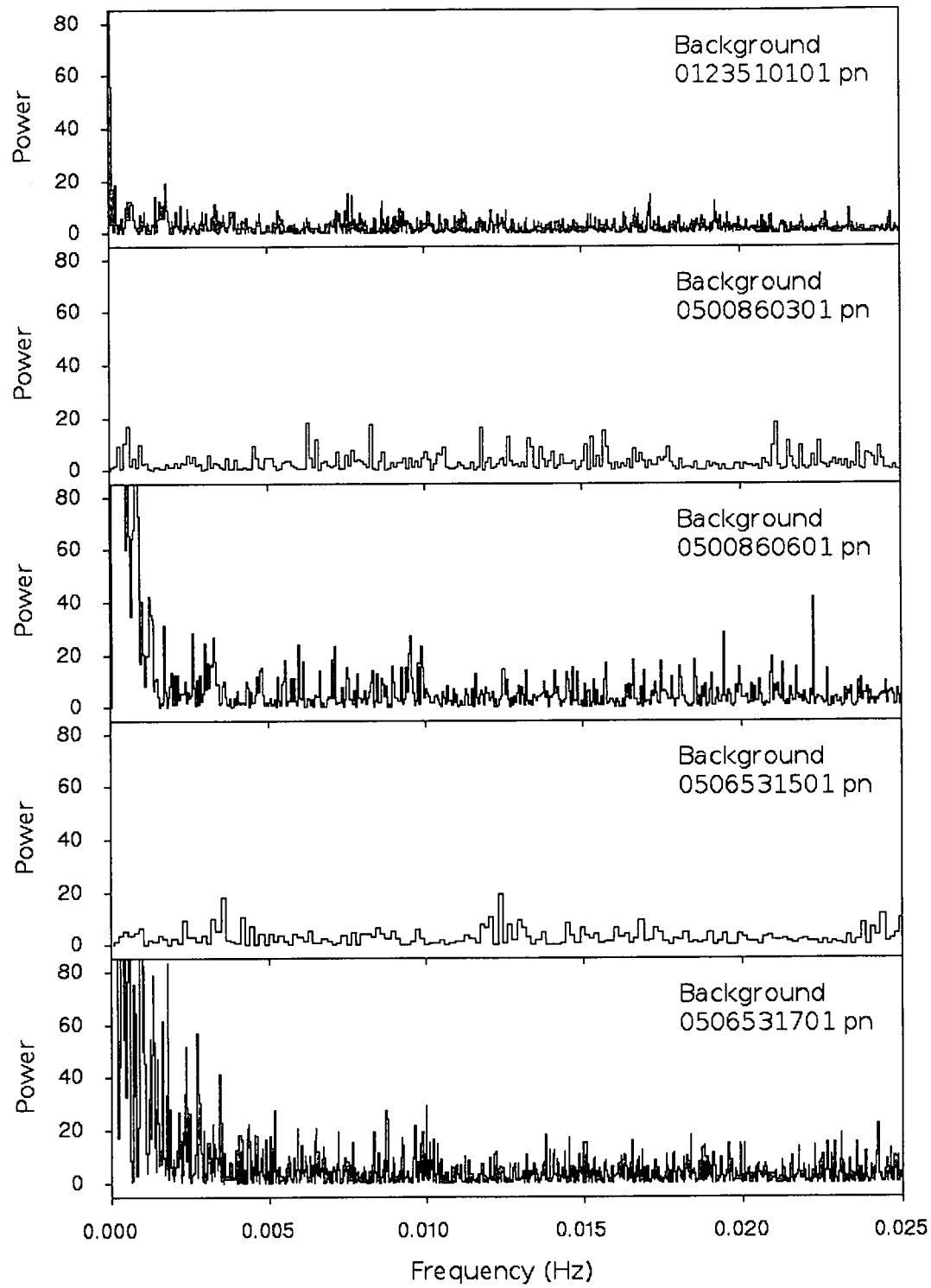

Fig. 7.10: Background power spectra of the 5 XMM-Newton EPIC pn data sets, created with **powspec**. Energy range: 0.15 – 2.5 keV.

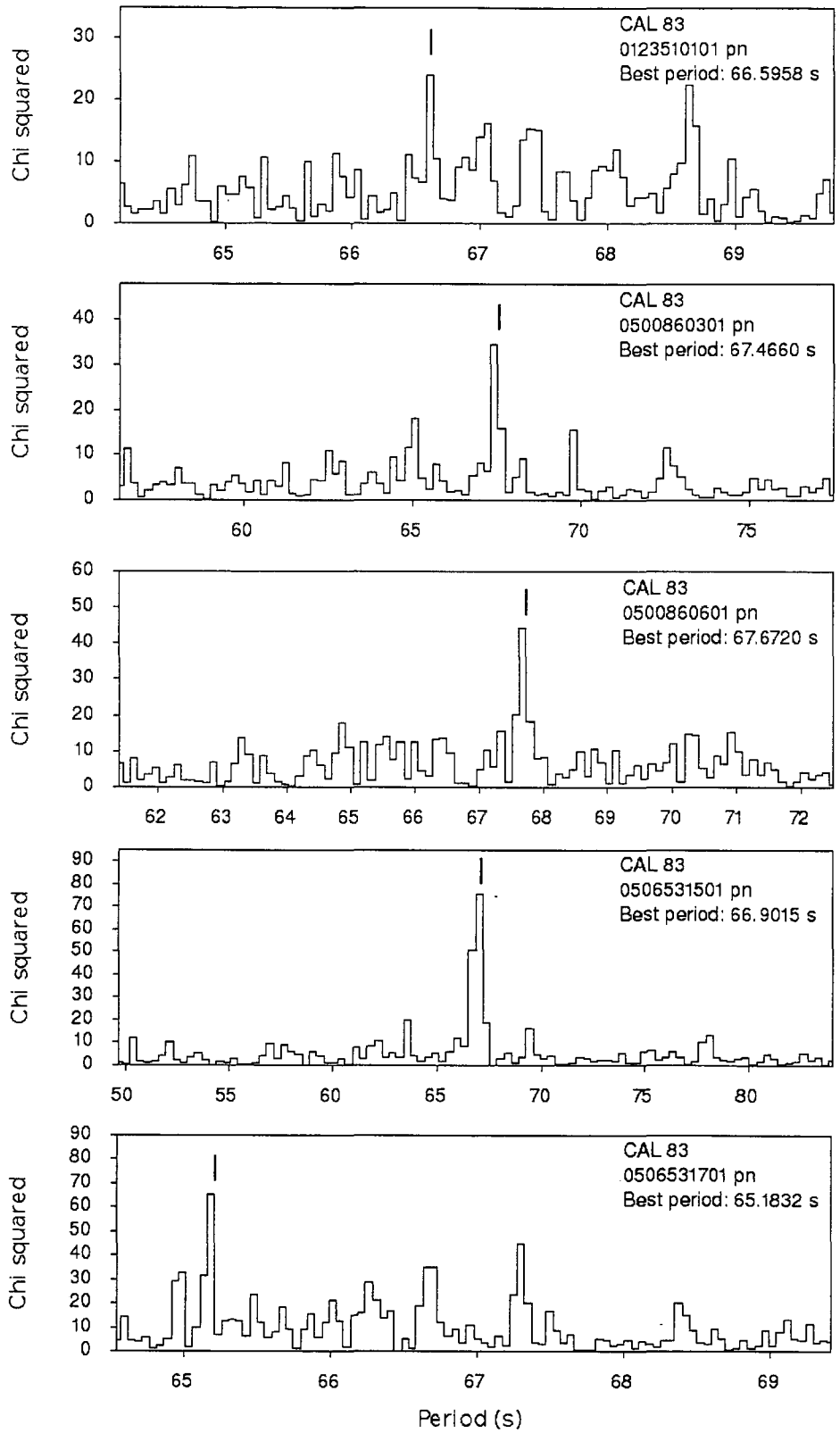

Fig. 7.11: Results of **efsearch** period search in XMM-Newton EPIC pn data sets of CAL 83. For each data set, 50 fourier resolution elements to either side of 67 s were tested. Energy range: 0.15 – 2.5 keV.

Observation	Best-fitting period (s)	Significance of power peak[a]
0123510101 pn	66.5958 ± 0.0564	3σ
0500860301 pn	67.4660 ± 0.2140	2σ
0500860601 pn	67.6720 ± 0.1120	4σ
0506531501 pn	66.9015 ± 0.3460	9σ
0506531701 pn	65.1832 ± 0.0491	5σ
Average period	66.7637	

Table 7.5: Best-fitting periods derived from CAL 83 periodograms.
[a]Strongest peak in power spectra in Fig. 7.9.

Discussion

One may expect that a periodicity in the X-ray emission should be reflected in the power spectra of all 5 of the X-ray detectors, as they are essentially observing the same source at the same time in the same waveband. However, at low energies, the effective area of the EPIC pn detector is significantly higher than that of the EPIC MOS detectors. Also, the EPIC detectors have a much higher sensitivity than the RGS. Therefore the signal-to-noise ratio (S/N) of our EPIC pn light curves is a factor of ~ 7 higher than the S/N of the EPIC MOS light curves, and a factor of ~ 23 higher than the S/N of the RGS light curves.

A period search on time-scales of ~ 1 min requires small binning intervals, and the light curves and power spectra of EPIC MOS and RGS are extremely noisy compared to those of EPIC pn. As an example, the MOS1 and RGS power spectra for observation 0506531701 are shown in Fig. 7.12, with MOS1 exhibiting a weak power peak at ~ 0.015 Hz, with no significant peak detected with the RGS. Therefore, we ascribe the non-detection of the periodicity in the RGS data and the marginal detection in the EPIC MOS data to these differences in sensitivity.

The strong periodic signal detected at ~ 67 s can be ascribed to rotational modulation in the system. The fact that the modulation at ~ 67 s is present in different data sets spanning over about 9 years makes it improbable that it originates from quasi-periodic oscillations, which would be short-lived. Therefore the periodicity most probably represents the spin period of the white dwarf in CAL 83. If it represents the white dwarf spin period, one would expect the detected period to have exactly the same value in different data sets. However, it is evident from Table 7.5 that there is a ~ 2.5 s difference between the lowest and highest periods, or, put differently, a deviation of up to ~ 1.6 s from the average value.

In order to explain these differences, it must be kept in mind that, although the arrival times have been corrected to the solar system barycentre, the orbital motion of the white dwarf will also modulate the detected spin period. Therefore the ob-

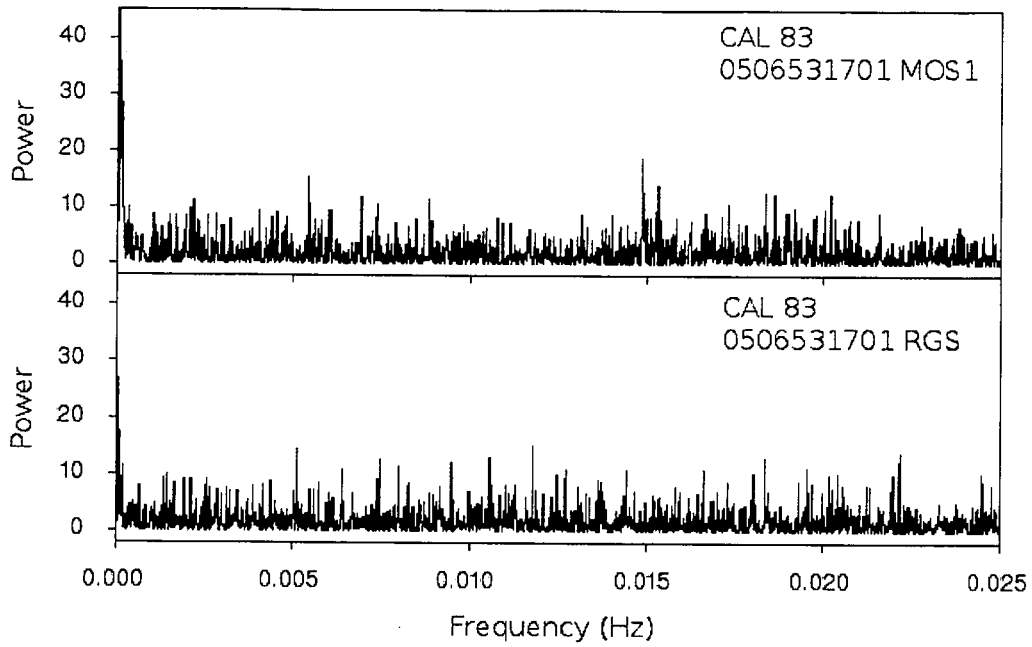

Fig. 7.12: CAL 83 power spectra for the MOS1 and RGS detectors of observation 0506531701. A weak power peak at ~ 0.015 Hz is present in the MOS1 spectrum, while the RGS power spectrum is completely dominated by noise.

served spin period will alternatingly be shifted to shorter and longer periods due to the Doppler effect as the white dwarf moves towards us and away from us. This modulating effect will now be quantified.

Modulation of the detected spin period by the binary orbital motion

From the discussion in Section 5.1, the inclination and the orbital period of CAL 83 were assumed to have the values $i = 25°$ and $P_{\rm orb} = 1.047568$ d. In Section 6.6, the distance from the WD to the system centre of mass was calculated to be $a_1 \sim 1.5 \times 10^{11}$ cm, and the ephemeris of Schmidtke et al. (2004) corrected to the solar system barycentre yields

$$T_0 = \text{BJD } 2451500.954 \pm 0.004 \quad + \quad 1.047568E \pm 0.000003 \text{ d} .$$

If A represents the light travel time between the WD primary and the centre of mass of the system, then

$$A = \frac{a_1}{c} = 5.0 \left(\frac{a_1}{1.5 \times 10^{11} \text{ cm}} \right) \text{ s} , \tag{7.5}$$

where c is the speed of light. The maximum phase shift in the detected spin period to either side of the true spin period ($P_{\rm spin} \sim 67$ s) is given by (e.g. Meintjes 1990, p. 25)

$$\Delta\phi_{\rm max} = \frac{A \sin i}{P_{\rm spin}} = 0.032 \left(\frac{A}{5.0 \text{ s}} \right) \left(\frac{\sin i}{\sin 25°} \right) \left(\frac{P_{\rm spin}}{67 \text{ s}} \right)^{-1} , \tag{7.6}$$

corresponding to a shift of 2.1 s from $P_{\rm spin}$. Therefore, if the assumed binary parameters for CAL 83 are approximately correct, the orbital motion can account for the small differences in the detected periods in Table 7.5.

It is also possible to correct the arrival times in the original event file (with solar barycentric corrections performed) to the barycentre of the binary system itself, prior to the fourier analysis. If it is assumed that the binary orbit is circular, this can be achieved by transforming each arrival time t_i to a corrected arrival time t_i' with the following formula (e.g. Meintjes 1990, p. 25):

$$t_i' = t_i - A \sin i \cos\left[\omega(t_i - t_0)\right] \ . \tag{7.7}$$

The parameter t_0 is a known reference time representing the time of minimum light, and

$$\omega = \frac{2\pi}{P_{\rm orb}} = 6.941989 \times 10^{-5} \left(\frac{P_{\rm orb}}{1.047568 \ {\rm d}}\right)^{-1} \ {\rm Hz} \ . \tag{7.8}$$

All the arrival times in the XMM-Newton event files are expressed relative to the reference time of JD 2450814.5, corresponding to BJD 2450814.500519663 for CAL 83. An appropriate value for t_0 can therefore be determined from the eclipse time in the orbital ephemeris:

$$t_0 = (2451500.954 - 2450814.500519663)(24 \times 3600) \ {\rm s} = 59309580.7011008 \ {\rm s} \ . \tag{7.9}$$

However, due to the uncertainty in the time of minimum light of the orbital ephemeris, it should be noted that the value of t_0 calculated above is accurate to no more than about 300 s.

Substituting the values above into Eq. (7.7) yields the following correction equation, which could be applied to the arrival times of photons from CAL 83 recorded in the XMM-Newton event files:

$$t_i' = t_i - (2.1 \ {\rm s}) \cos\left[6.941989 \times 10^{-5} \, (t_i - 59309580.7011008)\right] \ . \tag{7.10}$$

However, the accuracy of the transformation above is evidently strongly dependent on the choice of binary parameters, as well as the accuracy of the eclipse time in the orbital ephemeris. For this reason, the model-dependent transformation above was *not* applied to the event files used to obtain the results presented in this chapter, and is only included for completeness.

Concluding remarks

The widths of the optical spectral lines reported in the previous chapter are in favour of the presence of an accretion disc in the system. This supports the possibility that

the observed period might be the WD spin period, as the torques exerted by the accretion disc on the WD are able to spin up the WD to such short periods. The presence of a reasonably strong magnetic field coupled with the disc will enhance the spin-up effect. Such a magnetic field could lead to the ejection of mass from the system due to a propelling effect on material outside the corotation radius that are attempting to accrete along the magnetic field lines. Evidence for disc winds are indeed present in the optical spectra of CAL 83. Therefore the other observational evidence supports the possibility of the $\sim$ 67 s period being the spin period of the white dwarf in CAL 83.

Chapter 8

Conclusion

The discovery of binary systems associated with white dwarfs accreting mass from secondary stars at rates sufficient to drive nuclear burning and associated soft X-ray emission, provides an interesting snapshot of binary and stellar evolution. To investigate this aspect, a sample of supersoft sources have been identified for spectroscopic and X-ray studies, especially focusing on the identification of possible accretion disc signatures and mass outflows that are associated with the various phases of binary and stellar evolution. These aims necessitated a theoretical study of the properties of accreting binary systems and the technique of optical spectroscopy as a diagnostic tool to constrain the location and kinematics of the line-emitting plasma.

The observational component of the study included searching for accretion disc and mass outflow signatures in the newly obtained optical spectra. Since the presence and nature of accretion and mass outflow are strongly dependent on the basic parameters of a binary system, the constraining of the binary dimensions, including the region where the formation of an accretion disc can be expected, was a very important consideration. In turn, the binary dimensions depend on the component masses and orbital period, which were investigated by means of archived X-ray data for one of our targets. A search for temporal variations in archived X-ray data also yielded a short time-scale variability in one of our other targets that may support the evolutionary scenario proposed above.

The optical spectra of the Large Magellanic Cloud close binary supersoft source CAL 83 exhibit Balmer and He II emission lines that are broadened to a much greater extent than what can be accounted for by "ordinary" broadening mechanisms like temperature and pressure broadening. Translating these velocities to Keplerian velocities in the system yielded approximate Keplerian radii that are well within the Roche lobe of the white dwarf and are consistent with emission from an extended accretion disc. Evidence for a wind or a collimated outflow with a large opening angle is present in the extended wing of the He II λ4686 line that has also

been observed in previous studies. The radial velocity shifts of the line centroids indicate that the line-emitting regions are associated with the primary white dwarf and follow its orbital motion, rather than being associated with regions close to the secondary star.

During a systematic search for short orbital periods in the *Chandra* and XMM-Newton archived data for CAL 83, a periodic modulation of $P \sim 67$ s was found in five XMM-Newton data sets recorded at different epochs during 2000, 2007, 2008 and 2009. A tentative interpretation of the periodicity as the spin period of a spun-up white dwarf fits in remarkably well with the source properties inferred from optical observations.

The inferred presence of an accretion disc in the system provides the possibility of the white dwarf being spun-up by accretion disc torques during the accretion process. If the white dwarf is magnetized, coupling of the magnetic field with the disc increases the effectivity of the spin-up process notably. Additionally, the presence of a magnetic field could explain the detected mass ejection in terms of a propeller process as accreting material outside the corotation radius attempts to accrete along the field lines. The low ratio of Balmer to CNO emission reported in the literature indicates that the secondary may already have lost a significant part of its envelope, indicating that mass transfer has been taking place for a relatively long time, during which the WD could have been spun-up to a short spin period.

This places CAL 83 on a similar evolutionary track as the nova-like variable system AE Aqr, where the short ~ 33 s spin period is also associated with a period of enhanced mass accretion at rates comparable to the Eddington limit, with associated spin-up via accretion disc torques. However, if the mass estimate of $\sim 1.3 M_{\odot}$ for the WD in CAL 83 is correct, it is also quite possible that it will be driven over the Chandrasekhar limit before the system becomes a cataclysmic variable, and explode in a Type Ia supernova.

There are several aspects of CAL 83 that require further investigation. Optical spectra at several epochs during the orbital period are essential in order to monitor the changing structure of especially the He II λ4686 and also the Hβ emission. If the ~ 67 s periodicity represents a spin period, its presence in only some observations remains a puzzle. Could it be explained by the obscuration of the pulsed emission at certain times during the transient cycles of CAL 83? Archived observations of CAL 83 in other X-ray archives, as well as new X-ray observations, should be utilized to seek confirmation of the observed period. If CAL 83 possesses a reasonable magnetic field, as postulated above, possible non-thermal radio emission also makes it a promising candidate for radio studies with sensitive instruments like MeerKAT

and the SKA.

The single hot core of the planetary nebula N67 in the SMC is also a well-known supersoft source. Optical spectroscopy of this source reveals strong nebular emission of Hα and two [N II] lines in the red waveband. The widths of these lines are considerably narrower than the wide emission lines with extended wings that are often observed in accreting binary systems. The nebular expansion velocities derived from these lines are comparable to the known expansion velocity of 27.9 km s^{-1}, thereby confirming the slow outward flow of mass from the hot white dwarf.

The galactic symbiotic nova RR Tel was included in this study due to the fascinating mechanism by which Raman-scattered O VI lines in its spectrum provide evidence of an accretion disc in the system. Scattering of the 1032 Å component of the O VI doublet to a wavelength of $\sim$ 6828 Å by scatterers close to the red giant companion provides us with an $i \sim 90°$ perspective of the accretion disc at all times, as the observer is essentially observing the accretion disc from the perspective of the secondary star. Our observations confirmed the presence of the double-peaked Raman-scattered O VI line at $\sim$ 6828 Å, and this strengthens the notion of the presence of an accretion disc in RR Tel. The Keplerian radius derived from the velocity width of the line is consistent with emission from an accretion disc around the white dwarf. The nebular lines of RR Tel exhibit a much narrower profile that is compatible with the known velocity of the expanding nebular region, i.e. $\sim$ 30 km s^{-1}.

In future spectroscopic observations of this source, the spectral coverage will be extended to $\sim$ 7088 Å to include the Raman-scattered emission of the 1038 Å component of the O VI doublet, which is also known to exhibit a double-peaked structure. The polarization effects associated with the Raman scattering should also be investigated with the RSS.

The peculiar supersoft source SMC 13 in the Small Magellanic Cloud may consist of a white dwarf with a mass of $\sim 0.6M_{\odot}$, with a lower-mass secondary ($\sim 0.4M_{\odot}$). The blackbody fits that were performed on *Chandra* data of this source seem to indicate a white dwarf mass even lower than $\sim 0.6M_{\odot}$, but as blackbody fits to SSS spectra tend to overestimate the luminosity and therefore to underestimate the mass, it is believed that fitting more sophisticated white dwarf atmosphere models to the *Chandra* data will probably yield a WD mass closer to $\sim 0.6M_{\odot}$.

When deriving mass estimates from photospheric radii, it is also important to take into consideration the contribution of the hydrogen burning shell to the total photospheric radius, otherwise the WD mass will be underestimated. Obtaining a reliable estimate of the thickness of the hydrogen burning shell will therefore be a priority

for future analysis and interpretation of these data.

The *Chandra* light curves of SMC 13 provide clear evidence of orbital modulation in the X-ray flux, and the shape of the softer and harder components of the supersoft light curves agrees with the shape of the corresponding ROSAT light curves. The shape of the observed modulation may indicate that the WD has a strong magnetic field. This would make it another excellent candidate for studies with MeerKAT and SKA to search for possible non-thermal radio emission. The small orbital period and system mass imply a small binary separation, therefore the upper limit for the possible extent of an accretion disc, if present, will be much smaller than for wide systems like RR Tel. The inner border of the accretion disc will be limited by the Alfvén radius, the size of which will depend on the possible strength of the magnetic field. Follow-up studies of this source will include obtaining high-resolution optical spectra at several epochs during the orbital period of ~ 4.126 h. This will enable us to confirm whether an accretion disc is present and, if so, to determine its geometry and extent. Simultaneous photometric and X-ray observations are also needed to clarify the relative phasing of the minima in the optical and X-ray light curves, and to investigate whether orbital spin evolution may be responsible for the discrepancies in the relative phasing reported in the literature.

Although supersoft X-ray sources have been observed quite extensively since their discovery in the 1980s, many questions related to this heterogeneous class of objects still remain unanswered. The availability of modern telescopes with high sensitivity and resolution like SALT, *Chandra*, XMM-Newton, MeerKAT and ultimately the SKA, provide exciting possibilities in the field of SSS research. We are looking forward to extending this initial study to more detailed modelling that will enable a better understanding of the true nature of these fascinating multi-wavelength sources.

Acknowledgements

I hereby acknowledge and express my sincere gratitude to the following parties for their valuable contributions:

- Prof. P.J. Meintjes for his role as supervisor, and for all the encouragement and valuable guidance that I have received from him the past two years.
- The Department of Physics at the University at the Free State and in particular the head of department, Prof. H.C. Swart, for the opportunity to do this research.
- The Square Kilometre Array (SKA) Africa project for the bursary that supported this research.
- The staff of the SAAO, especially Hannah Worters, for assistance rendered during observations at Sutherland, and the SALT team for comments on the SALT proposals.
- Our co-investigators in the SALT RSS proposals, Prof. P.A. Charles and Andry Rajoelimanana, for useful discussions and for their advice and assistance in structuring the proposals.
- The principal investigators of the archived *Chandra* and XMM-Newton data discussed in this dissertation, i.e. J. Greiner, T. Lanz, F. Jansen and R. Schwarz, for the opportunity to analyse the data.
- Frank Haberl for his comments on the periodicity detected in CAL 83.
- Hester Odendaal for the extensive proofreading of the dissertation, and also Marietjie Wink, Brian van Soelen, Yolandie Loots and An-Mari Myburgh for additional assistance in the proofreading. I appreciate it immensely.
- My loving husband, Adriaan, for his never-ending patience and support while I was working on the project.

And above all, all honour and praise to our Heavenly Father, who grants us the privilege to explore the wonders of his creation.

Bibliography

Alcock, C., Allsman, R. A., Alves, D., Axelrod, T. S., Bennett, D. P., Charles, P. A., Cook, K. H., Freeman, K. C., Griest, K., Guern, J., Lehner, M. J., Livio, M., Marshall, S. L., Peterson, B. A., Pratt, M. R., Quinn, P. J., Rodgers, A. W., Southwell. K. A., Stubbs, C. W. and Sutherland, W. (1997), 'The X-ray off-state of the supersoft source CAL 83 and its interpretation', *Monthly Notices of the Royal Astronomical Society* **286**, 483–486.

Allen, C. W. (1964), *Astrophysical Quantities*, 2 edn, The Athlone Press, University of London, London.

Aller, L. H., Keyes, C. D., Maran, S. P., Gull, T. R., Michalitsianos, A. G. and Stecher, T. P. (1987), 'Physical parameters for 12 planetary nebulae and their central stars in the Magellanic Clouds', *The Astrophysical Journal* **320**, 159–177.

Arnaud, K., Dorman, B. and Gordon, C. (2011), *Xspec: An X-Ray Spectral Fitting Package. User's Guide for version 12.7.0*, HEASARC Astrophysics Science Division. Available at: `http://heasarc.gsfc.nasa.gov/xanadu/xspec/`.

Balbus, S. A. and Hawley, J. F. (1998), 'Instability, turbulence, and enhanced transport in accretion disks', *Reviews of Modern Physics* **70**, 1–53.

Barden, S. C., Arns, J. A., Colburn, W. S. and Williams, J. B. (2000), 'Volume-Phase Holographic Gratings and the Efficiency of Three Simple Volume-Phase Holographic Gratings', *PASP* **112**, 809.

Beiser, A. (2003), *Concepts of Modern Physics*, 6 edn, McGraw-Hill Companies, Inc., New York.

Bondi, H. and Hoyle, F. (1944), 'On the mechanism of accretion by stars', *Monthly Notices of the Royal Astronomical Society* **104**, 273–282.

Brinkworth, C. S., Hoard, D. W., Wachter, S., Howell, S. B., Ciardi, D. R., Szkody, P., Harrison, T. E., van Belle, G. T. and Esin, A. A. (2007), 'Spitzer Space Telescope Observations of Magnetic Cataclysmic Variables: Possibilities for the Presence of Dust in Polars', *The Astrophysical Journal* **659**, 1541–1562.

Brown, T., Cordova, F., Ciardullo, R., Thompson, R. and Bond, H. (1994), 'Einstein observations of ultrasoft X-ray sources in the Magellanic Clouds', *The Astrophysical Journal* **422**, 118–125.

Burgh, E. B. and Nordsieck, K. H. (2009), *Southern African Large Telescope: RSS Observer's Guide*. Available at: `http://www.salt.ac.za/telescope/instrumentation/rss`.

Burgh, E. B., Nordsieck, K. H., Kobulnicky, H. A., Williams, T. B., O'Donoghue, D., Smith, M. P. and Percival, J. W. (2003), The Prime Focus Imaging Spectrograph for the Southern African Large Telescope: optical design, *in* M. Iye and A. F. M. Moorwood, eds, 'Instrument Design and Performance for Optical/Infrared Ground-based Telescopes (Proceedings of SPIE)', Vol. 4841, p. 1463.

Cambridge X-ray Astronomy (2005), Chandra. Available at: `http://www-xray.ast.cam.ac.uk/xray_introduction/Chandra.html`. Accessed: 01/09/2010.

Carroll, B. W. and Ostlie, D. A. (1996), *An Introduction to Modern Astrophysics*, Addison-Wesley Publishing Company, Inc., USA.

Chiang, E. and Rappaport, S. (1996), 'Time-dependent Calculations of Ionization Nebulae Surrounding Supersoft X-Ray Sources', *The Astrophysical Journal* **469**, 255.

Cowley, A. P., Crampton, D., Hutchings, J. B., Helfand, D. J., Hamilton, T. T., Thorstensen, J. R. and Charles, P. A. (1984), 'Optical counterparts of the Large Magellanic Cloud X-ray point sources', *The Astrophysical Journal* **286**, 196–208.

Cowley, A. P., Schmidtke, P. C., Crampton, D. and Hutchings, J. B. (1990), 'CAL 87 - an eclipsing black hole binary?', *The Astrophysical Journal* **350**, 288–294.

Cowley, A. P., Schmidtke, P. C., Crampton, D. and Hutchings, J. B. (1998), 'Six Supersoft X-Ray Binaries: System Parameters and Twin-Jet Outflows', *The Astrophysical Journal* **504**, 854.

Crampton, D., Cowley, A. P., Hutchings, J. B., Schmidtke, P. C., Thompson, I. B. and Liebert, J. (1987), 'CAL 83 - A puzzling X-ray source in the Large Magellanic Cloud', *The Astrophysical Journal* **321**, 745–754.

Crampton, D., Hutchings, J. B., Cowley, A. P. and Schmidtke, P. C. (1997), 'The Small Magellanic Cloud, Supersoft X-Ray Binary 1E 0035.4-7230 (SMC 13)', *The Astrophysical Journal* **489**, 903.

Di Stefano, R. (1996), Luminous Supersoft X-Ray Sources as Progenitors of Type Ia Supernovae, *in* J. Greiner, ed., 'Supersoft X-Ray Sources', Vol. 472 of *Lecture Notes in Physics, Berlin Springer Verlag*, pp. 193–204.

Di Stefano, R. and Nelson, L. A. (1996), On the Evolution, Numbers and Characteristics of Close-Binary Supersoft Sources, *in* J. Greiner, ed., 'Supersoft X-Ray Sources', Vol. 472 of *Lecture Notes in Physics, Berlin Springer Verlag*, pp. 3–14.

Dopita, M. A. and Meatheringham, S. J. (1991), 'Photoionization modeling of Magellanic Cloud planetary nebulae.', *The Astrophysical Journal* **367**, 115–125.

Dotani, T., Asai, K., Ebisawa, K. and Greiner, J. (2000), ASCA and ROSAT Observations of Supersoft X-Ray Sources, *in* K. Makishima, L. Piro, & T. Takahashi, ed., 'Broad Band X-ray Spectra of Cosmic Sources', p. 375.

Eastman, J., Siverd, R. and Gaudi, B. S. (2010), 'Achieving Better Than 1 Minute Accuracy in the Heliocentric and Barycentric Julian Dates', *PASP* **122**, 935–946.

Eggleton, P. P. (1983), 'Approximations to the radii of Roche lobes', *The Astrophysical Journal* **268**, 368–369.

Chandra X-ray Center (2011), *The* Chandra *Proposers' Observatory Guide*. Version 14.0. Available at: `http://cxc.harvard.edu/proposer/POG/`.

Eracleous, M. and Horne, K. (1996), 'The Speedy Magnetic Propeller in the Cataclysmic Variable AE Aquarii', *The Astrophysical Journal* **471**, 427.

ESA (2011), *XMM-Newton Users Handbook*. Issue 2.9. Available at: `http://xmm.esac.esa.int/external/xmm_user_support/documentation/index.shtml`.

Espey, B. R., Schulte-Ladbeck, R. E., Kriss, G. A., Hamann, F., Schmid, H. M. and Johnson, J. J. (1995), 'Simultaneous Observation of Direct and Raman-scattered O VI Lines in the Symbiotic Nova RR Telescopii', *The Astrophysical Journal Letters* **454**, L61.

Fender, R. P., Southwell, K. and Tzioumis, A. K. (1998), 'A radio survey of supersoft, persistent and transient X-ray sources in the Magellanic Clouds', *Monthly Notices of the Royal Astronomical Society* **298**, 692–696.

Frank, J., King, A. R. and Lasota, J.-P. (1988), 'The soft X-ray excess in accreting magnetic white dwarfs', *Astronomy & Astrophysics* **193**, 113–118.

Frank, J., King, A. R. and Raine, D. (2002), *Accretion Power in Astrophysics*, 3 edn, Cambridge University Press, Cambridge.

Friedjung, M., Stencel, R. E. and Viotti, R. (1983), 'Evidence for a warm wind from the red star in symbiotic binaries', *Astronomy & Astrophysics* **126**, 407–411.

Fruscione, A., McDowell, J. C., Allen, G. E., Brickhouse, N. S., Burke, D. J., Davis, J. E., Durham, N., Elvis, M., Galle, E. C., Harris, D. E., Huenemoerder, D. P., Houck, J. C., Ishibashi, B., Karovska, M., Nicastro, F., Noble, M. S., Nowak,

M. A., Primini, F. A., Siemiginowska, A., Smith, R. K. and Wise, M. (2006), CIAO: Chandra's data analysis system, *in* 'Society of Photo-Optical Instrumentation Engineers (SPIE) Conference Series', Vol. 6270 of *Society of Photo-Optical Instrumentation Engineers (SPIE) Conference Series*.

Fujimoto, M. Y. (1982), 'A theory of hydrogen shell flashes on accreting white dwarfs. I - Their progress and the expansion of the envelope. II - The stable shell burning and the recurrence period of shell flashes', *The Astrophysical Journal* **257**, 752–779.

Fukue, J. (2000), 'Basic Properties of Supercritical Accretion Disks', *PASJ* **52**, 829–840.

Fukue, J. and Matsumoto, K. (2001), 'Superdisks in Supersoft X-Ray Sources', *PASJ* **53**, 111–117.

Gänsicke, B. T., van Teeseling, A., Beuermann, K. and de Martino, D. (1998a), 'Hubble Space Telescope ultraviolet spectroscopy of the supersoft X-ray binaries CAL83 and RXJ0513.9-6951', *Astronomy & Astrophysics* **333**, 163–171.

Greiner, ., Schwarz, R., Sala, G., Ness, J.-U. and Mennickent, R. (2008), 'Supersoft X-ray source CAL 83 in an optical-high, X-ray off state', *The Astronomer's Telegram* **1357**, 1.

Greiner, J. and Di Stefano, R. (2002), 'X-ray off states and optical variability in CAL 83', *Astronomy & Astrophysics* **387**, 944–954.

Greiner, J., Hasinger, G. and Kahabka, P. (1991), 'ROSAT observation of two supersoft sources in the Large Magellanic Cloud', *Astronomy & Astrophysics* **246**, L17–L20.

Greiner, J., Orio, M. and Schwarz, R. (2000), 'RX J0537.7-7034: The shortest-period supersoft X-ray source', *Astronomy & Astrophysics* **355**, 1041–1048.

Hachisu, I. and Kato, M. (2001), 'Recurrent Novae as a Progenitor System of Type Ia Supernovae. I. RS Ophiuchi Subclass: Systems with a Red Giant Companion', *The Astrophysical Journal* **558**, 323–350.

Hachisu, I. and Kato, M. (2006), 'A Universal Decline Law of Classical Novae', *The Astrophysical Journal Supplement Series* **167**, 59–80.

Hamada, T. and Salpeter, E. E. (1961), 'Models for Zero-Temperature Stars.', *The Astrophysical Journal* **134**, 683.

Harris, J. and Zaritsky, D. (2006), 'Spectroscopic Survey of Red Giants in the Small Magellanic Cloud. I. Kinematics', *The Astronomical Journal* **131**, 2514–2524.

HEASARC (2009), *Xronos: A Timing Analysis Software Package. User's Guide Version 5.22.* Available at: `http://heasarc.gsfc.nasa.gov/docs/xanadu/xronos/`.

Heise, J., van Teeseling, A. and Kahabka, P. (1994), 'The spectra and luminosity of super-soft X-ray sources', *Astronomy & Astrophysics* **288**, L45–L48.

Hilditch, R. W., Howarth, I. D. and Harries, T. J. (2005), 'Forty eclipsing binaries in the Small Magellanic Cloud: fundamental parameters and Cloud distance', *Monthly Notices of the Royal Astronomical Society* **357**, 304–324.

Horne, K. and Marsh, T. R. (1986), 'Emission line formation in accretion discs', *Monthly Notices of the Royal Astronomical Society* **218**, 761–773.

Houck, J. C. (2010), *ISIS 1.0 Technical Manual, Chandra* X-Ray Observatory Center. Revision 1.0. Available at: `http://space.mit.edu/cxc/isis/manual.html`.

Howell, S. B. (2006), *Handbook of CCD Astronomy*, number 5 *in* 'Cambridge Observing Handbooks for Research Astronomers', 2 edn, Cambridge University Press.

Iben, Jr., I. (1982), 'Hot accreting white dwarfs in the quasi-static approximation', *The Astrophysical Journal* **259**, 244–266.

Iben, Jr., I. and Tutukov, A. V. (1996), 'On the Evolution of Symbiotic Stars and Other Binaries with Accreting Degenerate Dwarfs', *The Astrophysical Journal Supplement Series* **105**, 145.

Ibragimov, A. A., Suleimanov, V. F., Vikhlinin, A. and Sakhibullin, N. A. (2003), 'Supersoft X-ray Sources. Parameters of Stellar Atmospheres', *Astronomy Reports* **47**, 186–196.

Jameson, R. F., King, A. R. and Sherrington, M. R. (1980), 'The UV spectrum of AE AQR', *Monthly Notices of the Royal Astronomical Society* **191**, 559–569.

Jimenez-Garate, M. A., Raymond, J. C. and Liedahl, D. A. (2002), 'The Structure and X-Ray Recombination Emission of a Centrally Illuminated Accretion Disk Atmosphere and Corona', *The Astrophysical Journal* **581**, 1297–1327.

Jones, L. R., Pye, J. P., McHardy, I. M. and Fairall, A. P. (1985), 'EXOSAT and Einstein high resolution images of the Small Magellanic Cloud', *Space Science Reviews* **40**, 693–699.

Jordan, S., Murset, U. and Werner, K. (1994), 'A model for the X-ray spectrum of the symbiotic nova RR Telescopii', *Astronomy & Astrophysics* **283**, 475–482.

Kahabka, P. (1995), Observed Characteristics of Supersoft ROSAT Sources in the LMC and Other Galaxies, *in* H. Böhringer, G. E. Morfill, & J. E. Trümper, ed..

'Seventeeth Texas Symposium on Relativistic Astrophysics and Cosmology', Vol. 759 of *Annals of the New York Academy of Sciences*, p. 324.

Kahabka, P. (1996a), 'Orbital modulation in X-rays in supersoft sources.', *Astronomy & Astrophysics* **306**, 795.

Kahabka, P. (1998), 'Modelling the temporary X-ray off-state of CAL 83', *Astronomy & Astrophysics* **331**, 328–334.

Kahabka, P. (2006), 'Supersoft X-ray sources', *Advances in Space Research* **38**, 2836–2839.

Kahabka, P. and Ergma, E. (1997), 'Small Magellanic Cloud 13 type supersoft sources.', *Astronomy & Astrophysics* **318**, 108–110.

Kahabka, P., Haberl, F., Pakull, M., Millar, W. C., White, G. L., Filipović, M. D. and Payne, J. L. (2008), 'Faint super-soft X-ray sources in XMM-Newton Large Magellanic Cloud fields', *Astronomy & Astrophysics* **482**, 237–245.

Kahabka, P., Parmar, A. N. and Hartmann, H. W. (1999b), 'A BeppoSAX observation of the supersoft source 1E 0035.4-7230', *Astronomy & Astrophysics* **346**, 453–458.

Kahabka, P., Pietsch, W. and Hasinger, G. (1994), 'Super-soft X-ray sources in the fields of the Magellanic Clouds', *Astronomy & Astrophysics* **288**, 538–550.

Kahabka, P. and van den Heuvel, E. P. J. (1997), 'Luminous Supersoft X-Ray Sources', *Annual Review of Astronomy & Astrophysics* **35**, 69–100.

Kahabka, P. and van den Heuvel, E. P. J. (2006), *Super Soft Sources*, Cambridge University Press, New York, chapter 11, pp. 461–474.

Kaler, J. B. and Jacoby, G. H. (1990), 'The relation between chemical enrichment and core mass in planetary nebulae', *The Astrophysical Journal* **362**, 491–502.

Karzas, W. J. and Latter, R. (1961), 'Electron Radiative Transitions in a Coulomb Field', *The Astrophysical Journal Supplement Series* **6**, 167–212.

Kato, M. (1996), White Dwarfs with H/He Burning as Supersoft X-Ray Sources, *in* J. Greiner, ed., 'Supersoft X-Ray Sources', Vol. 472 of *Lecture Notes in Physics, Berlin Springer Verlag*, pp. 15–24.

Kato, M. (2010), 'Accreting white dwarfs as supersoft X-ray sources', *Astronomische Nachrichten* **331**, 140–145.

Kilkenny, D. and Worters, H. (2011), *The SAAO 1.9-m Telescope and Grating Spectrograph.* Available at: `http://www.saao.ac.za/observing/operating-manuals/19-m-telescope-instruments/`.

King, A. R., Pringle, J. E. and Livio, M. (2007), 'Accretion disc viscosity: how big is alpha?', *Monthly Notices of the Royal Astronomical Society* **376**, 1740–1746.

Kitabatake, E., Fukue, J. and Matsumoto, K. (2002), 'Supercritical Accretion Disks with Superwinds', *PASJ* **54**, 235–240.

Kitchin, C. (1995), *Optical Astronomical Spectroscopy*, Series in Astronomy and Astrophysics, Institute of Physics Publishing, Bristol and Philadelphia.

Kobulnicky, H. A., Nordsieck, K. H., Burgh, E. B., Smith, M. P., Percival, J. W., Williams, T. B. and O'Donoghue, D. (2003), The Prime Focus Imaging Spectrograph for the Southern African Large Telescope: Operational Modes, *in* M. Iye and A. F. M. Moorwood, eds, 'Instrument Design and Performance for Optical/Infrared Ground-based Telescopes (Proceedings of SPIE)', Vol. 4841, p. 1634.

Kotnik-Karuza, D., Friedjung, M. and Exter, K. (2009), 'Variation of Fluxes of RR Tel Emission Lines Measured in 2000 with Respect to 1996', *PASJ* **61**, 147–.

Kramida, A. E. and Fuhr, J. R. (2011), Atomic Transition Probability Bibliographic Database. Available at: `http://physics.nist.gov/cgi-bin/ASBib1/TransProbBib.cgi`. Accessed: 01/12/2011.

Kylafis, N. D. and Xilouris, E. M. (1993), 'Low-mass X-ray binary models for the supersoft X-ray sources CAL 83, CAL 87 and RX J0527.8-6954 in the Large Magellanic Cloud', *Astronomy & Astrophysics* **278**, L43–L46.

Lang, K. R. (1999), *Astrophysical Formulae: Radiation, Gas Processes and High Energy Astrophysics*, Vol. 1, 3 edn, Springer-Verlag, Berlin and Heidelberg.

Lanz, T., Audard, M. and Walter, F. (2008), 'CAL 83 detected again in X-rays, dimming in optical', *The Astronomer's Telegram* **1438**, 1.

Lanz, T., Telis, G. A., Audard, M., Paerels, F., Rasmussen, A. P. and Hubeny, I. (2005), 'Non-LTE Model Atmosphere Analysis of the Large Magellanic Cloud Supersoft X-Ray Source CAL 83', *The Astrophysical Journal* **619**, 517–526.

Lee, H.-W. (2000), 'Raman-Scattering Wings of Hα in Symbiotic Stars', *The Astrophysical Journal Letters* **541**, L25–L28.

Lee, H.-W. and Park, M.-G. (1999), 'Toward the Evidence of the Accretion Disk Emission in the Symbiotic Star RR Telescopii', *The Astrophysical Journal Letters* **515**, L89–L92.

Lomb, N. R. (1976), 'Least-squares frequency analysis of unequally spaced data', *Astrophysics and Space Science* **39**, 447–462.

Long, K. S., Helfand, D. J. and Grabelsky, D. A. (1981), 'A soft X-ray study of the Large Magellanic Cloud', *The Astrophysical Journal* **248**, 925–944.

Longair, M. S. (1992), *High Energy Astrophysics*, Vol. 1, 2 edn, Cambridge University Press, Cambridge.

Longair, M. S. (1994), *High Energy Astrophysics*, Vol. 2, 2 edn, Cambridge University Press, Cambridge.

Loudon, R. (2000), *The quantum theory of light*, Oxford science publications, Oxford University Press.

Manousakis, A., Walter, R., Audard, M. and Lanz, T. (2009), 'Pulsed thermal emission from the accreting pulsar XMMU J054134.7-682550', *Astronomy & Astrophysics* **498**, 217–222.

Massey, P. (1997), *A User's Guide to CCD Reductions with IRAF*.

Massey, P. and Hanson, M. M. (2010), Astronomical Spectroscopy. Available at: `http://arxiv.org/abs/1010.5270`.

Massey, P., Valdes, F. and Barnes, J. (1992), *A User's Guide to Reducing Slit Spectra with IRAF*.

Mauche, C. W., Lee, Y. P. and Kallman, T. R. (1997), 'Ultraviolet Emission-Line Ratios of Cataclysmic Variables', *The Astrophysical Journal* **477**, 832.

McKenna, F. C., Keenan, F. P., Hambly, N. C., Prieto, C. A., Rolleston, W. R. J., Aller, L. H. and Feibelman, W. A. (1997), 'The optical spectral line list of RR Telescopii', *The Astrophysical Journal Supplement Series* **109**, 225–239.

Meatheringham, S. J. and Dopita, M. A. (1991), 'Optical spectroscopy of Magellanic Cloud planetary nebulae', *The Astrophysical Journal Supplement Series* **75**, 407–424.

Meintjes, P. J. (1990), Search for TeV Gamma-ray Emission from Cataclysmic Variables, Master's thesis, University of Potchefstroom for Christian Higher Education, Potchefstroom.

Meintjes, P. J. (2002), 'On the evolution of the nova-like variable AE Aquarii', *Monthly Notices of the Royal Astronomical Society* **336**, 265–275.

Meintjes, P. J., de Jager, O. C., Raubenheimer, B. C., Nel, H. I., North, A. R., Buckley, D. A. H. and Koen, C. (1994), 'Simultaneous optical and TeV gamma-ray observations of the cataclysmic variable AE Aquarii', *The Astrophysical Journal* **434**, 292–305.

Mereghetti, S., Krachmalnicoff, N., La Palombara, N., Tiengo, A., Rauch, T., Haberl, F., Filipović, M. D. and Sturm, R. (2010), 'An XMM-Newton view of planetary nebulae in the Small Magellanic Cloud. The X-ray luminous central star of SMP SMC 22', *Astronomy & Astrophysics* **519**, A42.

Mereghetti, S., La Palombara, N., Krachmalnicoff, N., Tiengo, A., Haberl, F., Sturm, R., Rauch, T. and Filipovic, M. (2011), The XMM-Newton survey of the SMC: SMP SMC 22 and other planetary nebulae, *in* J.-U. Ness & M. Ehle, ed., 'The X-ray Universe 2011', p. 253.

Metzger, B. D., Piro, A. L., Quataert, E. and Thompson, T. A. (2009), 'Observable Signatures of the Accretion-Induced Collapse of White Dwarfs', *ArXiv e-prints* .

Meyer-Hofmeister, E., Schandl, S. and Meyer, F. (1997), 'The structure of the accretion disk rim in supersoft X-ray sources.', *Astronomy & Astrophysics* **321**, 245–253.

Mürset, U., Schild, H. and Vogel, M. (1996), 'Extragalactic symbiotic systems. III. The stellar components of the systems in the Magellanic Clouds.', *Astronomy & Astrophysics* **307**, 516–528.

NIST (2011), Atomic Spectra Database. Available at: `http://www.nist.gov/pml/data/asd.cfm`. Accessed: 01/12/2011.

Nomoto, K. (1982), 'Accreting white dwarf models for type I supernovae. I - Presupernova evolution and triggering mechanisms', *The Astrophysical Journal* **253**, 798–810.

Nordsieck, K. H. and Babler, B. (2011), *Standard Arc Lamp Calibration Setups for RSS Grating Spectroscopy*. Available at: `http://www.salt.ac.za`.

Norton, A. J., Wynn, G. A. and Somerscales, R. V. (2004), 'The Spin Periods and Magnetic Moments of White Dwarfs in Magnetic Cataclysmic Variables', *The Astrophysical Journal* **614**, 349–357.

Nowak, M. (2011), Loving isis - confessions of a former xspec user. Available at: `http://space.mit.edu/home/mnowak/isis_vs_xspec/`. Accessed: 04/10/2011.

Ogley, R. N., Chaty, S., Crocker, M., Eyres, S. P. S., Kenworthy, M. A., Richards, A. M. S., Rodríguez, L. F. and Stirling, A. M. (2002), 'A search for radio emission from Galactic supersoft X-ray sources', *Monthly Notices of the Royal Astronomical Society* **330**, 772–777.

Oliveira, A. S. and Steiner, J. E. (2006), GMOS-IFU Spectrocopy of the CBSS CAL83, *in* 'Revista Mexicana de Astronomia y Astrofisica Conference Series', Vol. 26 of *Revista Mexicana de Astronomia y Astrofisica, vol. 27*, p. 174.

Orio, M., della Valle, M., Massone, G. and Ogelman, H. (1994), 'Optical identification of the supersoft X-ray source 1E 0035.4 in the Small Magellanic Cloud', *Astronomy & Astrophysics* **289**, L11–L14.

Paczyński. B. (1967). 'Gravitational Waves and the Evolution of Close Binaries', *Acta Astronomica* **17**(3), 287–296.

Paerels, F., Rasmussen, A. P., Hartmann, H. W., Heise, J., Brinkman, A. C., de Vries, C. P. and den Herder, J. W. (2001), 'A high resolution spectroscopic observation of CAL 83 with XMM-Newton/RGS', *Astronomy & Astrophysics* **365**, L308–L311.

Pakull, M. W., Ilovaisky, S. A. and Chevalier, C. (1985), 'LHG 83 - Another outstanding X-ray binary in the LMC', *Space Science Reviews* **40**, 229–232.

Parmar, A. N., Kahabka, P., Hartmann, H. W., Heise, J. and Taylor, B. G. (1998), 'A BeppoSAX LECS observation of the super-soft X-ray source CAL 83', *Astronomy & Astrophysics* **332**, 199–203.

Peach, G. (1975), 'The Width of Spectral Lines', *Contemporary Physics* **16**(1), 17–34.

Plavec, M. and Kratochvil, P. (1964), 'Tables for the Roche model of close binaries', *Bulletin of the Astronomical Institutes of Czechoslovakia* **15**(5), 165–170.

Podsiadlowski, P. (2010), 'Supersoft X-ray sources and the progenitors of Type Ia supernovae', *Astronomische Nachrichten* **331**, 218.

Popham, R. and Di Stefano, R. (1996), Accretion Disks in Supersoft X-Ray Sources, *in* J. Greiner, ed., 'Supersoft X-Ray Sources', Vol. 472 of *Lecture Notes in Physics, Berlin Springer Verlag*, pp. 65–72.

Prialnik, D. and Kovetz, A. (1995), 'An extended grid of multicycle nova evolution models', *The Astrophysical Journal* **445**, 789–810.

Rappaport, S. and Di Stefano, R. (1996), Luminous Supersoft X-ray Sources, *in* J. van Paradijs, E. P. J. van den Heuvel, & E. Kuulkers, ed., 'Compact Stars in Binaries', Vol. 165 of *IAU Symposium*, p. 415.

Rauch, T. and Werner, K. (2010), 'Non-LTE model atmospheres for supersoft X-ray sources', *Astronomische Nachrichten* **331**, 146.

Reinsch, K., van Teeseling, A., King, A. R. and Beuermann, K. (2000), 'A limit-cycle model for the binary supersoft X-ray source RX J0513.9-6951', *Astronomy & Astrophysics* **354**, L37–L40.

Remillard, R. A., Rappaport, S. and Macri, L. M. (1995), 'Ionization nebulae surrounding CAL 83 and other supersoft X-ray sources', *The Astrophysical Journal* **439**, 646–651.

Robinson, K. (2007), *Spectroscopy: The Key to the Stars, Reading the Lines in Stellar Spectra*, Patrick Moore's Practical Astronomy Series, Springer, London.

Rybicki, G. B. and Lightman, A. P. (2004), *Radiative Processes in Astrophysics*, 1 edn, WILEY-VCH.

Scargle, J. D. (1982), 'Studies in astronomical time series analysis. II - Statistical aspects of spectral analysis of unevenly spaced data', *The Astrophysical Journal* **263**, 835–853.

Schenker, K., King, A. R., Kolb, U., Wynn, G. A. and Zhang, Z. (2002), 'AE Aquarii: how cataclysmic variables descend from supersoft binaries', *Monthly Notices of the Royal Astronomical Society* **337**, 1105–1112.

Schmid, H. M. (1989). 'Identification of the emission bands at 6830, 7088 A'. *Astronomy & Astrophysics* **211**, L31–L34.

Schmid, H. M., Krautter, J., Appenzeller, I., Barnstedt, J., Dumm, T., Fromm, A., Gölz, M., Grewing, M., Gringel, W., Haas, C., Hopfensitz, W., Kappelmann, N., Krämer, G., Lindenberger, A., Mandel, H., Mürset, U., Schild, H., Schmutz, W. and Widmann, H. (1999), 'ORFEUS spectroscopy of the O BT VI lines in symbiotic stars and the Raman scattering process', *Astronomy & Astrophysics* **348**, 950–971.

Schmid, H. M. and Schild, H. (1990), 'Spectropolarimetric observations of Raman scattered emission lines in symbiotic stars', *Astronomy & Astrophysics* **236**, L13–L16.

Schmidtke, P. C. and Cowley, A. P. (2006), 'X-Ray Pulsations in the Supersoft X-Ray Binary CAL 83', *The Astronomical Journal* **131**, 600–602.

Schmidtke, P. C., Cowley, A. P., Hutchings, J. B., Winter, K. and Crampton, D. (2004), 'A Revised Ephemeris and FUSE Observations of the Supersoft X-Ray Source CAL 83', *The Astronomical Journal* **127**, 469–476.

Schmidtke, P. C., Cowley, A. P., McGrath, T. K., Hutchings, J. B. and Crampton, D. (1994), '1E 0035.4-7230 and RX J0122.9-7521', *IAU Circulars* **6107**, 1.

Schmidtke, P. C., Cowley, A. P., McGrath, T. K., Hutchings, J. B. and Crampton, D. (1996), 'A Supersoft X-Ray Binary in the Small Magellanic Cloud', *The Astronomical Journal* **111**, 788.

Seward, F. D. and Charles, P. A. (2010), *Exploring the X-ray Universe*, 2 edn, Cambridge University Press, New York.

Seward, F. D. and Mitchell, M. (1981), 'X-ray survey of the Small Magellanic Cloud', *The Astrophysical Journal* **243**, 736–743.

Shakura, N. I. and Sunyaev, R. A. (1973), 'Black holes in binary systems. Observational Appearance', *Astronomy & Astrophysics* **24**, 337–355.

Smak, J. (1969), 'On the Rotational Velocities of Gaseous Rings in Close Binary Systems', *Acta Astronomica* **19**(2), 155–164.

Smale, A. P., Corbet, R. H. D., Charles, P. A., Ilovaisky, S. A., Mason, K. O., Motch, C., Mukai, K., Naylor, T., Parmar, A. N., van der Klis, M. and van Paradijs, J. (1988), 'CAL 83 - A 1-day period low-mass X-ray binary in the LMC', *Monthly Notices of the Royal Astronomical Society* **233**, 51–63.

Sommerfeld, A. (1928), *Atomic Structure and Spectral Lines*, 2 edn, Methuen & Co. Ltd., London.

Southwell, K. A., Livio, M., Charles, P. A., O'Donoghue, D. and Sutherland, W. J. (1996), 'The Nature of the Supersoft X-Ray Source RX J0513-69', *The Astrophysical Journal* **470**, 1065.

Southwell, K. A., Livio, M. and Pringle, J. E. (1997), 'Precessing Jets in Supersoft X-Ray Sources', *The Astrophysical Journal* **478**, L29.

Stanghellini, L., Blades, J. C., Osmer, S. J., Barlow, M. J. and Liu, X.-W. (1999), 'Hubble Space Telescope Images of Magellanic Cloud Planetary Nebulae: Data and Correlations across Morphological Classes', *The Astrophysical Journal* **510**, 687–702.

Stanghellini, L., Shaw, R. A., Balick, B., Mutchler, M., Blades, J. C. and Villaver, E. (2003), 'Space Telescope Imaging Spectrograph Slitless Observations of Small Magellanic Cloud Planetary Nebulae: A Study on Morphology, Emission-Line Intensity, and Evolution', *The Astrophysical Journal* **596**, 997–1014.

Stasińska, G. and Tylenda, R. (1986), 'Intermediate mass stars undergoing a very hot phase - Can we measure their temperatures?', *Astronomy & Astrophysics* **155**, 137–144.

Struve, O. (1929), 'The Stark Effect in Stellar Spectra', *The Astrophysical Journal* **69**, 173.

Suleimanov, V. F. and Ibragimov, A. A. (2003), 'Supersoft X-ray Sources: Basic Parameters', *Astronomy Reports* **47**, 197–205.

Tennyson, J. (2005), *Astronomical Spectroscopy: An Introduction to the Atomic and Molecular Physics of Astronomical Spectra*, Imperial College Press, London.

Trümper, J., Hasinger, G., Aschenbach, B., Bräuninger, H., Briel, U. G., Burkert, W., Fink, H., Pfeffermann, E., Pietsch, W., Predehl, P., Schmitt, J. H. M. M., Voges, W., Zimmermann, U. and Beuermann, K. (1991), 'X-ray survey of the Large Magellanic Cloud by ROSAT', *Nature* **349**, 579–583.

van den Heuvel, E. P. J., Bhattacharya, D., Nomoto, K. and Rappaport, S. A. (1992), 'Accreting white dwarf models for CAL 83, CAL 87 and other ultrasoft X-ray sources in the LMC', *Astronomy & Astrophysics* **262**, 97–105.

van der Marel, R. P., Alves, D. R., Hardy, E. and Suntzeff, N. B. (2002), 'New Understanding of Large Magellanic Cloud Structure, Dynamics, and Orbit from Carbon Star Kinematics', *The Astronomical Journal* **124**, 2639–2663.

van Groningen, E. (1993), 'Further Evidence for Raman Scattering in RR Tel', *Monthly Notices of the Royal Astronomical Society* **264**, 975.

van Teeseling, A. (1998), Supersoft X-ray Binaries: The Observational Status, *in* S. Howell, E. Kuulkers, & C. Woodward, ed., 'Wild Stars in the Old West', Vol. 137 of *Astronomical Society of the Pacific Conference Series*, pp. 385–394.

van Teeseling, A. and King, A. R. (1998), 'Wind-driven evolution of supersoft X-ray binaries with low-mass secondaries', *Astronomy & Astrophysics* **338**, 957–964.

van Teeseling, A., Reinsch, K., Hessman, F. V. and Beuermann, K. (1997), 'RX J0439.8-6809: a double-degenerate supersoft X-ray source?', *Astronomy & Astrophysics* **323**, L41–L44.

van Teeseling, A., Reinsch, K., Pakull, M. W. and Beuermann, K. (1998), 'Phase-resolved optical photometry and spectroscopy of the supersoft X-ray binary 1E 0035.4-7230', *Astronomy & Astrophysics* **338**, 947–956.

Vassiliadis, E., Dopita, M. A., Bohlin, R. C., Harrington, J. P., Ford, H. C., Meatheringham, S. J., Wood, P. R., Stecher, T. P. and Maran, S. P. (1998), 'Hubble Space Telescope Observations of Planetary Nebulae in the Magellanic Clouds. VI. Cycles 4 and 5 Ultraviolet Spectroscopy Using the Faint Object Spectrograph', *The Astrophysical Journal Supplement Series* **114**, 237.

Vassiliadis, E., Dopita, M. A., Meatheringham, S. J., Bohlin, R. C., Ford, H. C., Harrington, J. P., Wood, P. R., Stecher, T. P. and Maran, S. P. (1998), 'Hubble Space Telescope Observations of Planetary Nebulae in the Magellanic Clouds. VII. Cycle 3 and Archive Narrowband [O iii] 500.7 Nanometer Imaging', *The Astrophysical Journal* **503**, 253.

Verbunt, F. (1993), 'Origin and evolution of X-ray binaries and binary radio pulsars', *Annual Review of Astronomy & Astrophysics* **31**, 93–127.

Vidal, C. R., Cooper, J. and Smith, E. W. (1973), 'Hydrogen Stark-Broadening Tables', *The Astrophysical Journal Supplement Series* **25**, 37.

Vietri, M. (2008), *Foundations of High-Energy Astrophysics*, 1 edn, The University of Chicago Press, Chicago and London.

Wang, Q. (1991), 'N67 as an X-ray bright planetary nebula in the Small Magellanic Cloud', *Monthly Notices of the Royal Astronomical Society* **252**, 47P–49P.

Wang, Q. and Wu, X. (1992), 'A comprehensive X-ray study of the Small Magellanic Cloud', *The Astrophysical Journal Supplement Series* **78**, 391–401.

Warner, B. (1995), *Cataclysmic Variable Stars*, number 28 *in* 'Cambridge Astrophysics Series', 2 edn, Cambridge University Press, Cambridge.

Whitelock, P. A. (2003), A Comparison of Symbiotic and Normal Miras (invited review talks), *in* R. L. M. Corradi, J. Mikolajewska, & T. J. Mahoney, ed., 'Astronomical Society of the Pacific Conference Series'. Vol. 303 of *Astronomical Society of the Pacific Conference Series*, p. 41.

Wodaski, R. (2002), *The New CCD Astronomy*, 1 edn, New Astronomy Press, Duvall.

Wyatt, S. P. and Cahn, J. H. (1983), 'Kinematics and ages of Mira variables in the greater solar neighborhood', *The Astrophysical Journal* **275**, 225–239.

XMM-Newton Science Operations Centre Team (2011), *Users Guide to the XMM-Newton Science Analysis System.* Available at: `http://xmm.esac.esa.int/external/xmm_user_support/documentation/index.shtml`.

Yungelson, L., Livio, M., Truran, J. W., Tutukov, A. and Fedorova, A. (1996), 'A Model for the Galactic Population of Binary Supersoft X-Ray Sources', *The Astrophysical Journal* **466**, 890–910.

Zhang, E., Robinson, E. L., Stiening, R. F. and Horne, K. (1995), 'The 71 Second Oscillation in the Light Curve of the Old Nova DQ Herculis', *The Astrophysical Journal* **454**, 447.

Zombeck, M. V. (1990), *Handbook of Space Astronomy and Astrophysics*, 2 edn, Cambridge University Press.

This research has made use of NASA's Astrophysics Data System.

Appendix A
Physical Constants

Constant	Symbol	Value
Speed of light in vacuum	c	2.998×10^{10} cm s^{-1}
Gravitational constant	G	6.672×10^{-8} dyn cm^2 g^{-2}
Planck's constant	h	6.626×10^{-27} erg s
Electron charge	e	4.803×10^{-10} esu
Electron mass	m_e	9.109×10^{-28} g
Proton mass	m_p	1.673×10^{-24} g
Boltzmann constant	k	1.381×10^{-16} erg K^{-1}
Stefan-Boltzmann constant	σ	5.671×10^{-5} erg cm^{-2} K^{-4} s^{-1}
Thomson cross-section	σ_T	0.665×10^{-24} cm^{-2}

Table A.1: Fundamental physical constants. (Adopted from Zombeck 1990, p. 10.)

	Symbol	Value
Solar mass	$M_\odot$	1.989×10^{33} g
Solar radius	$R_\odot$	6.960×10^{10} cm
Solar luminosity	$L_\odot$	3.826×10^{33} erg s^{-1}

Table A.2: Solar properties. (Adopted from Zombeck 1990, p. 25.)

Appendix B
Ionization potentials

Atom		Stage of ionization I	II	III	IV	V	VI	VII	VIII	IX	X	XI	XII
		ev	ev	ev	ev	ev	ev	ev	ev	ev	ev	ev	
1	H	13·595											
2	He	24·581	54·403										
3	Li	5·390	75·619	122·419									
4	Be	9·320	18·206	153·850	217·657								
5	B	8·296	25·149	37·920	259·298	340·127							
6	C	11·256	24·376	47·871	64·476	391·986	489·84						
7	N	14·53	29·593	47·426	77·450	97·863	551·925	666·83					
8	O	13·614	35·108	54·886	77·394	113·873	138·080	739·114	871·12				
9	F	17·418	34·98	62·646	87·14	114·214	157·117	185·139	953·60	1 102·0			
10	Ne	21·559	41·07	63·5	97·02	126·3	157·91	207·2	239·1	1 195·6	1 360·4		
11	Na	5·138	47·29	71·65	98·88	138·37	172·09	208·444	264·155	299·78	1 464·8	1 646·1	
12	Mg	7·644	15·031	80·12	109·29	141·23	186·49	224·90	265·957	327·90	367·36	1 761·2	
13	Al	5·984	18·823	28·44	119·96	153·77	190·42	241·38	284·53	330·1	398·5	441·9	
14	Si	8·149	16·34	33·46	45·13	166·73	205·11	246·41	303·07	350·96	401·3	476·0	
15	P	10·484	19·72	30·156	51·354	65·007	220·414	263·31	309·26	371·6	424·3	479·4	
16	S	10·357	23·4	35·0	47·29	72·5	88·029	280·99	328·80	378·95	447	505·8	
17	Cl	13·01	23·80	39·90	53·5	67·80	96·7	114·27	348·3	400·7	455·3	530·9	
18	Ar	15·755	27·62	40·90	59·79	75·0	91·3	124·0	143·46	422·6	479·4	538·9	
19	K	4·339	31·81	46	60·90	82·6	99·7	118	155	175·94	503·8	564	
20	Ca	6·111	11·868	51·21	67	84·39	109	128	143·3	188	211·3	591·8	
21	Sc	6·54	12·80	24·75	73·9	92	111	139	159	180	226	250	
22	Ti	6·82	13·57	27·47	43·24	99·8	120	141	172	193	217	266	
23	V	6·74	14·65	29·31	48	65	129	151	174	206	230·5	258	
24	Cr	6·764	16·49	30·95	50	73	91	161	185	210	249	272	
25	Mn	7·432	15·636	33·69	53	76	100	119	196	222	248	288	
26	Fe	7·87	16·18	30·643	57	79	103	130	151	235	262	290	
27	Co	7·86	17·05	33·49	53	83	108	134	164	190	290	305	
28	Ni	7·633	18·15	35·16	56	79	112	140	169	202	230	321	
29	Cu	7·724	20·29	36·83	59	82	110	140	170	206	241	265	
30	Zn	9·391	17·96	39·70	62	86	115	145	180	210	250		

Table B.1: Ionization potentials. (Adopted from Allen 1964, p. 37-40.)

Table B.1: Continued.

Atom		Stage of ionization										
		I	II	III	IV	V	VI	VII	VIII	IX	X	XI	XII
		ev	ev	ev	ev	ev	ev	ev	ev	ev	ev	ev	ev
31	Ga	6·00	20·51	30·70	64·2	90	118	144	174	218	255		
32	Ge	7·88	15·93	34·21	45·7	93·4	113	148	177	212	262		
33	As	9·81	18·63	28·34	50·1	62·6	127·5	150	182	218	253		
34	Se	9·75	21·5	32	43	68	82	155	187	223	260		
35	Br	11·84	21·6	35·9	47·3	59·7	88·6	103	193	228	266		
36	Kr	13·996	24·56	36·9	52	65	79	110	126	234	270		
37	Rb	4·176	27·5	40	52	71	85	100	135	151	277		
38	Sr	5·692	11·027	43	57	72	92	107	124	162	179	324	
39	Y	6·38	12·23	20·5	62	77	93	116	131	148	191	206	
40	Zr	6·84	13·13	22·98	34·33	82	99	117	141	157	176	222	
41	Nb	6·88	14·32	25·04	38·3	50	103	125	143	167	185	203	
42	Mo	7·10	16·15	27·13	46·4	61·2	68	126	153	169	197	210	
43	Tc	7·28	15·26	31	43	59	76	94	161	183	199	224	
44	Ru	7·364	16·76	28·46	46	63	81	100	119	193	216	225	
45	Rh	7·46	18·07	31·05	46	67	85	105	126	147	226	250	
46	Pd	8·33	19·42	32·92	49	66	90	110	132	155	178	261	
47	Ag	7·574	21·48	34·82	52	70	89	116	139	162	187		
48	Cd	8·991	16·904	37·47	55	73	94	115	146	170	195		
49	In	5·785	18·86	28·03	54·4	77	98	120	144	178	204		
50	Sn	7·342	14·628	30·49	40·72	72·3	103	126	150	176	213		
51	Sb	8·639	16·5	25·3	44·1	56	108	132	157	184	211		
52	Te	9·01	18·6	31	38	60	72	137	164	192	220		
53	I	10·454	19·09	32	42	66	81	99	170	200	229		
54	Xe	12·127	21·2	32·1	46	57	82	100	121	213	238		
55	Cs	3·893	25·1	35	46	62	74	101	120	144	253		
56	Ba	5·210	10·001	36	49	62	80	93	120	143	157		
57	La	5·61	11·43	19·17	52	66	80	100	114	144	165	204	
58	Ce	6·9	12·3	20	35	70	85	100	122	137	165	189	
59	Pr	5·8					89	106	122	146	162	197	
60	Nd	6·3						110	128	147	171		
61	Pm								135	154	173		
62	Sm	5·6	11·3							161	181		

Table B.1: Continued.

Atom	Stage of ionization										
	I	II	III	IV	V	VI	VII	VIII	IX	X	XI	XII
	ev	ev	ev	ev	ev	ev	ev	ev	ev	ev	ev	
63 Eu	5·67	11·2								187		
64 Gd	6·16	12										
65 Tb	6·7											
66 Dy	6·8											
67 Ho	6											
68 Er	6											
69 Tm	6											
70 Yb	6·2	12·1										
71 Lu	6·1	15	19									
72 Hf	7	14·9	21	31								
73 Ta	7·88	16·2	22	33	45							
74 W	7·98	17·7	24	35	48	61						
75 Re	7·87	16·6	26	38	51	64	79					
76 Os	8·7	17	25	40	54	68	83	99				
77 Ir	9	17	27	39	57	72	88	104	121			
78 Pt	9·0	18·56	28	41	55	75	92	109	127	146		
79 Au	9·22	20·5	30	44	58	73	96	114	133	153		
80 Hg	10·43	18·751	34·2	46	61	77	94	120	139	159		
81 Tl	6·106	20·42	29·8	50·7	64	81	98	116	145	166		
82 Pb	7·415	15·028	31·93	42·31	68·8	84	103	122	142	173		
83 Bi	7·287	16·68	25·56	45·3	56·0	88·3	107	127	148	169		
84 Po	8·43	19	27	38	61	73	112	132	154	176		
85 At	9·3	20	29	41	51	78	91	138	160	183		
86 Rn	10·746	21	29	44	55	67	97	111	166	190		
87 Fa	4·0	22	33	43	59	71	84	117	133	197		
88 Ra	5·277	10·144	34	46	58	76	89	103	140	156		
89 Ac	6·9	12·1	20	49	62	76	95	109	123	164		
90 Th	6	12	20	29·2	65	80	94	115	130	145		
91 Pa						84	100	115	138	154		
92 U	6						104	121	137	162		

Atom		Stage of ionization							
		XII	XIII	XIV	XV	XVI	XVII	XVIII	XIX	XX
		ev	ev	ev	ev	ev	ev	ev	ev
12	Mg	1 959							
13	Al	2 085·5	2 299						
14	Si	523·2	2 436	2 666					
15	P	560·3	611·4	2 815	3 061				
16	S	566	651	706	3 220	3 482			
17	Cl	593	663	749	807	3 654	3 931		
18	Ar	621	687	755	854	916	4 115	4 407	
19	K	629	717	788	870	966	1 031	4 603	4 910
20	Ca	655	727	820	896	990	1 084	1 153	5 119
21	Sc	687	758	830	930	1 010	1 115	1 210	1 282
22	Ti	291	788	864	941	1 046	1 132	1 245	1 341
23	V	309	336	897	976	1 057	1 170	1 260	1 380
24	Cr	299	355	384	1 013	1 095	1 182	1 301	1 395
25	Mn	315	350	404	435	1 136	1 222	1 313	1 438
26	Fe	330	355	390	457	489	1 266	1 354	1 450
27	Co	337	380	412	444	512	547	1 403	1 495
28	Ni	350	385	430	455	500	530	607	1 541
29	Cu	370	400	440	480	520	560	630	671
30	Zn	311	420	450	490	540	580	620	700

Table B.1: Continued.

Appendix C
Stark-broadening tables

Vidal et al. (1973) provides Stark-broadening tables for the first four Lyman lines and the first four Balmer lines for various temperatures and electron densities. A selection of the Hα and Hβ tables for densities of 10^{13} cm^{-3}, 10^{14} cm^{-3}, 10^{15} cm^{-3} and 10^{16} cm^{-3} are given in this appendix. For other densities and for tables of Lα, Lβ, Lγ and Lδ, see Vidal et al. (1973).

The first line of each table gives the upper and lower state principal quantum numbers, as well as the rest wavelength of the transition. In the second line, the electron density N_e is provided. It is assumed that the ion density is equal to the electron density. For a hydrogen gas with ion density N_i, the mean electric field strength is (e.g. Lang 1999, p.196)

$$F_0 = e\left(\frac{4\pi N_i}{3}\right)^{2/3} \approx 1.25 \times 10^{-9} N_i^{2/3} \approx 1.25 \times 10^{-9} N_e^{2/3} \; . \qquad \text{(C.1)}$$

The dispersion per unit field strength (in Å statvolt^{-1}) is defined as the quantity

$$\Delta\alpha = \frac{\Delta\lambda}{F_0} \qquad \text{(C.2)}$$

implying

$$F_0 = \frac{\Delta\alpha}{\Delta\lambda} \qquad \text{(C.3)}$$

and it can be seen that the second value on the second line of each table represents F_0 (as calculated from N_e).

The first column of the table gives the value of $\Delta\alpha$, which can be converted to $\Delta\lambda$ (in Å) by multiplying by F_0. The rest of the columns provide the normalized function $S(\Delta\alpha)$ for different temperatures, which are specfied on top of each column. In each column, the values of the unified Stark theory calculations are provided in brackets, and in front of the brackets the values obtained from the convolution of the unified theory with the thermal Doppler profile for the corresponding temperature are given.

The table only provides function values for $\Delta\alpha \geq 0$, but as the model profile is symmetrical, the blue half of the profile ($\Delta\alpha < 0$) will be a mirror image of the red half.

Table C.1: Stark-broadening table for Hα, with $N_e = 10^{13}$ cm^{-3}. (Adopted from Vidal et al. 1973, Table 44.)

N UPPER = 3 N LOWER = 2 WAVELENGTH = 6562.81 ANGSTROM

ELECTRON DENSITY = 1.000+013 CM**(-3) DLAMBDA/DALPHA = 5.8020-001 ASYMPTOTE = 1.2803-003*DALPHA**(-5/2)

ALPHA	2500 K	5000 K	10000 K	20000 K	40000 K
0	2.215 0 (5.429 1)	1.595 0 (6.459 1)	1.141 0 (7.910 1)	8.131 -1 (9.921 1)	5.777 -1 (1.271 2)
1.000 -4	2.215 0 (5.421 1)	1.595 0 (6.445 1)	1.141 0 (7.880 1)	8.131 -1 (9.859 1)	5.777 -1 (1.258 2)
1.585 -4	2.215 0 (5.410 1)	1.595 0 (6.423 1)	1.141 0 (7.836 1)	8.131 -1 (9.768 1)	5.777 -1 (1.238 2)
2.512 -4	2.215 0 (5.381 1)	1.595 0 (6.368 1)	1.141 0 (7.728 1)	8.131 -1 (9.545 1)	5.777 -1 (1.191 2)
3.981 -4	2.215 0 (5.311 1)	1.595 0 (6.236 1)	1.141 0 (7.470 1)	8.131 -1 (9.032 1)	5.777 -1 (1.088 2)
6.310 -4	2.215 0 (5.142 1)	1.595 0 (5.929 1)	1.141 0 (6.898 1)	8.131 -1 (7.970 1)	5.777 -1 (8.969 1)
1.000 -3	2.215 0 (4.769 1)	1.595 0 (5.289 1)	1.141 0 (5.809 1)	8.131 -1 (6.197 1)	5.777 -1 (6.297 1)
1.585 -3	2.215 0 (4.060 1)	1.595 0 (4.204 1)	1.141 0 (4.228 1)	8.131 -1 (4.068 1)	5.777 -1 (3.712 1)
2.512 -3	2.215 0 (3.032 1)	1.595 0 (2.878 1)	1.141 0 (2.636 1)	8.131 -1 (2.317 1)	5.777 -1 (1.957 1)
3.981 -3	2.215 0 (2.003 1)	1.595 0 (1.777 1)	1.141 0 (1.535 1)	8.131 -1 (1.292 1)	5.777 -1 (1.065 1)
6.310 -3	2.214 0 (1.296 1)	1.594 0 (1.141 1)	1.141 0 (9.942 0)	8.130 -1 (8.620 0)	5.776 -1 (7.476 0)
1.000 -2	2.211 0 (9.205 0)	1.594 0 (8.597 0)	1.141 0 (8.052 0)	8.129 -1 (7.581 0)	5.776 -1 (7.192 0)
1.585 -2	2.206 0 (6.763 0)	1.592 0 (6.699 0)	1.140 0 (6.673 0)	8.127 -1 (6.661 0)	5.775 -1 (6.689 0)
2.512 -2	2.193 0 (4.603 0)	1.587 0 (4.575 0)	1.139 0 (4.568 0)	8.120 -1 (4.569 0)	5.773 -1 (4.577 0)
3.981 -2	2.160 0 (2.491 0)	1.574 0 (3.009 0)	1.134 0 (3.019 0)	8.104 -1 (3.018 0)	5.767 -1 (3.013 0)
6.310 -2	2.079 0 (1.561 0)	1.544 0 (1.628 0)	1.123 0 (1.677 0)	8.063 -1 (1.712 0)	5.752 -1 (1.737 0)
1.000 -1	1.889 0 (5.780 -1)	1.470 0 (6.030 -1)	1.095 0 (6.225 -1)	7.962 -1 (6.373 -1)	5.716 -1 (6.482 -1)
1.585 -1	1.487 0 (1.774 -1)	1.300 0 (1.797 -1)	1.029 0 (1.811 -1)	7.714 -1 (1.818 -1)	5.626 -1 (1.821 -1)
2.512 -1	8.188 -1 (5.351 -2)	9.548 -1 (5.282 -2)	8.791 -1 (5.210 -2)	7.125 -1 (5.142 -2)	5.405 -1 (5.083 -2)
3.981 -1	1.924 -1 (1.669 -2)	4.424 -1 (1.622 -2)	5.927 -1 (1.579 -2)	5.836 -1 (1.544 -2)	4.889 -1 (1.514 -2)
6.310 -1	1.181 -2 (5.378 -3)	6.826 -2 (5.153 -3)	2.215 -1 (4.962 -3)	3.538 -1 (4.806 -3)	3.798 -1 (4.682 -3)
1.000 0	2.034 -3 (1.769 -3)	2.786 -3 (1.677 -3)	2.040 -2 (1.600 -3)	1.013 -1 (1.537 -3)	2.016 -1 (1.487 -3)
1.585 0	6.177 -4 (5.875 -4)	6.145 -4 (5.518 -4)	7.059 -4 (5.213 -4)	4.988 -3 (4.962 -4)	4.140 -2 (4.758 -4)
2.512 0	2.918 -4 (1.981 -4)	1.919 -4 (1.847 -4)	1.877 -4 (1.729 -4)	1.981 -4 (1.651 -4)	9.808 -4 (1.551 -4)
3.981 0	6.776 -5 (6.727 -5)	6.336 -5 (6.242 -5)	5.980 -5 (5.800 -5)	5.777 -5 (5.419 -5)	5.881 -5 (5.105 -5)
6.310 0	2.292 -5 (2.285 -5)	2.134 -5 (2.122 -5)	1.965 -5 (1.962 -5)	1.862 -5 (1.818 -5)	1.764 -5 (1.696 -5)
1.000 1	7.722 -6 (7.713 -6)	7.230 -6 (7.213 -6)	6.703 -6 (6.672 -6)	6.207 -6 (6.149 -6)	5.797 -6 (5.687 -6)
1.585 1	2.568 -6 (2.566 -6)	2.437 -6 (2.435 -6)	2.273 -6 (2.269 -6)	2.099 -6 (2.091 -6)	1.936 -6 (1.922 -6)
2.512 1	8.383 -7 (8.381 -7)	8.108 -7 (8.105 -7)	7.671 -7 (7.665 -7)	7.124 -7 (7.114 -7)	6.551 -7 (6.532 -7)
3.981 1	2.687 -7 (2.686 -7)	2.648 -7 (2.648 -7)	2.555 -7 (2.554 -7)	2.407 -7 (2.406 -7)	2.226 -7 (2.223 -7)
6.310 1	8.490 -8 (8.490 -8)	8.490 -8 (8.490 -8)	8.356 -8 (8.355 -8)	8.034 -8 (8.032 -8)	7.533 -8 (7.530 -8)
1.000 2	2.663 -8 (2.663 -8)	2.684 -8 (2.684 -8)	2.683 -8 (2.682 -8)	2.634 -8 (2.633 -8)	2.520 -8 (2.520 -8)
1.585 2	8.338 -9 (8.338 -9)	8.423 -9 (8.423 -9)	8.469 -9 (8.489 -9)	8.473 -9 (8.472 -9)	8.288 -9 (8.288 -9)
2.512 2	2.613 -9 (2.613 -9)	2.637 -9 (2.637 -9)	2.665 -9 (2.665 -9)	2.685 -9 (2.685 -9)	2.674 -9 (2.674 -9)
3.981 2	8.208-10 (8.208-10)	8.266-10 (8.266-10)	8.346-10 (8.346-10)	8.436-10 (8.436-10)	8.494-10 (8.494-10)
6.310 2	2.583-10 (2.583-10)	2.596-10 (2.596-10)	2.616-10 (2.616-10)	2.642-10 (2.642-10)	2.671-10 (2.671-10)
1.000 3	8.142-11 (8.142-11)	8.170-11 (8.170-11)	8.214-11 (8.214-11)	8.279-11 (8.279-11)	8.369-11 (8.369-11)
1.585 3		2.575-11 (2.575-11)	2.584-11 (2.584-11)	2.599-11 (2.599-11)	2.622-11 (2.622-11)
2.512 3		8.126-12 (8.126-12)	8.145-12 (8.145-12)	8.179-12 (8.179-12)	8.229-12 (8.229-12)
3.981 3			2.570-12 (2.570-12)	2.576-12 (2.576-12)	2.588-12 (2.588-12)
6.310 3				8.129-13 (8.129-13)	8.152-13 (8.152-13)
1.000 4				2.567-13 (2.567-13)	2.571-13 (2.571-13)
1.585 4					8.118-14 (8.118-14)

N UPPER = 3 N LOWER = 2 WAVELENGTH = 6562.81 ANGSTROM

ELECTRON DENSITY = 1.000E+14 CM**(-3) DLAMBDA/DALPHA = 2.693D+000 ASYMPTOTE = 1.2803-003*DALPHA**(-5/2)

ALPHA	2500 K	5000 K	10000 K	20000 K	40000 K
0	8.041 0 (3.641 1)	6.165 0 (4.257 1)	4.656 0 (4.905 1)	3.468 0 (5.849 1)	2.538 0 (7.208 1)
2.512 -4	8.041 0 (3.629 1)	6.165 0 (4.238 1)	4.656 0 (4.871 1)	3.468 0 (5.783 1)	2.538 0 (7.073 1)
3.981 -4	8.041 0 (3.611 1)	6.165 0 (4.210 1)	4.656 0 (4.821 1)	3.467 0 (5.687 1)	2.538 0 (6.879 1)
6.310 -4	8.040 0 (3.767 1)	6.165 0 (4.140 1)	4.656 0 (4.699 1)	3.467 0 (5.460 1)	2.538 0 (6.439 1)
1.000 -3	8.039 0 (3.663 1)	6.164 0 (3.977 1)	4.656 0 (4.422 1)	3.467 0 (4.970 1)	2.538 0 (5.566 1)
1.585 -3	8.036 0 (3.431 1)	6.163 0 (3.626 1)	4.655 0 (3.870 1)	3.467 0 (4.089 1)	2.538 0 (4.208 1)
2.512 -3	8.028 0 (2.981 1)	6.159 0 (3.010 1)	4.654 0 (3.004 1)	3.467 0 (2.915 1)	2.538 0 (2.721 1)
3.981 -3	8.007 0 (2.389 1)	6.151 0 (2.204 1)	4.651 0 (2.048 1)	3.465 0 (1.846 1)	2.537 0 (1.610 1)
6.310 -3	7.957 0 (1.598 1)	6.130 0 (1.472 1)	4.642 0 (1.329 1)	3.462 0 (1.177 1)	2.536 0 (1.026 1)
1.000 -2	7.831 0 (1.358 1)	6.078 0 (9.918 0)	4.621 0 (9.258 0)	3.454 0 (8.629 0)	2.533 0 (8.063 0)
1.585 -2	7.526 0 (7.062 0)	5.949 0 (6.882 0)	4.569 0 (6.760 0)	3.433 0 (6.687 0)	2.525 0 (6.648 0)
2.512 -2	6.810 0 (4.693 0)	5.639 0 (4.637 0)	4.439 0 (4.596 0)	3.381 0 (4.583 0)	2.505 0 (4.573 0)
3.981 -2	5.357 0 (2.949 0)	4.935 0 (2.998 0)	4.130 0 (3.020 0)	3.254 0 (3.048 0)	2.455 0 (3.023 0)
6.310 -2	3.066 0 (1.491 0)	3.562 0 (1.564 0)	3.452 0 (1.621 0)	2.956 0 (1.660 0)	2.334 0 (1.713 0)
1.000 -1	1.027 0 (5.619 -1)	1.670 0 (5.902 -1)	2.221 0 (6.126 -1)	2.326 0 (6.302 -1)	2.057 0 (6.431 -1)
1.585 -1	2.436 -1 (1.815 -1)	3.879 -1 (1.865 -1)	7.926 -1 (1.856 -1)	1.288 0 (1.850 -1)	1.501 0 (1.856 -1)
2.512 -1	6.380 -2 (5.752 -2)	7.272 -2 (5.648 -2)	1.171 -1 (9.530 -2)	3.222 -1 (5.410 -2)	6.877 -1 (5.299 -2)
3.981 -1	1.927 -2 (1.856 -2)	1.937 -2 (1.787 -2)	2.069 -2 (1.716 -2)	3.016 -2 (1.657 -2)	1.102 -1 (1.603 -2)
6.310 -1	6.237 -3 (6.151 -3)	6.005 -3 (5.832 -3)	5.880 -3 (5.528 -3)	6.031 -3 (5.264 -3)	7.522 -3 (5.040 -3)
1.000 0	2.078 -3 (2.067 -3)	1.964 -3 (1.948 -3)	1.864 -3 (1.824 -3)	1.801 -3 (1.718 -3)	1.603 -3 (1.629 -3)
1.585 0	8.985 -4 (6.970 -4)	6.547 -4 (6.518 -4)	6.130 -4 (6.076 -4)	5.778 -4 (5.674 -4)	5.532 -4 (5.328 -4)
2.512 0	2.358 -4 (2.356 -4)	2.212 -4 (2.209 -4)	2.061 -4 (2.054 -4)	1.919 -4 (1.906 -4)	1.799 -4 (1.774 -4)
3.981 0	7.903 -5 (7.900 -5)	7.482 -5 (7.477 -5)	6.987 -5 (6.977 -5)	6.475 -5 (6.457 -5)	6.081 -5 (5.968 -5)
6.310 0	2.609 -5 (2.609 -5)	2.507 -5 (2.507 -5)	2.365 -5 (2.364 -5)	2.198 -5 (2.196 -5)	2.028 -5 (2.024 -5)
1.000 1	8.453 -6 (8.453 -6)	8.267 -6 (8.266 -6)	7.928 -6 (7.926 -6)	7.449 -6 (7.446 -6)	6.892 -6 (6.886 -6)
1.585 1	2.692 -6 (2.691 -6)	2.674 -6 (2.674 -6)	2.614 -6 (2.614 -6)	2.499 -6 (2.499 -6)	2.338 -6 (2.337 -6)
2.512 1	8.472 -7 (8.472 -7)	8.506 -7 (8.506 -7)	8.453 -7 (8.453 -7)	8.247 -7 (8.247 -7)	7.855 -7 (7.854 -7)
3.981 1	2.653 -7 (2.653 -7)	2.676 -7 (2.676 -7)	2.689 -7 (2.689 -7)	2.670 -7 (2.670 -7)	2.594 -7 (2.597 -7)
6.310 1	8.387 -8 (8.387 -8)	8.382 -8 (8.382 -8)	8.460 -8 (8.460 -8)	8.499 -8 (8.499 -8)	8.427 -8 (8.427 -8)
1.000 2	2.606 -8 (2.606 -8)	2.625 -8 (2.625 -8)	2.650 -8 (2.650 -8)	2.676 -8 (2.676 -8)	2.687 -8 (2.687 -8)
1.585 2	9.191 -9 (8.191 -9)	8.235 -9 (8.235 -9)	8.300 -9 (8.300 -9)	8.385 -9 (8.385 -9)	8.464 -9 (8.468 -9)
2.512 2	2.579 -9 (2.579 -9)	2.589 -9 (2.589 -9)	2.604 -9 (2.604 -9)	2.626 -9 (2.626 -9)	2.654 -9 (2.654 -9)
3.981 2		8.154-10 (8.154-10)	8.188-10 (8.188-10)	8.238-10 (8.238-10)	8.312-10 (8.312-10)
6.310 2			2.579-10 (2.579-10)	2.590-10 (2.590-10)	2.607-10 (2.607-10)
1.000 3			8.133-11 (8.133-11)	8.156-11 (8.156-11)	8.195-11 (8.195-11)
1.585 3				2.572-11 (2.572-11)	2.580-11 (2.580-11)
2.512 3					8.136-12 (8.136-12)
3.981 3					2.568-12 (2.568-12)

Table C.2: Stark-broadening table for Hα, with $N_e = 10^{14}$ cm^{-3}. (Adopted from Vidal et al. 1973, Table 46.)

Table C.3: Stark-broadening table for Hα, with $N_e = 10^{15}$ cm^{-3}. (Adopted from Vidal et al. 1973, Table 48.)

N UPPER = 3 N LOWER = 2 WAVELENGTH = 6562.81 ANGSTROM

ELECTRON DENSITY = 1.000+015 CM**(-3) DLAMBDA/DALPHA = 1.2500+001 ASYMPTOTE = 1.2803-003*DALPHA**(-5/2)

ALPHA	2500 K	5000 K	10000 K	20000 K	40000 K
0	1.962 1 (3.076 1)	1.655 1 (3.206 1)	1.360 1 (3.459 1)	1.097 1 (3.867 1)	8.716 0 (4.487 1)
3.981 -4	1.962 1 (3.065 1)	1.655 1 (3.192 1)	1.360 1 (3.438 1)	1.097 1 (3.832 1)	8.715 0 (4.425 1)
6.310 -4	1.961 1 (3.049 1)	1.654 1 (3.171 1)	1.360 1 (3.407 1)	1.097 1 (3.782 1)	8.714 0 (4.334 1)
1.000 -3	1.959 1 (3.009 1)	1.652 1 (3.119 1)	1.359 1 (3.333 1)	1.097 1 (3.663 1)	8.713 0 (4.124 1)
1.585 -3	1.953 1 (2.914 1)	1.647 1 (2.999 1)	1.356 1 (3.163 1)	1.096 1 (3.400 1)	8.708 0 (3.689 1)
2.512 -3	1.933 1 (2.707 1)	1.634 1 (2.744 1)	1.350 1 (2.820 1)	1.093 1 (2.906 1)	8.697 0 (2.960 1)
3.981 -3	1.869 1 (2.319 1)	1.603 1 (2.292 1)	1.336 1 (2.262 1)	1.087 1 (2.201 1)	8.669 0 (2.084 1)
6.310 -3	1.719 1 (1.762 1)	1.527 1 (1.694 1)	1.299 1 (1.611 1)	1.070 1 (1.502 1)	8.599 0 (1.365 1)
1.000 -2	1.435 1 (1.192 1)	1.359 1 (1.135 1)	1.214 1 (1.073 1)	1.031 1 (1.006 1)	8.427 0 (9.366 0)
1.585 -2	9.803 0 (7.635 0)	1.041 1 (7.355 0)	1.032 1 (7.108 0)	9.405 0 (6.909 0)	8.013 0 (6.766 0)
2.512 -2	5.506 0 (4.852 0)	6.256 0 (4.779 0)	7.187 0 (4.698 0)	7.551 0 (4.634 0)	7.077 0 (4.594 0)
3.981 -2	3.019 0 (2.892 0)	3.255 0 (2.972 0)	3.793 0 (3.012 0)	4.684 0 (3.031 0)	5.264 0 (3.030 0)
6.310 -2	1.461 0 (1.416 0)	1.595 0 (1.508 0)	1.755 0 (1.583 0)	2.091 0 (1.650 0)	2.771 0 (1.669 0)
1.000 -1	5.664 -1 (5.544 -1)	6.100 -1 (5.833 -1)	6.600 -1 (6.008 -1)	7.545 -1 (6.266 -1)	9.392 -1 (6.410 -1)
1.585 -1	1.919 -1 (1.899 -1)	1.975 -1 (1.932 -1)	2.036 -1 (1.946 -1)	2.148 -1 (1.937 -1)	2.425 -1 (1.927 -1)
2.512 -1	6.339 -2 (6.314 -2)	6.272 -2 (6.219 -2)	6.165 -2 (6.052 -2)	6.097 -2 (5.868 -2)	6.176 -2 (5.684 -2)
3.981 -1	2.108 -2 (2.105 -2)	2.039 -2 (2.032 -2)	1.956 -2 (1.943 -2)	1.876 -2 (1.850 -2)	1.814 -2 (1.763 -2)
6.310 -1	7.109 -3 (7.104 -3)	6.803 -3 (6.794 -3)	6.436 -3 (6.419 -3)	6.065 -3 (6.033 -3)	5.737 -3 (5.675 -3)
1.000 0	2.409 -3 (2.409 -3)	2.291 -3 (2.290 -3)	2.158 -3 (2.156 -3)	2.016 -3 (2.012 -3)	1.883 -3 (1.875 -3)
1.585 0	8.014 -4 (8.013 -4)	7.680 -4 (7.679 -4)	7.251 -4 (7.248 -4)	6.767 -4 (6.762 -4)	6.281 -4 (6.271 -4)
2.512 0	2.632 -4 (2.632 -4)	2.554 -4 (2.554 -4)	2.438 -4 (2.438 -4)	2.290 -4 (2.289 -4)	2.124 -4 (2.123 -4)
3.981 0	8.492 -5 (8.491 -5)	8.363 -5 (8.362 -5)	8.183 -5 (8.108 -5)	7.714 -5 (7.713 -5)	7.207 -5 (7.205 -5)
6.310 0	2.696 -5 (2.696 -5)	2.688 -5 (2.688 -5)	2.649 -5 (2.649 -5)	2.566 -5 (2.565 -5)	2.432 -5 (2.431 -5)
1.000 1	8.470 -6 (8.470 -6)	8.509 -6 (8.509 -6)	8.499 -6 (8.498 -6)	8.379 -6 (8.379 -6)	8.095 -6 (8.095 -6)
1.585 1	2.651 -6 (2.651 -6)	2.670 -6 (2.670 -6)	2.687 -6 (2.687 -6)	2.686 -6 (2.686 -6)	2.646 -6 (2.646 -6)
2.512 1	8.298 -7 (8.298 -7)	8.358 -7 (8.358 -7)	8.430 -7 (8.430 -7)	8.492 -7 (8.492 -7)	8.489 -7 (8.489 -7)
3.981 1	2.603 -7 (2.603 -7)	2.618 -7 (2.618 -7)	2.639 -7 (2.639 -7)	2.664 -7 (2.664 -7)	2.685 -7 (2.685 -7)
6.310 1	8.185 -8 (8.185 -8)	8.218 -8 (8.218 -8)	8.269 -8 (8.269 -8)	8.341 -8 (8.341 -8)	8.427 -8 (8.427 -8)
1.000 2		2.586 -8 (2.586 -8)	2.597 -8 (2.597 -8)	2.614 -8 (2.614 -8)	2.638 -8 (2.638 -8)
1.585 2			8.171 -9 (8.171 -9)	8.210 -9 (8.210 -9)	8.269 -9 (8.269 -9)
2.512 2			2.575 -9 (2.575 -9)	2.584 -9 (2.584 -9)	2.597 -9 (2.597 -9)
3.981 2				8.143-10 (8.143-10)	8.172-10 (8.172-10)
6.310 2					2.575-10 (2.575-10)
1.000 3					8.126-11 (8.126-11)

N UPPER = 3 N LOWER = 2 WAVELENGTH = 6562.81 ANGSTROM

ELECTRON DENSITY = 1.000+016 CM**(-3) DLAMBDA/DALPHA = 5.8020+001 ASYMPTOTE = 1.2803-003*DALPHA**(-5/2)

ALPHA	2500 K	5000 K	10000 K	20000 K	40000 K
0	2.600 1 (2.695 1)	2.478 1 (2.655 1)	2.385 1 (2.729 1)	2.247 1 (2.895 1)	2.027 1 (3.168 1)
1.000 -3	2.571 1 (2.658 1)	2.454 1 (2.617 1)	2.365 1 (2.683 1)	2.233 1 (2.834 1)	2.022 1 (3.075 1)
1.585 -3	2.529 1 (2.606 1)	2.418 1 (2.563 1)	2.335 1 (2.618 1)	2.211 1 (2.747 1)	2.014 1 (2.947 1)
2.512 -3	2.431 1 (2.484 1)	2.333 1 (2.438 1)	2.264 1 (2.472 1)	2.158 1 (2.557 1)	1.984 1 (2.678 1)
3.981 -3	2.216 1 (2.234 1)	2.145 1 (2.182 1)	2.101 1 (2.181 1)	2.031 1 (2.200 1)	1.894 1 (2.213 1)
6.310 -3	1.828 1 (1.812 1)	1.788 1 (1.759 1)	1.776 1 (1.723 1)	1.765 1 (1.683 1)	1.711 1 (1.620 1)
1.000 -2	1.310 1 (1.289 1)	1.288 1 (1.246 1)	1.287 1 (1.201 1)	1.317 1 (1.150 1)	1.357 1 (1.089 1)
1.585 -2	8.368 0 (8.271 0)	8.224 0 (8.033 0)	8.125 0 (7.740 0)	8.242 0 (7.442 0)	8.800 0 (7.170 0)
2.512 -2	5.051 0 (5.027 0)	5.054 0 (5.007 0)	5.006 0 (4.913 0)	4.991 0 (4.803 0)	5.115 0 (4.707 0)
3.981 -2	2.828 0 (2.823 0)	2.957 0 (2.947 0)	3.028 0 (3.011 0)	3.072 0 (3.040 0)	3.116 0 (3.049 0)
6.310 -2	1.353 0 (1.351 0)	1.463 0 (1.459 0)	1.548 0 (1.541 0)	1.620 0 (1.607 0)	1.681 0 (1.657 0)
1.000 -1	5.456 -1 (5.451 -1)	5.848 -1 (5.836 -1)	6.141 -1 (6.116 -1)	6.389 -1 (6.337 -1)	6.567 -1 (6.455 -1)
1.585 -1	1.959 -1 (1.958 -1)	2.038 -1 (2.036 -1)	2.060 -1 (2.056 -1)	2.081 -1 (2.072 -1)	2.068 -1 (2.049 -1)
2.512 -1	6.833 -2 (6.833 -2)	6.909 -2 (6.907 -2)	6.812 -2 (6.808 -2)	6.596 -2 (6.586 -2)	6.345 -2 (6.325 -2)
3.981 -1	2.325 -2 (2.325 -2)	2.313 -2 (2.313 -2)	2.244 -2 (2.243 -2)	2.140 -2 (2.139 -2)	2.023 -2 (2.020 -2)
6.310 -1	7.853 -3 (7.853 -3)	7.757 -3 (7.757 -3)	7.501 -3 (7.500 -3)	7.115 -3 (7.114 -3)	6.667 -3 (6.663 -3)
1.000 0	2.636 -3 (2.636 -3)	2.590 -3 (2.590 -3)	2.504 -3 (2.504 -3)	2.386 -3 (2.385 -3)	2.234 -3 (2.234 -3)
1.585 0	8.516 -4 (8.516 -4)	8.428 -4 (8.428 -4)	8.241 -4 (8.241 -4)	7.928 -4 (7.928 -4)	7.492 -4 (7.492 -4)
2.512 0	2.708 -4 (2.708 -4)	2.700 -4 (2.700 -4)	2.673 -4 (2.673 -4)	2.612 -4 (2.612 -4)	2.505 -4 (2.505 -4)
3.981 0	8.515 -5 (8.515 -5)	8.532 -5 (8.532 -5)	8.530 -5 (8.530 -5)	8.458 -5 (8.458 -5)	8.259 -5 (8.259 -5)
6.310 0	2.663 -5 (2.663 -5)	2.674 -5 (2.674 -5)	2.688 -5 (2.688 -5)	2.694 -5 (2.694 -5)	2.674 -5 (2.674 -5)
1.000 1	8.328 -6 (8.328 -6)	8.363 -6 (8.363 -6)	8.419 -6 (8.419 -6)	8.480 -6 (8.480 -6)	8.511 -6 (8.511 -6)
1.585 1		2.619 -6 (2.619 -6)	2.634 -6 (2.634 -6)	2.656 -6 (2.656 -6)	2.679 -6 (2.679 -6)
2.512 1		8.219 -7 (8.219 -7)	8.256 -7 (8.256 -7)	8.314 -7 (8.314 -7)	8.390 -7 (8.390 -7)
3.981 1			2.594 -7 (2.594 -7)	2.607 -7 (2.607 -7)	2.627 -7 (2.627 -7)
6.310 1				8.194 -8 (8.194 -8)	8.239 -8 (8.239 -8)
1.000 2				2.580 -8 (2.580 -8)	2.590 -8 (2.590 -8)
1.585 2					8.157 -9 (8.157 -9)

Table C.4: Stark-broadening table for Hα, with $N_e = 10^{16}$ cm^{-3}. (Adopted from Vidal et al. 1973, Table 50.)

Table C.5: Stark-broadening table for Hβ, with $N_e = 10^{13}$ cm^{-3}. (Adopted from Vidal et al. 1973, Table 59.)

N UPPER = 4 N LOWER = 2 WAVELENGTH = 4861.33 ANGSTROM

ELECTRON DENSITY = 1.000*013 CM**(-3) DLAMBDA/DALPHA = 5.802D-001 ASYMPTOTE = 3.5261-003*DALPHA**(-5/2)

ALPHA	2500 K	5000 K	10000 K	20000 K	40000 K
0	2.531 0 (1.314 0)	1.937 0 (1.021 0)	1.441 0 (7.949 -1)	1.057 0 (6.180 -1)	7.617 -1 (4.775 -1)
3.981 -4	2.531 0 (1.319 0)	1.937 0 (1.026 0)	1.441 0 (8.001 -1)	1.057 0 (6.234 -1)	7.617 -1 (4.831 -1)
6.310 -4	2.531 0 (1.326 0)	1.937 0 (1.033 0)	1.441 0 (8.080 -1)	1.057 0 (6.315 -1)	7.617 -1 (4.914 -1)
1.000 -3	2.531 0 (1.346 0)	1.937 0 (1.053 0)	1.441 0 (8.275 -1)	1.057 0 (6.514 -1)	7.617 -1 (5.118 -1)
1.585 -3	2.531 0 (1.394 0)	1.937 0 (1.100 0)	1.441 0 (8.751 -1)	1.057 0 (6.997 -1)	7.617 -1 (5.608 -1)
2.512 -3	2.531 0 (1.508 0)	1.937 0 (1.214 0)	1.441 0 (9.886 -1)	1.057 0 (8.140 -1)	7.617 -1 (6.762 -1)
3.981 -3	2.531 0 (1.775 0)	1.937 0 (1.477 0)	1.441 0 (1.251 0)	1.057 0 (1.079 0)	7.617 -1 (9.441 -1)
6.310 -3	2.529 0 (2.355 0)	1.936 0 (2.052 0)	1.441 0 (1.830 0)	1.056 0 (1.665 0)	7.616 -1 (1.542 0)
1.000 -2	2.526 0 (3.461 0)	1.935 0 (3.166 0)	1.440 0 (2.958 0)	1.056 0 (2.814 0)	7.615 -1 (2.715 0)
1.585 -2	2.517 0 (5.048 0)	1.931 0 (4.801 0)	1.439 0 (4.632 0)	1.056 0 (4.522 0)	7.613 -1 (4.454 0)
2.512 -2	2.496 0 (6.226 0)	1.922 0 (6.126 0)	1.435 0 (6.060 0)	1.054 0 (6.022 0)	7.608 -1 (5.995 0)
3.981 -2	2.443 0 (5.651 0)	1.899 0 (5.738 0)	1.426 0 (5.782 0)	1.051 0 (5.895 0)	7.594 -1 (5.910 0)
6.310 -2	2.314 0 (3.563 0)	1.842 0 (3.691 0)	1.402 0 (3.771 0)	1.041 0 (3.842 0)	7.561 -1 (3.889 0)
1.000 -1	2.022 0 (1.596 0)	1.707 0 (1.652 0)	1.346 0 (1.695 0)	1.019 0 (1.726 0)	7.477 -1 (1.748 0)
1.585 -1	1.448 0 (5.467 -1)	1.410 0 (5.535 -1)	1.214 0 (5.573 -1)	9.652 -1 (5.583 -1)	7.270 -1 (5.583 -1)
2.512 -1	6.499 -1 (1.699 -1)	8.802 -1 (1.663 -1)	9.372 -1 (1.628 -1)	8.422 -1 (1.595 -1)	6.776 -1 (1.565 -1)
3.981 -1	1.258 -1 (5.345 -2)	2.861 -1 (5.139 -2)	4.940 -1 (4.939 -2)	5.987 -1 (4.766 -2)	5.680 -1 (4.621 -2)
6.310 -1	2.156 -2 (1.742 -2)	3.419 -2 (1.654 -2)	1.081 -1 (1.569 -2)	2.568 -1 (1.495 -2)	3.650 -1 (1.434 -2)
1.000 0	6.211 -3 (5.793 -3)	6.342 -3 (5.416 -3)	8.580 -3 (5.120 -3)	3.482 -2 (4.827 -3)	1.217 -1 (4.581 -3)
1.585 0	1.995 -3 (1.943 -3)	1.912 -3 (1.811 -3)	1.899 -3 (1.685 -3)	2.200 -3 (1.572 -3)	9.370 -3 (1.475 -3)
2.512 0	6.615 -4 (6.548 -4)	6.250 -4 (6.123 -4)	5.925 -4 (5.683 -4)	5.757 -4 (5.267 -4)	6.082 -4 (4.898 -4)
3.981 0	2.201 -4 (2.192 -4)	2.087 -4 (2.070 -4)	1.960 -4 (1.929 -4)	1.843 -4 (1.783 -4)	1.765 -4 (1.646 -4)
6.310 0	7.235 -5 (7.223 -5)	6.959 -5 (6.936 -5)	6.575 -5 (6.534 -5)	6.141 -5 (6.063 -5)	5.728 -5 (5.581 -5)
1.000 1	2.337 -5 (2.335 -5)	2.288 -5 (2.285 -5)	2.196 -5 (2.190 -5)	2.067 -5 (2.056 -5)	1.918 -5 (1.899 -5)
1.585 1	7.424 -6 (7.422 -6)	7.389 -6 (7.385 -6)	7.228 -6 (7.220 -6)	6.915 -6 (6.901 -6)	6.473 -6 (6.447 -6)
2.512 1	2.333 -6 (2.333 -6)	2.346 -6 (2.346 -6)	2.335 -6 (2.334 -6)	2.280 -6 (2.278 -6)	2.171 -6 (2.168 -6)
3.981 1	7.302 -7 (7.301 -7)	7.373 -7 (7.372 -7)	7.417 -7 (7.416 -7)	7.374 -7 (7.372 -7)	7.176 -7 (7.171 -7)
6.310 1	2.286 -7 (2.285 -7)	2.307 -7 (2.307 -7)	2.331 -7 (2.331 -7)	2.345 -7 (2.345 -7)	2.327 -7 (2.326 -7)
1.000 2	7.169 -8 (7.169 -8)	7.224 -8 (7.224 -8)	7.297 -8 (7.297 -8)	7.375 -8 (7.375 -8)	7.414 -8 (7.413 -8)
1.585 2	2.254 -8 (2.254 -8)	2.266 -8 (2.266 -8)	2.285 -8 (2.285 -8)	2.309 -8 (2.309 -8)	2.334 -8 (2.334 -8)
2.512 2	7.101 -9 (7.101 -9)	7.128 -9 (7.128 -9)	7.168 -9 (7.168 -9)	7.229 -9 (7.229 -9)	7.311 -9 (7.311 -9)
3.981 2	2.240 -9 (2.240 -9)	2.245 -9 (2.245 -9)	2.254 -9 (2.254 -9)	2.268 -9 (2.268 -9)	2.289 -9 (2.289 -9)
6.310 2	7.070-10 (7.070-10)	7.081-10 (7.081-10)	7.100-10 (7.100-10)	7.130-10 (7.130-10)	7.177-10 (7.177-10)
1.000 3		2.236-10 (2.236-10)	2.239-10 (2.239-10)	2.246-10 (2.246-10)	2.256-10 (2.256-10)
1.585 3			7.070-11 (7.070-11)	7.083-11 (7.083-11)	7.105-11 (7.105-11)
2.512 3			2.233-11 (2.233-11)	2.236-11 (2.236-11)	2.240-11 (2.240-11)
3.981 3				7.063-12 (7.063-12)	7.072-12 (7.072-12)

N UPPER = 4 N LOWER = 2 WAVELENGTH = 4861.33 ANGSTROM

ELECTRON DENSITY = 1.000+014 CM**(-3) DLAMBDA/DALPHA = 2.6930+000 ASYMPTOTE = 3.5261-003*DALPHA**(-5/2)

ALPHA	2500 K	5000 K	10000 K	20000 K	40000 K
0	4.475 0 (2.048 0)	4.286 0 (1.634 0)	3.929 0 (1.306 0)	3.401 0 (1.041 0)	2.791 0 (8.238 -1)
6.310 -4	4.475 0 (2.058 0)	4.286 0 (1.644 0)	3.928 0 (1.316 0)	3.401 0 (1.052 0)	2.791 0 (8.354 -1)
1.000 -3	4.475 0 (2.073 0)	4.286 0 (1.659 0)	3.928 0 (1.332 0)	3.401 0 (1.068 0)	2.791 0 (8.526 -1)
1.585 -3	4.476 0 (2.110 0)	4.285 0 (1.697 0)	3.928 0 (1.371 0)	3.401 0 (1.109 0)	2.791 0 (8.950 -1)
2.512 -3	4.476 0 (2.201 0)	4.285 0 (1.788 0)	3.927 0 (1.465 0)	3.400 0 (1.206 0)	2.790 0 (9.966 -1)
3.981 -3	4.478 0 (2.416 0)	4.283 0 (2.004 0)	3.925 0 (1.685 0)	3.399 0 (1.434 0)	2.790 0 (1.233 0)
6.310 -3	4.481 0 (2.886 0)	4.279 0 (2.479 0)	3.920 0 (2.172 0)	3.395 0 (1.937 0)	2.788 0 (1.755 0)
1.000 -2	4.489 0 (3.785 0)	4.269 0 (3.404 0)	3.908 0 (3.128 0)	3.387 0 (2.931 0)	2.783 0 (2.793 0)
1.585 -2	4.502 0 (5.081 0)	4.241 0 (4.791 0)	3.877 0 (4.592 0)	3.366 0 (4.464 0)	2.772 0 (4.388 0)
2.512 -2	4.497 0 (6.000 0)	4.167 0 (5.910 0)	3.799 0 (5.859 0)	3.312 0 (5.839 0)	2.743 0 (5.843 0)
3.981 -2	4.316 0 (5.361 0)	3.956 0 (5.474 0)	3.607 0 (5.576 0)	3.183 0 (5.667 0)	2.672 0 (5.756 0)
6.310 -2	3.481 0 (3.407 0)	3.358 0 (3.547 0)	3.153 0 (3.662 0)	2.879 0 (3.742 0)	2.503 0 (3.830 0)
1.000 -1	1.848 0 (1.569 0)	2.079 0 (1.636 0)	2.216 0 (1.684 0)	2.238 0 (1.722 0)	2.125 0 (1.747 0)
1.585 -1	6.429 -1 (5.709 -1)	7.484 -1 (5.779 -1)	9.504 -1 (5.803 -1)	1.210 0 (5.792 -1)	1.418 0 (5.757 -1)
2.512 -1	1.979 -1 (1.878 -1)	2.064 -1 (1.838 -1)	2.346 -1 (1.784 -1)	3.301 -1 (1.728 -1)	5.451 -1 (1.674 -1)
3.981 -1	6.257 -2 (6.134 -2)	6.123 -2 (5.872 -2)	6.115 -2 (5.564 -2)	6.574 -2 (5.318 -2)	9.237 -2 (5.066 -2)
6.310 -1	2.054 -2 (2.039 -2)	1.966 -2 (1.936 -2)	1.881 -2 (1.823 -2)	1.832 -2 (1.712 -2)	1.874 -2 (1.611 -2)
1.000 0	6.805 -3 (6.785 -3)	6.477 -3 (6.437 -3)	6.107 -3 (6.032 -3)	5.799 -3 (5.657 -3)	5.551 -3 (5.270 -3)
1.585 0	2.245 -3 (2.243 -3)	2.149 -3 (2.144 -3)	2.029 -3 (2.020 -3)	1.900 -3 (1.881 -3)	1.777 -3 (1.741 -3)
2.512 0	7.322 -4 (7.318 -4)	7.109 -4 (7.102 -4)	6.785 -4 (6.773 -4)	6.375 -4 (6.352 -4)	5.926 -4 (5.883 -4)
3.981 0	2.358 -4 (2.358 -4)	2.318 -4 (2.317 -4)	2.249 -4 (2.247 -4)	2.141 -4 (2.137 -4)	2.000 -4 (1.995 -4)
6.310 0	7.433 -5 (7.432 -5)	7.426 -5 (7.424 -5)	7.331 -5 (7.329 -5)	7.105 -5 (7.101 -5)	6.735 -5 (6.727 -5)
1.000 1	2.330 -5 (2.330 -5)	2.345 -5 (2.345 -5)	2.346 -5 (2.346 -5)	2.317 -5 (2.316 -5)	2.239 -5 (2.238 -5)
1.585 1	7.288 -6 (7.287 -6)	7.350 -6 (7.350 -6)	7.406 -6 (7.406 -6)	7.415 -6 (7.415 -6)	7.312 -6 (7.311 -6)
2.512 1	2.281 -6 (2.281 -6)	2.299 -6 (2.299 -6)	2.321 -6 (2.321 -6)	2.341 -6 (2.340 -6)	2.343 -6 (2.343 -6)
3.981 1	7.160 -7 (7.160 -7)	7.202 -7 (7.202 -7)	7.261 -7 (7.261 -7)	7.336 -7 (7.335 -7)	7.402 -7 (7.402 -7)
6.310 1	2.252 -7 (2.252 -7)	2.261 -7 (2.261 -7)	2.275 -7 (2.275 -7)	2.295 -7 (2.295 -7)	2.321 -7 (2.321 -7)
1.000 2	7.096 -8 (7.096 -8)	7.116 -8 (7.116 -8)	7.146 -8 (7.146 -8)	7.193 -8 (7.193 -8)	7.262 -8 (7.262 -8)
1.585 2	2.238 -8 (2.238 -8)	2.243 -8 (2.243 -8)	2.249 -8 (2.249 -8)	2.259 -8 (2.259 -8)	2.276 -8 (2.276 -8)
2.512 2		7.077 -9 (7.077 -9)	7.093 -9 (7.090 -9)	7.113 -9 (7.113 -9)	7.147 -9 (7.147 -9)
3.981 2			2.237 -9 (2.237 -9)	2.242 -9 (2.242 -9)	2.250 -9 (2.250 -9)
6.310 2			7.066-10 (7.066-10)	7.075-10 (7.075-10)	7.091-10 (7.091-10)
1.000 3				2.234-10 (2.234-10)	2.237-10 (2.237-10)

Table C.6: Stark-broadening table for Hβ, with $N_e = 10^{14}$ cm^{-3}. (Adopted from Vidal et al. 1973, Table 61.)

Table C.7: Stark-broadening table for Hβ, with $N_e = 10^{15}$ cm^{-3}. (Adopted from Vidal et al. 1973, Table 63.)

N UPPER = 4 N LOWER = 2 WAVELENGTH = 4861.33 ANGSTROM

ELECTRON DENSITY = 1.000+015 CM**(-3) DLAMBDA/DALPHA = 1.2500+001 ASYMPTOTE = 3.5261-003*DALPHA**(-5/2)

ALPHA	2500 K	5000 K	10000 K	20000 K	40000 K
0	3.347 0 (2.892 0)	3.154 0 (2.378 0)	3.225 0 (1.963 0)	3.503 0 (1.616 0)	3.847 0 (1.319 0)
1.000 -3	3.357 0 (2.910 0)	3.161 0 (2.396 0)	3.230 0 (1.981 0)	3.505 0 (1.636 0)	3.848 0 (1.341 0)
1.585 -3	3.373 0 (2.936 0)	3.173 0 (2.423 0)	3.237 0 (2.009 0)	3.509 0 (1.666 0)	3.850 0 (1.374 0)
2.512 -3	3.410 0 (3.002 0)	3.201 0 (2.488 0)	3.256 0 (2.078 0)	3.519 0 (1.740 0)	3.854 0 (1.454 0)
3.981 -3	3.501 0 (3.156 0)	3.270 0 (2.645 0)	3.302 0 (2.242 0)	3.544 0 (1.914 0)	3.863 0 (1.642 0)
6.310 -3	3.715 0 (3.500 0)	3.435 0 (2.996 0)	3.413 0 (2.610 0)	3.604 0 (2.306 0)	3.886 0 (2.062 0)
1.000 -2	4.169 0 (4.160 0)	3.801 0 (3.687 0)	3.668 0 (3.343 0)	3.746 0 (3.090 0)	3.940 0 (2.906 0)
1.585 -2	4.915 0 (5.101 0)	4.474 0 (4.737 0)	4.173 0 (4.496 0)	4.048 0 (4.343 0)	4.060 0 (4.258 0)
2.512 -2	5.529 0 (5.714 0)	5.218 0 (5.581 0)	4.877 0 (5.523 0)	4.531 0 (5.520 0)	4.268 0 (5.557 0)
3.981 -2	5.005 0 (5.040 0)	5.033 0 (5.140 0)	4.973 0 (5.250 0)	4.751 0 (5.367 0)	4.387 0 (5.485 0)
6.310 -2	3.273 0 (3.251 0)	3.438 0 (3.401 0)	3.585 0 (3.528 0)	3.696 0 (3.635 0)	3.698 0 (3.724 0)
1.000 -1	1.569 0 (1.557 0)	1.658 0 (1.633 0)	1.741 0 (1.690 0)	1.833 0 (1.726 0)	1.970 0 (1.759 0)
1.585 -1	6.017 -1 (5.988 -1)	6.210 -1 (6.148 -1)	6.322 -1 (6.188 -1)	6.448 -1 (6.167 -1)	6.710 -1 (6.098 -1)
2.512 -1	2.073 -1 (2.068 -1)	2.073 -1 (2.063 -1)	2.037 -1 (2.017 -1)	1.985 -1 (1.945 -1)	1.947 -1 (1.864 -1)
3.981 -1	6.907 -2 (6.901 -2)	6.790 -2 (6.778 -2)	6.540 -2 (6.516 -2)	6.229 -2 (6.183 -2)	5.905 -2 (5.814 -2)
6.310 -1	2.281 -2 (2.280 -2)	2.234 -2 (2.232 -2)	2.145 -2 (2.142 -2)	2.033 -2 (2.027 -2)	1.905 -2 (1.895 -2)
1.000 0	7.406 -3 (7.405 -3)	7.301 -3 (7.299 -3)	7.063 -3 (7.059 -3)	6.709 -3 (6.701 -3)	6.309 -3 (6.295 -3)
1.585 0	2.377 -3 (2.377 -3)	2.354 -3 (2.353 -3)	2.303 -3 (2.302 -3)	2.216 -3 (2.215 -3)	2.092 -3 (2.090 -3)
2.512 0	7.488 -4 (7.488 -4)	7.481 -4 (7.480 -4)	7.424 -4 (7.419 -4)	7.260 -4 (7.259 -4)	6.966 -4 (6.963 -4)
3.981 0	2.343 -4 (2.342 -4)	2.352 -4 (2.352 -4)	2.357 -4 (2.356 -4)	2.342 -4 (2.341 -4)	2.290 -4 (2.289 -4)
6.310 0	7.313 -5 (7.313 -5)	7.356 -5 (7.356 -5)	7.405 -5 (7.405 -5)	7.434 -5 (7.434 -5)	7.392 -5 (7.392 -5)
1.000 1	2.287 -5 (2.287 -5)	2.299 -5 (2.299 -5)	2.316 -5 (2.316 -5)	2.335 -5 (2.335 -5)	2.348 -5 (2.348 -5)
1.585 1	7.170 -6 (7.170 -6)	7.199 -6 (7.199 -6)	7.244 -6 (7.244 -6)	7.307 -6 (7.307 -6)	7.377 -6 (7.377 -6)
2.512 1	2.254 -6 (2.254 -6)	2.260 -6 (2.260 -6)	2.271 -6 (2.271 -6)	2.287 -6 (2.287 -6)	2.309 -6 (2.309 -6)
3.981 1		7.115 -7 (7.115 -7)	7.136 -7 (7.136 -7)	7.172 -7 (7.172 -7)	7.227 -7 (7.227 -7)
6.310 1		2.242 -7 (2.242 -7)	2.247 -7 (2.247 -7)	2.255 -7 (2.255 -7)	2.267 -7 (2.267 -7)
1.000 2			7.085 -8 (7.085 -8)	7.102 -8 (7.102 -8)	7.129 -8 (7.129 -8)
1.585 2				2.240 -8 (2.240 -8)	2.246 -8 (2.246 -8)
2.512 2				7.071 -9 (7.071 -9)	7.082 -9 (7.082 -9)
3.981 2					2.236 -9 (2.236 -9)

N UPPER = 4 N LOWER = 2 WAVELENGTH = 4861.33 ANGSTROM

ELECTRON DENSITY = 1.000+016 CM**(-3) DLAMBDA/DALPHA = 5.8020+001 ASYMPTOTE = 3.5261-003*DALPHA**(-5/2)

ALPHA	2500 K	5000 K	10000 K	20000 K	40000 K
0	3.798 0 (3.777 0)	3.173 0 (3.135 0)	2.738 0 (2.664 0)	2.423 0 (2.270 0)	2.238 0 (1.923 0)
1.000 -3	3.811 0 (3.791 0)	3.184 0 (3.147 0)	2.749 0 (2.676 0)	2.434 0 (2.284 0)	2.248 0 (1.938 0)
1.585 -3	3.831 0 (3.811 0)	3.200 0 (3.165 0)	2.765 0 (2.694 0)	2.450 0 (2.303 0)	2.264 0 (1.960 0)
2.512 -3	3.879 0 (3.860 0)	3.242 0 (3.209 0)	2.806 0 (2.739 0)	2.490 0 (2.352 0)	2.302 0 (2.014 0)
3.981 -3	3.993 0 (3.978 0)	3.342 0 (3.314 0)	2.903 0 (2.847 0)	2.589 0 (2.469 0)	2.397 0 (2.146 0)
6.310 -3	4.247 0 (4.239 0)	3.570 0 (3.553 0)	3.130 0 (3.093 0)	2.818 0 (2.736 0)	2.622 0 (2.444 0)
1.000 -2	4.729 0 (4.731 0)	4.050 0 (4.028 0)	3.601 0 (3.594 0)	3.306 0 (3.285 0)	3.112 0 (3.057 0)
1.585 -2	5.374 0 (5.385 0)	4.765 0 (4.758 0)	4.373 0 (4.398 0)	4.144 0 (4.190 0)	3.992 0 (4.078 0)
2.512 -2	5.655 0 (5.663 0)	5.282 0 (5.299 0)	5.101 0 (5.134 0)	5.023 0 (5.089 0)	4.991 0 (5.128 0)
3.981 -2	4.822 0 (4.823 0)	4.829 0 (4.833 0)	4.874 0 (4.884 0)	4.957 0 (4.980 0)	5.058 0 (5.111 0)
6.310 -2	3.086 0 (3.085 0)	3.268 0 (3.267 0)	3.397 0 (3.395 0)	3.508 0 (3.503 0)	3.611 0 (3.601 0)
1.000 -1	1.500 0 (1.499 0)	1.632 0 (1.631 0)	1.711 0 (1.709 0)	1.761 0 (1.757 0)	1.794 0 (1.785 0)
1.585 -1	5.959 -1 (5.958 -1)	6.449 -1 (6.446 -1)	6.667 -1 (6.661 -1)	6.710 -1 (6.697 -1)	6.657 -1 (6.630 -1)
2.512 -1	2.116 -1 (2.116 -1)	2.244 -1 (2.243 -1)	2.272 -1 (2.271 -1)	2.233 -1 (2.231 -1)	2.149 -1 (2.145 -1)
3.981 -1	7.131 -2 (7.130 -2)	7.415 -2 (7.414 -2)	7.417 -2 (7.416 -2)	7.220 -2 (7.217 -2)	6.878 -2 (6.874 -2)
6.310 -1	2.347 -2 (2.347 -2)	2.400 -2 (2.400 -2)	2.395 -2 (2.394 -2)	2.339 -2 (2.338 -2)	2.236 -2 (2.236 -2)
1.000 0	7.520 -3 (7.520 -3)	7.593 -3 (7.593 -3)	7.605 -3 (7.605 -3)	7.507 -3 (7.507 -3)	7.275 -3 (7.274 -3)
1.585 0	2.388 -3 (2.388 -3)	2.390 -3 (2.390 -3)	2.391 -3 (2.391 -3)	2.380 -3 (2.380 -3)	2.343 -3 (2.343 -3)
2.512 0	7.444 -4 (7.444 -4)	7.440 -4 (7.440 -4)	7.462 -4 (7.462 -4)	7.486 -4 (7.485 -4)	7.470 -4 (7.469 -4)
3.981 0	2.319 -4 (2.319 -4)	2.317 -4 (2.317 -4)	2.326 -4 (2.326 -4)	2.340 -4 (2.340 -4)	2.354 -4 (2.354 -4)
6.310 0	7.243 -5 (7.243 -5)	7.237 -5 (7.237 -5)	7.261 -5 (7.261 -5)	7.306 -5 (7.306 -5)	7.367 -5 (7.367 -5)
1.000 1		2.268 -5 (2.268 -5)	2.274 -5 (2.274 -5)	2.285 -5 (2.285 -5)	2.303 -5 (2.303 -5)
1.585 1			7.141 -6 (7.141 -6)	7.166 -6 (7.166 -6)	7.209 -6 (7.209 -6)
2.512 1			2.248 -6 (2.248 -6)	2.253 -6 (2.253 -6)	2.263 -6 (2.263 -6)
3.981 1				7.099 -7 (7.099 -7)	7.120 -7 (7.120 -7)
6.310 1					2.243 -7 (2.243 -7)
1.000 2					7.078 -8 (7.078 -8)

Table C.8: Stark-broadening table for Hβ, with $N_e = 10^{16}$ cm^{-3}. (Adopted from Vidal et al. 1973, Table 65.)

Appendix D
Chandra instrumentation

Focal Plane Arrays		
HRC-I:	CsI-coated MCPpair	90 × 90 mm coated (93 × 93 mm open)
HRC-S:	CsI-coated MCPpairs	3-100 × 20 mm
Field of view	HRC-I:	∼ 30 × 30 arcmin
	HRC-S:	6 × 99 arcmin
MCP Bias angle:		6°
UV/Ion Shields:		
	HRC-I:	5520 Å Polyimide, 763 Å Al
	HRC-S:	
	Inner segment	2750 Å Polyimide, 307 Å Al
	Inner segment "I"	2750 Å Polyimide, 793 Å Al
	Outer segment	2090 Å Polyimide, 304 Å Al
	Outer segment (LESF)	2125 Å Polyimide, 1966 Å Al
Spatial resolution	FWHM	∼ 20μm, ∼ 0.4 arcsec
	HRC-I: pore size	10μm
	HRC-S: pore size	12.5μm
	HRC-I: pore spacing	12.5μm
	HRC-S: pore spacing	15μm
	pixel size (electronic readout)	6.42938μm [0.13175 arcsec pixel^{-1}]
Energy range:		0.08 – 10.0 keV
Spectral resolution	$\Delta E/E$	∼ 1 @1keV
MCP Quantum efficiency		30% @ 1.0 keV 10% @ 8.0 keV
On-Axis Effective Area:	HRC-I, @ .277 keV	133 cm^2
	HRC-I, @ 1 keV	227 cm^2
Time resolution		16 μsec (see Section 7.11)
Limiting Sensitivity	point source, 3σ detection in 3×10^5 s (power law spectrum: $\alpha = 1.4$, $N_H = 3 \times 10^{20}$ cm^{-2})	9×10^{-16}erg cm^{-2} s^{-1}
Quiescent background	HRC-I	1.7×10^{-5} cts s^{-1} arcsec^{-2}
in level 2 data	HRC-S	6.3×10^{-5} cts s^{-1} arcsec^{-2}
Intrinsic dead time		50 μs
Constraints:	telemetry limit	184 cts s^{-1}
	maximum counts/observation/aimpoint	450000 cts
	linearity limit (on-axis point source)	
	HRC-I	∼ 5 cts s^{-1} (2 cts s^{-1} pore^{-1})
	HRC-S	∼ 25 cts s^{-1} (10 cts s^{-1} pore^{-1})

Table D.1: HRC parameters. (Adopted from *Chandra* X-ray Center 2011, p. 137, Table 7.1.)

Wavelength range	1.2 -175 Å (HRC-S)
	1.2 60 Å (ACIS-S)
Energy range	70–10000 eV (HRC-S)
	200–10000 eV (ACIS-S)
Resolution ($\Delta\lambda$, FWHM)	0.05 Å
Resolving Power ($E/\Delta E$)	$\geq$ 1000 (50–160 Å)
	$\approx 20 \times \lambda$ (3-50 Å)
Dispersion	1.148 Å/mm
Plate scale	48.80 μm/arcsecond
Effective area (1st order)	1–25 cm^2 (with HRC-S)
	4–200 cm^2 (with ACIS-S)
Background (quiescent)	12–26 (at 50 and 175 Å) cts/0.07-Å/100-ksec (HRC-S after LETG/PI filtering)
	$\ll$ 0.01 cts/pixel/100-ksec (ACIS-S, order sorted)
Detector angular size	3.37' $\times$ 101' (HRC-S)
	8.3' $\times$ 50.6' (ACIS-S)
Pixel size	6.43 $\times$ 6.43 μm (HRC-S)
	24.0 $\times$ 24.0 μm (ACIS-S)
Temporal resolution	16 μsec (HRC-S in Imaging Mode, center segment only)
	$\sim$10 msec (HRC-S in default mode)
	2.85 msec–3.24 sec (ACIS-S, depending on mode)
Rowland diameter	8637 mm (effective value)
Grating material	gold
Facet frame material	stainless steel
Module material	aluminum
LETG grating parameters	
Period	0.991216 $\pm$0.000087 μm
Thickness	0.474 $\pm$0.0305 μm
Width	0.516 $\pm$0.0188 μm
Bar Side Slope	83.8 $\pm$2.27 degrees
Fine-support structure	
Period	25.4 μm
Thickness	2.5 μm
Obscuration	$<$ 10%
Dispersion	29.4 Å/mm
Material	gold
Coarse-support structure	
Triangular height	2000 μm
Width	68 μm
Thickness	$<$ 30 μm
Obscuration	$<$ 10%
Dispersion	2320 Å/mm
Material	gold

Table D.2: LETG parameters. (Adopted from *Chandra* X-ray Center 2011, p. 226, Table 9.1.)

Focal plane arrays:	
I-array	4 CCDs placed to lie tangent to the focal surface
S-array	6 CCDs in a linear array tangent to the grating Rowland circle
CCD format	1024 by 1024 pixels
Pixel size	23.985 microns (0.4920±0.0001 arcsec)
Array size	16.9 by 16.9 arcmin ACIS-I 8.3 by 50.6 arcmin ACIS-S
On-axis effective Area	110 cm^2 @ 0.5 keV (FI)
(integrated over the *PSF*	600 cm^2 @ 1.5 keV (FI)
to >99% encircled energy)	40 cm^2 @ 8.0 keV (FI)
Quantum efficiency	> 80% between 3.0 and 6.5 keV
(frontside illumination)	> 30% between 0.7 and 11.0 keV
Quantum efficiency	> 80% between 0.8 and 5.5 keV
(backside illumination)	> 30% between 0.4 and 10.0 keV
(QEs do not include contaminant layer transmission)	
Charge transfer inefficiency(parallel)	FI: $\sim 2\times10^{-4}$; BI: $\sim 2\times10^{-5}$
Charge transfer inefficiency(serial)	S3(BI): $\sim 7\times10^{-5}$; S1(BI): $\sim 1.5\times10^{-4}$; FI: $< 2\times10^{-5}$
System noise	$<\sim$ 2 electrons (rms) per pixel
Max readout-rate per channel	$\sim$ 100 kpix/sec
Number of parallel signal channels	4 nodes per CCD
Pulse-height encoding	12 bits/pixel
Event threshold	FI: 38 ADU ($\sim$150–350 eV) BI: 20 ADU ($\sim$150–220 eV)
Split threshold	13 ADU
Max internal data-rate	6.4 Mbs (100 kbs $\times 4 \times 16$)
Output data-rate	24 kb per sec
Minimum row readout time	2.8 ms
Nominal frame time	3.2 sec (full frame)
Allowable frame times	0.2 to 10.0 s
Frame transfer time	40 μsec (per row)
Point-source sensitivity	4×10^{-15} ergs cm^{-2} s^{-1} in 10^4 s (0.4-6.0 keV)
Detector operating temperature	−90 to −120°C

Table D.3: ACIS parameters. (Adopted from *Chandra* X-ray Center 2011, p. 85, Table 6.1.)

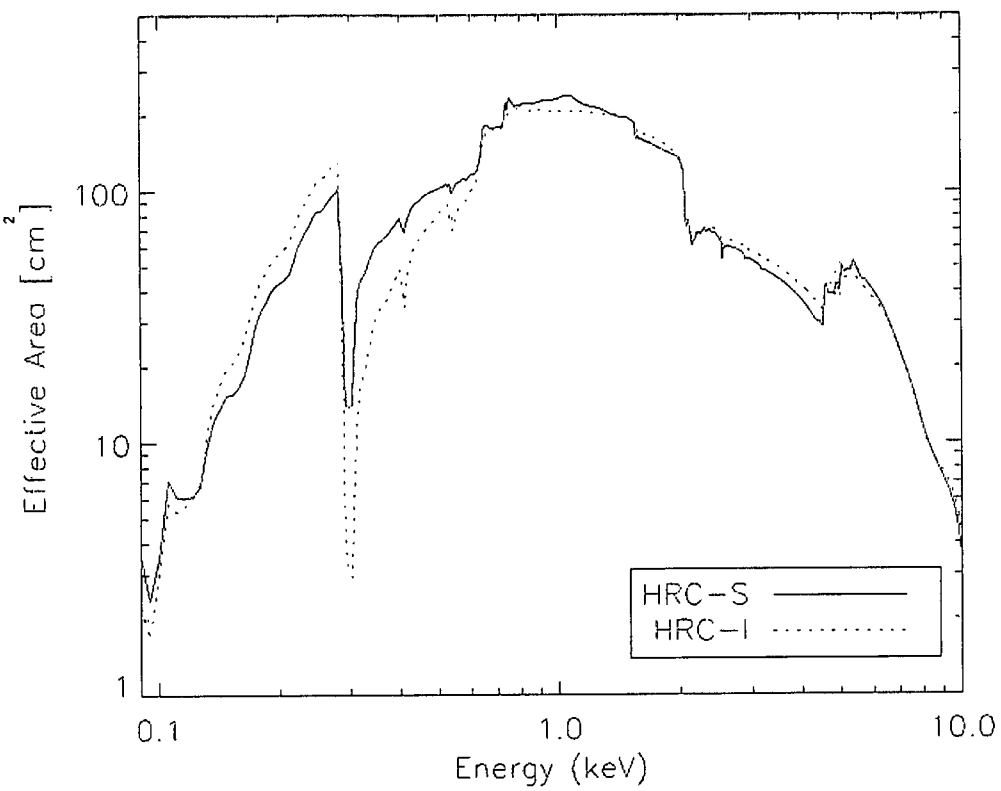

Fig. D.1: The effective area of the HRMA/HRC-I combination and the HRMA/HRC-S combination in imaging mode. (Adopted from *Chandra* X-ray Center 2011, p. 155, Fig. 7.16.)

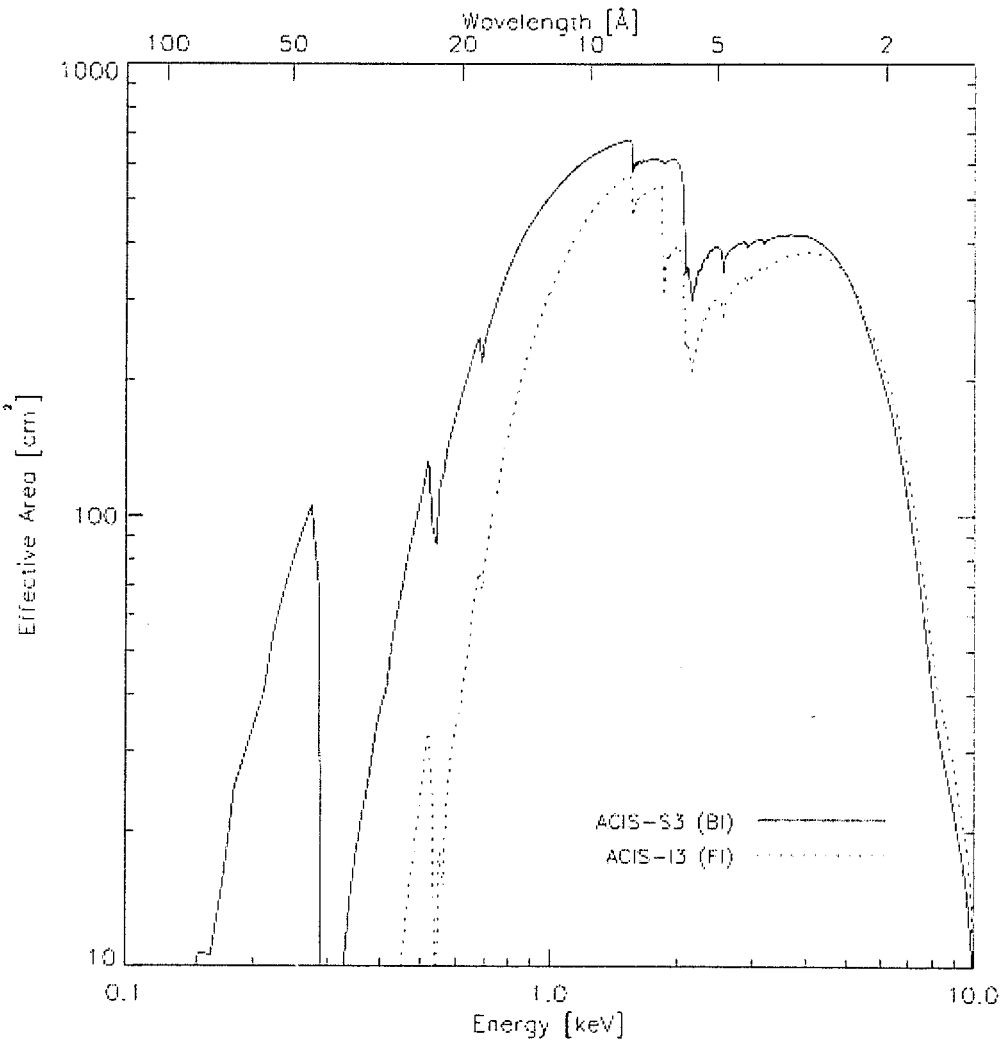

Fig. D.2: The HRMA/ACIS effective area. The dashed line is for the front-illuminated (FI) CCD I3, and the solid line is for the back-illuminated (BI) CCD S3. (Adopted from *Chandra* X-ray Center 2011, p. 89, Fig. 6.4.)